Journal of Heat Transfer

Published Monthly by ASME

VOLUME 127 • NUMBER 11 • NOVEMBER 2005

Editor, **YOGESH JALURIA (2010)**

Associate Editors
S. ACHARYA (2006)
N. K. ANAND (2006)
L. C. BURMEISTER (2008)
B. FAROUK (2006)
S. V. GARIMELLA (2007)
C. P. GRIGOROPOULOS (2006)
A. HAJI-SHEIKH (2008)
A. M. JACOBI (2008)
Y. JOSHI (2008)
S. G. KANDLIKAR (2007)
J. M. KHODADADI (2007)
J. LAGE (2008)
J. H. LIENHARD V (2006)
P. M. LIGRANI (2006)
R. M. MANGLIK (2006)
C. H. OH (2007)
R. PITCHUMANI (2007)
R. P. ROY (2007)
B. SUNDEN (2008)
K. A. THOLE (2007)
W. W. YUEN (2008)

Past Editors
V. DHIR
J. R. HOWELL
R. VISKANTA
G. M. FAETH
K. T. YANG
E. M. SPARROW

HEAT TRANSFER DIVISION
Chair, **MICHAEL K. JENSEN**
Vice Chair, **RODNEY W. DOUGLASS**
Past Chair, **R. D. SKOCYPEC**

PUBLICATIONS COMMITTEE
Chair, **ARTHUR G. ERDMAN**

OFFICERS OF THE ASME
President, **RICHARD E. FEIGEL**
Executive Director,
VIRGIL R. CARTER
Treasurer,
THOMAS D. PESTORIUS

PUBLISHING STAFF

Managing Director, Publishing
PHILIP DI VIETRO

Production Coordinator
COLIN McATEER

Production Assistant
MARISOL ANDINO

Transactions of the ASME, Journal of Heat Transfer (ISSN 0022-1481) is published monthly by The American Society of Mechanical Engineers, Three Park Avenue, New York, NY 10016. Periodicals postage paid at New York, NY and additional mailing offices. POSTMASTER: Send address changes to Transactions of the ASME, Journal of Heat Transfer, c/o THE AMERICAN SOCIETY OF MECHANICAL ENGINEERS, 22 Law Drive, Box 2300, Fairfield, NJ 07007-2300. **CHANGES OF ADDRESS** must be received at Society headquarters seven weeks before they are to be effective. Please send old label and new address.

STATEMENT from By-Laws. The Society shall not be responsible for statements or opinions advanced in papers or ... printed in its publications (B7.1, Para. 3).

COPYRIGHT © 2005 by The American Society of Mechanical Engineers. For authorization to photocopy material for internal or personal use under those circumstances not falling within the fair use provisions of the Copyright Act, contact the Copyright Clearance Center (CCC), 222 Rosewood Drive, Danvers, MA 01923, tel: 978-750-8400, www.copyright.com. Request for special permission or bulk copying should be addressed to Reprints/Permission Department. Canadian Goods & Services Tax Registration #126148048

TECHNICAL PAPERS

Evaporation, Boiling, and Condensation

Micro/Nanoscale Heat Transfer

Radiative Heat Transfer

Two-Phase Flow and Heat Transfer

Bubbles, Particles, and Droplets

(Contents continued on inside back cover)

This journal is printed on acid-free paper, which exceeds the ANSI Z39.48-1992 specification for permanence of paper and library materials. ∞™
♲ 85% recycled content, including 10% post-consumer fibers.

Downloaded 05 Feb 2011 to 141.219.44.39. Redistribution subject to ASME license or copyright; see http://www.asme.org/terms/Terms_Use.cfm

(**Contents continued**)

Journal of Heat Transfer **Volume 127, Number 11** **NOVEMBER 2005**

TECHNICAL BRIEFS

ANNOUNCEMENTS

The ASME Journal of Heat Transfer is abstracted and indexed in the following:

Applied Science and Technology Index, Chemical Abstracts, Chemical Engineering and Biotechnology Abstracts (Electronic equivalent of Process and Chemical Engineering), Civil Engineering Abstracts, Compendex (The electronic equivalent of Engineering Index), Corrosion Abstracts, Current Contents, E & P Health, Safety, and Environment, Ei EncompassLit, Engineered Materials Abstracts, Engineering Index, Enviroline (The electronic equivalent of Environment Abstracts), Environment Abstracts, Environmental Engineering Abstracts, Environmental Science and Pollution Management, Fluidex, Fuel and Energy Abstracts, Index to Scientific Reviews, INSPEC, International Building Services Abstracts, Mechanical & Transportation Engineering Abstracts, Mechanical Engineering Abstracts, METADEX (The electronic equivalent of Metals Abstracts and Alloys Index), Petroleum Abstracts, Process and Chemical Engineering, Referativnyi Zhurnal, Science Citation Index, SciSearch (The electronic equivalent of Science Citation Index), Theoretical Chemical Engineering

Heterogeneous Nucleation With Artificial Cavities

Yusen Qi

James F. Klausner
e-mail: klaus@ufl.edu

Department of Mechanical and Aerospace Engineering,
University of Florida,
P.O. Box 116300,
Gainesville, FL 32611-6300

Bubble incipience in artificial cavities manufactured from silicon has been studied using gas nucleation and pool boiling. Moderately wetting water and highly wetting ethanol have both been used as the bulk fluid with cylindrical cavities, as well as those with a triangle, square, and rectangle shape cross section. Nominal cavity sizes range from 8 to 60 μm. *The incipience conditions observed for water using both gas nucleation and pool boiling suggest that bubble initiation originates from a concave meniscus. Cornwell's contact angle hysteresis theory for vapor-trapping cavities is used to explain the gas nucleation results. The pool boiling results are more difficult to explain. Using ethanol, cavities appeared to be completely flooded and were not activated using either gas nucleation or pool boiling. Using water and gas nucleation, cavities were almost always activated, provided the incipience criterion was satisfied; in contrast cavities in pool boiling with water activated with different superheats during different experiments. The difference in incipience behavior between gas nucleation and pool boiling with water is explained based on vapor-trapping and thermal suppression considerations. Based on limited experimental results, it appears that the backpressure does not influence gas bubble incipience, provided the pressure difference is the same. The experimental results presented affirm the theory of heterogeneous nucleation from vapor-trapping cavities provided contact angle hysteresis and vapor trapping are fully accounted for. However, the results also suggest that the theoretical considerations required for a deterministic model for incipience from vapor-trapping cavities during boiling is more complex than previously hypothesized.* [DOI: 10.1115/1.2039111]

1 Introduction

Vapor bubble nucleation in boiling systems has been the focus of many experimental investigations over half a century. From these, it has been well established that surface topography, surface wettability, fluid properties, and wall superheat exert a controlling influence on the formation of nucleation sites. However, a general model that reliably predicts the nucleation site density during boiling remains elusive. It has been generally accepted that heterogeneous nucleation in boiling systems originates from vapor-trapping cavities, and heterogeneous nucleation theories based on vapor trapping have been accordingly developed. Contrary to this long held belief, Qi and Klausner [1] and Theofanous [2] recently demonstrated that heterogeneous nucleation does not exclusively originate from vapor-trapping cavities, although when vapor-trapping cavities are available those are the most likely locations for nucleation to occur. This work will focus on heterogeneous nucleation from artificial cavities with the purpose of validating heterogeneous nucleation theory.

Griffith and Wallis [3] developed a predictive model for the minimum wall superheat required to activate a conical vapor-trapping cavity formed on a copper surface with a steel gramophone needle. With water, they observed that the measured wall superheat required to activate the artificial cavity is in reasonably good agreement with the prediction. Sernas and Hooper [4] observed boiling nucleation from artificial cavities made with a diamond phonograph needle on a chromel heating strip. It was observed that the activation of water vapor bubbles from the cavities was unstable. Ebullition from the artificial cavities ceased after some time, leaving boiling activity at only naturally formed sites. Preckshot and Denny [5] studied the ebullition of carbon tetrachloride from conical and cylindrical cavities. It was observed that steep walled and deep cavities served as the best sites for nucleation. They suggested the cavity depth-to-mouth diameter ratio should exceed unity in order to activate cavities with a highly wetting fluid. Rammig and Weiss [6] investigated nitrogen incipience, bubble growth and departure from artificial cavities with mouth diameters ranging in size from 27 to 70 μm. It was observed that the 0.04 K superheat required to activate the 70 μm cavity is in good agreement with the incipience model suggested by Griffith and Wallis. Kosky [7] studied the dynamics of the meniscus as water vapor bubbles depart from a 100 μm glass capillary tube. High speed cinematography revealed that the meniscus penetrates deep into the capillary tube just following bubble departure. The maximum penetration ranged from 200 to 300 μm.

Heled et al. [8] manufactured an array of cylindrical cavities on a highly smooth surface electroplated with nickel. They studied pool boiling heat transfer rates with highly and moderately wetting fluids. Surfaces with more densely packed arrays of cavities yielded higher heat transfer rates. Messina and Park [9] also studied pool boiling heat transfer of R113 from polished copper surfaces in which a precise array of pits was formed using wet etching. It was observed that increasing the pit density enhances the heat transfer rate. It was also observed that extremely shallow or jagged pits were substantially more efficient for nucleation than well-formed pits.

Recently, Shoji et al. [10,11] conducted extensive stability and dynamical studies of bubble incipience with water on a thin copper surface. The smooth surface contained conical, cylindrical, and re-entrant artificial cavities that were manufactured using diamond bit pricking and microelectrical discharge machining. It was observed that cylindrical and re-entrant cavities are typically stable, while conical cavities demonstrate intermittent behavior. It was also found that cavities with a smaller mouth diameter are typically more stable than those with a larger mouth diameter.

In a very recent investigation, Pesse et al. [12] studied the gas entrapment process in precisely manufactured rectangular cavities with entrance widths of 5, 15, 30, and 50 μm. The cavities were manufactured by micromachining rectangular channels into sili-

---

Contributed by the Heat Transfer Division of ASME for publication in the Journal of Heat Transfer. Manuscript received January 6, 2005; final manuscript received May 27, 2005. Review conducted by: Ramendra P. Roy.

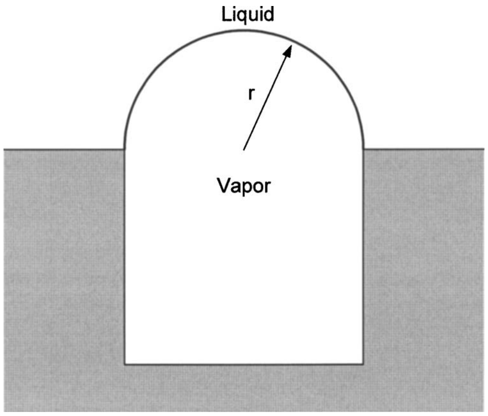

Fig. 1 Convex vapor meniscus protruding from a cylindrical cavity

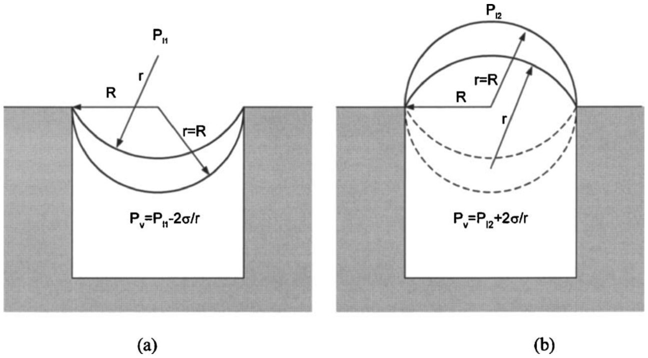

(a) (b)

Fig. 2 Schematic drawing of liquid/vapor interface

con and adhering a glass cover over the channels to form the cavities. Isothermal tests were conducted with water flooding the test surface. Different cleaning procedures were used to alter the wettability conditions. In all cases, the liquid/solid contact angle is less than the cavity minimum side angle (90°). Air is initially trapped as water spreads over the cavities, and the cavities eventually flood as air diffuses into the water. The time scale for flooding ranges from hours to days. For larger contact angles a single meniscus typically forms, while for smaller contact angles two menisci typically form within the cavity. One is located at the entrance and the other at the closed end of the microchannel. The meniscus at the closed end is concave toward the opening of the channel.

According to the vapor-trapping heterogeneous nucleation theory proposed by Griffith and Wallis, a convex vapor meniscus will protrude from a vapor-trapping cavity, with radius r, as shown in Fig. 1 and the amount of wall superheat required to activate that cavity for boiling is

$$\Delta T_{sat} = \frac{2\sigma T_{sat}}{\rho_v h_{fg} r} \tag{1}$$

where σ is the surface tension, ρ_v is the vapor density, and h_{fg} is the latent heat of vaporization. When the gas nucleation technique (discussed in detail by Lorenz [13], Eddington and Kenning [14–16], and Qi et al. [17]) is used to activate the same cavity, the magnitude of depressurization required is

$$\Delta P = \frac{2\sigma}{r}. \tag{2}$$

Cornwell [18] was unconvinced that re-entrant cavities on naturally formed surfaces were responsible for incipience in boiling. Instead, he studied the microroughness inside cavities and taking into account contact angle hysteresis, he demonstrated that a concave vapor meniscus is stable in a conical cavity. Based on similar arguments, a concave meniscus as shown in Fig. 2(*a*) can exist in a cylindrical cavity, although stability cannot be claimed. The observations of Kosky in a glass capillary tube seem to support this idea. The magnitude of ΔP required to activate a cavity with a concave meniscus will depend on its radius of curvature R. The maximum ΔP required occurs when the meniscus radius of curvature equals the cavity radius: $r=R$. In order to activate the cavity, the meniscus first needs to be flipped over as shown in Fig. 2(*b*), and then activated. The magnitude of the maximum depressurization required to activate a cavity with a concave meniscus, as shown in Fig. 2(*a*), is double that given by Eq. (2).

This work considers the activation of artificial cavities with mouth diameters ranging from 8–60 μm manufactured on silicon using deep reactive ion etching (DRIE). Experiments with both moderately wetting water and highly wetting ethanol are considered. The objective of this work is to systematically evaluate the usefulness of the incipience models proposed by Griffith and Wallis and Cornwell for boiling and gas nucleation systems.

2 Experimental Facilities

2.1 Gas Nucleation Facility. An existing gas nucleation facility, described previously by Qi et al. [17] and shown in Fig. 3, was used for the present experiments. The gas nucleation experiments are operated at temperature 25°C. A brief description of the facility operation is given here. A magnetically driven micropump is used to circulate high-pressure liquid that is maintained under high pressure with charged air cylinders. As circulating liquid is sprayed into the half filled epoxy-lined steel storage tank, air diffuses into the liquid and eventually saturates it. The typical circulating time to ensure complete saturation is 40 min. With valves 3 and 4 closed, valve 2 is opened and then valve 1 is opened in sequence. Adjusting the valves in this sequence allows the test section to equilibrate to the same pressure as the liquid storage tank prior to flooding. The test section is mounted horizontally 30 cm below the centerline of the liquid tank. The liquid gravitates into the test section while high pressure is maintained. Once filled, the pressure and temperature of the liquid in the test section are recorded. Discharge valve 3 is opened to allow depressurization of the test section, and nucleation sites that form on the microfabricated silicon surface are captured with a NAC high-speed digital camera from the side view. The test section pressure and temperature are again recorded following depressurization. The time elapsed prior to recording temperature and pressure is on the

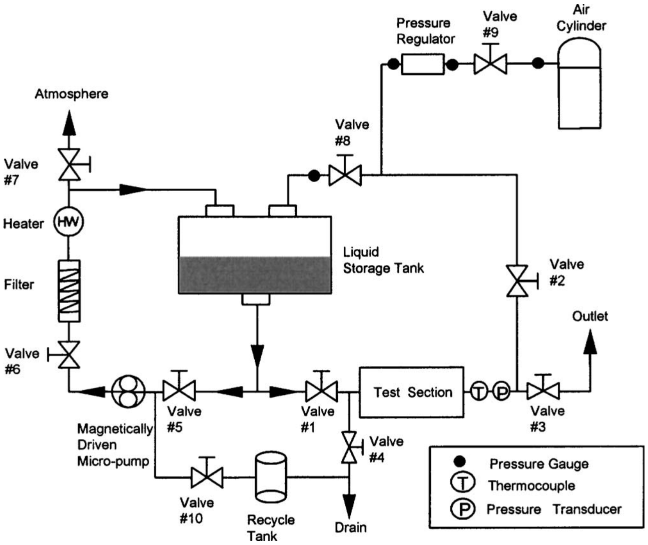

Fig. 3 Schematic diagram of gas nucleation facility

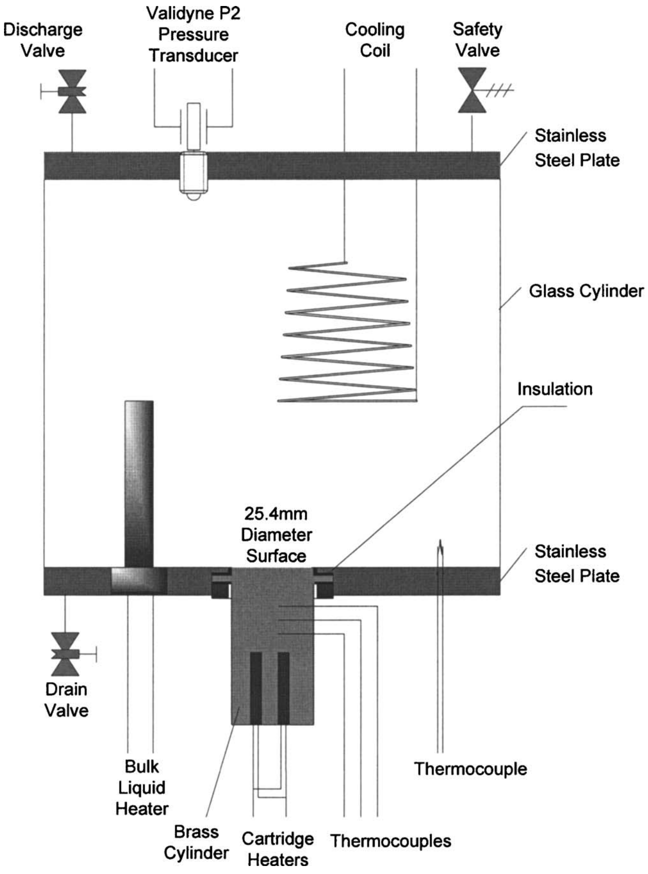

Fig. 4 Assembled view of pool boiling chamber

order of 10 s. The silicon surface is adhered to a brass insert, which resides in a 25.4 mm recess in the test section. The outlet of valve 3 leads either to atmosphere or a pressure regulator attached to a compressed air supply. The pressure regulator permits backpressure to be placed on the test section following depressurization. After recording all necessary data, the test section is drained and the silicon surface is dried by blowing dry air on the top of the surface with the help of radiation from a 1000 W mercury lamp.

Since the pressure observed during the experiments covers a wide range, two types of pressure transducers are used to cover different pressure ranges. A Viatran strain gauge type pressure transducer is used to measure the high-pressure range (35–150 kPa). A Validyne magnetic reluctance pressure transducer is used to measure the low-pressure range (0–35 kPa). The uncertainty of the Viatran pressure measurement is ±0.2 kPa and that of the Validyne pressure measurement is ±0.08 kPa. The uncertainty of the temperature measurement is ±0.5°C.

2.2 Pool Boiling Facility. An existing pool boiling facility, described previously by Qi and Klausner [1] and shown in Fig. 4, is used to compare boiling incipience on the microfabricated surface with that in the gas nucleation facility. The boiling chamber consists of a borosilicate cylinder that is compressed between two stainless steel end plates and sealed with Viton®. A cooling coil that is connected with a small chiller is mounted on the upper part of the boiling chamber to maintain a constant pressure, 100 KPa. Heat is supplied to the boiling surface by four high-density cartridge heaters embedded in a brass cylinder. The upper surface of the cylinder is mounted flush with the lower end plate. The silicon boiling substrate with 500 μm thickness is adhered to the brass surface using aluminum-based high conductivity Duralco™ 132 cement. Five thermocouples, with a bead diameter of approximately 500 μm, are adhered directly underneath five fabricated cavities. The thermocouple response time is insufficient to capture the transient temperature associated with bubble growth and detachment, and thus only average temperature is measured. The pressure in the boiling chamber is measured with a Validyne P2 pressure transducer and has an uncertainty of ±0.2 kPa. The uncertainty of the temperature measurements is ±0.5°C. The boiling chamber is initially filled with cold liquid that contains air. Prior to recording data, the boiling chamber is allowed to operate with high heat flux (vigorous boiling) for an hour in order to achieve a steady thermal state and degas the facility. The heat flux is then reduced so that all nucleation sites are deactivated, but the heating surface temperature remains above the saturation temperature. Incipience measurements are then made with increasing heat flux. After a daily experimental operation, the system is turned off and it cools down to room temperature. The degassing and operational procedure are performed again the next time the system is placed in operation. The boiling chamber is oriented vertically for all experiments and visualization of vapor bubble incipience is accomplished with the high-speed digital camera from the side view.

2.3 Artificial Cavities. Cylindrical cavities as well as those with triangle, square, and rectangle shape cross sections have been manufactured on the silicon surface using photolithography and DRIE. The process of manufacturing the cavities involves designing a mask using computer-aided design software and having the mask fabricated. A thin layer of photosensitive coating (photoresist) is applied to the silicon wafer. The mask is placed over the wafer and exposed to ultraviolet light. The exposed photoresist will be dissolved in the developer, while the unexposed area remains unchanged. The next process is to apply DRIE to form the cavities. The advantage of using DRIE over wet etching is that very small features can be achieved on the surface. Following DRIE, the silicon is thoroughly rinsed in acetone, methanol, and deionized water to remove the photoresist and other contaminants. Figure 5 shows the two-dimensional profiles of a 60 μm nominal diameter artificial cavity that was scanned using a Wyko NT 1000 interferometer. It is observed that the cross section of the cavity is very uniform, and although microroughness within the cavity is not evident from this profile, an impression of the cavity was made using metallic glass modeling and shows significant microroughness within the cavity. The bottom of the cavity is nearly flat with some curvature at the corners. Different samples were made with different arrays of cavity sizes and shapes. Those different layouts will be discussed when describing different experiments.

Activation of artificial cavities on the silicon surface has been studied with distilled water and ethanol. The measured contact angle of water on silicon is 21° with a standard deviation of 1.2°. An ethanol droplet will spread spontaneously on a horizontally mounted silicon surface.

3 Experimental Results

3.1 Effect of Backpressure on Gas Nucleation Bubble Activation. According to Eq. (2), whether or not a bubble is activated at a vapor-trapping cavity during gas nucleation depends only on the pressure change during depressurization. It should be independent of the backpressure. However, there has been recent concern [19] that the magnitude of the backpressure may influence bubble activation. In order to study the effect of backpressure on gas nucleation cavity activation, a silicon surface containing a linear array of cylindrical cavities ranging in diameter from 8 to 60 μm was prepared. Each cavity has a depth of 45 μm and is separated by a spacing of 4 mm, as shown in the layout in Fig. 6. The surface was placed in the gas nucleation facility using water as the test fluid with different magnitudes of depressurization (ΔP). During depressurization the test section was either allowed to expand to atmospheric pressure or to a backpressure ranging from 25 to 45 kPa. The net depressurization ranged from 11 to 76 kPa. Following depressurization, the bubble formation process was recorded using the high-speed video camera, and

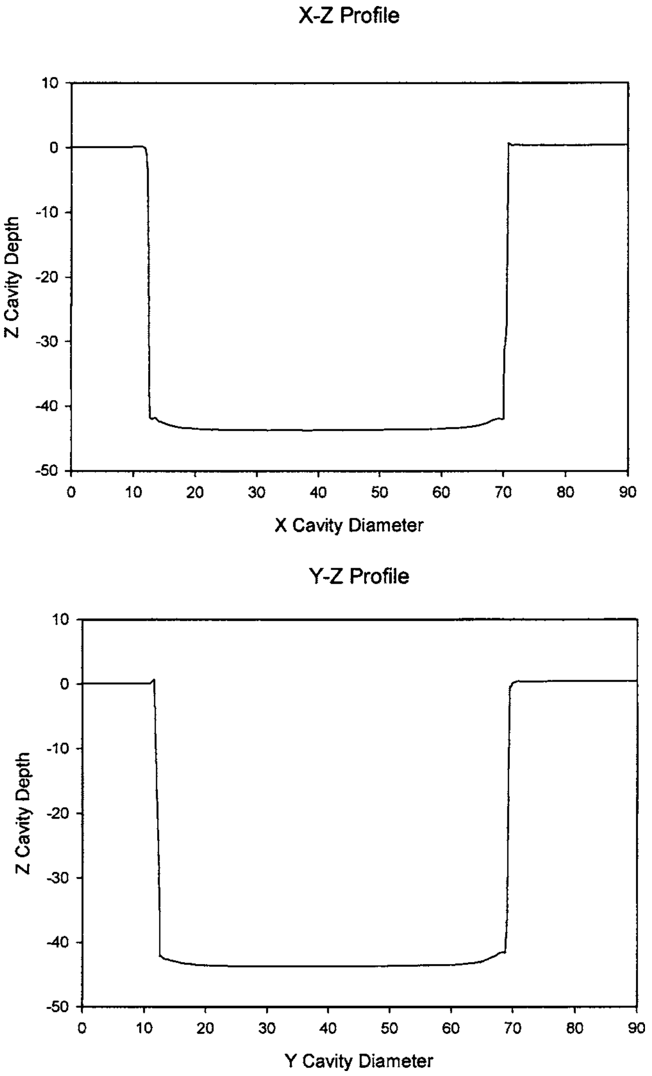

Fig. 5 Two-dimensional measurement of cylindrical cavity with 60 μm mouth diameter and 45 μm depth

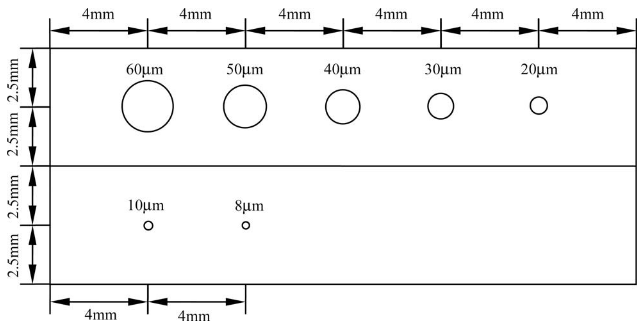

Fig. 6 Layout of cylindrical cavities on silicon surface

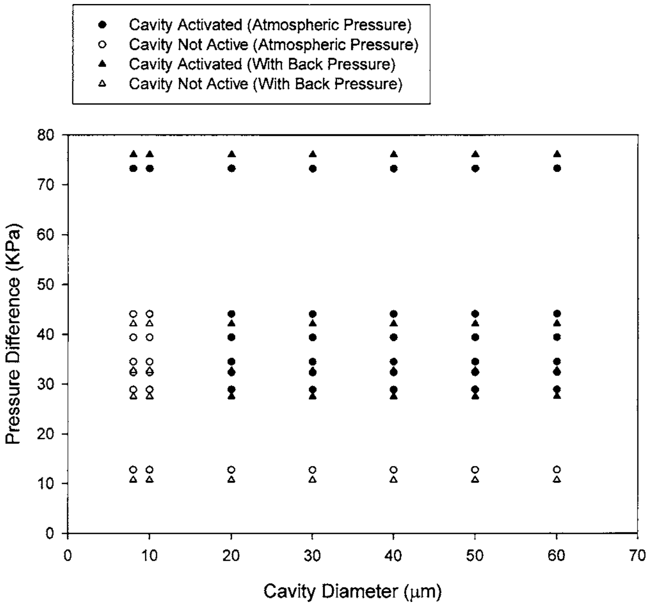

Fig. 7 The influence of backpressure on gas bubble activation

each cavity was visually examined to determine whether or not it activated. The limited results are summarized in Fig. 7. Whether or not backpressure is applied to the test section, there is essentially no difference in the magnitude of depressurization required to activate a cavity with a particular size. The remainder of gas nucleation experiments were done with the test section expanding to atmospheric pressure. One uncertainty associated with these data is that the change in the magnitude of depressurization is finite and data are lacking in the 44–73 kPa range, which corresponds to ±1.3 μm uncertainty in the computed cavity critical radius using Eq. (2).

3.2 Activation of an Array of Cylindrical Cavities Using Gas Nucleation. Extensive gas nucleation tests were done with water on the silicon surface with an array of cylindrical cavities laid out as shown in Fig. 6. Figures 8(*a*)–8(*g*) show photographs of the vapor bubbles protruding the artificial cavities following activation. Knowing the precise location of the cavities relative to one another aided in the identification of site activation. In order to find the minimum depressurization required to activate a cylindrical cavity with a specific size, an attempt was made to control the depressurization step within ±1 kPa. Repeatability experiments were conducted at the outset of this study. Experiments were repeated three times, and the activation outcome remained consistent for all cavities for each of the three tests. The activation results are summarized in Fig. 9. Also shown in Fig. 9 is the predicted depressurization required to activate the cavities using the Griffith and Wallis model [Eq. (2)] and the maximum depressurization required based on the Cornwell hypothesis [double the prediction from Eq. (2)]. There is reasonable agreement between the observed cavity activation and the prediction based on the Cornwell hypothesis for cavities below 20 μm. These data provide additional evidence to support the supposition that a concave meniscus within the cavity is probable. This is quite a significant result because it demonstrates that the energy potential required to activate a gas-trapping cavity is twice that predicted from Eq. (2).

There are two additional observations of importance from Fig. 9. The first is that all cylindrical cavities are stable when activated using gas nucleation. That is, once the depressurization exceeds that required for activation, the cavity activates; adjacent cavities do not interfere with one another. The second observation is that there appears to be a threshold magnitude of depressurization below which no cavity will activate, even when the cavity is sufficiently large. For cavities 30 μm or larger, a threshold depressurization of 13 kPa is required for activation. It is believed that this is due to gas trapping considerations and will be discussed later.

The experiments were repeated with ethanol. None of the cavities were activated despite the application of very high levels of depressurization (up to 350 kPa). Presumably, all of the cavities are flooded with ethanol.

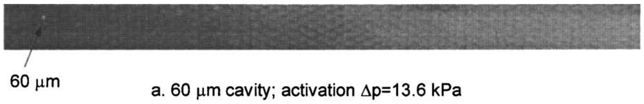

a. 60 μm cavity; activation Δp=13.6 kPa

b. 60, 50 μm cavities; activation Δp=13.9 kPa

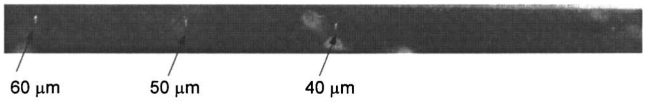

c. 60, 50, 40 μm cavities; activation Δp=14.3 kPa

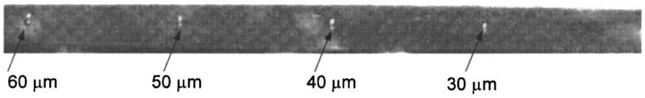

d. 60, 50, 40, 30 μm cavities; activation Δp=22.5 kPa

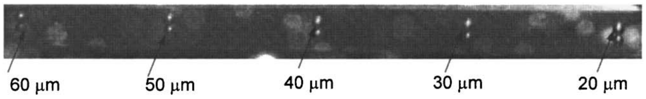

e. 60, 50, 40, 30, 20 μm cavities; activation Δp=39.4 kPa

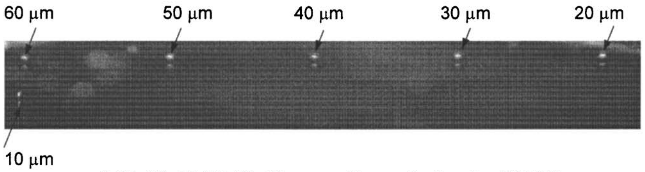

f. 60, 50, 40, 30, 20, 10 μm cavities; activation Δp=55.3 kPa

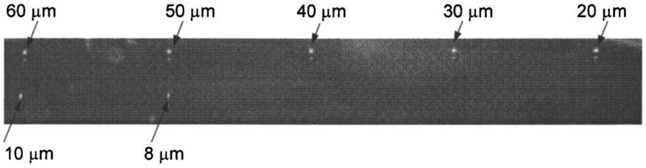

g. 60, 50, 40, 30, 20, 10, 8 μm cavities; activation Δp=73.2 kPa

Fig. 8 Typical images of bubble activation on cavities with different diameters

3.3 Activation of an Array of Cylindrical Cavities in Pool Boiling. Incipience experiments with water on the silicon surface imbedded with cylindrical cavities, laid out as shown in Fig. 6, were also done in the pool boiling facility. The measured wall superheat required to activate the cavities is summarized in Fig. 10. Also shown in Fig. 10 are the predicted incipience wall superheats based on Eq. (1) and those predicted assuming incipience is initiated from a concave meniscus [double that predicted by Eq. (1)]. Several observations are in order. The artificial cavities are not stable for boiling. It is observed that cavities are selectively active, depending on the magnitude of the wall superheat. The separation distance between adjacent cavities is 4 mm center-to-center and the bubble detachment diameters are on the order of 1 mm. Due to the large separation distance, it is not expected that cavity-to-cavity thermal conductive interference is the cause for the site instability. During the boiling mode, there is significant ebullition around the periphery of the silicon test surface. This ebullition creates strong convective currents that sweep across the silicon surface, and it is likely that these strong convective currents act to suppress incipience at some of the cavities as the thermal boundary layer is thinned.

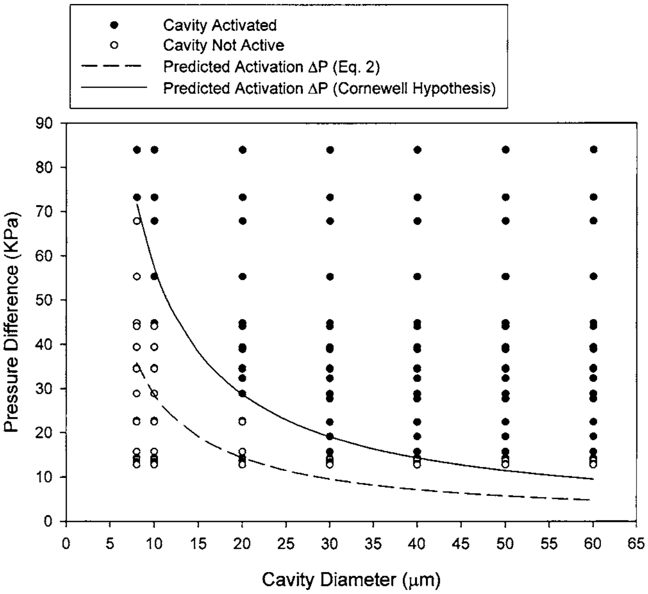

Fig. 9 Comparison between measured and predicted gas bubble incipience

It is also observed the minimum superheat required to activate the artificial cavities agrees reasonably well with the superheat calculated assuming the activation meniscus is concave. Classical nucleation theory assumes equilibrium states, and does not permit a concave vapor meniscus that is superheated. Thus, a convincing physical explanation for these results is currently lacking. However, vapor bubble incipience is a very dynamic process, and an equilibrium assumption may not hold.

The agreement in the measured incipience criteria using gas nucleation and pool boiling, suggests that gas nucleation experiments are useful for studying incipience criteria. However, the instability of active cavities observed during pool boiling suggests that gas nucleation is not very useful to study nucleation site density.

The pool boiling experiments were repeated with ethanol on the silicon surface. The wall superheat of the surface was gradually raised near 60°C, and no ebullition was observed from the cavities. Eventually, the silicon surface delaminated from the brass heater and cracked; no more experiments were possible. These

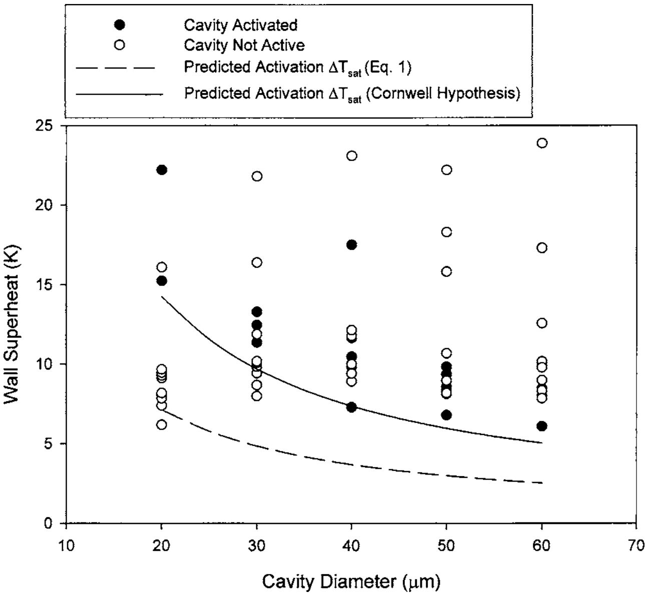

Fig. 10 Comparison between measured and predicted boiling incipience

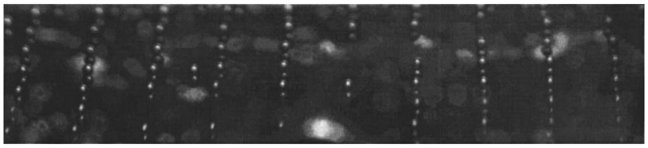

Fig. 11 Gas bubble activation on a 10×10 matrix of 10-μm cylindrical cavities

results are consistent with the gas nucleation experiments, where none of the cavities were activated, presumably due to flooding. In contrast, Qi and Klausner [1] recently reported that a highly polished brass surface (18 nm rms roughness) without any vapor-trapping cavities, efficiently produced nucleation sites during pool boiling with a wall superheat as low as 10°C. Additional experiments were done with ethanol on a 28 nm rms roughness stainless steel surface, and the incipient superheat is found to be 13.6°C. In this study, the ethanol pool boiling experiments were repeated on a smooth silicon surface (1 nm rms roughness) with no vapor-trapping cavities. The wall superheat was gradually raised, and when it reached 60°C, several nucleation sites formed on the surface.

3.4 Gas Nucleation Experiments With a Cavity Matrix. A silicon surface was prepared in which a 10×10 matrix of cylindrical cavities was etched into the silicon. All the cavities are separated by a distance of 2 mm in the transverse and longitudinal directions and have a uniform diameter of 10 μm and depth of 45 μm. With water covering the silicon surface, a depressurization of 73 kPa activates nearly all of the 100 cavities on the surface, as shown in Fig. 11. This test provides additional evidence of the stability of bubble producing cavities using gas nucleation incipience.

3.5 Activation of Different Shape Cavities Using Gas Nucleation. A silicon surface was prepared in which four different shaped cavities were placed adjacent to one another, separated by a distance 10 mm, as shown in Fig. 12(*a*). Also shown in Fig. 12(*a*) is the size of the cavities relative to the cylindrical cavity, which has a diameter of 14 μm. As shown, the cavities were designed so that the diameter of the cylindrical cavity, the width of the square cavity, the width of the rectangular cavity and the diameter of the circumscribed circle around the triangular cavity have the same dimension. All cavities have the same depth: 45 μm. A series of experiments were done using water in the gas nucleation facility with different magnitudes of depressurization. A typical image of bubble activation is shown in Fig. 12(*b*), where the triangular cavity is not activated. The results are summarized in Fig. 13. As shown, the cylindrical, rectangular, and square cavity all activate at the same depressurization. The triangular cavity requires almost twice the depressurization to activate than the others since the meniscus curvature formed in the triangular cavity is smaller than the others. The fact that the rectangular cavity (14 ×140 μm) activates at the same depressurization as the cylindrical cavity suggests that the meniscus radius of curvature is governed by the width of the rectangular cavity. Thus when scratches on surfaces serve as potential nucleation sites, the appropriate length scale to consider for activation is the width.

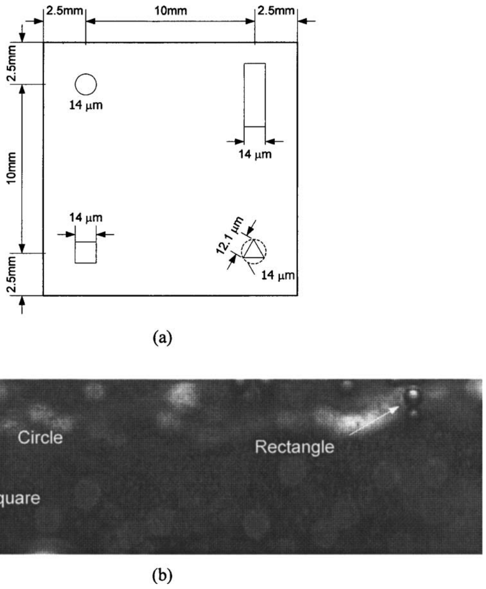

(a)

(b)

Fig. 12 Gas bubble activation on cavities with different shapes

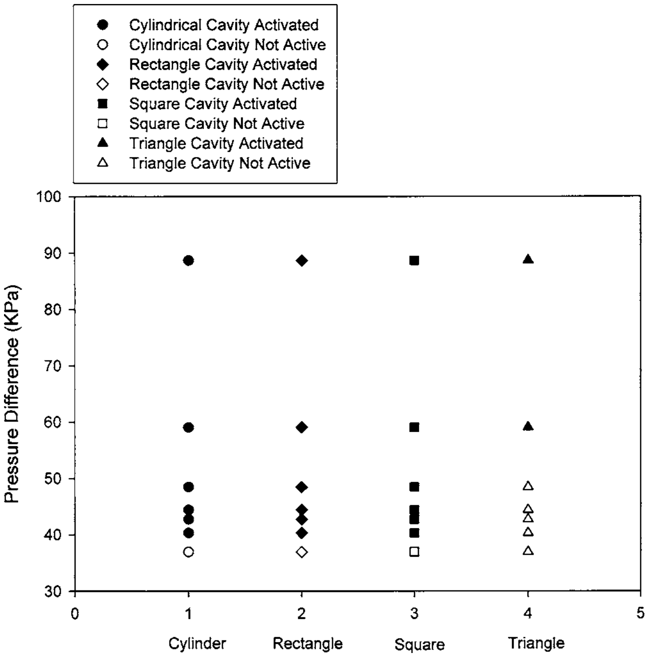

Fig. 13 The influence of cavity shape on gas bubble activation

4 Discussion

Incipience experiments with precisely manufactured artificial cavities reveal that the wall superheat and depressurization typically required to activate vapor-trapping cavities are $\Delta T_{sat} = 4\sigma T_{sat}/\rho_v h_{fg} r$ and $\Delta P = 4\sigma/r$, respectively. The gas nucleation result is consistent with the hypothesis of Cornwell that a concave meniscus, as shown in Fig. 2(*a*), is possible within a vapor-trapping cavity. As a matter of fact, Kosky's [7] study provides evidence that large pressure fluctuations are present during boiling, and are sufficient to push the meniscus into the cavity to form a concave shape. However, as gas-trapping cavities increase in size, there exists a threshold depressurization needed to activate a cavity, as observed in Fig. 9. In order to offer an explanation for this and other observed phenomena, it is necessary to consider the mechanics of gas trapping.

There are currently two theories to describe the mechanism of vapor entrapment. Bankoff [20] proposed a vapor-trapping criterion based on the incomplete displacement of gas from the cavity by an advancing liquid front. Wang and Dhir [21] developed a criterion based on equilibrium considerations and concluded that the liquid/solid contact angle must be larger than the cavity mouth angle in order for a cavity to trap the vapor. For a cylindrical cavity, the cavity mouth angle is 90°. The water/silicon contact angle is only 21°, yet the cylindrical cavities considered in this

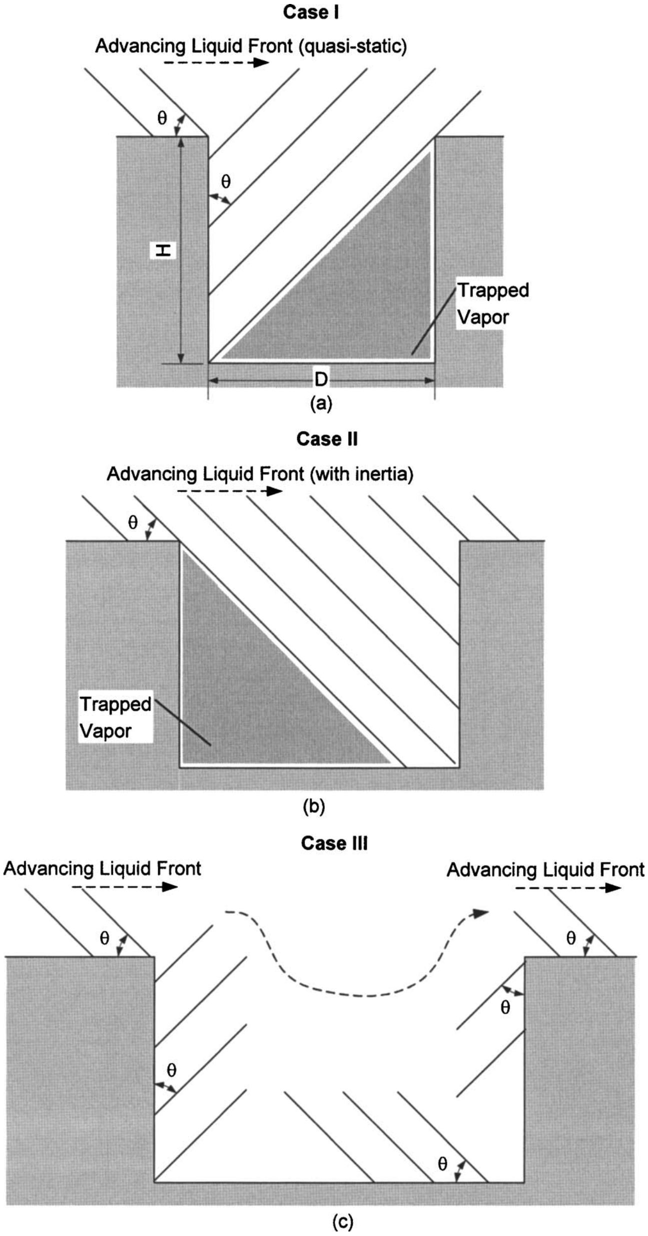

Fig. 14 Vapor-trapping mechanism in cylindrical cavities

study clearly trap vapor and gas. In order to explain vapor trapping in cavities with a rectangular cross section, consideration is first given to case I, where an advancing liquid front spreads over a cavity with a small diameter to depth ratio as shown in Fig. 14(*a*). Using a quasistatic model, the liquid front creeps along with no inertia and follows the path shown in Fig. 14(*a*). Based on geometrical considerations, such a cavity will always trap vapor when $\theta \geqslant \tan^{-1}(D/H)$, where θ is the liquid/solid contact angle, D is the cavity mouth diameter, and H is the cavity height. Applying this criterion to a cylindrical cavity with depth of 45 μm and water/silicon contact angle of 21°, according to the above criterion, any cavity with a mouth diameter less than 17 μm will trap vapor. This threshold is consistent with the experimental observation in Fig. 9 where the predicted depressurization agrees with the measured data with cavity sizes below 20 μm. Cylindrical cavities with a large diameter to depth ratio which do not satisfy the above vapor-trapping criterion will flood, shown as case III in Fig. 14(*c*). In reality, wetting and vapor trapping are dynamic processes, and the liquid inertia of the wetting front can be important.

The liquid momentum in the gas nucleation experiment is governed by the velocity of the advancing liquid, which depends on the liquid gravity potential. When consideration is given to an advancing liquid front with inertia over a cylindrical cavity with a moderate diameter to depth ratio, it is likely that the liquid front will overshoot the back side of the cavity and trap gas or vapor in a crevice, shown as case II in Fig. 14(*b*). Cylindrical cavities have a variable rectangular cross section, which adds further complexity to the vapor-trapping process. The radius of curvature of the meniscus formed in the cavity, shown in case II, depends on the amount of vapor trapped and is smaller than that of the mouth cavity radius. In addition, the amount of vapor trapped will typically depend on the liquid momentum and not on the cavity size. This provides a possible explanation as to why the amount of depressurization required to activate cavities greater than 40 μm is the same and is more than that predicted when it is assumed the meniscus radius of curvature equals the cavity mouth radius. Here the vapor trapping process has been simplified by considering an advancing front in a single direction. It is possible for liquid to advance down the sides of a rectangular cavity or the periphery of a cylindrical cavity. In both cases, pockets of vapor can be trapped in the corner of the cavity.

Clark et al. [22] observed that scratches on heating surfaces make very efficient nucleation sites. The fact that cavities with a rectangular cross section are capable of trapping pockets of vapor, as depicted in Fig. 14(*b*), offers a plausible explanation for their observation.

Nucleation site instability has been observed with pool boiling on the silicon surface with an array of cylindrical cavities, as is evident in Fig. 10. Hsu [23] identified both a minimum and maximum cavity radius that will permit the incipience of vapor bubbles, depending on the thickness of the liquid thermal boundary layer surrounding the vapor embryo. A thinning thermal boundary layer reduces the maximum cavity diameter that will permit an active nucleation site. As observed in Fig. 10, as the wall superheat increases, the size of active cavities decreases, which is consistent with thermal boundary layer thinning. At the interface between the brass heater and silicon test surface, significant ebullition was observed with increasing superheat. Strong convective currents, which sweep across the silicon surface were observed, which result in thermal boundary layer thinning. This leads to deactivation of the larger cylindrical cavities on the test surface, as was observed.

Lastly, the observations of Pesse et al. [12] suggest that even though a cavity is efficient at trapping gas, it will eventually flood due to diffusion given enough time. The implication is that the wetting history of the heating surface may be important in incipience considerations.

5 Summary

A detailed experimental investigation of heterogeneous nucleation with artificial cavities has been presented. The results are summarized as follows:

(1) The incipient depressurization or wall superheat required for activating vapor trapping cavities is twice that predicted from the Griffith and Wallis model. The gas nucleation result is consistent with a concave meniscus residing within a vapor-trapping cavity as was proposed by Cornwell.
(2) Vapor-trapping cavities are stable, with no site interaction, when activated using gas nucleation depressurization. They are not stable during boiling, and the larger cavities are suppressed with boundary layer thinning, which occurs with increasing superheat.
(3) Vapor-trapping mechanisms have been proposed for cylindrical cavities, and a vapor-trapping criterion has been introduced for an ideal rectangular cavity based on a creeping wetting front.
(4) Square and rectangle cavities with a width equal to the

diameter of a cylindrical cavity require the same incipient depressurization for activation as the cylindrical cavity.

(5) Limited data suggest that the backpressure exerted during gas nucleation does not influence the incipience as long as the magnitude of the depressurization is fixed.

(6) All artificial cavities are flooded with ethanol covering the surface. An incipient superheat of 60°C was required to activate nucleation sites on a smooth silicon surface.

Nomenclature

D = cavity mouth diameter, μm
H = cavity depth, μm
ΔP = change in pressurization, MPa
R = cavity radius, μm
T_{sat} = saturation temperature, °K
ΔT_{sat} = wall superheat, °C or K
h_{fg} = latent heat of vaporization, J/kg
r = radius of curvature, μm
θ = liquid/solid contact angle, radians or degrees
ρ_v = density of vapor, kg/m^3
σ = liquid/gas interfacial surface tension, N/m

References

[1] Qi, Y., and Klausner, J. F., 2004, "Comparison of Gas Nucleation and Pool Boiling Site Densities," *2004 ASME International Mechanical Engineering Congress*, Anaheim, CA.
[2] Theofanous, T. G., Tu, J. P., Dinh, A. T., and Dinh, T. N., 2002, "The Boiling Crisis Phenomenon Part I: Nucleation and Nucleate Boiling Heat Transfer," Exp. Therm. Fluid Sci., **26**, pp. 775–792.
[3] Griffith, P., and Wallis, J. D., 1960, "The Role of Surface Conditions in Nucleate Boiling," Chem. Eng. Prog., Symp. Ser., **30**(56), pp. 49–63.
[4] Sernas, V., and Hooper, F. C., 1969, "The Initial Vapor Bubble Growth on a Heated Wall During Nucleation Boiling," Int. J. Heat Mass Transfer, **12**, pp. 1627–1639.
[5] Preckshot, G. W., and Denny, V. E., 1967, "Explorations of Surface and Cavity Properties on the Nucleation Boiling of Carbon Tetrachloride," Can. J. Chem. Eng., **45**, pp. 241–249.
[6] Rammig, R., and Weiss, R., 1991, "Growth of Vapor Bubbles From Artificial Nucleation Sites," Cryogenics, **31**, pp. 64–69.
[7] Kosky, P. G., 1968, "Nucleation Site Instability in Nucleate Boiling," Int. J. Heat Mass Transfer, **11**, pp. 929–932.
[8] Heled, Y., Ricklis, J., and Orell, A., 1970, "Pool Boiling From Large Arrays of Artificial Nucleation Sites," Int. J. Heat Mass Transfer, **13**, pp. 503–516.
[9] Messina, A. D., and Park, E. L., 1981, "Effects of Precise Arrays of Pits on Nucleate Boiling," Int. J. Heat Mass Transfer, **24**, pp. 141–145.
[10] Shoji, M., and Takagi, Y., 2001, "Bubbling Features From a Single Artificial Cavity," Int. J. Heat Mass Transfer, **44**, pp. 2763–2776.
[11] Shoji, M., and Zhang, L., 2003, "Boiling Features on Artificial Surfaces," *5th International Conference on Boiling Heat Transfer*, Montego Bay, Jamaica.
[12] Pesse, A. V., Warrier, G. R., and Dhir, V. K., 2004, "Experimental Study of the Gas Entrapment Process in Close-End Microchannels," *2004 ASME International Mechanical Engineering Congress*, Anaheim, CA.
[13] Lorenz, J. J., Mikic, B. B., and Rohsenow, W. M., 1974, "Effect of Surface Conditions on Boiling Characteristics," *Proc. 5th Int. Heat Transfer Conf.*, Tokyo, Japan, pp. 35–39.
[14] Eddington, R. I., and Kenning, D. B. R., 1978, "The Prediction of Flow Boiling Bubble Populations From Gas Bubble Nucleation Experiments," *Proc. 6th Int. Heat Transfer Conf.*, 1, pp. 275–280.
[15] Eddington, R. I., Kenning, D. B. R., and Korneichev, A. I., 1978, "Comparison of Gas and Vapor Bubble Nucleation on a Brass Surface in Water," Int. J. Heat Mass Transfer, **21**, pp. 855–862.
[16] Eddington, R. I., and Kenning, D. B. R., 1979, "The Effect of Contact Angle on Bubble Nucleation," Int. J. Heat Mass Transfer, **22**, pp. 1213–1236.
[17] Qi, Y., Klausner, J. F., and Mei, R., 2004, "Role of Surface Structure in Heterogeneous Nucleation," Int. J. Heat Mass Transfer, **47**, pp. 3097–3107.
[18] Cornwell, K., 1982, "On Boiling Incipience due to Contact Angle Hysteresis," Int. J. Heat Mass Transfer, **25**, pp. 205–211.
[19] Kenning, D. B. R., May 2004, private communication.
[20] Bankoff, S. G., 1958, "Entrainment of Gas in the Spreading of Liquid Over a Rough Surface," AIChE J., **4**(1), pp. 24–26.
[21] Wang, C. H., and Dhir, V. K., 1993, "Effect of Surface Wettability on Active Nucleation Site Density During Pool Boiling of Saturated Water," J. Heat Transfer, **115**, pp. 659–669.
[22] Clark, H. B., Strenge, P. S., and Westwater, J. W., 1959, "Active Sites for Nucleate Boiling," Chem. Eng. Prog., **55**(29), pp. 103–110.
[23] Hsu, Y. Y., 1962, "On the Size Range of Active Nucleation Cavities on a Heating Surface," J. Heat Transfer, **84**, pp. 207–216.

Condensation of Ethylene Glycol on Integral-Fin Tubes: Effect of Fin Geometry and Vapor Velocity

Satesh Namasivayam

Adrian Briggs[1]

Department of Engineering,
Queen Mary, University of London,
Mile End Road,
London, E1 4NS, UK
e-mail: A.Briggs@qmul.ac.uk

New experimental data are reported for forced-convection condensation of ethylene glycol on a set of nine single, copper, integral-fin tubes. The first set of five tubes had fin height and thickness of 1.6 and 0.25 mm*, respectively, with fin spacings of 0.25, 0.5, 1.0, 1.5, and* 2.0 mm*. The second set of four tubes had fin spacing and thickness of 1.0 and* 0.5 mm*, respectively, and fin heights of 0.5, 0.9, 1.3, and* 1.6 mm*. The fins were rectangular in cross section. All tubes had a fin root diameter of* 12.7 mm*. A plain tube of outside diameter* 12.7 mm *was also tested. The tests, which were performed at a near constant pressure of* ~15 kPa*, covered vapor velocities between 10 and* 22 m/s *and a wide range of heat fluxes. The best performing tube was that with fin spacing, height, and thickness of 0.5, 1.6, and* 0.25 mm*, respectively, which had an enhancement ratio (compared to the plain tube at the same vapor-side temperature difference and vapor velocity) of 2.5 at the lowest vapor velocity tested, increasing to 2.7 at the highest. For all but two of the tubes, the effect of vapor velocity on the heat-transfer coefficient of the finned tubes was less than on the plain tube, leading to a decrease in enhancement ratio with increasing vapor velocity. For two of the tubes, however, the enhancement ratio increased with increasing vapor velocity, which is the opposite trend to that found in most earlier experimental studies. This effect was thought to be due to the slight reduction in condensate flooding between the fins of these two tubes because of vapor shear.*

[DOI: 10.1115/1.2039112]

Introduction

The mechanism of condensation of quiescent vapor on integral-fin tubes has been studied in detail for several decades. For horizontal tubes, condensate retention (or flooding) between the fins at the bottom of the tube reduces the surface area available for heat transfer. The angle, measured from the top of the tube, at which the interfin space becomes filled with condensate, is known as the flooding angle (see Fig. 1). At the fin tips, and on the fin flanks and root above the flooding angle, surface tension acts to thin the condensate film and increase the local heat-transfer coefficient. For low surface-tension fluids, such as refrigerants, the enhancing effect of surface tension dominates, leading to increases in heat transfer greater than the increase in surface area due to the fins. For a high surface-tension fluid, such as water, however, the two effects appear to be of similar magnitude and the increase in heat transfer is comparable to the increase in surface area. (See, for instance, [1] for a general review of the important factors and [2] for quantitative comparisons of theoretical models and experimental data).

Much work has been published on the effects of vapor shear on condensation on plain tubes (for an overview, see [3]). There is less published work, however, on the effects of vapor shear on condensation on finned tubes. Michael et al. [4] presented data for condensation of atmospheric pressure R-113 and low-pressure (~12 kPa) steam on three integral-fin tubes with fin spacings of 0.25, 1.5, and 4 mm. Vapor velocities upstream of the test section ranged from 0.4 to 1.9 m/s for R-113 and 4.8 to 31.5 m/s for steam. For both fluids and all three finned tubes the relative increase in heat-transfer coefficient due to increase of vapor velocity was smaller than for a plain tube with diameter equal to the fin-root diameter of the finned tubes. This resulted in a decrease in the vapor-side enhancement ratio (defined as the vapor-side, heat-transfer coefficient for the finned tube divided by that for the plain tube under the same vapor-side conditions). For R-113 the decrease in enhancement ratio was greatest for the tubes with fin spacings of 0.25 and 1.5 mm, being about 20%, over the range of vapor velocities tested. For steam the greatest decrease in enhancement ratio, about 37%, over the range of velocities tested was for the tube with 4 mm fin spacing.

Briggs et al. [5] tested three finned tubes with fin spacings of 0.5, 1.0, and 1.5 mm and a plain tube, condensing atmospheric pressure steam, and R-113 as well as low-pressure steam (14 kPa) and ethylene glycol (2.5 kPa). Although the vapor velocity ranges obtained for the atmospheric pressure tests were limited, all the data showed decreasing vapor-side enhancement ratios (as defined above) with increasing vapor velocity with the exception of the data for ethylene glycol and fin spacings of 0.5 and 1.5 mm, where enhancement ratio was found to be independent of vapor velocity over the range tested.

Bella et al. [6] and Cavallini et al. [7] presented data for condensation of R-113 and R-11 on three finned tubes at upstream vapor velocities between 0.3 and 10 m/s. They measured a 50% increase in heat-transfer coefficient for the finned tubes (at the same vapor-side temperature difference) at the highest vapor velocity compared to the lowest, but observed that the enhancement due to vapor velocity was again less than that for a plain tube under the same conditions.

Namasivayam and Briggs [8] presented experimental data for forced-convection condensation of saturated steam at atmospheric pressure on a set of five single, integral-fin tubes. All the tubes had the same geometry except for fin spacing, which was varied from 0.25 to 2 mm. The data covered upstream vapor velocities be-

---

[1] Corresponding author.

Contributed by the Heat Transfer Division of ASME for publication in the JOURNAL OF HEAT TRANSFER. Manuscript received January 13, 2005; final manuscript received June 18, 2005. Review conducted by: Anthony M. Jacobi. Paper presented at the 2004 ASME International Mechanical Engineering Congress (IMECE2004), November 13, 2004–November 19, 2004, Anaheim, CA, USA.

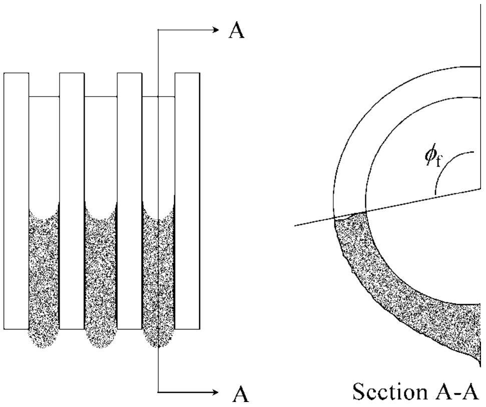

Fig. 1 Condensate flooding on a horizontal integral-fin tube

tween 2.3 and 10.2 m/s, and again it was found that vapor-side enhancement ratio decreased with increasing vapor velocity.

Cavallini et al. [9] correlated the data of Bella et al. [6] and Cavallini et al. [7] using the model of Briggs and Rose [10] at low vapor velocity and an empirical relation involving an "equivalent Reynolds number" (a function of film and vapor Reynolds numbers) at high vapor velocity. Namasivayam and Briggs [8] compared the model of Cavallini et al. [9] with most of the experimental data discussed above. The model showed reasonable agreement with the refrigerant data, since most of these data were used in the evaluation of the empirical constants in the model. For steam, however, the model was less successful, underpredicting the majority of the data, in some cases by up to 50%.

From the above studies, it can be concluded that the combined effects of surface tension and vapor shear on enhancing condensation heat-transfer coefficients for integral-fin tubes are still not fully understood. The present study presents data for forced-convection condensation of ethylene glycol on a set of single, integral-fin tubes. By focusing initially on single tubes, rather than a complete tube bank, a large number of tube geometries can be tested. It is acknowledged, however, that this approach ignores any complications due to the interaction of adjacent tubes in a bank. The reasons for the choice of ethylene glycol as the test fluid were twofold. First, the high saturation temperature of ethylene glycol meant that tests could be conducted at low pressure, giving high vapor velocities while still maintaining a sufficiently high vapor-to-coolant temperature difference to give accurately measurable heat-transfer rates. Second, ethylene glycol has thermophysical properties, in particular surface tension, which fall between those of steam and most refrigerants. Studies into free-convection condensation on integral-fin tubes (for example, [1,2]) have highlighted the value of obtaining data for a wide range of conditions in order to understand the underlying physical mechanism behind the enhancement in heat transfer.

Apparatus and Data Reduction

The closed-loop, stainless-steel test rig is shown in Fig. 2. Vapor was generated in electrically heated boilers (maximum power 60 kW) and flowed through a 180 deg bend to pass vertically

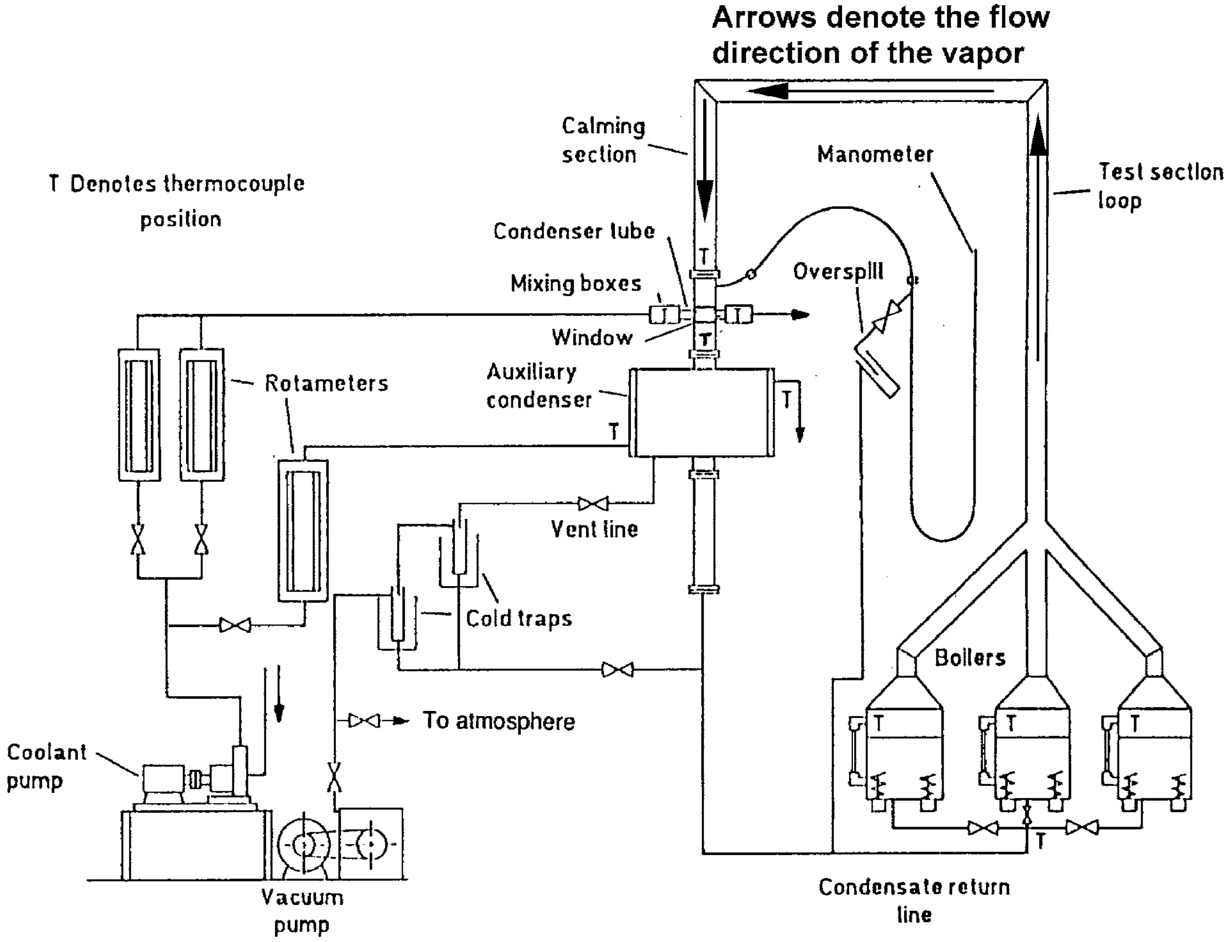

Fig. 2 Apparatus

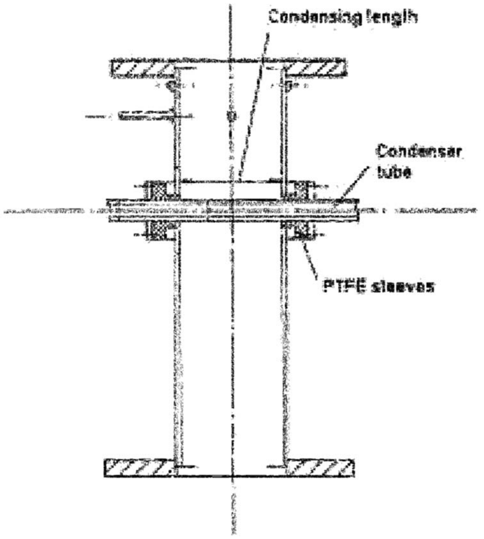

Fig. 3 Test section and test condenser tube arrangement

downward, through a calming section, to the horizontal, water-cooled test-condenser tube. The internal diameter of the test section (shown in Fig. 3) and, hence, the length of test tube exposed to the vapor, was 70 mm. Excess vapor passed to a water-cooled auxiliary condenser from which the condensate returned to the boiler by gravity. Pressure in the apparatus was controlled by a vacuum pump attached to the auxiliary condenser. The apparatus was pumped down to the required pressure (~15 kPa, corresponding to a saturated vapor temperature of ~145 °C) before turning on the heaters. The required pressure was maintained by alternately pumping out or bleeding in small amounts of air into the auxiliary condenser well downstream of the test section, to lower or raise the pressure, respectively, as required. Although there was a theoretical possibility that air could enter the test section from the auxiliary condenser, in practice, the vapor velocity at the outlet of the test section was always sufficiently high to prevent this from happening. The mass fraction of air present in the vapor in the test section was continually checked to ensure that no air was entering the test section from the auxiliary condenser (or from any leaks in the apparatus). This was done by comparing the temperature (measured using K-type thermocouples) and pressure (measured using a mercury-in-glass manometer) and assuming saturation conditions and the Gibbs-Dalton ideal gas mixture equation. Based on the estimated uncertainty in the measuring devices, this method could detect noncondensing gas concentrations as low as 0.1% by mass.

The test tube was mounted horizontally in the test section using PTFE (Teflon®) bushes, which also served to insulate the tube from the body of the test section. The tube was cooled internally by water. PTFE inserts were used to insulate the inside of the test tubes at entry to and exit from the test section, so that the inside and outside surface areas available to heat transfer were of equal length. A glass window in the test section allowed observation of the test condenser tube in order to confirm filmwise condensation was maintained throughout all the tests.

The vapor velocity at approach to the test section was found from the measured power input to the boilers. A preliminary experiment had been conducted to estimate the heat loss from the apparatus during operation. This was done by reducing the boiler power gradually until the readings from the test section thermocouples dropped below saturation temperature, indicating that all the vapor from the boilers was condensing on the inside of the apparatus due to thermal losses. This small correction for the heat loss from the well-insulated apparatus was then included in the calculation of the vapor velocity.

The rise in bulk-cooling water temperature, from which the heat-transfer rate to the test tube was calculated, was measured using a ten-junction thermopile constructed of K-type thermocouple wire. The use of a ten-junction arrangement increased the sensitivity to ~400 μV/K. Special mixing boxes were constructed for the inlet and outlet of the test tube. The end of the entrance pipe for each box was blocked off, and water entered the box through six holes in the sides of the pipe. The thermopile junctions were inserted into the boxes to a distance of 6 cm to ensure adequate isothermal immersion. A predetermined small correction for the dissipative temperature rise of the cooling water was incorporated in the calculation of the heat-transfer rate. With these careful arrangements, the estimated accuracy of the measurement of the coolant temperature rise was better than 0.01 K (equivalent to 4 μV using the ten-junction thermopile arrangement described above), while the coolant temperature rise was in the range of 0.4–2.8 K. The coolant flow rate through the test tube was measured with a variable aperture, float-type flowmeter, calibrated to an accuracy of better than 2%.

Nine copper integral-fin tubes were tested. All the tubes had an inside diameter of 9.4 mm and a diameter at the fin root of 12.7 mm. Five of the nine tubes had fin height and thickness of 1.6 and 0.25 mm, respectively. For these five tubes, fin spacings were 0.25, 0.5, 1.0, 1.5, and 2.0 mm. The remaining four tubes had fin spacing and thickness of 1.0 and 0.5 mm, respectively. For these four tubes, fin heights were 0.5, 0.9, 1.3, and 1.6 mm. A plain copper tube with 9.4 mm i.d. and 12.7 mm o.d. was also tested. All tube dimensions are ±0.05 mm.

The outside wall temperature at the fin root was found by subtracting the coolant and wall (inside surface to fin root) resistances from the measured overall thermal resistance, the latter calculated by assuming uniform radial conduction in the tube wall. To obtain a correlation for the coolant-side heat-transfer coefficient a "modified Wilson plot" technique was applied to the data for the plain tube at the lowest vapor velocity. This involved selecting expressions, containing unknown constants, for the vapor-side and coolant-side heat-transfer coefficients. The unknown constants were found by minimizing the sum of squares of residuals (measured minus calculated values) of the average vapor-to-coolant temperature difference. For the coolant side, an expression based on Sieder and Tate [11] for turbulent flow in pipes was adopted

$$\mathrm{Nu}_c = a\ \mathrm{Re}_c^{0.8}\ \mathrm{Pr}_c^{1/3}\left(\frac{\mu_c}{\mu_{\mathrm{wi}}}\right)^{0.14} \tag{1}$$

where a is a constant to be found. For the vapor side, an equation based on Shekriladze and Gomelauri [12] was used

$$\frac{\mathrm{Nu}}{\mathrm{Re}_{tp}^{1/2}} = b\left(\frac{0.9 + 0.728F^{1/2}}{(1 + 3.44F^{1/2} + F)^{1/4}}\right) \tag{2}$$

where b is a constant to be found. Note that in Eq. (2) the properties of the condensate were evaluated at the reference temperature defined as follows:

$$T_{\mathrm{ref}} = \tfrac{2}{3}T_w + \tfrac{1}{3}T_v \tag{3}$$

The specific enthalpy of evaporation h_{fg} was evaluated at T_v.

The modified Wilson plot was applied to the data from the plain tube at low vapor velocity since these are the conditions under which Eq. (2) is most applicable.[2] For these data the values of a and b were found to be 0.030 and 1.06, respectively. The value of a is slightly higher than the often quoted value of 0.027 for the original work of Sieder and Tate [11] due to the short test tubes used in the present investigation. Equation (1), with $a=0.030$ was used to analyze all of the data for both plain and finned tubes and at all vapor velocities by subtraction of the coolant-side and wall

---

[2] Note that previous experimental investigations for condensation on plain tubes have shown good agreement with Shekriladze and Gomelauri [12] at low to moderate vapor velocities, but less good agreement at high velocities.

resistances from the measured overall resistance as described above. Note that the finned tubes were manufactured with identical internal geometry to the plain tube, including inlet and exit lengths and arrangements, so that the coolant-side correlation found from the plain tube would be directly applicable to the finned tubes. The data used in the Wilson plot also covered the same range of Reynolds numbers as those for the finned tubes.

An uncertainty analysis was carried out on the results using the method described by Moffat [13]. This method uses the estimated uncertainties in the experimental measurements (e.g., in coolant flow rate, coolant temperature rise, etc.) and calculates the propagation of these uncertainties in the reported results (e.g., heat flux, vapor-side temperature difference, etc). Using this method and the uncertainties in the measured parameters given above the calculated uncertainty in the heat flux was never greater than 4%. The main uncertainty in the vapor-side temperature difference arose from the use of Eq. (1) to calculate the coolant-side thermal resistance and is strongly affected by, among other factors, the balance of thermal resistances between the coolant and vapor sides; high coolant-side thermal resistances lead to high uncertainties on the vapor side. In the present investigation, the coolant-side resistance was never greater than 57% of the total. The uncertainty in the coolant-side correlation was estimated to be 5% based on [14] where coolant-side correlations for plain tubes obtained by the modified Wilson plot method, as used in the present study, were compared to those obtained by direct measurement of the tube wall temperature using thermocouples embedded in the tube walls. This led to a maximum uncertainty in the vapor-side temperature difference of 12%. The uncertainty in the vapor velocity in the test section was estimated to be <3%.

Results

All tests were performed at pressures between 15 and 15.5 kPa and were repeated on different days to ensure accuracy and consistency. The maximum vapor velocity achieved (based on the total cross-sectional area of the test section) was 22.1 m/s (equivalent to 30 kW of heater power in the boilers). At higher velocities, the pressure drop from the boilers to the test section prevented adequate drainage of condensate back to the boilers and risked dry out of the heaters.

Results for Plain Tube. For free-convection condensation on horizontal plain tubes, we have the classic solution of Nusselt [15], which can be written as

$$\frac{\mathrm{Nu}}{\mathrm{Re}_{tp}^{1/2}} = 0.728F^{1/4} \tag{4}$$

while for forced-convection condensation, the approach of Shekriladze and Gomelauri [12] who used the asymptotic, infinite condensation rate approximation for vapor shear at the condensate surface, gives a result that can be expressed as follows (see [3]):

$$\frac{\mathrm{Nu}}{\mathrm{Re}_{tp}^{1/2}} = \frac{0.9 + 0.728F^{1/2}}{(1 + 3.44F^{1/2} + F)^{1/4}} \tag{5}$$

Note that Eq. (5) tends to Eq. (4) for large F (low vapor velocity) and to $\mathrm{Nu}/\mathrm{Re}_{tp}^{1/2}=0.9$ for small F (high vapor velocity).

Figures 4(*a*) and 4(*b*) show the present results for the plain tube plotted on the basis of Eqs. (4) and (5). Also shown in Figure 4(*a*) are selected data of Memory and Rose [16] for the same vapor pressure used in the present investigation. Condensate properties were again evaluated at the reference temperature defined by Eq. (3), whereas the specific enthalpy of evaporation h_{fg} was evaluated at T_v. It can be seen that both data sets are in good agreement with each other. Memory and Rose [16] used direct measurements of the tube wall temperature using a plain tube instrumented with six thermocouples embedded in the tube wall. The good agreement with the present data is, therefore, validation of the indirect method of establishing vapor-side, heat-transfer coefficients used in the present work. Both data sets fall ~5% above Eq. (5). Given the simplicity of the model this could be considered reasonable. The Nusselt model, Eq. (4), underpredicts the data by a large margin due to the neglect of vapor-shear effects.

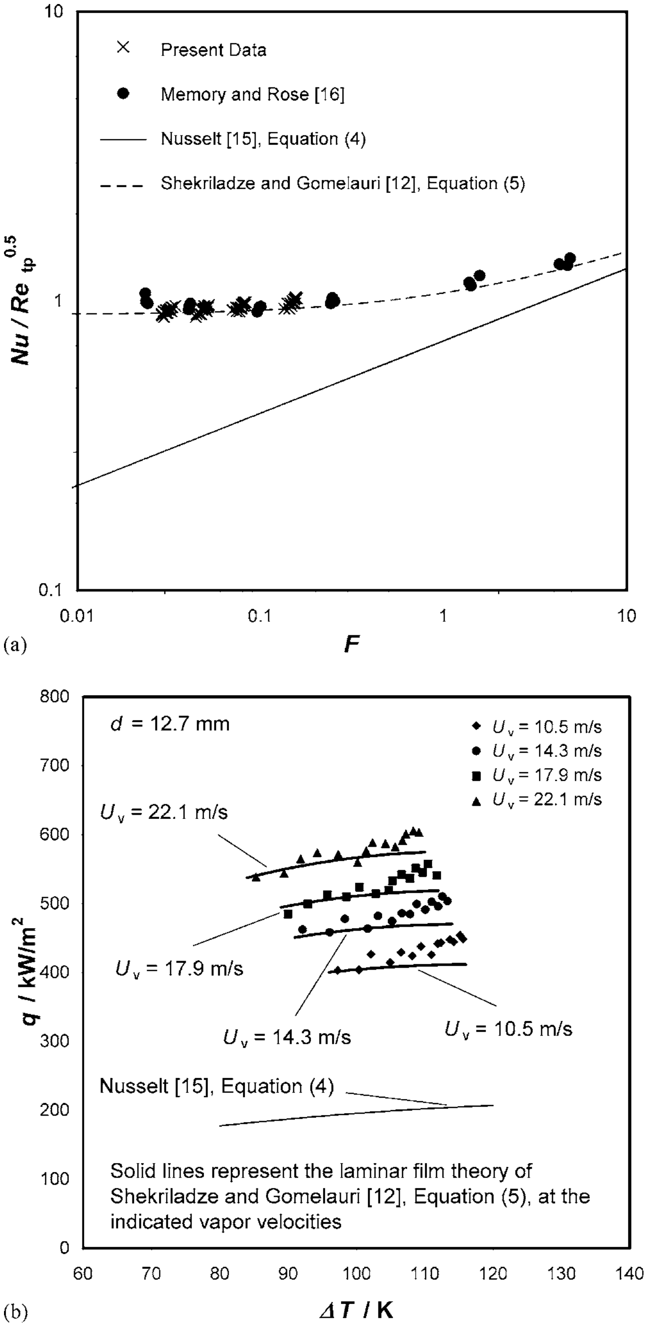

Fig. 4 (***a***) **Plain tube results and (*b*) variation of heat flux with vapor-side temperature difference for the plain tube**

Results for Finned Tubes. Figure 5 shows data for the first set of tubes (i.e., where fin spacing was the only variable) and for the lowest and highest vapor velocities tested (10.5 and 22.1 m/s), respectively. The data are plotted as heat flux (based on the surface area of a plain tube with diameter equal to that at the fin root) against vapor-side temperature difference (vapor temperature minus surface temperature at the fin root). In all cases, data from two

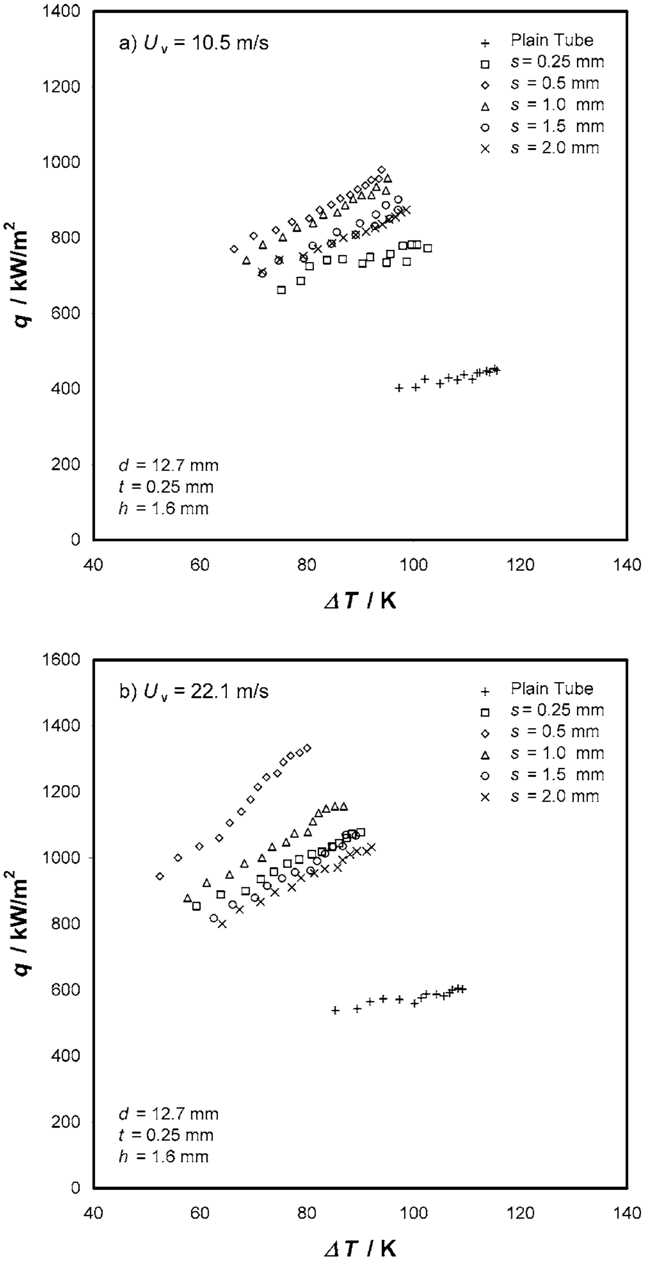

Fig. 5 Variation of heat flux with vapor-side temperature difference. Effect of fin spacing.

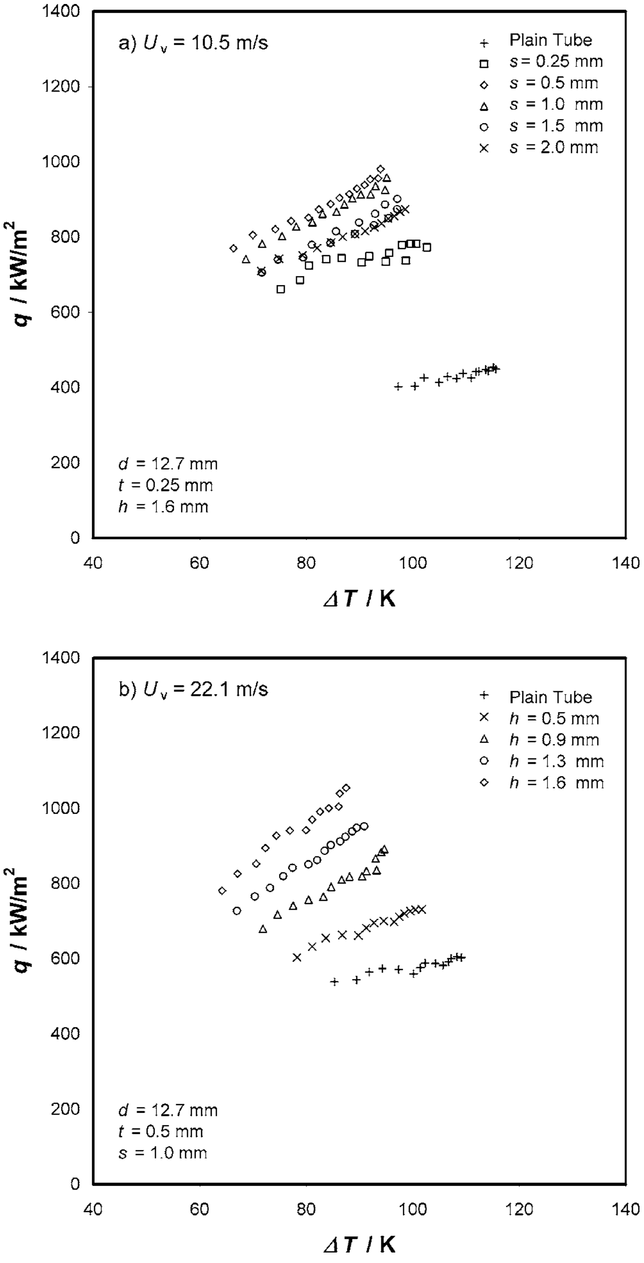

Fig. 6 Variation of heat flux with vapor-side temperature difference. Effect of fin height.

different runs, taken on separate days, are shown and it can be seen that the results show excellent repeatability. Also shown on the plots are the plain tube data for comparison purposes. The best performing tube at both velocities (and also at vapor velocities of 17.9 and 14.3 m/s, not shown in Fig. 5) is that with a fin spacing of 0.5 mm. Figure 6 shows data for the second set of tubes, where fin height was the only variable. In this case, the best performing tube at all vapor velocities was that with a fin height of 1.6 mm.

Figures 7 and 8 show the data for each of the nine finned tubes with vapor velocity as a parameter. For all tubes tested, including the plain tube, heat flux increases with vapor velocity (for the same vapor-side temperature difference) as expected. The relative effect of vapor velocity on heat flux is strongest for the tubes with the smallest fin spacings (i.e., 0.25 and 0.5 mm), where the heat flux increases by over 50% (at the same vapour-side temperature difference) over the range of vapor velocities tested. For the tubes with the highest fin spacing (i.e., 2 mm), however, the heat flux increases by only 24% over the same range of vapor velocity.

Heat Transfer Enhancement Ratios

In order to better quantify the relative effect of vapor velocity on each of the tubes tested, it is advantageous to define and evaluate enhancement ratios for each of the tubes and at each of the vapor velocities tested. To this end, Figs. 7 and 8 show curve fits to the data of the form

$$q = B\Delta T^{3/4} \tag{6}$$

where B is a constant found for each tube and vapor velocity combination. The index of $\frac{3}{4}$ is suggested by the Nusselt [15] theory for laminar film condensation on plain tubes at zero vapor velocity. Although better fits could be obtained if the index was allowed to vary, fixing it to a single value for all the tubes has the advantage that it allows an enhancement ratio to be calculated, defined as the vapor-side, heat-transfer coefficient for the finned tube based on the fin-root diameter, divided by that for the plain tube, at the same vapor-side, temperature difference, and vapor

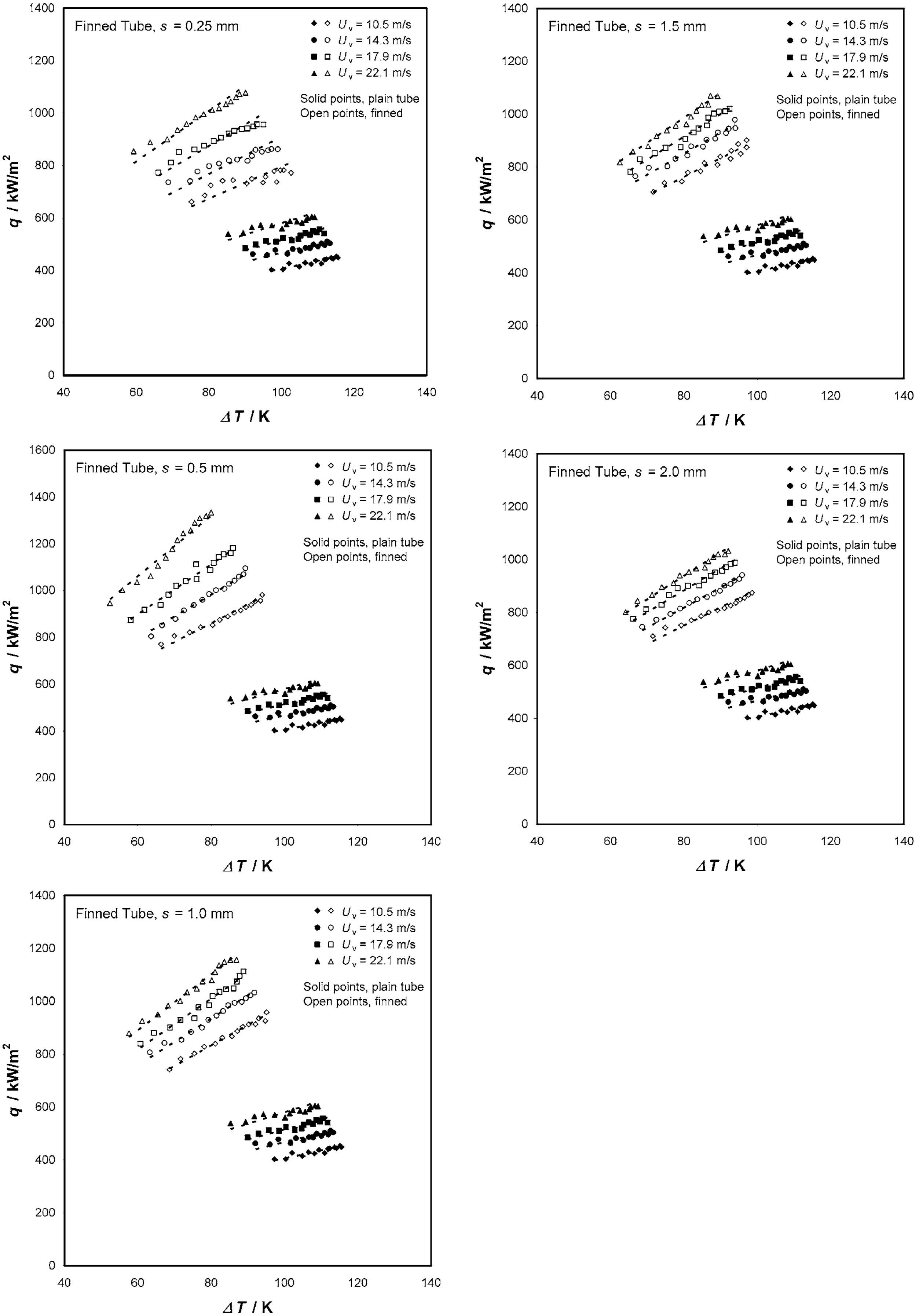

Fig. 7 Variation of heat flux with vapor-side temperature difference. Effect of vapor velocity (d=12.7 mm, t=0.25 mm, h=1.6 mm, s as a variable).

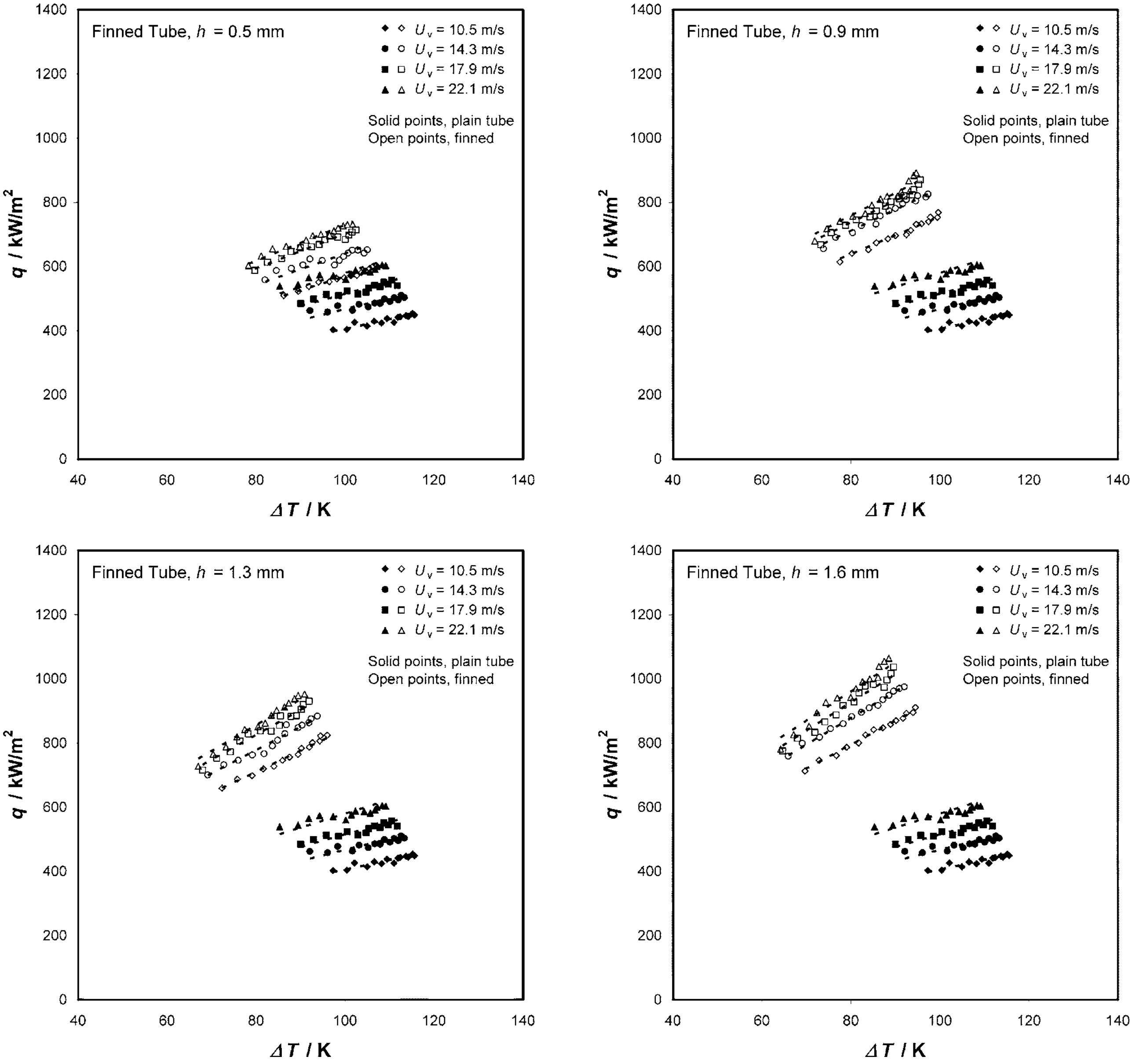

Fig. 8 Variation of heat flux with vapor-side temperature difference. Effect of vapor velocity (d=12.7 mm, t=0.5 mm, s=1.0 mm, h as a variable).

velocity, which is independent of vapor-side, temperature difference. Thus,

$$\varepsilon = \left(\frac{\alpha_{\text{finned tube}}}{\alpha_{\text{plain tube}}}\right)_{\text{same } \Delta T \text{ and } U_v} = \left(\frac{q_{\text{finned tube}}}{q_{\text{plain tube}}}\right)_{\text{same } \Delta T \text{ and } U_v}$$

$$= \left(\frac{B_{\text{finned tube}}}{B_{\text{plain tube}}}\right)_{\text{same } U_v} \tag{7}$$

Enhancement ratios were calculated on the above basis for each of the finned tubes and at each of the vapor velocities tested. Tables 1 and 2 list the values obtained.

Figures 9–11 show the variation of vapor-side enhancement ratio for the finned tubes. For almost all of the tubes, enhancement ratio decreases, albeit in some cases slightly, with increasing vapor velocity. This indicates that vapor shear has a smaller effect on the condensate film on the finned tubes than on the plain tube and is in line with many previous investigations (see, for example, [4,6–8]). For the tubes with fin spacings of 0.25 and 0.5 mm (see Fig. 9), however, we have the unfamiliar trend of increasing enhancement ratio with increasing vapor velocity. A possible explanation for this can be found if we look at the extent of condensate flooding on the tubes. Listed in Tables 1 and 2 are the calculated flooding angle ratios for each of the tubes, where flooding angle is

Table 1 Heat transfer enhancement ratios and flooding angle ratios (d=12.7 mm, t=0.25 mm, h=1.6 mm, s as a variable)

s / mm	0.25	0.5	1.0	1.5	2.0
ϕ_f / π (Eqn. 8)	0	0.18	0.53	0.63	0.68
$\varepsilon(U_v = 10.5$ m/s$)$	1.96	2.51	2.43	2.22	2.19
$\varepsilon(U_v = 14.3$ m/s$)$	1.94	2.49	2.37	2.16	2.07
$\varepsilon(U_v = 17.9$ m/s$)$	2.01	2.55	2.32	2.10	2.03
$\varepsilon(U_v = 22.1$ m/s$)$	2.06	2.68	2.25	2.01	1.91

Table 2 Heat transfer enhancement ratios and flooding angle ratios (d=12.7 mm, t=0.5 mm, s=1.0 mm, h as a variable)

h / mm	0.5	0.9	1.3	1.6
ϕ_f / π (Eqn. 8)	0.47	0.49	0.51	0.53
$\varepsilon (U_v = 10.5$ m/s)	1.40	1.86	2.07	2.32
$\varepsilon (U_v = 14.3$ m/s)	1.37	1.80	1.97	2.22
$\varepsilon (U_v = 17.9$ m/s)	1.36	1.69	1.90	2.13
$\varepsilon (U_v = 22.1$ m/s)	1.26	1.55	1.75	1.96

defined as the angle measured from the top of the tube to the point where the interfin space is just filled with retained condensate. These were calculated using the well-known equation of Honda et al. [17] as follows:

$$\phi_f = \cos^{-1}\left[\frac{4\sigma}{\rho g s d_o} - 1\right] \quad \text{for } s < 2h \tag{8}$$

Note that Eq. (8) assumes quiescent vapor conditions. The actual flooding angle on the tubes under the current test conditions was estimated by visual observation of the test tube through the window in the test section. These observations were in good agreement with Eq. (8) in all but two instances. These were at the highest vapor velocity of 22.1 m/s and for the tubes with fin spacings of 0.25 and 0.5 mm, where the flooding angle ratios were increased to 0.05 and 0.24, respectively; i.e., the tubes were less flooded than predicted by Eq. (8) because of vapor shear acting on the condensate between the fins. This could explain the unusual trend of increasing enhancement ratio with vapor velocity, seen in Fig. 9 and Table 1, for these two tubes. A decrease in flooding of the tubes because of vapor shear at high vapor velocities would result in more surface area available for heat transfer and, hence, result in higher enhancement ratios.

Another interesting trend can be seen in Fig. 10. Here the decrease in enhancement ratio as vapor velocity increases for the tube with a fin height of 0.5 mm is less than that observed for the other three tubes. A possible explanation is that the weaker effect of vapor velocity on the finned tubes could be due to parts of the fin tube, at the bottom of the fins and on the tube root surface, being "sheltered" from the effects of vapor shear. At the lowest fin heights, this sheltering effect would be smallest, resulting in an effect of vapor velocity on the tube with the lowest fins of similar magnitude to that on a plain tube and, hence, less change in enhancement ratio with increasing vapor velocity. A similar effect was reported in [18] where the effect of a noncondensing gas on the heat-transfer rate to finned tubes in a bank was markedly greater than on plain tubes, possibly because of gas building up at the tube surface between the fins where vapor velocity was less effective at removing it. Finally, Fig. 11 demonstrates that, when

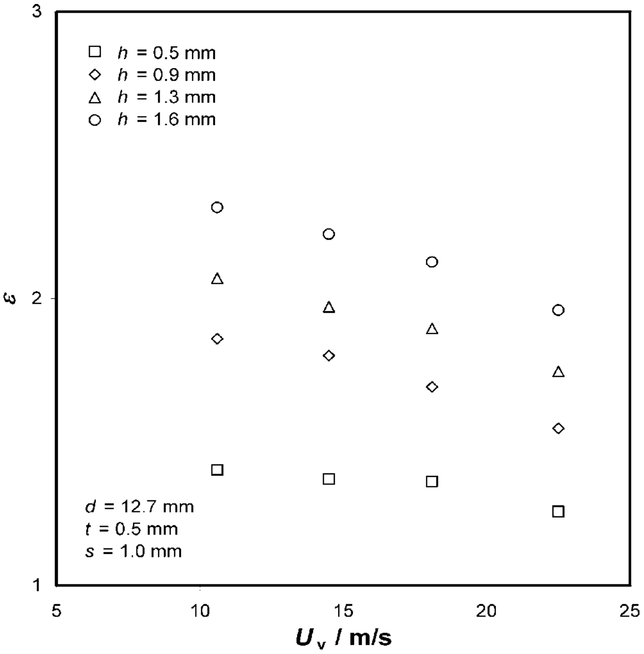

Fig. 10 Variation of enhancement ratio with vapor velocity. Effect of fin height.

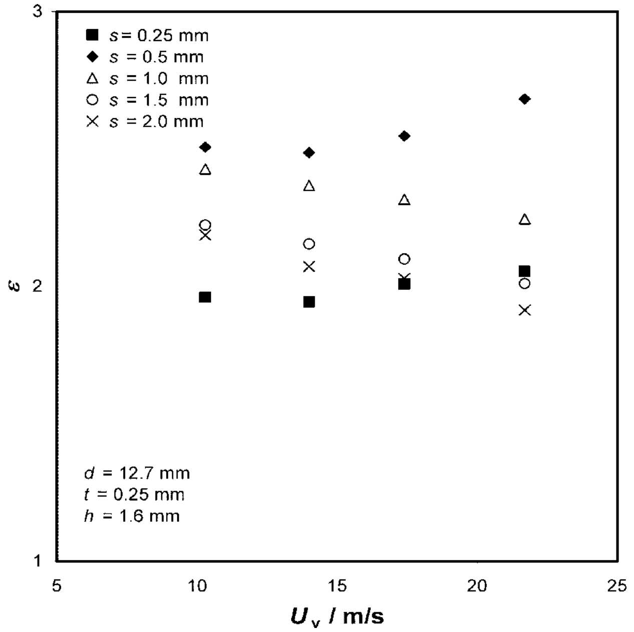

Fig. 9 Variation of enhancement ratio with vapor velocity. Effect of fin spacing.

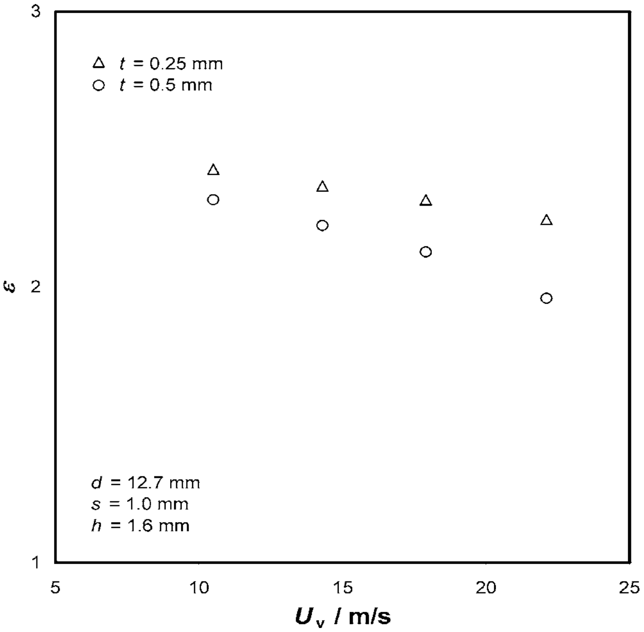

Fig. 11 Variation of enhancement ratio with vapor velocity. Effect of fin thickness.

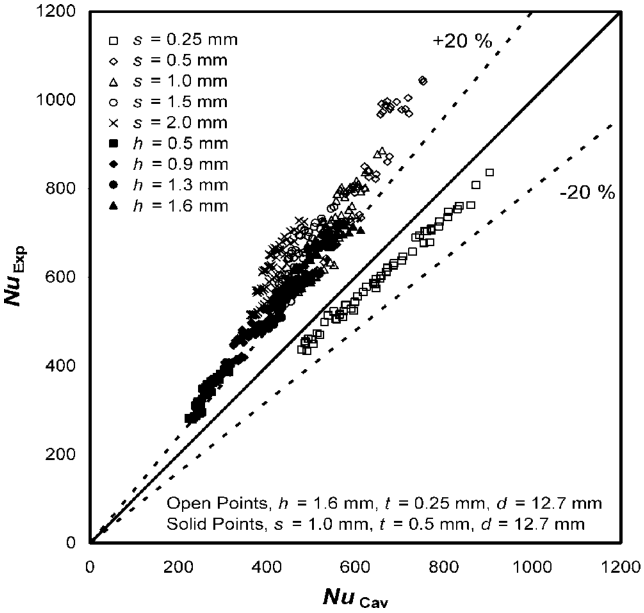

Fig. 12 Comparison of experimental data to model of Cavallini et al. [9]

all other geometric variables are held constant, thinner fins increase the enhancement ratio as expected, since they provide more surface area per unit length.

Comparison With Theory

Cavallini et al. [9] presented a semi-empirical correlation based on their data for condensation of R-11 and R-113 condensing on three finned tubes at upstream vapor velocities up to 10 m/s. Figure 12 compares the model to the data of the present investigation. It can be seen that the model underpredicts the majority of the data by at least 20% and, in many cases, by as much as 50%. The model gives good agreement, however, with one particular tube with a fin spacing, height, and thickness of 0.25, 1.6, and 0.25 mm, respectively. The reasons for this are not obvious except that this tube had geometry quite close to that of one of the tubes tested by Cavallini et al. and used in the correlation.

Conclusions

New experimental data are presented for forced-convection condensation of ethylene glycol on a set of nine single, integral-fin tubes. The data covered vapor velocities between 10 and 22 m/s and a wide range of heat fluxes. Fin spacing and fin height were varied systematically while other geometric variables were held constant. The best performing tube was that with a fin spacing, height, and thickness of 0.5, 1.6, and 0.25 mm, respectively, which had an enhancement ratio (compared to a plain tube at the same vapor-side temperature difference and vapor velocity) of 2.5 and 2.7, at the lowest and highest vapor velocities, respectively. The increase in enhancement ratio with increasing vapor velocity for this tube, and also for the tube with a fin spacing of 0.25 mm, is contrary to the results found in most earlier experimental studies and can be explained by a slight reduction in condensate flooding between the fins due to increased vapor shear.

When compared to the semi-empirical model of Cavallini et al. [9], developed using data for R-11 and R-113, the majority of the present data were underpredicted by up to 50%, indicating the need to develop a model capable of predicting forced-convection, condensation heat-transfer coefficients for a wider range of fluid properties.

Nomenclature

a = constant in Eq. (1)
B = constant in Eq. (6)
b = constant in Eq. (2)
c_p = specific isobaric heat capacity
d = diameter of plain tube or fin-root diameter of finned tube
d_i = inside diameter of tube
d_o = fin-tip diameter of finned tube
F = dimensionless parameter, $(\mu g d h_{\mathrm{fg}}/k U_v^2 \Delta T)$
g = specific force of gravity
h = fin height
h_{fg} = specific enthalpy of evaporation
k = thermal conductivity
Nu = vapor-side Nusselt number, $\alpha d/k$
Nu_c = coolant-side Nusselt number, $\alpha_c d_i/k_c$
q = Heat flux, based on outside area of plain tube with diameter equal to fin-root diameter
q_i = Heat flux, based on inside area of tube
Pr_c = coolant Prandtl number, $\mu_c c_{pc}/k_c$
Re_c = coolant Reynolds number, $\rho_c u_c d_i/\mu_c$
Re_{tp} = "Two-phase" Reynolds number, $\rho U_v d/\mu$
s = Fin spacing
T_{ref} = Reference temperature for evaluation of condensate properties (see Eq. (3))
T_v = vapor temperature
t = fin thickness
U_v = vapor velocity upstream of test tube
u_c = mean coolant velocity

Greek Symbols

α = vapor-side, heat-transfer coefficient, $q/\Delta T$
α_c = coolant-side, heat-transfer coefficient, $q_i/\Delta T_c$
ΔT = Vapor-side temperature difference (vapor saturation temperature minus mean outside wall temperature at fin root)
ΔT_c = coolant-side temperature difference (inside wall temperature minus mean coolant temperature)
ρ = density
ε = heat-transfer enhancement ratio (heat flux for finned tube based on fin-root diameter divided by heat flux for plain tube with fin-root diameter at same vapor-side temperature difference and vapor velocity)
μ = viscosity
σ = surface tension of condensate
ϕ_f = retention angle (position at which fin space becomes fully flooded with condensate) measured from top of tube

Subscripts

none = condensate
Cav = theoretical, using model of Cavallini et al. [9]
c = evaluated at mean coolant temperature
exp = experimental
wi = Evaluated at tube inside wall temperature

References

[1] Marto, P. J., 1988, "An Evaluation of Film Condensation on Horizontal Integral Fin Tubes," ASME J. Heat Transfer, **110**, pp. 1287–1305.
[2] Briggs, A., and Rose, J. W., 1999, "An Evaluation of Models for Condensation Heat Transfer on Low-Finned Tubes," J. Enhanced Heat Transfer, **6**, pp. 51–60.
[3] Rose, J. W., 1988, "Fundamentals of Condensation Heat Transfer: Laminar Film Condensation," JSME Int. J., Ser. II, **31**, pp. 357–375.
[4] Michael, A. G., Marto, P. J., Wanniarachchi, A. S., and Rose, J. W., 1989, "Effect of Vapor Velocity During Condensation on Horizontal Smooth and Finned Tubes," *Proc. ASME Winter Annual Meeting, San Francisco*, ASME, New York, ASME Paper No. HTD-114, pp. 1–10.
[5] Briggs, A., Wen, X. L., and Rose, J. W., 1992, "Accurate Heat-Transfer Measurements for Condensation on Horizontal Integral-Fin Tubes," ASME J. Heat Transfer, **114**, pp. 719–726.

[6] Bella, A., Cavallini, A., Longo, G. A., and Rossetto, L., 1993, "Pure Vapor Condensation of Refrigerants 11 and 113 on a Horizontal Integral-Fin Tube at High Vapor Velocity," J. Enhanced Heat Transfer, **1**, pp. 77–86.
[7] Cavallini, A., Doretti, L., Longo, G. A., and Rossetto, L., 1994, "Experimental Investigation of Condensate Flow Patterns on Enhanced Surfaces," *Proc. CFC's, The Day After, IIR International Conference, Padua*, pp. 627–634.
[8] Namasivayam, S., and Briggs, A., 2004, "Effect of Vapor Velocity on Condensation of Atmospheric Pressure Steam on Integral-Fin Tubes," Appl. Therm. Eng., **24**, pp. 1353–1364.
[9] Cavallini, A., Doretti, L., Longo, G. A., and Rossetto, L., 1996, "A New Model for Forced-Convection Condensation on Integral-Fin Tubes," ASME J. Heat Transfer, **118**, pp. 689–693.
[10] Briggs, A., and Rose, J. W., 1994, "Effect of 'Fin Efficiency' on a Model for Condensation Heat Transfer on a Horizontal Integral-Fin Tube," Int. J. Heat Mass Transfer, **37**(Suppl. 1), pp. 457–463.
[11] Sieder, E. N., and Tate, G. E., 1936, "Heat Transfer and Pressure Drop of Liquids in Tubes," Ind. Eng. Chem., **28**, pp. 1429–1435.
[12] Shekriladze, I. G., and Gomelauri, V. I., 1966, "Theoretical Study of Laminar Film Condensation of Flowing Vapor," Int. J. Heat Mass Transfer, **9**, pp. 581–591.
[13] Moffat, R. J., 1988, "Describing the Uncertainties in Experimental Results," Exp. Therm. Fluid Sci., **1**, pp. 3–17.
[14] Briggs, A., 1991, "Forced-Convection Condensation on Horizontal, Integral-Fin Tubes," Ph.D. Thesis, University of London.
[15] Nusselt, W., 1916, "Die Oblerflachenkondensation des Wasserdampfes," Z. Vereines Deutsch. Ing., **60**, pp. 541–546, 569–575.
[16] Memory, S., and Rose, J. W., 1986, "Filmwise Condensation of Ethylene Glycol on a Horizontal Tube at High Vapor Velocity," *Proc. of 8th Int Heat Transfer Conf., San Francisco*, Vol. 4, pp. 1607–1612.
[17] Honda, H., Nozu, S., and Mitsumori, K., 1983, "Augmentation of Condensation on Finned Tubes by Attaching a Porous Drainage Plate," *Proc. ASME-JSME Thermal Engineering Joint Conf.*, Vol. 3, p. 289.
[18] Briggs, A., and Sabaratnam, S., 2005, "Condensation From Pure Steam and Steam-Air Mixtures on Integral-Fin Tubes in a Bank," ASME J. Heat Transfer, **127**, pp. 571–580.

Condensation on a Horizontal Wire-Wrapped Tube

Takahiro Murase

Adrian Briggs

Hua Sheng Wang
e-mail: h.s.wang@qmul.ac.uk

John W. Rose
e-mail: j.w.rose@qmul.ac.uk

Department of Engineering,
Queen Mary, University of London,
Mile End Road,
London E1 4NS, UK

Measurements for film condensation of steam, R113 and ethylene glycol on a horizontal wire-wrapped tube are reported. All measurements were made at near atmospheric vapor pressure and with coolant at around 20 °C. *Care was taken to avoid error due to the presence of air in the vapor. Complete wetting (film condensation) was observed in all cases. Wire diameter and pitch of winding were systematically varied and heat-transfer measurements made for a range of coolant flow rates. Data, in the form of heat flux and vapor-to-surface temperature difference, are presented. These were used to determine enhancement ratios (ratio of heat flux or heat-transfer coefficient for a wire-wrapped tube to the corresponding value for a plain tube at the same vapor-to-surface temperature difference). Enhancement ratios exceeding 3 for R113 and 2 for steam and ethylene glycol were obtained. The results are discussed in the light of earlier measurements and theory.* [DOI: 10.1115/1.2039113]

Keywords: heat transfer enhancement, condensation, wire-wrapped tube, surface tension, steam, R113, ethylene glycol

Introduction

Winding fine wires on a condenser tube is a simple and cheap way to enhance condensation heat transfer. This problem may be largely of academic interest since higher enhancement can be obtained for low surface tension refrigerants using low integral-finned tube. The wire wrap case differs from the integral fin case in that, even with high conductivity wire, line contact between the wire and tube surface means that conduction through the wire is negligible and heat transfer enhancement is due solely to the surface-tension effect that thins the condensate film on the tube surface between adjacent wires. In practice, a wire-wrapped tube condenser may be useful where finned copper tube may not be suitable, for example, condensers used for the Ocean Thermal Energy Conversion (OTEC) application [1].

Several earlier experimental investigations have been done on condensation on horizontal wire-wrapped tubes. In performance tests on a compact heat exchanger for OTEC application, Thomas et al. [1] reported data for condensation of ammonia on an internally enhanced (axial fins) externally wire-wrapped tube. Based on a Wilson plot calculation, the authors reported that the ammonia-side, heat-transfer coefficient was around twice the value predicted by the Nusselt theory for a smooth tube. It was not clear which parameter was the same for the two cases, e.g., temperature difference, heat flux, coolant flow rate, other. The authors acknowledge that their Wilson plot calculation is susceptible to large error. Also using ammonia, Rifert et al. [2] reported enhancement ratios (for the same heat flux) varying from around 2 at 5 $\mathrm{kW/m^2}$ to around 1.6 at 50 $\mathrm{kW/m^2}$ for condensation on wire-wrapped tubes with wire diameter and pitch 1.5 and 8 mm, respectively. Smaller enhancements were reported for pitches of 4 and 16 mm. The vapor-side heat-transfer coefficients were obtained from overall measurements using a predetermined coolant-side correlation and are consequently subject to significant error.

Fujii et al. [3] conducted heat-transfer measurements for condensation of R11 and ethanol on a horizontal tube having an outside diameter of 18 mm with wires of diameter 0.1, 0.2, and 0.3 mm and pitch of winding 0.5, 1.0, and 2.0 mm. The condenser tube served as a resistance thermometer for measurement of the surface temperature. Marto et al. [4] obtained data for steam condensation at atmospheric pressure and under vacuum conditions on a horizontal tube having an outside diameter 19 mm with wire diameters of 0.5, 1.0, and 1.6 mm, and pitch of winding from 1.60 to 4.62 mm. Vapor-side, heat-transfer coefficients were obtained using a modified Wilson plot. Further measurements for steam have been reported more recently by Briggs et al. [5] who used a tube of diameter 12.2 mm fitted with embedded thermocouples for measurement of the surface temperature, wire diameters of 0.4, 0.75, and 1.00 mm and pitch of winding from 1.0 to 6.0 mm. In these investigations the enhancement ratio was found to depend on wire diameter and pitch of winding with maximum values a little above and a little below 3 for R11 and ethanol, respectively, by Fujii et al. [3] and for steam around 2 by both Marto et al. [4] and Briggs et al. [5].

Fujii et al. [3] made an approximate theoretical analysis of film condensation on wire-wrapped tubes. By applying the conservation equations, together with the Nusselt approximations and including the surface tension-generated axial pressure gradient, they obtained the following differential equation for the condensate film thickness δ:

$$\rho g x \frac{\partial}{\partial \phi}(\delta^3 \sin \phi) - \frac{d}{2}\delta^3 \frac{\partial P}{\partial x} = \frac{3}{2}\frac{\mu k d \Delta T x}{\rho h_{\mathrm{fg}} \delta} \tag{1}$$

where ρ is the density of condensate, g is the specific force of gravity, d is the outside diameter of the tube, μ is the dynamic viscosity of condensate, k is the conductivity of condensate, ΔT is the vapor-to-surface temperature difference, h_{fg} is the specific latent heat of evaporation, x is distance measured axially along the tube surface from the midpoint between adjacent wire turns (see Fig. 1), ϕ is angle around the tube measured from the top, and P is the pressure in the condensate. The axial pressure gradient due to surface tension and variable surface curvature is given by

$$\frac{\partial P}{\partial x} = -\sigma \frac{\partial}{\partial x}\left(\frac{1}{r}\right) = -\sigma \frac{\partial}{\partial x}\left\{\frac{\partial^2 \delta/\partial x^2}{[1 + (\partial \delta/\partial x)^2]^{3/2}}\right\} \tag{2}$$

where σ is the surface tension and r is the radius of curvature of condensate surface in the radial plane measured on the vapor side.

An essential feature of the approach of Fujii et al. [3] was the simplification achieved when solving Eq. (1) by assuming an axially uniform condensate film thickness between adjacent wires and an abrupt change to constant curvature (constant arc radius r_s)

Contributed by the Heat Transfer Division of ASME for publication in the JOURNAL OF HEAT TRANSFER. Manuscript received January 17, 2005; final manuscript received June 20, 2005. Review conducted by: Raj M. Manglik.

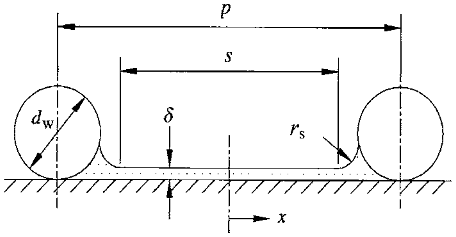

Fig. 1 Condensate film between adjacent wires in Fujii et al. [3] theory

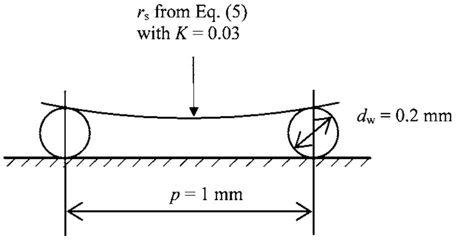

Fig. 2 Example of geometry incompatibility (compare Fig. 1) in Fujii et al. [3] theory (R11, $d = 18$ mm, saturation pressure 1.02 bar, saturation temperature 24 °C).

near the wires (see Fig. 1). This meant that the transverse (axial) pressure gradient $\partial P/\partial x$ was zero except near the wire where it underwent a step change σ/r_s. Equation (1) could then be integrated twice with respect to x without having recourse to the curvature expression in Eq. (2). This resulted in an ordinary differential equation for δ in terms of ϕ, expressible, as shown later by Rose [6], as

$$\delta\frac{d}{d\phi}(\delta^3 \sin \phi) + \frac{4d\sigma\delta^4}{\rho g s^2 r_s} = \frac{3}{2}\left(\frac{\mu k d \Delta T}{\rho^2 g h_{\mathrm{fg}}}\right) \tag{3}$$

The length of the uniform thickness portion of the film s and arc radius r_s were assumed to be constant around the tube. s was taken as

$$s = p - d_w \tag{4}$$

and an empirical equation

$$r_s = K(2\sigma/\rho g)^{3/2}/d_w^2 \tag{5}$$

was used for r_s, where K is a constant subsequently assigned a value of 0.03 so as best to fit their experimental heat-transfer data for R11 and ethanol. Solution of Eq. (3) indicated that the film thickness was essentially uniform around the tube when

$$4\sigma d/(\rho g s^2 r_s) > 15 \tag{6}$$

so that only the solution for the top of the tube was required when the inequality (6) was satisfied and the enhancement ratio $\varepsilon_{\Delta T}$ (heat flux or heat-transfer coefficient for wire-wrapped tube divided by the corresponding value for a plain tube for the same ΔT) is given by

$$\varepsilon_{\Delta T} = \frac{p - d_w}{0.9p}\left\{\frac{4(1 + A)}{3}\right\}^{1/4} \tag{7}$$

where

$$A = \frac{\sqrt{2}}{0.03}\frac{dd_w^2}{(p - d_w)^2}\sqrt{\frac{\rho g}{\sigma}} \tag{8}$$

Perhaps not too surprisingly, since the constant K was chosen to fit the data, the theory and heat-transfer measurements of Fujii et al. [3] were in fair accord.

Apart from the method of handling of the transverse pressure gradient, several features of this analysis may be questioned, namely, r_s and s taken as constant and given by Eqs. (4) and (5), the fact that the quantity $4\sigma d/(\rho g s^2 r_s)$ is often <15 and, perhaps most importantly, Eq. (5), with $K = 0.03$, is incompatible with the geometry (wire diameter and pitch of winding) in most cases as illustrated in Fig. 2 (compare model illustrated in Fig. 1).

Marto et al. [4] found that the model of Fujii et al. [3] overestimated the heat transfer in their measurements for condensation of steam on a wire-wrapped tube. They attributed this to condensate retention between adjacent wires on the lower part of the tube in the same manner as occurs for condensation on integral-finned tubes. They noted, however, that for a wire-wrapped tube there was no abrupt, well-defined, condensate retention location as found with low-finned tubes. From their visual observations, an approximate expression for a retention angle was obtained in this case. By using the Fujii et al. [3] approach for the "unflooded region" above the retention position and one-dimensional conduction in the "flooded" region below the retention position they were able to modify the result of Fujii et al. [3] to bring the calculated enhancement ratios into closer accord with their steam data. They did not, however, examine the consequence of their modification for comparison to the earlier data of Fujii et al. [3] for R11 and ethanol.

On the basis that films resulting from condensation are very thin compared to those due to static capillary retention, Rose [6] noted that r_s, and, consequently, the length of the uniform film thickness portion of the condensate film between adjacent wires in the Fujii et al. [3] approach, must vary around the tube as illustrated in Fig. 3. He obtained an expression for r_s in terms of the angle around the tube ϕ using an approach based on that of Masuda and Rose [7] for static retention of liquid on integral-fin tubes. In this way empiricism was removed from the model of Fujii et al. [3]. Rose [6] further neglected heat transfer over the curved part of the condensate surface (which included the whole of the lower part of the tube where $\phi > \phi_f$, see Eq. (10) below) and obtained the following analytical expression for the enhancement ratio

$$\varepsilon_{\Delta T} = \frac{z_0^{-1/4}}{2.287p}\left[p\phi_f - 4\left(\frac{2d_w\sigma}{\rho g d}\right)^{1/2}\ln\left\{\tan\left(\frac{\phi_f}{4} + \frac{\pi}{4}\right)\right\}\right] \tag{9}$$

where

$$\phi_f = \cos^{-1}\{16d_w\sigma/(\rho g d p^2) - 1\} \tag{10}$$

$$z_0 = \frac{3}{2[1 + 4d^2/s_0^2]} \tag{11}$$

$$s_0 = p - 4[d_w\sigma/(2\rho g d)]^{1/2} \tag{12}$$

ϕ_f in Eq. (10) is the angle, measured from the top of the tube, to the position at which the retained liquid "wedges" meet midway between adjacent wire turns (see Fig. 3). For $\phi > \phi_f$ there can be no uniform thickness portion of the condensate film between the wires as in the original Fujii et al. [3] model. This picture is in

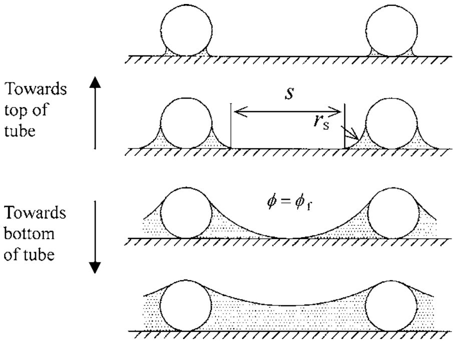

Fig. 3 Condensate retention between adjacent wires

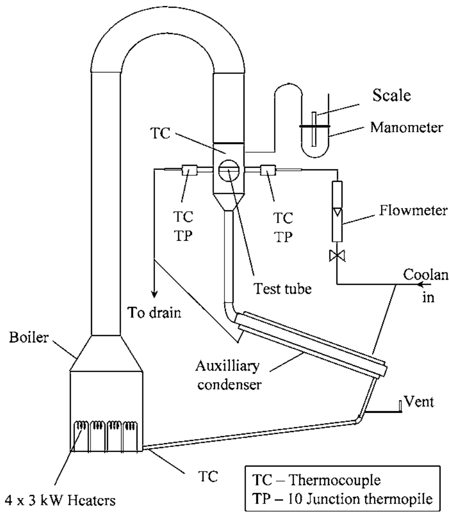

Fig. 4 Apparatus

accord with the visual observations of Marto et al. [4].

Comparisons of Eq. (9) with the steam data of Marto et al. [4] and Briggs et al. [5] and the R11 and ethanol data of Fujii et al. [3] were inconclusive. The theoretical trends (dependence of enhancement ratio on wire diameter and pitch of winding) agreed with those found by Marto et al. [4] for steam but generally underestimated the enhancement ratio. In the case of the Fujii et al. [3] measurements the theory and experiment showed opposite trends, the theory underestimating the enhancement ratio for larger pitch and smaller diameter and overestimating for smaller pitch and larger wire diameter.

It is evident from the above that significant questions remain over the mechanism and theory of condensation on wire-wrapped tubes. The present work was undertaken to throw more light on the subject by conducting further careful measurements and including those with a fluid, ethylene glycol, with properties (in particular, surface tension) intermediate between those of the fluids used earlier.

Present Experimental Investigation

Apparatus The stainless-steel test apparatus, shown schematically in Fig. 4, consisted of a closed loop, with vapor generated in an electrically heated boiler (maximum power 12 kW). The vapor was directed vertically downward through a calming section before flowing over the horizontal, water-cooled, test condenser tube. The copper test condenser tube had an outside diameter of 12.2 mm, active heat transfer length 90 mm, and was fitted with four embedded wall thermocouples located as shown in Fig. 5. PTFE (polytetrafluoroethylene, Teflon) sleeves were inserted at both ends of the tube so that the cooled length of tube was the same as that exposed to vapor. Steel wires having diameters of 0.2, 0.35, 0.4, 0.75, and 1.0 mm were wound, in turn, tightly (but not soldered) on the outside surface with winding pitches ranging from values a little larger than the wire diameter in each case up to 6.0 mm for R113 and steam and up to 4.5 mm for ethylene glycol. Uniformity of spacing was judged by eye. Before installation the tube was thoroughly cleaned with a mixture (distilled water (2000 ml), sulphuric acid (H_2SO_4, 100 ml) and sodium dichromate ($Na_2Cr_2O_7$, 200 g)) and rinsed with the condensing fluid to be used. Tube and wire surfaces were always observed to be fully wetted during subsequent tests.

All tests were done at a little above atmospheric pressure with vapor approach velocity of ~0.23 m/s for R113, 0.41 m/s for ethylene glycol, and 0.57 m/s for steam. Excess vapor passed to an auxiliary condenser from which the condensate returned to the boiler by gravity.

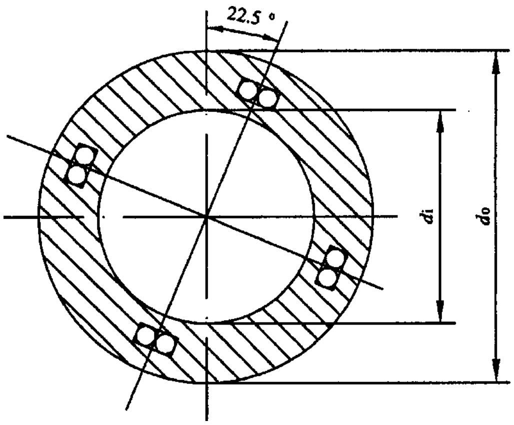

Fig. 5 Location of thermocouples in the tube wall (inside diameter d_i=8.35 mm, outside diameter d_o=12.2 mm)

The cooling water temperature rise was measured using a ten-junction thermopile. Care was taken to ensure adequate mixing and isothermal immersion of the leads in the vicinity of the junctions. The heat flux was found from the coolant flow rate and temperature rise, and the surface temperature was taken as the mean of the temperatures indicated by the embedded thermocouples with a small correction for the depth of the thermocouples below the condensing surface. A small predetermined correction (dependent on coolant flow rate) for the dissipative temperature rise of the cooling water in the tube and mixing boxes was incorporated in the calculation of the heat-transfer rate. The vapor velocity at approach to the test section was found from the measured power input to the boiler (together with the condensate return temperature) with a small, predetermined correction for the heat loss from the well-insulated apparatus (see [8]). All thermocouples were calibrated in a high-precision constant-temperature bath against a platinum resistance thermometer, accurate to 0.005 K. The accuracy of the thermo emf measurement was 2 μV, equivalent to 0.005 K for the ten-junction thermopile. Er-

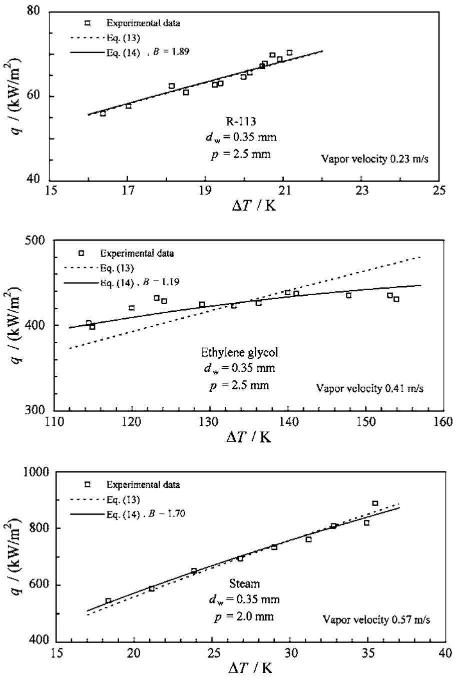

Fig. 6 Effect of variable properties on curve fit

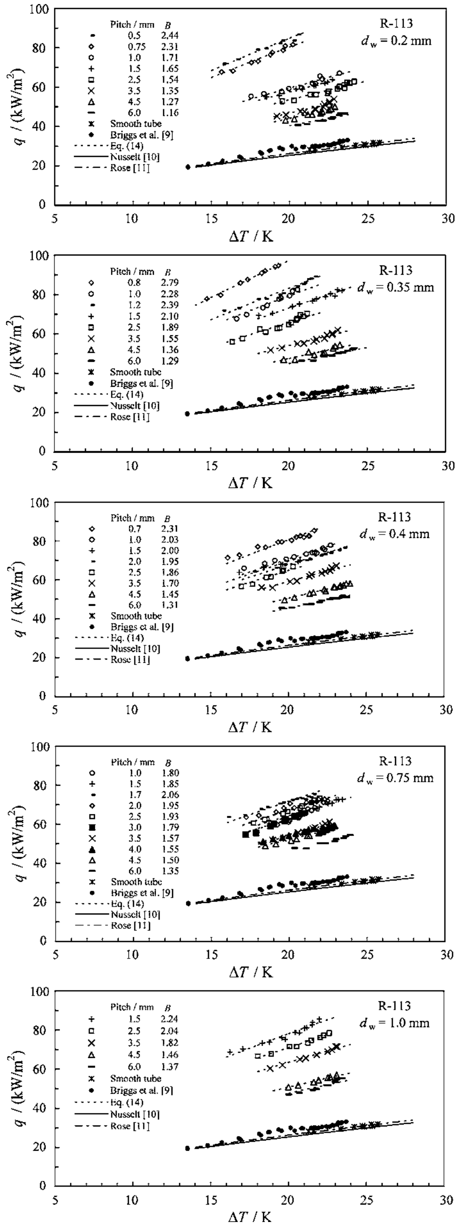

Fig. 7 Dependence of heat flux on vapor-to-surface temperature difference for condensation of R113 (*B* is 0.758 for smooth tube, vapor velocity 0.23 m/s).

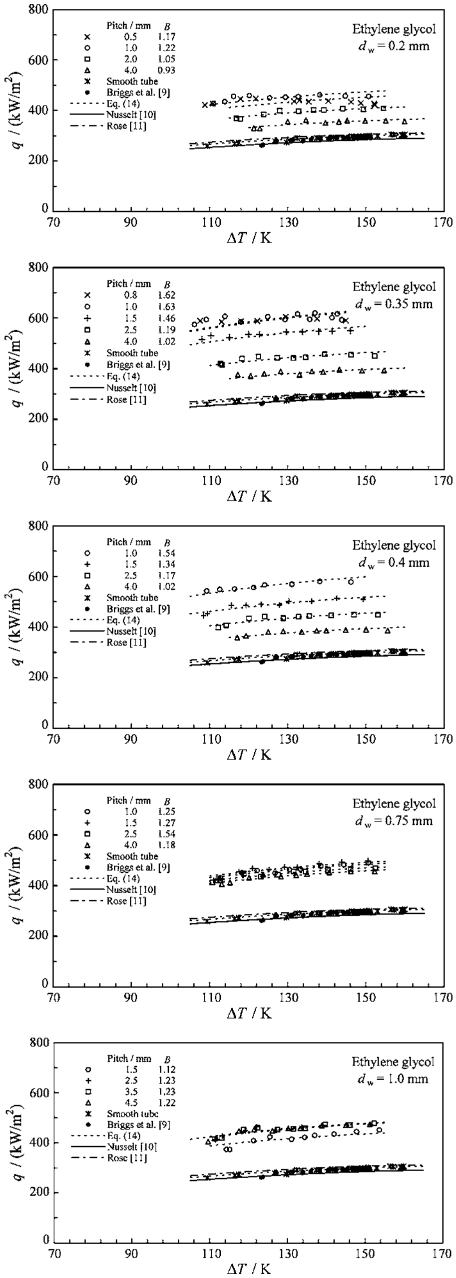

Fig. 8 Dependence of heat flux on vapor-to-surface temperature difference for condensation of ethylene glycol (*B* is 0.766 for smooth tube, vapor velocity 0.41 m/s)

rors and uncertainty in heat flux, vapor-to-surface temperature difference, and enhancement ratio are discussed in the Appendix.

Results. In earlier experiments using steam and refrigerants for both low-finned and wire-wrapped tubes, it has been found that the heat flux varies approximately as the $\frac{3}{4}$ power of the vapor-to-surface temperature difference as in the Nusselt smooth-tube case. This has the advantage that the enhancement ratio obtained by fitting the data by a Nusselt-type expression is independent of temperature difference or heat flux. When property variation is small, the data may be satisfactorily fitted by

$$q = \text{const}\ \Delta T^{3/4} \tag{13}$$

In the case of ethylene glycol, some of the data are not well represented by Eq. (13). This is because of the strong dependence of viscosity on temperature for ethylene glycol and the relatively large temperature differences across the condensate film under the present experimental conditions. In this case it is better to fit the data by

$$q = B\left\{\frac{\rho(\rho-\rho_v)gh_{\mathrm{fg}}k^3}{\mu d}\right\}^{1/4}\Delta T^{3/4} \tag{14}$$

where ρ_v is the vapor density and B is a constant found by minimizing the sum of squares of residuals of q.

Figure 6 shows a set of data for all three fluids fitted by both Eqs. (13) and (14). For R113 and steam, the curves obtained when using Eqs. (13) and (14) do not differ substantially, but Eq. (14) is evidently more satisfactory for ethylene glycol. Equation (14) has been used for all data and the properties, with the exception of h_{fg}, taken at reference temperature

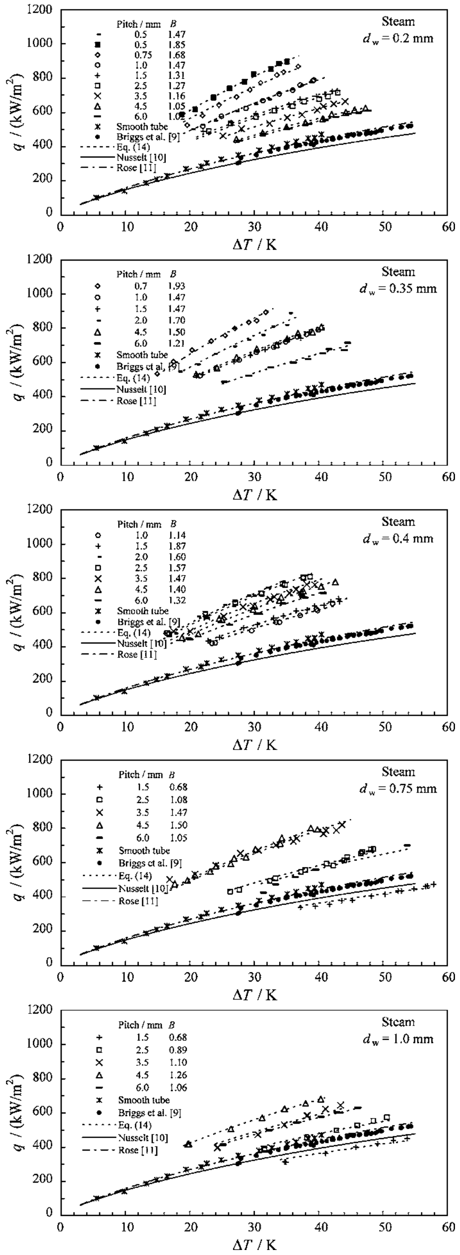

Fig. 9 Dependence of heat flux on vapor-to-surface temperature difference for condensation of steam (*B* is 0.835 for smooth tube, vapor velocity 0.57 m/s)

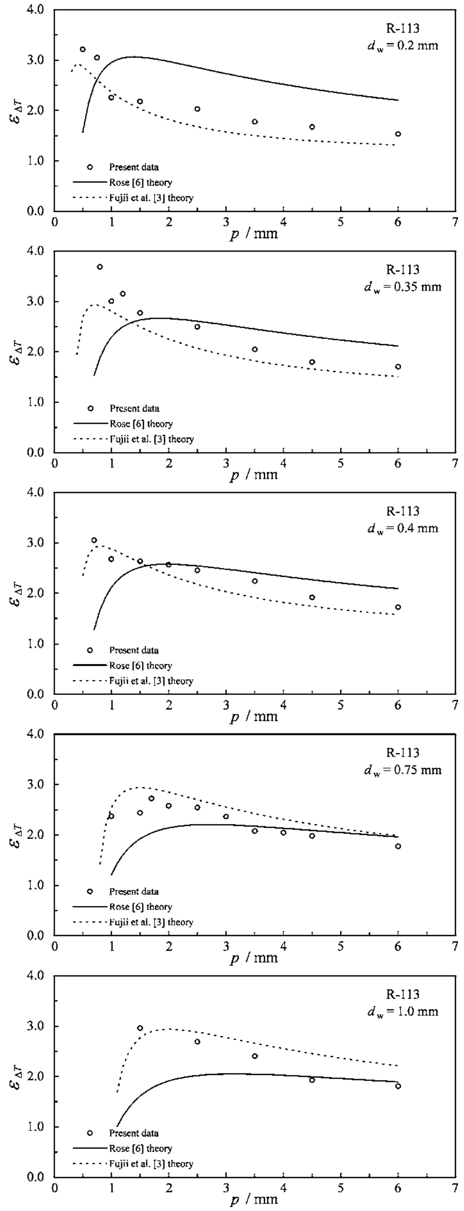

Fig. 10 Dependence of enhancement ratio on pitch for condensation of R113 (vapor velocity 0.23 m/s)

$$T^* = \left(\tfrac{1}{3}\right)T_v + \left(\tfrac{2}{3}\right)T_w \tag{15}$$

where T_v is the vapor temperature and T_w is the tube wall temperature. h_{fg} was evaluated at T_v. The heat flux versus temperature difference results for all three fluids are shown in Figs. 7–9, which include reprocessed data of Briggs et al. [5] for steam. It is seen that Eq. (14) gives a satisfactory fit in all cases. It may be noted that the smooth tube data (present data and Briggs et al. [9]) lie a little above the Nusselt [10] line and are in close agreement with

$$\mathrm{Nu}\,\widetilde{\mathrm{Re}}^{-1/2} = \frac{0.9 + 0.728F^{1/2}}{(1 + 3.44F^{1/2} + F)^{1/4}} \tag{16}$$

where

$$F = \frac{\mu d h_{fg} g}{u_\infty^2 k \Delta T} \tag{17}$$

and $\widetilde{\mathrm{Re}} = u_\infty \rho d/\mu$ is the so-called two-phase Reynolds number, u_∞ is the vapor approach velocity. F indicates the relative importance of gravity and vapor velocity. Equation (16) is from Rose [11] and is based on the analysis of Shekriladze and Gomelauri [12] for forced convection condensation on a horizontal tube.

The enhancement ratio for a given data set is the constant B in Eq. (14) divided by the value of B obtained from the smooth tube data. Figures 10–12 show enhancement ratios for the three fluids plotted against pitch of winding for each wire diameter, together with theoretical results of Fujii et al. [3] and Rose [6]. It may be seen that the Eq. (7) from Fujii et al. [3] is, in many cases, closer to the data than Eq. (9) from Rose [6] but that neither can be said to be in good agreement with the data as a whole.

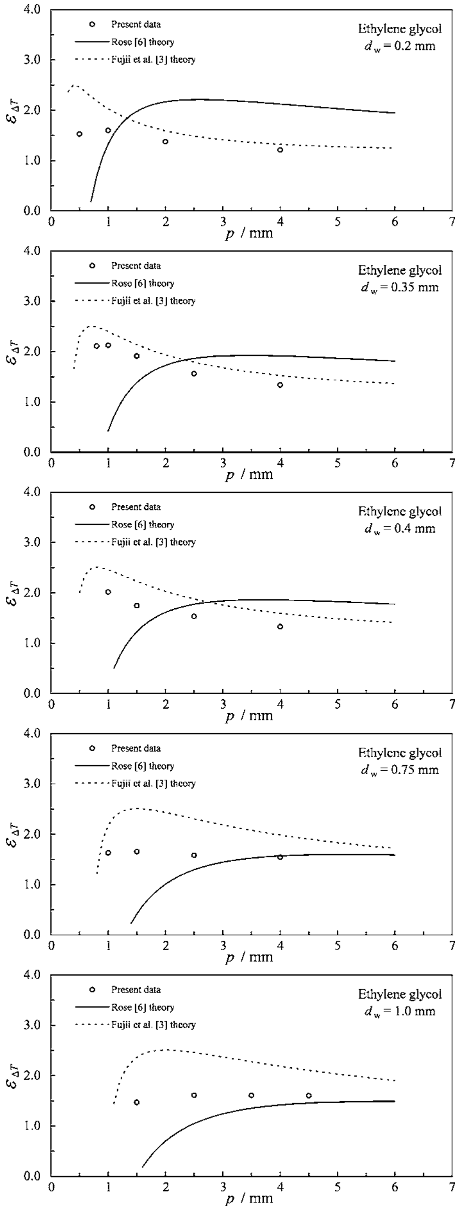

Fig. 11 Dependence of enhancement ratio on pitch for condensation of ethylene glycol (vapor velocity 0.41 m/s)

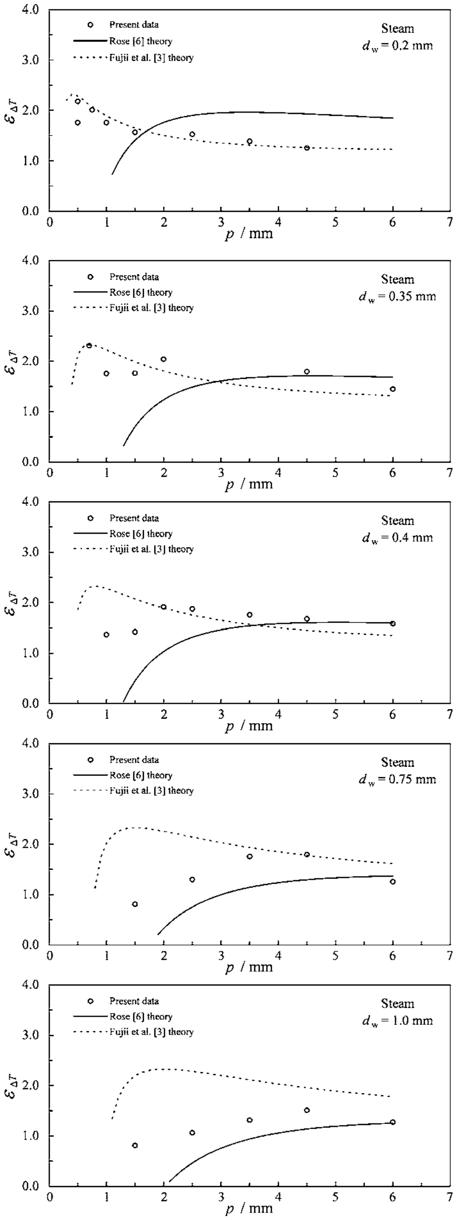

Fig. 12 Dependence of enhancement ratio on pitch for condensation of steam (vapor velocity 0.57 m/s)

Conclusion

Extensive new accurate data have been obtained for heat transfer during condensation of R113, ethylene glycol, and steam on a wire-wrapped tube. Deficiencies of existing theoretical results have been highlighted. The validity of the treatment of the condensate film in the model of Fujii et al. [3] remains to be established. Furthermore, the assumption of uniform condensate fillet radius at the wire is incorrect and, with the empirical equation for fillet radius, is incompatible in many cases with the assumed geometry of the condensate film. The modification by Rose [6] removes the incompatibility and empiricism from the Fujii et al. [3] model, but probably significantly underestimates the heat transfer by taking those parts of the surface where the condensate surface is curved to be adiabatic. Neither result gives satisfactory agreement with the data taken as a whole. The fact that the Fujii et al. [3] result is, in many cases, in better agreement is, in part, because the result incorporates an empirical constant chosen so as to fit some of the data. Evidently, a more detailed theoretical approach is needed.

Nomenclature

A = defined in Eq. (8)
B = constant in Eq. (14)
d = outside diameter of the tube
d_w = wire diameter
F = defined in Eq. (17)
g = specific force of gravity
h_{fg} = specific latent heat of evaporation
k = conductivity of condensate
K = constant in Eq. (5)
Nu = Nusselt number, $(q/\Delta T)(d/k)$
p = pitch of winding
P = pressure in the condensate film
q = heat flux based on smooth tube area
r = radius of curvature of condensate surface in the radial plane measured on the vapor side
r_s = radius of curvature of condensate film at wire
Re = "two-phase Reynolds number," $u_\infty \rho d/\mu$

s = axial length of uniform film thickness portion
s_0 = defined in Eq. (12)
T_v = vapor temperature
T_s = saturation temperature
T_w = tube wall temperature
T^* = reference temperature, see Eq. (15)
ΔT = vapor-to-surface temperature difference
u_∞ = vapor approach velocity
x = distance measured axially along tube surface from midpoint between adjacent wire turns (see Fig. 1)
z_0 = defined in Eq. (11)

Greek Symbols

ρ = density of condensate
ρ_v = density of vapor
δ = condensate film thickness, see Fig. 1
μ = dynamic viscosity of condensate
σ = surface tension
$\varepsilon_{\Delta T}$ = Enhancement ratio, heat flux or heat-transfer coefficient for wire-wrapped tube divided by the corresponding value for a plain tube for the same ΔT
ϕ = angle measured from the top of the tube
ϕ_f = value of ϕ at $s=0$, see Fig. 3 and Eq. (10)

Appendix: Error Estimates

It is not easy to quantify the uncertainty in the enhancement ratio $\varepsilon_{\Delta T}$. This depends not only on the accuracy of the measured quantities q and ΔT, but also uncertainty introduced by forcing the data to fit Eq. (14). The standard deviations from the fits are typically $<1.0\%$ for R113 and $<2.0\%$ for steam and ethylene glycol. The error in q is largely determined by that in the temperature rise of the coolant. Using the ten-junction thermopile, coolant mixing arrangements, and calibration procedure we estimate the accuracy in coolant temperature rise to be better than 0.01 K. The range of temperature rise measured was 1.00–6.98 K for steam, 0.89–9.28 K for ethylene glycol, and 0.11–0.77 K for R113. The maximum error in q on this basis, and including a maximum coolant flow-rate error of 2.0%, would be around 2.5% for steam and ethylene glycol and between 2.5% and 9.0% for R113, the higher values being at the higher coolant flow rates where the temperature rise is least. The uncertainty in the vapor-to-surface temperature difference is not primarily due to the accuracy of vapor and wall temperature measurements (each measurement judged to have accuracy better than 0.1 K), but rather to the variation in temperature around the tube perimeter. The temperatures were highest near the top of the tube and lowest near the bottom. The surface temperature used to calculate the vapor-to-surface temperature difference was the arithmetic mean of the four measurements. The largest difference between the highest and lowest of these was around 30, 23, and 6 K for steam, ethylene glycol and R113, respectively.

References

[1] Thomas, A., Lorenz, J. J., Hillis, D. L., Yung, D. T., and Sather, N. F., 1979, “Performance Tests of 1 MWt Shell-and-Tube and Compact Heat Exchangers for OTEC,” *Proc. of 6th OTEC Conference*, Washington, D.C., Vol. 2, Paper No. 11–1, pp. 1–12.

[2] Rifert, V. G., Trokoz, Y. Y., and Zadiraka, V. Y., 1984, “Enhancement of Heat Transfer in Condensation of Ammonia Vapor on a Bundle of Wire-Finned Tubes,” Heat Transfer-Sov. Res., **16**(1), pp. 36–41.

[3] Fujii, T., Wang, W. C., Koyama, S., and Shimizu, Y., 1985, “Heat Transfer Enhancement for Gravity Controlled Condensation on a Horizontal Tube by Coiling Wires,” *Proc. of 2nd International Symposium on Heat Transfer*, Tsinghua Univ., Beijing, Oct. 15–18, 1985; and in *Heat Transfer Science and Technology*, Bu-Xuan Wang, ed., Hemisphere, New York pp. 773–780, 1987.

[4] Marto, P. J., Mitrou, E., Wanniarachchi, A. S., and Katsuta, M., 1987, “Film Condensation of Steam on a Horizontal Wire-Wrapped Tube,” *Proc. 2nd ASME-JSME Thermal Engineering Joint Conference*, Honolulu, HI, Vol. 1, pp. 509–516.

[5] Briggs, A., Wang, H. S., Murase, T., and Rose, J. W., 2003, “Heat Transfer Measurements for Condensation of Steam on a Horizontal Wire-Wrapped Tube,” J. Enhanced Heat Transfer, **10**, pp. 383–390.

[6] Rose, J. W., 2002, “An Analysis of Laminar Film Condensation on a Horizontal Wire-Wrapped Tube,” Trans. Inst. Chem. Eng., Part A, **80**(A), pp. 290–294.

[7] Masuda, H., and Rose, J. W., 1987, “Static Configuration of Liquid Films on Horizontal Tubes With Low Radial Fins: Implications for Condensation Heat Transfer,” Proc. R. Soc. London, Ser. A, **410**, pp. 125–139.

[8] Lee, W. C., and Rose, J. W., 1984, “Forced-Convection Film Condensation on a Horizontal Tube With and Without Non-Condensing Gases,” Int. J. Heat Mass Transfer, **27**, pp. 519–528.

[9] Briggs, A., Wen, X. L., and Rose, J. W., 1992, “Accurate Heat Transfer Measurements for Condensation on Horizontal, Integral-Fin Tubes,” ASME J. Heat Transfer, **114**, pp. 719–726.

[10] Nusselt, W., 1916, “Die Oberflächenkondensation des Wasserdampfes,” Z. Ver. Dt. Ing., **60**, pp. 569–575.

[11] Rose, J. W., 1984, “Effect of Pressure Gradient in Forced Convection Film Condensation on a Horizontal Tube,” Int. J. Heat Mass Transfer, **27**, pp. 39–47.

[12] Shekriladze, I. G., and Gomelauri, V. I., 1966, “The Theoretical Study of Laminar Film Condensation of a Flowing Vapor,” Int. J. Heat Mass Transfer, **9**, pp. 581–591.

Correlation for Flow Boiling Heat Transfer at Low Liquid Reynolds Number in Small Diameter Channels

Weizhong Zhang
Graduate School of Energy Science,
Kyoto University,
Kyoto 606-8317, Japan

Takashi Hibiki
Research Reactor Institute,
Kyoto University, Kumatori, Sennan, Osaka
590-0494, Japan
Phone: +81-724-51-2373
Fax: +81-724-51-2461
e-mail: hibiki@rri.kyoto-u.ac.jp

Kaichiro Mishima
Research Reactor Institute,
Kyoto University,
Kumatori, Sennan, Osaka 590-0494, Japan
Phone: +81-724-51-2449
Fax: +81-724-51-2637
e-mail: mishima@rri.kyoto-u.ac.jp

In view of significance of a heat transfer correlation of flow boiling under the conditions of low liquid Reynolds number or liquid laminar flow, and very few correlations in principle suitable for such flow conditions, this study is aiming at developing a heat transfer correlation of flow boiling at low liquid Reynolds number for small diameter channels. The correlation is developed based on superimposition of two main flow boiling mechanisms, namely nucleate boiling and forced convection. In the correlation, two terms corresponding to nucleate boiling and forced convection are obtained from the pool boiling correlation by Forster and Zuber and the analytical annular flow model by Hewitt and Hall-Taylor, respectively. An extensive comparison with a collected database indicates that the developed correlation works satisfactorily with mean deviation and rms errors of 19.1% and 24.3%, respectively, under many experimental conditions such as different channel geometries (circular and rectangular) and flow orientations (vertical and horizontal) for some test fluids (water, R11, R12, and R113). A detailed discussion reveals that existing correlations for turbulent flow boiling such as Chen's correlation, Schrock and Grossman's correlation, and Dengler and Addoms's correlation may be derived from a generalized form of the newly developed correlation.

[DOI: 10.1115/1.2039105]

Keywords: heat transfer, flow boiling, mini channel, laminar flow, small diameter

1 Introduction

Flow boiling at low liquid Reynolds number is often encountered in many practical engineering devices where small diameter channels are employed, such as compact heat exchangers and heat sinks for electronic chips, for the reason that the inherent small dimension of channel and limitation on flow rate due to high pressure drop gradient in such channels often lead to low Reynolds number. Liquid flow at low Reynolds number conditions may have features of laminar flow. However, most of the existing well-known heat transfer correlations for saturated flow boiling, such as the Chen [1], Shah [2], Winterton and co-workers [3,4], Kandlikar [5], and Steiner and Taborek [6] correlations, were developed based on data for relatively high liquid Reynolds number. In these correlations, a heat transfer correlation for single-phase turbulent flow, say the Dittus-Boelter correlation [7], is adopted to predict the heat transfer coefficient for liquid single phase flow. Thus, laminar liquid flow conditions are out of verified parametric ranges of these correlations. In principle, all these correlations may need to be modified when applied to liquid laminar flow conditions, even though some of them may still work beyond their verified ranges.

From this point of view, this study is aiming at developing a heat transfer correlation for saturated flow boiling at low liquid Reynolds number. The newly developed heat transfer correlation is compared with an extensively collected database including data taken under various experimental conditions such as different channel geometries (circular and rectangular), flow orientations (vertical and horizontal), and working fluids (water, R11, R12, and R113). The newly developed correlation can be generalized for any flow conditions. It will be demonstrated that some existing correlations, for example the Chen correlation [1], can be derived from the generalized form of the newly developed correlation.

2 Development of Heat Transfer Correlation at Low Liquid Reynolds Number

2.1 Modeling Concept. This study focuses on the development of a heat transfer correlation for predicting the local heat transfer coefficient of saturated flow boiling at low liquid Reynolds number or liquid laminar flow.

It is noticeable that Thome et al. [8] recently successfully developed a three-zone flow boiling model to describe evaporation of elongated bubbles in microchannels. This model describes the transient variation in local heat transfer coefficient, having three adjustable parameters related to the bubble frequency, the minimum liquid film thickness at dryout and the initial liquid film formation thickness. However, these parameters are difficult to predict theoretically, limiting the applicable range of the model. This study aims at developing a practical correlation with sound physical arguments.

As is well known, flow boiling heat transfer in conventional channels is governed mainly by two important mechanisms: nucleate boiling and forced convection. Nucleate boiling is characterized by the formation of vapor bubbles at a heated wall when the superheat of a thin liquid layer near the surface is enough to allow nucleation. Forced convection, however, is characterized by heat transferred by means of conduction and convection through the liquid film near the wall and vaporization at the liquid/vapor interface. Usually at low quality, the nucleate boiling mechanism is dominant, but when quality is higher than 20–30%, flow boiling heat transfer is controlled mainly by the forced convection mechanism. A literature survey indicates that either nucleate boiling mechanism or force convection mechanism could be predominant

---

Contributed by the Heat Transfer Division of ASME for publication in the Journal of Heat Transfer. Manuscript received July 31, 2004; final manuscript received June 20, 2005. Review conducted by: Raj M. Manglik.

for flow boiling in small diameter channels. Some experimental investigations (see for example Lee and Lee [9], Sumith et al. [10], and Qu and Mudawar [11]) show that slug flow and annular flow are dominant flow patterns. However, there are also some experimental investigations (see for example Wambsganss et al. [12], Tran et al. [13,14], Yu et al. [15] and Bao et al.[16]) reported that nucleate boiling could be a dominant mechanism for flow boiling in small diameter channels. Therefore, both nucleate boiling mechanism and forced convection mechanism will be included in the development of correlation.

The following assumptions are made in the development of correlation:

(i) Following the additive concept suggested by Rohsenow [17], it is assumed that in the saturated flow boiling region the heat transfer coefficients associated with the two flow boiling mechanisms can be superimposed as

$$h_{\mathrm{tp}} = h_{\mathrm{nb}} + h_{\mathrm{fc}} \tag{1}$$

where h_{nb} and h_{fc} represent the heat transfer coefficients due to nucleate boiling and forced convection mechanisms, respectively. This additive concept is often used in many existing correlations, for instance, the Chen correlation [1]. According to Steiner and Taborek [6], the asymptotic method is normally more successful to combine the two flow boiling terms. However, this study employs the additive concept in consideration of the reasons, which will be demonstrated later, that the new correlation to be developed for low Reynolds number flow conditions may also be extendedly applied under high Reynolds number flow conditions, and a generalization of the long-standing Chen correlation for flow boiling heat transfer may be obtained.

(ii) The heat transfer coefficient of flow boiling associated with the nucleate boiling mechanism at low liquid Reynolds number conditions may be approximately predicted by a heat transfer correlation for pool boiling, i.e.

$$h_{\mathrm{nb}} \approx h_{\mathrm{pb}} \tag{2}$$

where h_{pb} denotes the heat transfer coefficient of pool boiling.

This assumption may be acceptable on the following grounds. Nucleate boiling is characterized by two separate processes: the formation of bubbles (nucleation), and the subsequent growth and motion of these bubbles. These two processes take place mostly in the boundary layer, and are affected by its characteristics such as the superheat and the boundary layer thickness. Thus, they determine the heat transfer coefficient of nucleate boiling. In flow boiling systems, the flow makes the boundary layer thin and its effective superheat small. Thus, the flow suppresses the bubble formation and subsequent growth, resulting in the reduced heat transfer coefficient of nucleate boiling. Consequently, Chen [1] introduced a suppression factor S for the nucleate boiling component in his correlation to account for the smaller effective superheat than in a pool boiling case. However, when the flow rate in flow boiling systems is low, the effect of flow may be comparable to that of natural circulation in pool boiling systems. Thus, the heat transfer coefficient due to nucleate boiling in low flow rate boiling systems may be approximated by that for pool boiling. This has been confirmed by the Chen correlation in which the suppression factor S approaches unity at low liquid Reynolds number flow conditions, namely $h_{\mathrm{nb}} \approx h_{\mathrm{pb}}$.

(iii) The heat transfer coefficient of flow boiling associated with the forced convection mechanism at relatively high quality may be related to that in the annular flow regime, h_{annular}, i.e.

$$h_{\mathrm{fc}} \sim h_{\mathrm{annular}} \tag{3}$$

providing that an appropriate adjustable parameter reflecting the contribution of flow regime deviation from annular flow is introduced.

This assumption may also be acceptable on the following grounds. From the experimental observations [10,11], it has been obtained that a slug-annular or an annular flow may be a dominant flow pattern at the saturated nucleate boiling region in relatively small-diameter channels. Qu and Mudawar [18] has shown that the analytical annular flow model by Hewitt and Hall-Taylor [19] with the assumption of liquid film laminar flow can be used to predict their observed heat transfer tendencies in their experiment. Thus, it may be reasonably assumed that the heat transfer coefficient of flow boiling associated with the forced convection mechanism at relatively high quality may be related to that in the annular flow regime. An adjustable parameter to be introduced later in the forced convection term will take account of the deviation between the assumed annular flow regime and the real one.

2.2 Correlation Development.

2.2.1 Pool Boiling. The heat transfer for pool boiling, h_{pb}, can be obtained from the following correlation by Forster and Zuber [20]:

$$h_{\mathrm{pb}} = 0.00122\left(\frac{k_f^{0.79} c_{pf}^{0.45} \rho_f^{0.49}}{\sigma^{0.5} \mu_f^{0.29} h_{fg}^{0.24} \rho_g^{0.24}}\right) \Delta T_{\mathrm{sat}}^{0.24} \Delta p_{\mathrm{sat}}^{0.75} \tag{4}$$

where k_f represents the thermal conductivity, c_{pf} is the heat capacity, ρ_f is the liquid density, ρ_g is the vapor density, σ is the surface tension, μ_f is the viscosity, h_{fg} is the latent heat of evaporation, ΔT_{sat} is the superheat, and Δp_{sat} is the vapor pressure difference corresponding to ΔT_{sat}. It should be mentioned that the Cooper equation [21] may be more successful for describing pool boiling data. The Cooper equation may take the place of the Forster and Zuber equation. This study utilizes the old Forster and Zuber equation in consideration of the reasons that our newly developed correlation for low Reynolds number flow conditions may be extendedly applied under high Reynolds number flow conditions and a generalization of the long-standing Chen correlation for flow boiling heat transfer may be obtained. In high quality regions, since the forced convection component h_{fc} is predominant, even the improper prediction of h_{pb} will not much affect the predictive accuracy of heat transfer coefficient practically.

2.2.2 Analytical Correlation for Annular Flow. In what follows, the heat transfer coefficient due to the evaporation of thin liquid film in the annular flow regime will be deduced based on the analytical annular flow model of Hewitt and Hall-Taylor [19]. Despite the limited range of application, it is convenient to start by considering the entire liquid flow to be in the film close to the channel wall and the interface to be smooth. This assumption would be most closely satisfied for the case of a high gas flow and a low liquid flow [19].

By assuming that the liquid film is thin enough for the flow to be considered on a flat plate basis, and then integrating the universal velocity profile, the following relationships for the mass flow rate of liquid film have already been obtained by Hewitt and Hall-Taylor [19]

$$W^{+} = 0.5m^{+2}, 0 < m^{+} < 5$$

$$W^{+} = -8.05m^{+} + 5m^{+} \ln m^{+} + 12.45, 5 \leqslant m^{+} < 30$$

$$W^{+} = 8.0m^{+} + 2.5m^{+} \ln m^{+} - 214, m^{+} \geqslant 30 \tag{5}$$

where dimensionless variables W^{+} and m^{+} are defined, respectively, as

$$W^{+} \equiv \frac{W_{\mathrm{LF}}}{\pi D_h \cdot \mu_f} = \frac{\mathrm{Re}_f}{4} \tag{6}$$

and

$$m^{+} \equiv \frac{\delta \sqrt{\tau_w \rho_f}}{\mu_f} \tag{7}$$

In the above equations, W_{LF} stands for the mass flow rate of liquid film, δ denotes the liquid film thickness, τ_w represents the wall shear stress, and Re_f is the liquid Reynolds number, defined as

$$\mathrm{Re}_f \equiv \frac{G(1 - x_{\mathrm{eq}})D_h}{\mu_f} \tag{8}$$

where G, x_{eq}, andD_h are the total mass flux of both phases, the thermodynamic equilibrium quality, and the hydraulic diameter of channel, respectively.

At laminar sublayer, Eq. (5) yields

$$m^{+^2} \sim W^{+} \tag{9}$$

It can be assumed that the above relationship may also be approximately valid for the whole liquid film flow in the annular flow regime when the liquid flow rate is low. Considering the definitions of W^{+} and m^{+}, Eqs. (6) and (7), respectively, Eq. (9) yields

$$\delta \sim \frac{\mu_f}{\sqrt{\rho_f \tau_w}} \mathrm{Re}_f^{0.5} \tag{10}$$

The wall shear stress may be obtained from the equation for the frictional pressure gradient of two-phase flow, $(-dp/dz)_F$, as follows [19]

$$\left(-\frac{dp}{dz}\right)_F = \frac{4\tau_w}{D_h} \tag{11}$$

Thus from Eqs. (10) and (11), the film thickness, δ, might further be expressed as

$$\delta \sim \frac{\mu_f}{\sqrt{\rho_f D_h}} \mathrm{Re}_f^{0.5} \left(-\frac{dp}{dz}\right)_F^{-0.5} \tag{12}$$

According to Lockhart and Martinelli [22], the frictional pressure gradient of two-phase flow can also be represented by

$$\left(-\frac{dp}{dz}\right)_F = \phi_{\mathrm{f}}^2 \left(-\frac{dp}{dz}\right)_f \tag{13}$$

where $\phi^2{}_f$ is the two-phase friction multiplier, and $(-dp/dz)_f$ is the frictional pressure gradient of liquid single phase flow, given by

$$\left(-\frac{dp}{dz}\right)_f = \frac{2f_f}{D_h} \cdot \frac{G^2(1 - x_{\mathrm{eq}})^2}{\rho_f} \tag{14}$$

Here the friction coefficient, f_f, can be calculated by the following friction law, according to Lockhart and Martinelli [22]

$$f_k = C_k \cdot \mathrm{Re}_k^{-n}, k = f \text{ or } g \tag{15}$$

where for laminar flow in a circular channel ($\mathrm{Re}_k < 1000$) $C_k = 16$ and $n = 1$ whereas for turbulent flow ($\mathrm{Re}_k > 2000$) $C_k = 0.046$ and $n = 0.20$. Equations (12) and (13) yield

$$\delta \sim \phi_f^{-1} \left(-\frac{dp}{dz}\right)_f^{-0.5} \frac{\mu_f}{\sqrt{\rho_f D_h}} \mathrm{Re}_f^{0.5} \tag{16}$$

A relationship similar to Eq. (16) is also deduced by Lee and Lee [9].

When the liquid film is thin and the flow is laminar, heat is transferred mainly by conduction through the liquid film, as

$$h_{\mathrm{annular}} \approx \frac{k_f}{\delta} \tag{17}$$

Combining Eqs. (14), (16), and (17) gives

$$h_{\mathrm{annular}} \approx \frac{k_f}{\delta} \sim \phi_f \left(-\frac{dp}{dz}\right)_f^{0.5} \frac{k_f \sqrt{\rho_f D_h}}{\mu_f} \mathrm{Re}_f^{-0.5} \sim \phi_f \cdot f_f^{0.5} \cdot \mathrm{Re}_f^{0.5} \cdot \frac{k_f}{D_h} \tag{18}$$

Considering the friction law of laminar flow, Eq. (15), it yields

$$h_{\mathrm{annular}} \sim \phi_f \cdot \frac{k_f}{D_h} \tag{19}$$

By noting that the term of k_f/D_h may be relevant to the single-phase heat transfer coefficient, $h_{\mathrm{sp},v}$, for fully developed laminar flow in a uniformly heated circular channel, i.e.

$$h_{\mathrm{sp},v} = 4.36 \cdot \frac{k_f}{D_h} \tag{20}$$

then Eq. (19) can also be represented as follows:

$$h_{\mathrm{annular}} \sim \phi_f \cdot h_{\mathrm{sp},v} \tag{21}$$

In view of assumption (iii), one obtains

$$h_{\mathrm{fc}} = \xi \cdot \phi_f \cdot h_{\mathrm{sp},v} \tag{22}$$

where ξ is an adjustable parameter accounting for distortions due to some assumptions.

It is noticeable that Eq. (22) shows that h_{fc} becomes small when the root of the two-phase friction multiplier, ϕ_f, approaches to unity at low quality. At low quality region, since the nucleate boiling component h_{nb} is predominant, even the improper prediction of h_{fc} will not much affect the predictive accuracy of heat transfer coefficient.

2.2.3 Heat Transfer Correlation. The heat transfer coefficient of flow boiling at low liquid Reynolds number conditions is then given by

$$h_{\mathrm{tp}} = h_{\mathrm{pb}} + \xi \cdot \phi_f \cdot h_{\mathrm{sp},v} \tag{23}$$

where h_{pb} can be calculated by Eq. (4), $h_{\mathrm{sp},v}$ may be obtained from Eq. (20) for circular channels, ξ should be determined later by extensive databases, and the root of the two-phase friction multiplier, ϕ_f, can be given by [23]

$$\phi_f = \sqrt{1 + \frac{C}{X} + \frac{1}{X^2}} \tag{24}$$

where the Martinelli parameter X is defined by [22]

$$X^2 \equiv \frac{(dp/dz)_f}{(dp/dz)_g} = \left(\frac{f_f}{f_g}\right)\left(\frac{1 - x_{\mathrm{eq}}}{x_{\mathrm{eq}}}\right)^2 \left(\frac{\rho_g}{\rho_f}\right) \tag{25}$$

and the value of Chisholm parameter C is given in terms of flow conditions [23]. For example, $C = 12$ for $\mathrm{Re}_f < 1000$ and $\mathrm{Re}_g > 2000$, and $C = 20$ for $\mathrm{Re}_f > 2000$ and $\mathrm{Re}_g > 2000$. The friction factors, f_f and f_g, can be obtained from the friction law, Eq. (15).

When Eq. (23) is applied to rectangular channels, the following $h_{\mathrm{sp},v}$ and f_f should be used instead of Eqs. (15) and (20):

Single-phase heat transfer coefficient, $h_{\mathrm{sp},v}$, for rectangular channels under uniform heat flux conditions [24]:

$$h_{\mathrm{sp},v} = 8.235(1 - 2.042\eta + 3.085\eta^2 - 2.4765\eta^3 + 1.058\eta^4 - 0.186\eta^5) \cdot \frac{k_f}{D_h} \tag{26}$$

Friction factor, f_f, for laminar flow in rectangular channels [24]:

$$f_f = 24(1 - 1.355\eta + 1.947\eta^2 - 1.701\eta^3 + 0.956\eta^4 - 0.254\eta^5) \cdot \mathrm{Re}_f^{-1} \tag{27}$$

where η represents the aspect ratio, defined as the ratio of the height with the width of channel cross section.

Table 1 Collected database for saturated flow boiling heat transfer at low liquid Reynolds number

Symbol	Reference	Fluid/ Orient.†/Geom.‡	D_h (mm)	p (MPa)	G (kg/m^{2}s)	Re$_f$ (-)	Re$_g$ (-)	q (kW/m^2)	No. of Data	Mean Deviation*/rms (%)
○	Sumith et al. [10]	Water/V/C	1.45	0.101	23.4 – 153	68.1 – 772	125 – 9.49×10^3	10.3 – 715	214	25.3/34.8
◇	Yu et al. [15]	Water/H/C	2.98	0.200	103	442 – 1222	1.70×10^3 – 1.59×10^4	50 – 163	34	11.1/13.3
▽	Kureta et al. [25]	Water/V/C	6.00	0.101	100	658 – 1993	3.12×10^3 – 3.45×10^4	645 – 803	21	25.0/26.1
◁	Bao et al. [16]	R11/H/C	1.95	0.294 – 0.470	167 – 560	503 – 1924	1.98×10^3 – 4.64×10^4	55.0 – 125	16	21.5/23.0
⬡	Tran et al. [13,14]	R12/H/R	2.40 (1.70×4.06)	0.825 – 0.845	54.6 – 354	222 – 1942	1.36×10^3 – 4.10×10^4	4.10 – 33.7	64	16.0/20.2
□	Tran et al. [14]	R12/H/C	2.46	0.825	63.3 – 264	369 – 1898	2.24×10^3 – 2.30×10^4	7.50 – 59.4	48	10.7/13.5
⬠	Lee and Lee [9]	R113/H/R	0.780 (0.400×20.0)	0.101	104 – 209	52.3 – 264	2.03×10^3 – 1.03×10^4	2.98 – 10.0	89	16.1/17.3
△	Lee and Lee [9]	R113/H/R	1.90 (1.00×20.0)	0.101	51.6 – 208	69.1 – 650	2.25×10^3 – 2.59×10^4	2.95 – 15.0	171	19.9/21.9
⦶	Wambsganss et al. [12]	R113/H/C	2.92	0.124 – 0.160	50.0 – 300	118 – 1994	587 – 4.54×10^4	8.80 – 90.8	82	17.7/21.2
▷	Lee and Lee [9]	R113/H/R	3.64 (2.00×20.0)	0.101	51.7 – 182	121 – 1065	3.43×10^3 – 3.11×10^4	4.52 – 15.8	169	16.1/19.4
Total		Water,R11,R12, R113/V,H/C,R	0.780 – 6.00	0.101 – 0.853	23.4 – 560	52.3 – 1998	125 – 4.64×10^4	2.95 – 803	929	19.1/24.3

†Orientation V: Vertical, H: Horizontal; ‡Geometry C: Circular, R: Rectangular

* Mean Deviation: $(1/N)\sum\left|\left(h_{\mathrm{tp,cal}} - h_{\mathrm{tp,exp}}\right)/h_{\mathrm{tp,exp}}\right| \times 100\%$.

3 Results and Discussion

3.1 Collected Databases and Finalization of Correlation. Many experimental studies related to saturated flow boiling heat transfer at low liquid Reynolds number conditions have been performed. Wambsganss and co-workers [12–15] performed a series of study on flow boiling heat transfer in horizontal channels with hydraulic diameters ranging from 2.40 to 2.98 mm using different test fluids (R12, R113 and water) and geometries (circular and rectangular). Kureta et al. [25] studied flow boiling heat transfer of water in tubes with diameters of 2.00 and 6.00 mm at the atmospheric pressure and provided a database of saturated flow boiling over a range of mass fluxes from 100 to 1000 kg/m^{2}s, heat fluxes up to 3,638 kW/m^2. Bao et al. [16] experimentally investigated flow boiling heat transfer coefficients for Freon R11 and HCFC123 in a smooth copper tube with the inner diameter of 1.95 mm. The parameter ranges examined are: heat fluxes from 5 to 200 kW/m^2, mass fluxes from 50.0 to 1,800.0 kg/m^2 s, vapor qualities from 0 to 0.9, system pressures from 0.2 to 0.5 MPa. Lee and Lee [9] experimented flow boiling heat transfer through horizontal rectangular channels with low aspect ratios (D_h ranging from 0.78 to 3.64 mm) using R113 as a test fluid. Mass flux varied from 51.6 to 209.0 kg/m^2 s and heat flux was up to 16 kW/m^2. Sumith et al. [10] surveyed flow boiling heat transfer of water experimentally in a vertical tube with the diameter of 1.45 mm under atmospheric pressure over a range of mass fluxes from 23.4 to 152.7 kg/m^2 s, heat fluxes from 10 to 715 kW/m^2 and qualities up to 0.8. A common feature of the above experimental investigations is that most of collected data falls into the region of low liquid Reynolds number.

Collected heat transfer data sets for saturated flow boiling at low liquid Reynolds number flow conditions are shown in Table 1. As it is difficult to obtain many original data from their authors and some physical properties of fluids, for example HCFC123, are not available in hand, available data in the literature are included in our collected database. Many of our collected data were obtained through careful reading from figures when enough related parameters and information were presented. There are ten collected data sets in all. Only taking saturated flow boiling data at low liquid Reynolds number (Re$_f<2000$), the collected database is reduced to a total of 929 data points, covering a range of system pressures from 0.101 to 0.853 MPa, mass fluxes from 23.4 to 560 kg/m^2 s, liquid Reynolds numbers Re$_f$ from 52.3 to 1998, gas Reynolds numbers Re$_g$ from 125 to 4.64×10^4, heat fluxes from 2.95 to 803 kW/m^2, and hydraulic diameters of channels from 0.78 to 6.00 mm. The test fluids include water and refrigerants (R11, R12, and R113), flowing in a single circular or rectangular channel at the orientation of vertical or horizontal.

Although the adjustable parameter ξ accounts for distortion due to some assumptions and may be a complicated function of some system parameters, it comes out a constant of 0.64 in comparison to the collected experimental data.

3.2 Evaluation of Correlation With Data.

3.2.1 Evaluation With All Experimental Data. In this section, the newly developed correlation is evaluated by the collected data tabulated in Table 1. The meanings of all types of symbols used in Figs. 1–4 are identified in Table 1, and in other figures they may be clearly identified from figures. First, the developed correlation is compared with all data to show the whole behaviors of predic-

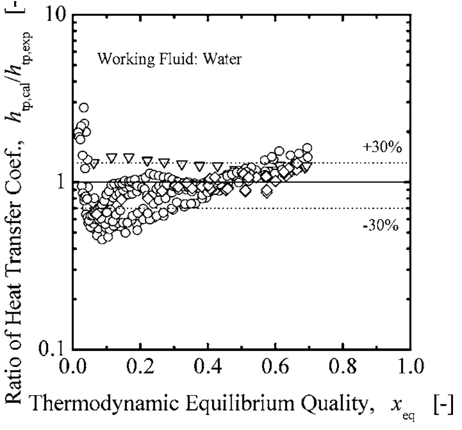

Fig. 1 Evaluation of newly developed correlation with data for water

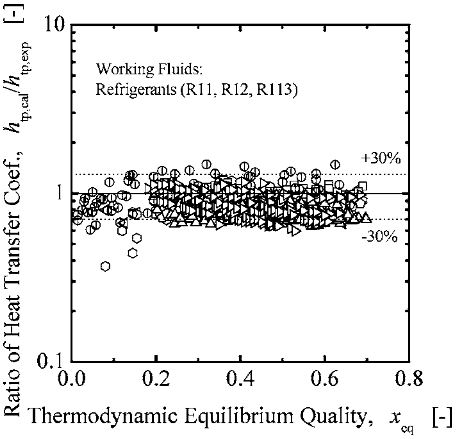

Fig. 2 Evaluation of newly developed correlation with data for refrigerants

tion. Figures 1 and 2 illustrate comparisons with data using water and refrigerants as test fluids, respectively, in the form of the ratio of the heat transfer coefficients predicted by the developed correlation to experimental values as a function of thermodynamic equilibrium quality.

Figure 1 indicates that most of the predictions by the developed correlation are within an error band of ±30% and no significant systematic deviation tendency can be observed, although there is a little over-prediction in the high quality range and some under-prediction in the low quality range for data by Sumith et al. From the figure, it appears that the correlation over-predicts the data by Kureta et al. [25] with an error of 30% in the whole quality range. Most of predictions by this correlation for the data by Yu et al. are well centered within the error band of ±30%. Figure 2 show the comparison of the newly developed correlation with data using refrigerants (R11, R12, and R113) as test fluids. It indicates that most of the data from a total of seven data sets can also be well predicted within an error band of ±30%. No significant systematic deviation can be observed. The data by Lee and Lee [9] with the smallest hydraulic diameter of channel (D_h=0.78 mm) in this collected database can be predicted well by this correlation.

No matter which test fluid (R11, R12, or R113) is used, and at what flow orientation (vertical or horizontal) and in what geometry (circular or rectangular) data are taken, the newly developed correlation with one empirical parameter works satisfactorily. Considering some measurement errors in experiments on small diameter channel, different geometries, flow orientations, and test fluids employed, the prediction results appear to be acceptable for all the data under low liquid Reynolds number conditions. Mean deviations and root-mean-square (rms) errors for each data set are tabulated in Table 1. Seven of the total ten data sets are predicted within mean deviations of 20%. In total, the newly developed correlation yields mean deviation and rms errors of 19.1 % and 24.3 %, respectively, for all collected data.

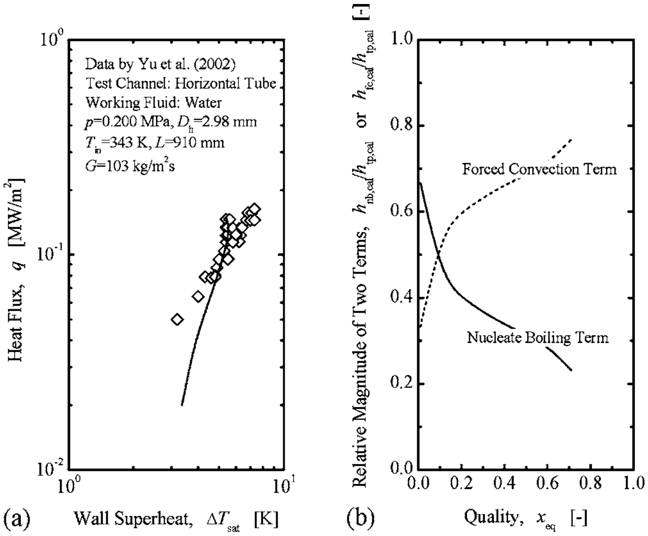

Fig. 4 Comparison of newly developed correlation with boiling curves for water flow in a 2.98 mm tube [15]: (a) boiling curve, (b) relative magnitude of two terms

3.2.2 Evaluation With Boiling Curves. In what follows, the newly developed correlation is evaluated with boiling curves available in some databases. Data from Kureta et al. [25], Yu et al. [15], and Sumith et al. [10] are presented in Figs. 3(*a*), 4(*a*), and 5(*a*), respectively. Open symbols and lines in these figures represent experimental data and predictions by the newly developed correlation, respectively. Comparison is made in the saturated

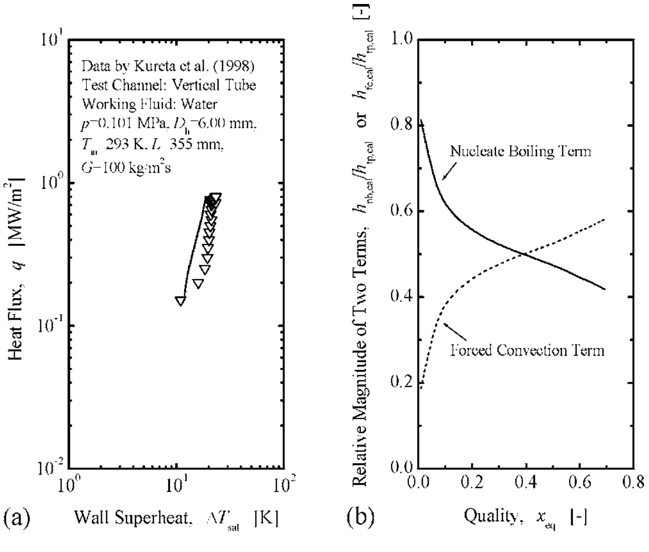

Fig. 3 Comparison of newly developed correlation with boiling curves for water flow in a 6.00 mm tube [25]: (a) boiling curve, (b) relative magnitude of two terms

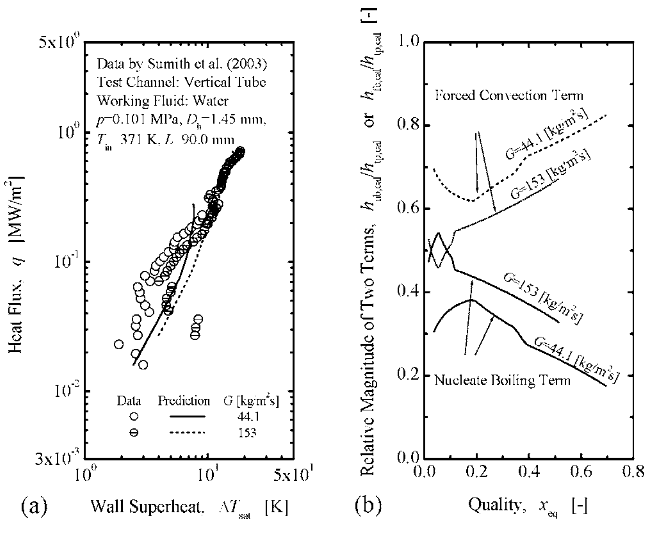

Fig. 5 Comparison of newly developed correlation with boiling curves for water flow in a 1.45 mm tube [10]: (a) boiling curve, (b) relative magnitude of two terms

flow boiling region ($0 < x_{\text{eq}} < 0.7$), where heat flux is lower than the critical heat flux. Figure 3(*a*) indicates that the prediction by the developed correlation agrees with the tendency of boiling curve for water flow in a vertical tube with the diameter of 6.00 mm under atmospheric pressure. Figure 3(*b*) shows the variation of the relative magnitude of the two boiling terms, i.e., nucleate boiling term and forced convection term, predicted by the newly developed correlation versus thermodynamic equilibrium quality corresponding to the predicted boiling curve shown in Fig. 3(*a*). It indicates that in the low quality range, nucleate boiling is dominant and its relative magnitude decreases with increasing quality. Finally, the forced convection term becomes dominant at quality over about 0.4. Figure 4(*a*) shows the comparison with data for flow boiling of water in a horizontal tube with the diameter of 2.98 mm under the pressure of 0.200 MPa. It verifies that the prediction by the developed correlation is in agreement with the tendency of the experimental data. The variation of relative magnitudes of the two terms, illustrated in Fig. 4(*b*), is similar to that in Fig. 3(*b*). The only difference is that in the case of Fig. 4(*b*) the quality (equal to about 0.1) is lower at the transition point where the forced convection term becomes dominant. Figure 5(*a*) shows the comparison with the boiling curves for water flow in a vertical tube with the diameter of 1.45 mm under the atmospheric pressure at two different mass fluxes. From the figure, it can be seen that the effect of mass flux on heat transfer coefficient is small. Usually, it will be deemed that nucleate boiling may be dominant in the experiment. However, this account is obviously contradictory to what Sumith et al. [10] reported that the dominant flow patterns in their experiment were slug-annular and annular flows. Figure 5(*b*) illustrates the forced convection term is dominant for both cases of mass fluxes in the predictions of the developed correlation, in agreement with what Sumith et al. [10] reported. The relative magnitude of the forced convection term decreases with increasing mass fluxes from 44.1 to 153 $\text{kg}/\text{m}^2\,\text{s}$. The reason is due to the dominant effect of the decrease of the two-phase friction multiplier in Eq. (23). Equations. (15), (24), and (25) indicate that the two-phase friction multiplier decreases with increasing mass flux. Thus, the newly developed correlation can correctly predict the effect of mass flux in this case. Zigzags in Fig. 5(*b*) are due to the complexity of the forced convection term in the newly developed correlation, where many different equations, such as friction laws, Eq. (15), and values of Chisholm parameter, *C*, are switched when flow conditions vary with quality. There may be no physical justification for these zigzags. Further work may be needed on this point.

3.3 Generalization of Newly Developed Correlation. In what follows, the newly developed correlation, Eq. (23), will be generalized at any flow conditions based on some discussions. First, a generalized form of h_{nb} at any flow conditions may be given as

$$h_{\text{nb}} = S \cdot h_{\text{pb}} \tag{28}$$

where *S* is a suppression factor for the nucleate boiling mechanism in flow boiling. The suppression factor at low liquid Reynolds number conditions is approximately unity, and then Eq. (28) is reduced to Eq. (2). As already proved by Chen [1], h_{nb} at high liquid Reynolds number conditions is given by Eq. (28).

Second, if an *F* factor for flow boiling is defined by $h_{\text{fc}}/h_{\text{sp}}$, a generalized form of Eq. (22) at any flow conditions may be given as

$$h_{\text{fc}} = F \cdot h_{\text{sp}} \tag{29}$$

where

$$F = \xi \cdot \phi_f = 0.64\phi_f \tag{30}$$

and h_{sp} represents the liquid single-phase heat transfer coefficient for laminar or turbulent flow.

From the above discussion, a generalized form of the newly developed correlation may be given as

$$h_{\text{tp}} = S \cdot h_{\text{pb}} + F \cdot h_{\text{sp}} \tag{31}$$

3.4 Interpretation of Existing Correlations Based on Generalized Correlation. In what follows, it will be expected that some existing correlations can be derived from the generalized form of newly developed correlation since the new method here is primarily a new recipe using a new combination of old ideas and does not add any new "physics or physical insight" or flow phenomena ideas to the new correlation.

3.4.1 Interpretation of Chen's Correlation. Here, it will be demonstrated that Chen's correlation [1] can be interpreted by the newly developed generalized correlation. It is assumed that the suppression factor in the generalized correlation, Eq. (31), can be approximated by the functional form of the suppression factor for the Chen correlation as [26]

$$S = 1/(1 + 2.53 \times 10^{-6}\text{Re}_f^{1.17}) \tag{32}$$

This assumption may be acceptable on the following grounds. As the liquid Reynolds number decreases, the suppression factor predicted by Eq. (32) asymptotically approaches to unity. Equation (32) at high liquid Reynolds number conditions, namely, turbulent liquid flow conditions has been validated by various experimental data [1].

As for the *F* factor under turbulent liquid flow conditions, Eqs. (24) and (30) yield

$$F = 0.64 \cdot \phi_f = 0.64(1 + 20/X + 1/X^2)^{0.5} \approx 2.35(1/X + 0.213)^{0.736} \tag{33}$$

The right-hand side of the above equation is a curve fit [26] to the graphical function of the Reynolds number factor *F* in the Chen correlation.

As for the liquid single-phase heat transfer coefficient for turbulent flow, the following Dittus-Boelter correlation [7] is adopted

$$h_{\text{sp}} = 0.023\,\text{Re}_f^{0.8}\text{Pr}_f^{0.4}\left(\frac{k_f}{D_h}\right) \tag{34}$$

Thus it is demonstrated that the generalized correlation, Eq. (31) with Eqs. (4) and (32)–(34) is similar to Chen's correlation at turbulent liquid flow conditions. Since Chen's correlation has been validated at high liquid Reynolds number conditions, the generalized correlation may be expected to work well at any flow conditions.

3.4.2 Interpretation of Schrock and Grossman's Correlation. Here, the generalized correlation is compared with the following Schrock and Grossman's correlation [27] for liquid-turbulent and gas-turbulent flow at high quality

$$\frac{h_{\text{tp}}}{h_{\text{sp}}} = 2.5X^{-0.75} \tag{35}$$

In such flow conditions, the generalized correlation can be simplified approximately as

$$\frac{h_{\text{fc}}}{h_{\text{sp}}} = F = 0.64 \cdot \phi_f = 0.64(1 + 20/X + 1/X^2)^{0.5} \tag{36}$$

As can be seen from Fig. 6, Schrock and Grossman's correlation can be approximated by the *F* factor in Eq. (36) reasonably well. Thus, it is demonstrated that the generalized correlation, Eq. (31), is identical with Schrock and Grossman's correlation for turbulent liquid flow at high quality.

3.4.3 Interpretation of Dengler and Addoms's Correlation. Dengler and Addoms [28] obtained local boiling coefficients for water in upward vertical flow through a 25.4 mm tube over a range of pressure from 0.050 to 0.276 MPa. They correlated 85% of the purely convective data points, where it was believed that nuclear boiling had been suppressed, to ±20% by an expression for liquid-turbulent and gas-turbulent flow. This expression can be

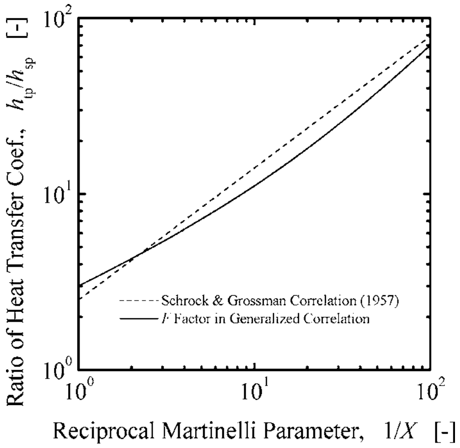

Fig. 6 Comparison of newly developed correlation with Schrock and Grossman's correlation [27]

rewritten explicitly as a function of thermodynamic equilibrium quality, x_{eq}, at certain pressure with the use of the single-phase heat transfer coefficient for turbulent flow of liquid alone, h_{sp}, in place of that for total flow assumed liquid, in the form of

$$\frac{h_{tp}}{h_{sp}} = 3.5\left(\left(\frac{x_{eq}}{1-x_{eq}}\right)^{0.9}\left(\frac{\rho_f}{\rho_g}\right)^{0.5}\left(\frac{\mu_g}{\mu_f}\right)^{0.1}\right)^{0.5} \Bigg/ (1-x_{eq})^{0.8} \tag{37}$$

Under such flow conditions, the generalized correlation can also be simplified by Eq. (36). As can be seen from Fig. 7, Dengler and Addoms's correlation can be approximated by the F factor in Eq. (36) reasonably well over the experimental range of pressure from 0.050 to 0.276 MPa. Thus, it is demonstrated that the generalized correlation, Eq. (31), is identical with Dengler and Addoms's correlation for liquid-turbulent and gas-turbulent flow with high quality.

These interpretations discussed in Secs. 3.4.1, 3.4.2, and 3.4.3 imply that the general form of the heat transfer coefficient correlation may be approximated by Eq. (31) with the suppression factor given by Eq. (32) and the F factor given by Eq. (30).

4 Conclusions

In view of the practical importance of a heat transfer correlation for designing and prediction in engineering, a heat transfer correlation has been developed for saturated flow boiling at low liquid Reynolds number conditions. The obtained results are as follows:

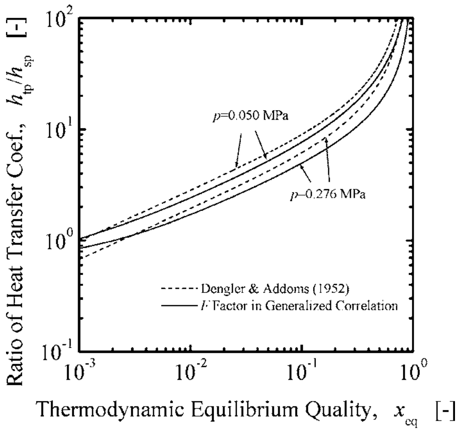

Fig. 7 Comparison of newly developed correlation with Dengler and Addoms's correlation [28]

1. A heat transfer correlation has been developed for saturated flow boiling at low liquid Reynolds number conditions based on superimposition of two boiling mechanisms, namely nucleate boiling and forced convection. In the newly developed correlation, two terms corresponding to the mechanisms of nucleate boiling and forced convection are obtained from the pool boiling correlation by Forster and Zuber and the analytical annular flow model by Hewitt and Hall-Taylor, respectively.
2. An extensive database was collected for saturated flow boiling heat transfer at low liquid Reynolds number conditions, including data for different channels geometries (circular and rectangular), flow orientations (vertical and horizontal), and working fluids (water, R11, R12, and R113).
3. An extensive comparison of the newly developed correlation with the collected database shows that the newly developed correlation works satisfactorily with mean deviation and rms errors of 19.1 % and 24.3%, respectively, for saturated flow boiling at low liquid Reynolds number conditions.
4. A detailed discussion revealed that existing correlations for turbulent flow boiling such as Chen's correlation, Schrock and Grossman's correlation, and Dengler and Addoms's correlation may be derived from a generalized form of the newly developed correlation.

Acknowledgments

The authors would like to express their sincere appreciation to Drs. M. Kureta (Japan Atomic Energy Research Institute), Y. Saito (Kyoto Univ.), X. Shen (Kyoto Univ.), and J. Zhang (Kyoto Univ.) for their kind help. One of the authors (W. Zhang) gratefully acknowledges the support of Japan Government (Monbukagakusho) Scholarship during his stay in Japan.

Nomenclature

C = Chisholm parameter
C_k = constant in friction law
c_p = specific heat capacity
D_h = hydraulic equivalent diameter of channel
dp/dz = friction pressure gradient along channel axis
F = Reynolds number factor
f = friction factor
G = mass flux
h = heat transfer coefficient
h_{fg} = latent heat of evaporation
k = thermal conductivity
L = length from channel inlet
m^+ = dimensionless variable
n = exponent in friction law
p = pressure
ΔT_{sat} = superheat, T_w-T_{sat}
Pr = Prandtl number
q = heat flux
Re = Reynolds number
S = suppression factor
T = temperature
W^+ = dimensionless variable
W_{LF} = mass flow rate of liquid film
X = Martinelli parameter
x_{eq} = thermodynamic equilibrium quality

Greek symbols

δ = liquid film thickness
η = aspect ratio
μ = dynamic viscosity
ξ = adjustment parameter
ρ = density
σ = surface tention
τ = shear stress

ϕ^2 = two-phase friction multiplier

Subscripts

annular = annular flow
cal = calculational value
exp = experimental value
F = friction
f = saturated liquid
fc = forced convection
g = saturated vapor
in = inlet of channel
nb = nucleate boiling
pb = pool boiling
sat = saturated state
sp = single-phase
tp = two-phase
v = laminar
w = wall

References

[1] Chen, J. C., 1966, "A Correlation for Boiling Heat Transfer to Saturated Fluid in Convective Flow," Ind. Eng. Chem. Process Des. Dev., **5**, pp. 322–329.
[2] Shah, M. M., 1976, "A New Correlation for Heat Transfer during Flow Boiling through Pipes," ASHRAE Trans., **82**, pp. 66–86.
[3] Gungor, K. E., and Winterton, R. H. S., 1986, "A General Correlation for Flow Boiling in Tubes and Annuli," Int. J. Heat Mass Transfer, **29**, pp. 351–358.
[4] Liu, Z., and Winterton, R. H. S., 1991, "A General Correlation for Saturated and Subcooled Flow Boiling in Tube and Annuli," Int. J. Heat Mass Transfer, **34**, pp. 2759–2766.
[5] Kandlikar, S. G., 1990, "A General Correlation for Saturated Two-phase Flow Boiling Heat Transfer Inside Horizontal and Vertical Tubes," ASME J. Heat Transfer, **112**, pp. 219–228.
[6] Steiner, D., and Taborek, J., 1992, "Flow Boiling Heat Transfer in Vertical Tubes Correlated by an Asymptotic Model," Heat Transfer Eng., **13**, pp. 43–69.
[7] McAdams, W. H., 1942, *Heat Transmission*, 2nd ed., McGraw-Hill, New York.
[8] Thome, J. R., Dupont, V., and Jacobi, A. M., 2004, "Heat Transfer Model for Evaporation in Microchannel. I. Presentation of the Model," Int. J. Heat Mass Transfer, **47**, pp. 3375–3385.
[9] Lee, H. J., and Lee, S. Y., 2001, "Heat Transfer Correlation for Boiling Flows in Small Rectangular Horizontal Channels with Low Aspect Ratios," Int. J. Multiphase Flow, **27**, pp. 2043–2062.
[10] Sumith, B., Kaminaga, F., and Matsumura, K., 2003, "Saturated Flow Boiling of Water in a Vertical Small Diameter Tube," Exp. Therm. Fluid Sci., **27**, pp. 789–801.
[11] Qu, W., and Mudawar, I., 2003, "Flow Boiling Heat Transfer in Two-phase Micro-Channel Heat Sinks—-I. Experimental Investigation and Assessment of Correlation Methods," Int. J. Heat Mass Transfer, **46**, pp. 2755–2771.
[12] Wambsganss, M. W., France, D. M., Jendrzejczyk, J. A., and Tran T. N., 1993, "Boiling Heat Transfer in a Horizontal Small-diameter Tube," J. Heat Transfer, **115**, pp. 963–972.
[13] Tran, T. N., Wambsganss, M. W., France, D. M., and Jendrzejczyk, J. A., 1993, "Boiling Heat Transfer in a Small, Horizontal, Rectangular Channel," AIChE Symp. Ser., **89**, pp. 253–261.
[14] Tran, T. N., Wambsganss, M. W., and France, D. M., 1996, "Small Circular- and Rectangular-Channel Boiling with Two Refrigerants," Int. J. Multiphase Flow, **22**, pp. 485–498.
[15] Yu, W., France, D. M., Wambsganss, M. W., and Hull, J. R., 2002, "Two-phase Pressure Drop, Boiling Heat Transfer, and Critical Heat Flux to Water in a Small-diameter Horizontal Tube," Int. J. Multiphase Flow, **28**, pp. 927–941.
[16] Bao, Z. Y., Fletcher, D. F., and Haynes, B. S., 2000, "Flow Boiling Heat Transfer of Freon R11 and HCFC123 in Narrow Passages," Int. J. Heat Mass Transfer, **43**, pp. 3347–3358.
[17] Rohsenow, W. M., 1952, "A Method of Correlating Heat Transfer Data for Surface Boiling of Liquids," ASME Trans. J. Appl. Mech. **74**, pp. 969–976.
[18] Qu, W., and Mudawar, I., 2003, "Flow Boiling Heat Transfer in Two-phase Micro-Channel Heat Sinks—-II. Annular Two-phase Flow Model," Int. J. Heat Mass Transfer, **46**, pp. 2773–2784.
[19] Hewitt, G. F., and Hall-Taylor, N., 1970, *Annular Two-phase Flow*, Pergamon, New York.
[20] Forster, H. K., and Zuber, N., 1955, "Dynamics of Vapor Bubbles and Boiling Heat Transfer," AIChE J. **1**, pp. 531–535.
[21] Cooper, M. G., 1984, "Heat Flow Rates in Saturated Nucleate Pool BoilingA Wide-Ranging Correlation Using Reduced Properties," Adv. Heat Transfer, **16**, pp. 158–239.
[22] Lockhart, R. W., and Martinelli, R. C., 1949, "Proposed Correlation of Data for Isothermal Two-Phase Two-Component Flow in Pipes," Chem. Eng. Prog., **45**, pp. 39–48.
[23] Chisholm, D., 1967, "A Theoretical Basis for the Lockhart-Martinelli Correlation for Two-Phase Flow," Int. J. Heat Mass Transfer, **10**, pp. 1767–1778.
[24] Hartnett, J. P., and Kostic, M., 1989, "Heat Transfer to Newtonian and Non-Newtonian Fluid in Rectangular Ducts," Adv. Heat Transfer, **19**, pp. 247–356.
[25] Kureta, M., Kobayashi, T., Mishima, K., and Nishihara, H., 1998, "Pressure Drop and Heat Transfer for Flow-Boiling of Water in Small-Diameter Tubes," JSME Int. J., Ser. B, **41**, pp. 871–879.
[26] Bergles, A. E., Collier, J. G., Delhaye, J. M., Hewitt, G. F., and Mayinger, F., 1981, *Two-phase Flow and Heat Transfer in the Power and Process Industries*, Hemisphere, New York, Chap. 8.
[27] Schrock, V. E., and Grossman, L. M., 1957, "Local Heat Transfer Coefficient and Pressure Drop in Forced Convection Boiling," UCRL-13062, University of California, Berkeley.
[28] Dengler, C. E., and Addoms, J. N., 1952, "Heat Transfer Mechanism for Vaporization of Water in a Vertical Tube," Chem. Eng. Prog., Symp. Ser. **52**, pp. 95–103.

Numerical Analysis of Metallic Nanoparticle Synthesis Using RF Inductively Coupled Plasma Flows

Masaya Shigeta[1]
JSPS Fellow
Department of Environmental Chemistry and Engineering,
Interdisciplinary Graduate School of Science and Engineering,
Tokyo Institute of Technology,
2-12-1 Ookayama, Meguro-ku,
Tokyo 152-8550, Japan
e-mail: shigeta@nr.titech.ac.jp

Hideya Nishiyama
Professor
Electromagnetic Intelligent Fluids Laboratory,
Institute of Fluid Science, Tohoku University,
2-1-1 Katahira, Aoba-ku,
Sendai 980-8577, Japan
e-mail: nishiyama@ifs.tohoku.ac.jp

A thermal plasma flow is regarded as a multifunctional fluid with high energy density, high chemical reactivity, variable properties, and controllability by electromagnetic fields. Especially a radio frequency inductively coupled plasma (RF-ICP) flow has a large plasma volume, long chemical reaction time, and a high quenching rate. Besides, it is inherently clean because it is produced without internal electrodes. An RF-ICP flow is, therefore, considered to be very useful for nanoparticle synthesis. However, nanoparticle synthesis using an RF-ICP flow includes complicated phenomena with field interactions. In the present study, numerical analysis was conducted to investigate the synthesis of metallic nanoparticles using an advanced RF-ICP reactor. An advanced RF-ICP flow is generated by adding direct current (DC) discharge to a conventional RF-ICP flow in order to overcome the disadvantages of a conventional one. The objectives of the present work are to clarify the formation mechanism of metallic nanoparticles in advanced RF-ICP flow systems and to detect effective factors on required synthesis. A two-dimensional model as well as a one-dimensional model was introduced for nanoparticle growth to investigate effects of spatial distributions of thermofluid fields in RF-ICP flows on synthesized nanoparticles. In an advanced RF-ICP flow, a characteristic recirculation zone disappears due to a DC plasma jet. Larger numbers of nanoparticles with smaller size are produced by using an advanced RF-ICP flow. Thermofluid fields in RF-ICP flows can be controlled by applied coil frequency by means of skin effect. Larger numbers of nanoparticles with smaller size are produced near the central axis. Dispersion of particle size distributions can be suppressed by higher applied coil frequency through control of RF-ICP flows. Applied coil frequency can be a remarkably effective factor to control nanoparticle size distribution. [DOI: 10.1115/1.2039106]

1 Introduction

Ultrafine particles in the range of several nanometers to tens of nanometers, so-called nanoparticles, have exhibited high and intriguing performance, such as hardness, ductility, and interesting electronic, optical, and catalytic properties than those larger particles in micron size [1]. Thus, they are attractively expected to be utilized in the industrial, biomedical and environmental purification processes. Since thermal plasma flows as a multifunctional fluid are considerably effective for the synthesis of such nanoparticles, quite a few studies and researches about the nanoparticle synthesis using thermal plasma flows have been conducted theoretically and experimentally. Particularly, a radio frequency inductively coupled plasma (RF-ICP) flow has been considered to be very useful for the synthesis because it has advantages of large volume, high energy density, and high chemical reactivity. Moreover, it is inherently clean because of no-electrode discharge, and long chemical reaction time is obtained [2–7]. The formation of nanoparticles of metals and ceramics with high purity can be easily achieved by the steep temperature gradients at the tail of the RF-ICP flow. Nanoparticles are produced by evaporation and following recondensation of coarser particles injected into the RF-ICP reactor, which allows the formation of very fine nonagglomerated particles. Nowadays, it is considerably important to control the particle size distribution of nanoparticles for extensive applications. Thus, numerical studies have been conducted for nanoparticle synthesis in thermal plasmas thus far [8–13]. Furthermore, a conventional RF-ICP flow displays a backward flow under typical operating conditions, which sometimes prevents raw materials from being injected properly. In order to overcome this disadvantage, an advanced RF-ICP combined with direct current (DC) discharge has been proposed as a more effective method for higher process efficiency and convenience in the processes [14–16]. However, studies and researches concerning nanoparticle synthesis using RF-ICP flows are still deficient.

In the present study, numerical analysis is conducted to investigate the synthesis of metallic nanoparticles using an advanced RF-ICP reactor. The objectives of the present work are to clarify the formation mechanism of metallic nanoparticles in advanced RF-ICP flow systems and to detect effective factors on required synthesis. First, it is clarified how thermofluid fields of an advanced RF-ICP flow with DC discharge support. Subsequently, effects of the manipulated plasma flows on formation mechanism and particle size distribution of synthesized metallic nanoparticles are investigated by one-dimensional analysis. Furthermore, two-dimensional (2D) analysis is carried out to clarify more precise spatial distribution and effects of applied coil frequency on nanoparticle synthesis. At last, numerical results are compared to various available experimental data to verify the present nanoparticle synthesis model.

2 Numerical Model

Figure 1 shows a schematic illustration of a nanoparticle synthesis reactor consisting of a particle growth tube and an advanced RF-ICP torch. In the present study, powders of aluminum or titanium are supplied with the carrier Ar gas from the top nozzle 1 of

---

[1] Corresponding author.

Contributed by the Heat Transfer Division of ASME for publication in the JOURNAL OF HEAT TRANSFER. Manuscript received July 29, 2004; final manuscript received June 3, 2005. Review conducted by: Jacob Chung.

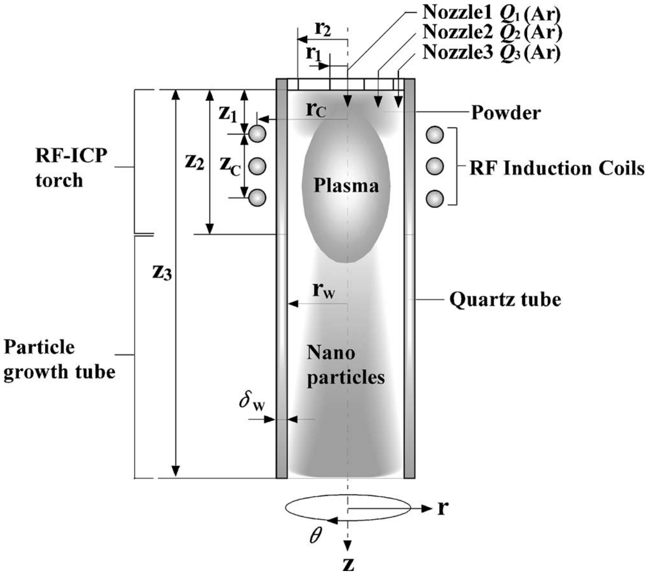

Fig. 1 Schematic illustration of a nanoparticle synthesis reactor

the torch. Supplied powders obtain thermal energy from the plasma and consequently, evaporate. The metal vapor is transported and injected with plasma flow into the particle growth tube. The rapid temperature decrease leads to supersaturation of the metal vapor, which promotes recondensation of the metal vapor. Nanoparticles are synthesized from the vapor by using this recondensation, including homogeneous nucleation and heterogeneous condensation.

2.1 RF-ICP Flow Model.

2.1.1 Assumptions and Conditions. The nanoparticle synthesis reactor is totally 200 mm in length and 25 mm in radius. The advanced RF-ICP torch and the particle growth tube are connected at axial distance from the top of the nozzle $z = 75$ mm. An RF-ICP is produced and maintained in the torch by RF induction operation. Powders of raw materials are injected with the carrier gas. In the present study, since the injected powders are assumed to be fine $(1-10\ \mu\text{m})$ and the powder feed rate is relatively low $(0.02-0.5\ \text{g/min})$, the powders are assumed to evaporate completely by the high energy density of the RF-ICP. The plasma-particulate flow is considered as a dilute condition in which the variation of the plasma properties by particle evaporation and the plasma-particle interaction are negligibly small.

Under this condition, the plasma model is proposed on the following assumptions. The thermofluid fields, such as the temperature field and the flow field, are steady, two-dimensional (2D) axial-symmetric, and laminar flow that is adequate since the Reynolds number is estimated to be from 400 to 500 in the present conditions. The induction electromagnetic fields are considered to be 2D axial symmetric with negligible displacement currents. Gravitational forces and viscous dissipation are negligible. The plasma condition is optically thin, electrically neutral, and has the temperature of electrons identical with the temperature of the heavy particles of the plasma species.

2.1.2 Governing Equations. The governing equations of continuity, momentum, energy, and plasma species per unit volume are summarized in the following general form in cylindrical coordinates:

$$\frac{\partial}{\partial z}(\psi u \phi) + \frac{1}{r}\frac{\partial}{\partial r}(r\psi v \phi) = \frac{\partial}{\partial z}\left(\Gamma\frac{\partial \phi}{\partial z}\right) + \frac{1}{r}\frac{\partial}{\partial r}\left(r\Gamma\frac{\partial \phi}{\partial r}\right) + S_C \quad (1)$$

where ϕ corresponds to physical variables such as u, v, w, h, and n. ψ and Γ correspond to density and diffusion coefficient, respectively. In Eq. (1), the terms on the left-hand side mean the convection, the first and second terms on the right-hand side mean diffusion, and the third term S_C represents the source term for each governing equation. Table 1 shows the transport variables and the source terms in the governing equations for the plasma flow. To estimate the electrical conductivity, which is a significant function of plasma flow, the conservation equation of the argon ion number density should be solved. In Eq. (1), ambipolar diffusion, a phenomenon that ions in the plasma diffuse accompanied with the electrons, are taken into account. The electron number density is determined from the electric neutrality.

Table 1 Transport variables and the source terms in Eq. (1)

ϕ	ψ	Γ	S_C
1	ρ	0	0
u	ρ	η	$-\frac{\partial p}{\partial z}+\frac{\partial}{\partial z}\left(\eta\frac{\partial u}{\partial z}\right)+\frac{1}{r}\frac{\partial}{\partial r}\left(r\eta\frac{\partial v}{\partial z}\right)$ $-\frac{2}{3}\frac{\partial}{\partial z}\left\{\eta\left[\frac{\partial u}{\partial z}+\frac{1}{r}\frac{\partial(rv)}{\partial r}\right]\right\}-\frac{1}{2}\mu_0\sigma_e Real\left(E_\theta\overline{H}_r\right)$
v	ρ	η	$-\frac{\partial p}{\partial r}+\frac{\partial}{\partial z}\left(\eta\frac{\partial u}{\partial r}\right)+\frac{1}{r}\frac{\partial}{\partial r}\left(r\eta\frac{\partial v}{\partial r}\right)-\frac{2}{3}\frac{\partial}{\partial r}\left\{\eta\left[\frac{\partial u}{\partial z}+\frac{1}{r}\frac{\partial(rv)}{\partial r}\right]\right\}$ $-\eta\frac{2v}{r^2}+\rho\frac{w^2}{r}+\frac{1}{2}\mu_0\sigma_e Real\left(E_\theta\overline{H}_z\right)$
w	ρ	η	$-\frac{w}{r^2}\frac{\partial}{\partial r}(r\eta)-\rho\frac{vw}{r}$
h	ρ	λ/Cp	$\frac{1}{2}\sigma_e E_\theta \overline{E}_\theta - Q_r$
n_{Ar^+}	1	$D_{Ar^+\,amb}$	$k_{Ar\,ion}n_{Ar}n_e - k_{Ar\,re}n_{Ar^+}n_e$

The governing equation of the induction electromagnetic fields is expressed as

$$\frac{\partial^2 A_\theta}{\partial z^2} + \frac{1}{r}\frac{\partial}{\partial r}\left(r\frac{\partial A_\theta}{\partial r}\right) - \frac{A_\theta}{r^2} = i\mu_0\sigma_e\omega A_\theta \quad (2)$$

where i is equal to $\sqrt{-1}$. The induction electromagnetic fields are represented using the electromagnetic vector potential to consider the interaction between the applied electromagnetic field of the coils and the induction electromagnetic field of the plasma. Then the induction electromagnetic fields are given by Maxwell's equations

$$E_\theta = -i\omega A_\theta \quad (3)$$

$$\mu_0 H_z = \frac{1}{r}\frac{\partial(rA_\theta)}{\partial r} \quad (4)$$

$$\mu_0 H_r = -\frac{\partial A_\theta}{\partial z}. \quad (5)$$

2.1.3 Transport Properties and Boundary Conditions. The density, viscosity, thermal conductivity, specific heat at constant pressure, and radiation loss are obtained from the data [17,18], and the electrical conductivity is estimated from the formula [6]. The recombination coefficients k_{re} of argon are taken from the data [19]. Then the ionization coefficient k_{ion} is expressed by

$$k_{ion} = k_{eq}k_{re} \quad (6)$$

where the equilibrium coefficient k_{eq} is estimated by Saha's equation in local thermodynamic equilibrium and under the condition where no change in composition takes place.

As boundary conditions, nonslip condition, thermal conduction, and electrical insulation are taken into account at the inner surface of the RF-ICP torch and the particle growth tube. For the vector potential at the wall, the contributions of both the coil currents and the induction currents in the plasma are taken into account. Since vector potential A_θ is complex, it is divided into the real part A_R and the imaginary part A_I in the present simulation. The inlet temperature T_{in} and the outer-surface temperature of the torch and the tube T_w are set at 300 K.

The governing equations of the velocity, temperature, number density of ions, and electromagnetic fields for the nanoparticle synthesis reactor, along with the boundary conditions, were simultaneously solved using the SIMPLE algorithm [20]. The computation was performed for a 101 in the r direction by 101 in the z direction uniform staggered grid system.

2.2 Nanoparticle Synthesis Model.

2.2.1 Assumptions and Conditions. The particle growth tube is a cylinder of 25 mm in radius and 125 mm in length. The metal vapor is transported downstream with the plasma gas decreasing the temperature. The decrease in the temperature causes the decrease in the saturation pressure of the metal vapor; consequently, the saturation pressure falls below the vapor pressure. This supersaturation state leads to production of the metal nuclei by nucleation (homogeneous nucleation). Simultaneously, the vapor condenses on the produced nuclei (heterogeneous condensation). These combined mechanisms lead to nanoparticle growth [21].

First, a one-dimensional practical model is adopted to clarify how the operating conditions and the kinds of materials affect the nanoparticle growth mechanism and the finally obtained particle size distributions. The nanoparticle synthesis model is proposed on the following assumptions. The nanoparticles nucleate and grow up just in the particle growth tube. Produced particles are spherical. The particle inertia can be neglected due to the small size. The density of produced particles is estimated 10^{-4}–10^{-3} kg/m^3, whereas the density of argon is 0.327 kg/m^3 at 1500 K where nanoparticles grow. The velocity of the condensing phase and the condensed phase is the same as that of the plasma gas. The temperature of the synthesized nanoparticles is the same as that of the plasma gas. The heat generation caused by condensation is neglected. The metal vapor is considered as an ideal gas. The agglomeration among the nanoparticles and the precipitation of the nanoparticles on the inside of the tube are negligible. The total pressure in the particle growth tube is atmospheric.

For the conditions of the particle growth tube, the information obtained by the computation of the plasma flow is adopted and modified for the one-dimensional model of the nanoparticle synthesis. The computation was conducted for a 5000 in the z direction uniform grid system.

2.2.2 Governing Equations. The concentration of the metal vapor in the particle growth tube is obtained from the conservation equation written as

$$\rho u \frac{\partial c}{\partial z} = -G \tag{7}$$

where c and G represent the mass fraction of the metal vapor and the vapor consumption rate by the nucleation and condensation, respectively.

Supersaturated vapor creates nuclei by homogeneous nucleation. The nanoparticle number density is determined from the homogeneous nucleation rate that is proposed [22]

$$J = \frac{\beta_{11} n_s^2 S}{12}\sqrt{\frac{\Theta}{2\pi}}\exp\left(\Theta - \frac{4\Theta^3}{27(\ln S)^2}\right) \tag{8}$$

where S is the supersaturation ratio defined as

$$S = \frac{n_1}{n_s} = \frac{p_1}{p_s} \tag{9}$$

and Θ is the normalized surface tension written as

$$\Theta = \frac{\sigma s_1}{kT} \tag{10}$$

When Knudsen number Kn, which is the ratio of the mean free path to the particle diameter, is more than 10, the collision frequency function between i-mer and j-mer β_{ij} can be written as

$$\beta_{ij} = \left(\frac{3v_1}{4\pi}\right)^{1/6}\sqrt{\frac{6kT}{\rho}\left(\frac{1}{i}+\frac{1}{j}\right)}(i^{1/3}+j^{1/3})^2 \tag{11}$$

where i and j are equal to 1 for the collision between the molecules.

Since the nuclei in the low supersaturation are unstable due to large growth rate and large evaporation rate, particles are considered to be produced by homogeneous nucleation in higher supersaturation. The particles have the critical diameters expressing the well-balanced condition of nucleation and evaporation. The critical diameter is written as

$$d_{pcr} = \frac{4\sigma v_m}{kT \ln S} \tag{12}$$

The vapor condenses on the surface of the nuclei or the existing nanoparticles. In heterogeneous condensation, the net molecular flux from the vapor to the condensed phase considering the entire range of Knudsen numbers is proposed [21]

$$F = 2\pi D d_p (n_1 - n_s)\left\{\frac{1+\mathrm{Kn}}{1+1.7\mathrm{Kn}+1.333\mathrm{Kn}^2}\right\} \tag{13}$$

The particle diameters are determined from the particle growth rate estimated by this net molecular flux

$$\frac{d(d_p)}{dt} = \frac{F v_m}{\pi d_p^2} \tag{14}$$

2.2.3 Material Properties. In the present numerical investigation, the data of temperature-dependent properties (such as the saturation pressure, density, and surface tension of the materials), which are considerably important factors for the nucleation and condensation, are obtained from Ref. [23]. Since the values of especially the surface tension are given within the limited ranges of temperature, they should be carefully dealt with and applied to the computation. The diffusion coefficients are estimated from the formula [24].

3 Results and Discussion

A summary of the torch geometry and the operating conditions in the present investigation is given in Table 2 with reference to a commercial RF-ICP torch connected with a particle growth

Table 2 Advanced RF-ICP reactor geometry and operating conditions

Radius of nozzle 1	r_1 (mm)	2.5
Radius of nozzle 2	r_2 (mm)	17.0
Torch radius	r_W (mm)	25.0
Coil radius	r_C (mm)	33.0
Coil length	z_C (mm)	20.0
Axial position of coil	z_1 (mm)	30.0
Torch length	z_2 (mm)	75.0
Reactor length	z_3 (mm)	200.0
Wall thickness	δ_W (mm)	5.0
Coil turn number	N (turns)	3.0
Inlet temperature	T_{in} (K)	300.0
Operating pressure	p (atm)	1.0

Table 3 Operating conditions of the conventional and advanced RF-ICP flows

	Q_1	Q_2	Q_3	f	P_{DC}	P_{RF}
	(Sl/min)			(MHz)	(kW)	(kW)
Conventional	5.0	8.0	30.0	6.0	0.0	16.0
Advanced	22.7	8.0	30.0	6.0	4.0	12.0

tube. Argon gas is injected from the nozzles. The swirl ratio $[=w(r_W/ur)]$ is set to be 5.0 at nozzle 3 to stabilize the plasma flow.

In the present study, two kinds of materials, aluminum and titanium, are chosen since their nanoparticles are strongly expected to be applied to the industrial and biomedical processes.

3.1 Effect of Input DC Power on Nanoparticle Synthesis. In this section, the effects of input DC power on nanoparticle synthesis are investigated. The operating conditions are shown in Table 3. The coil frequency f is chosen as 6.0 MHz. Argon gas is injected from the nozzles. The inlet flow rates Q_2 and Q_3 are 8.0 Sl/min and 30.0 Sl/min, respectively. The conventional RF-ICP flow has Q_1 equal to 0.5 Sl/min. The RF input power P_{RF} is set to be 16.0 kW. On the other hand, a DC plasma jet nozzle is installed at the top nozzle 1 of the advanced RF-ICP torch to overcome the disadvantages of the conventional RF-ICP flow. To produce a stable DC plasma jet, the inlet flow rate Q_1 and the DC input power P_{DC} are calculated to be 22.7 Sl/min and 4.0 kW, respectively. The RF input power P_{RF} is set to be 12.0 kW. In the conventional RF-ICP and the advanced RF-ICP, the total input powers are equal to 16.0 kW.

Figure 2 shows the thermofluid fields of the conventional and advanced RF-ICP flows. In Fig. 2(*a*), high temperature regions exist near the induction coils due to the Joule heating. The conventional RF-ICP flow has a larger high-temperature zone near the wall owing to the higher applied RF power, whereas the advanced RF-ICP flow has a high-temperature zone shifted downstream due to the additional momentum and energy of a DC plasma jet. In Fig. 2(*b*), a conventional RF-ICP flow has a characteristic recirculation zone near the induction coils, since the flow is pinched by Lorentz forces caused by the induced electromagnetic fields. On the other hand, in the advanced RF-ICP flow, the recirculation zone near the inlet disappears since the momentum of DC plasma jet overcomes the pinch effect.

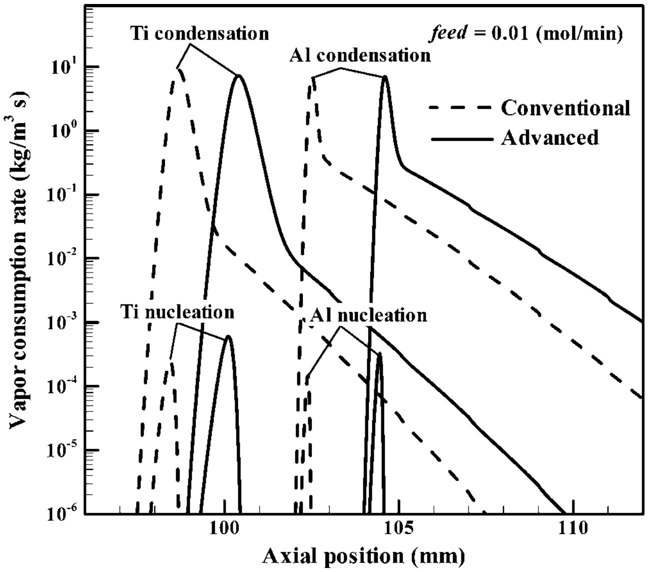

Fig. 3 Vapor consumption rate evolutions with different flow types

Figure 3 shows the vapor consumption rate evolution by homogeneous nucleation and heterogeneous condensation of two metals. In all the cases, the number of the nuclei produced by nucleation increases drastically in a short time; subsequently, the vapor condenses on the nuclei surface. The vapor consumption rates by heterogeneous condensation show 10^4–10^5 times as large as those by homogeneous nucleation. Therefore, most of the metal vapors are transferred to their condensed phases by heterogeneous condensation. Regardless of materials, nucleation and condensation in the advanced RF-ICP flow occur more downstream than those in the conventional one due to the higher temperature in the downstream region. However, the vapor consumption rates by the nucleation are larger in the advanced RF-ICP flow that has the higher velocity. Higher velocity field leads to more rapid quenching, which causes higher supersaturation. As a result, homogeneous nucleation is promoted in a higher supersaturated state as indicated by Eq. (8).

Figure 4 shows the particle size distribution of synthesized

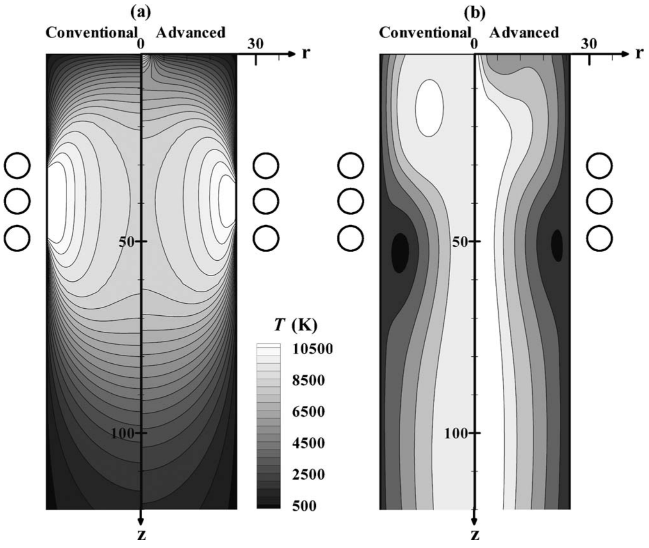

Fig. 2 Thermofluid fields of a conventional and advanced RF-ICP flows

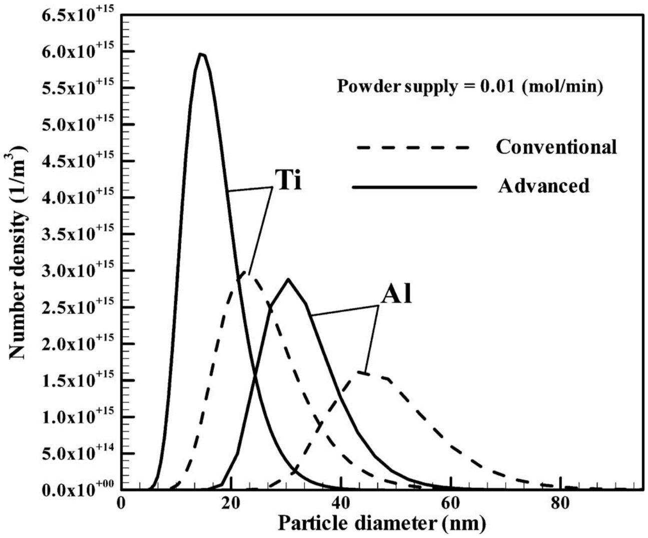

Fig. 4 Particle size distributions with different flow types

nanoparticles of two metals. In both materials, the particles produced by the advanced RF-ICP flow have the larger number densities and smaller diameters than those by the conventional RF-ICP flow. This is because of the large quenching rate along with the higher velocity in the advanced RF-ICP as discussed in Fig. 3. High quenching also leads to more generation of smaller nuclei as expressed by Eq. (12). In the advanced RF-ICP flow, the larger number of the nuclei simultaneously consumes a larger amount of the vapor. Thus, this means that a smaller amount of the vapor is consumed per each nucleus. As the result, the advanced RF-ICP flow system produces more nanoparticles with smaller diameter.

3.2 Effect of Applied Coil Frequency on Two-Dimensional Nanoparticle Synthesis.

Thermofluid fields in RF-ICP flows are affected by applied coil frequency due to skin effect [6]. Skin effect is a phenomenon where electromagnetic waves with higher frequency are absorbed in shallower surfaces of electrical-conductive bodies. Therefore, thermofluid fields formed by Joule heating and Lorentz forces can be controlled by manipulating applied coil frequency by means of skin effect. As a result, this leads to indirect control of heat and mass transfer characteristics in nanoparticle synthesis systems using RF-ICP flows. In this section, two-dimensional analysis is conducted to clarify the applied coil frequency effects on nanoparticle synthesis since skin effect affects mainly radial distribution of thermofluid fields.

The particle growth tube is uniformly divided into 5000 in the z direction and 25 in the r direction for calculation. In this grid system, the axial velocity is much larger than the radial velocity. Furthermore, transport by convection is predominant over transport by diffusion. The diffusion velocity caused by Brownian motion U_{Br} can be calculated by [25,26]. In the present operating condition, U_{Br} is much smaller than the convection velocity U_{con}, and the ratio of U_{Br} to U_{con} is estimated to be $10^{-4}-10^{-3}$. Therefore, the effect of Brownian diffusion can be neglected. The velocity caused by thermophoresis U_{th} can also be calculated by [27]. The ratio of U_{th} to U_{con} is estimated to be $\sim 10^{-6}$, which indicates that the effect of thermophoresis can be neglected as well. It is, therefore, reasonable to use the Eq. (7) for each radial position. The calculation with the same algorithm as the one-dimensional analysis is performed in the z direction for each radial position.

In this section, argon gas is injected from the nozzles and then the inlet flow rates Q_1, Q_2, and Q_3 are 10.0, 10.0, and 30.0 Sl/min, respectively. The swirl ratio $[=w(r_W/ur)]$ is set to be 5.0 at nozzle 3 to stabilize the plasma flow. The coil frequency f, DC input power P_{DC} and RF input power P_{RF} are chosen as 3.0–13.56 MHz, 0.0 kW, and 8.0 kW, respectively. Titanium is chosen here as a raw material. The powder feed rate *feed* is given as 0.002 mol/min. The powder is assumed to vaporize completely and have uniform concentration at the inlet of the particle growth tube ($z=75$ mm).

Figures 5(*a*) and 5(*b*) show the comparison of the thermofluid fields in the RF-ICP flows generated with the different applied coil frequencies. When the applied coil frequency is 13.56 MHz, Joule heating concentrates near the wall due to skin effect. Consequently, the high-temperature region exists near the wall in the RF-ICP torch, which causes the flatter radial distribution in the particle growth tube in Fig. 5(*a*). In Fig. 5(*b*), the characteristic recirculation regions are generated by Lorentz forces in the case of $f=3.0$ MHz. These recirculation regions cause a narrow flow channel that increases the velocity near the central axis. Thus, a higher cooling rate is obtained near the central axis at the inlet of the particle growth tube. On the other hand, the recirculation regions disappear in the case of $f=13.56$ MHz since Lorentz forces affect only the surface layer of the RF-ICP due to skin effect. As the result, a uniform velocity distribution is obtained at the inlet of the particle growth tube. Therefore, thermofluid fields in RF-ICP flows are controllable by the applied coil frequency for required applications.

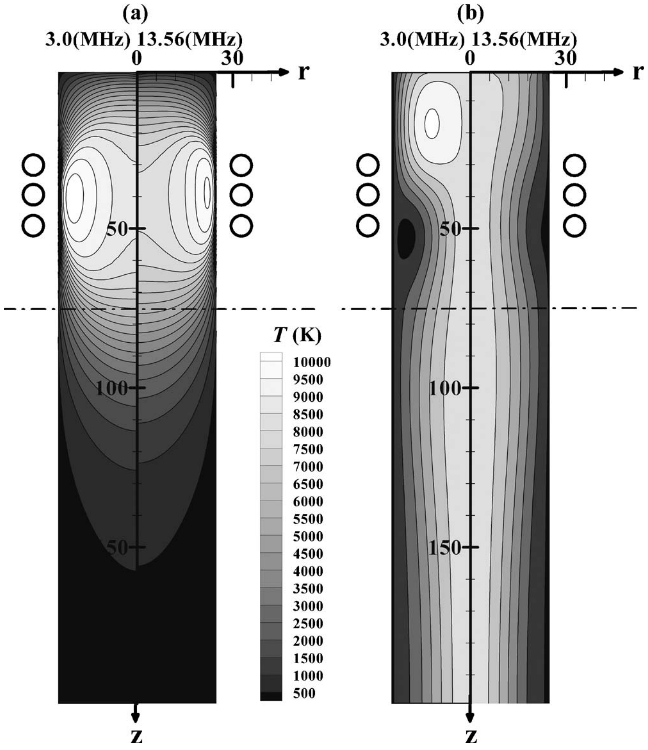

Fig. 5 Thermofluid fields of the RF-ICP flows with the different applied coil frequencies: (*a*) temperature fields and (*b*) flow fields

Figures 6(*a*) and 6(*b*) show the total number densities of titanium particles produced in the particle growth tube for the different applied coil frequencies. In both cases, the particles are produced drastically in the axial position 85–110 mm from the wall to the central axis. The total particle number densities show large especially near the central axis, since a higher quenching rate is obtained near the central axis owing to higher velocity and a steeper temperature gradient. In the case of $f=13.56$ MHz, the total particle number density increases near the wall, while that decreases near the central axis. The uniform distributions of the thermofluid fields as shown in Fig. 5 leads to a relatively uniform amount of nanoparitle production compared to the case of $f=3.0$ MHz. This indicates that an amount of nanoparticle production can also be controlled through plasma manipulation. Each distribution shows somewhat irregular because a nucleation rate is quite delicate for temperature-dependent properties as well as supersaturation ratio as expressed in Eq. (8). This means that a homogeneous nucleation rate is remarkably influenced by the balance between temperature and velocity in an RF-ICP flow.

Figures 7(*a*) and 7(*b*) show the particle size distributions for the different applied coil frequencies. The particles produced near the wall show the broader particle size distribution with the smaller number density and the larger diameters, since the quenching rate is lower near the wall because of the low velocity. When the applied coil frequency is increased from 3.0 to 13.56 MHz, the nanoparticles produced near the wall show increase in the number density and decrease in the particle diameter, whereas the nanoparticles produced near the central axis show the opposite tendency. Thus, dispersion of particle size distributions at the different radial positions can be suppressed by higher applied coil frequency for a RF-ICP flow.

Figure 8 shows the radial distribution of the mean volume diameter estimated from the particle size distributions as shown in Fig. 7. The results obtained from the one-dimensional model are displayed as well for comparison. The two-dimensional model expresses spatial distribution much better than the one-

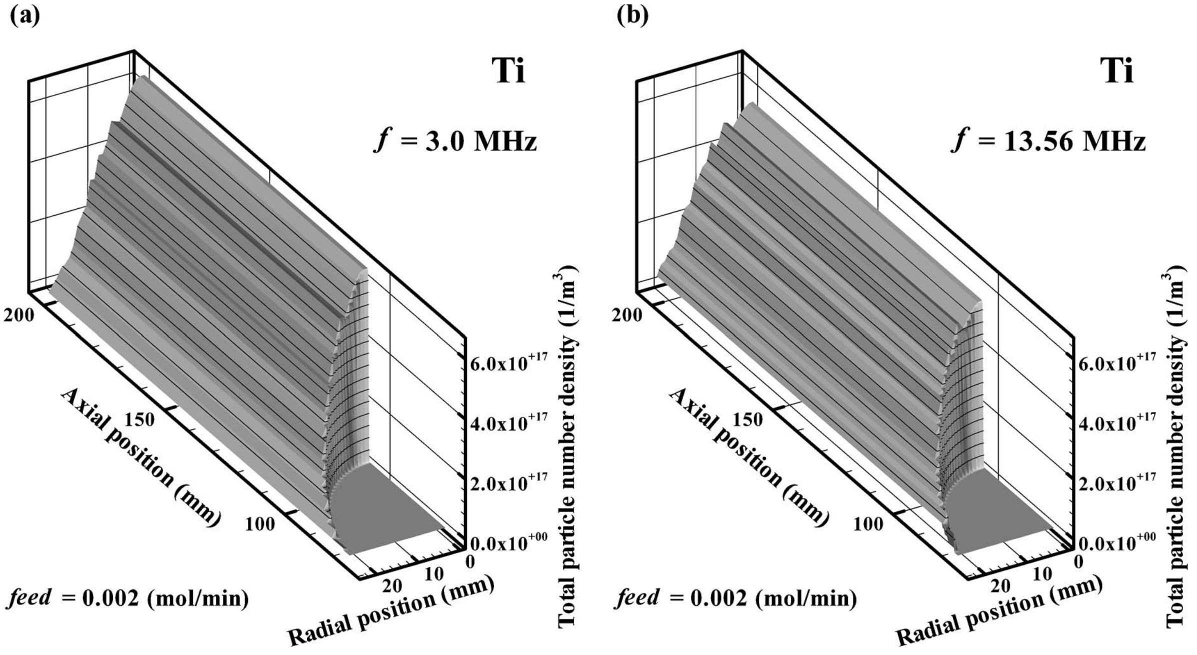

Fig. 6 Total particle number density distribution: (*a*) $f=3.0$ MHz and (*b*) $f=13.56$ MHz

dimensional model. Regardless of applied coil frequency, the larger mean volume diameters are obtained near the wall. They are remarkably different from those calculated by the one-dimensional model. The mean volume diameters near the wall decrease along with the increase in the applied coil frequency. Consequently, the more uniform distribution is obtained by synthesis with the higher applied coil frequency. These results suggest that coil frequency applied on a RF-ICP flow can be a remarkably effective factor to control nanoparticle size distribution for a required production rate and a required particle diameter.

4 Verification of the Present Nanoparticle Synthesis Model

To verify the present nanoparticle synthesis model, the numerical results obtained from the present model should be compared to data obtained from experimental study. It is, however, very difficult to compare both results exactly in the same conditions since only little data of experiments for nanoparticle synthesis systems using RF-ICP flows is available. Therefore, the numerical results calculated by the present model were compared to the experimental data in similar conditions [2,28]. The operating gas was argon in atmospheric pressure. The feed material was iron.

Figure 9 presents the first comparison of the particle size distributions obtained by the present one-dimensional model and the other experimental data [2]. The inlet flow rates Q_1, Q_2, and Q_3 were set to be 0.5, 8.0, and 30.0 Sl/min, respectively. The inlet temperature T_{in}, the input RF power P_{RF}, and the applied coil frequency f were 300 K, 15.0 kW, and 4.5 MHz, respectively. The powder feed rate was 3.85×10^{-3} mol/min.

The present model provides the particle diameter around 30 nm. The experimental result provides almost the same size order as the present result, which shows a good agreement. How-

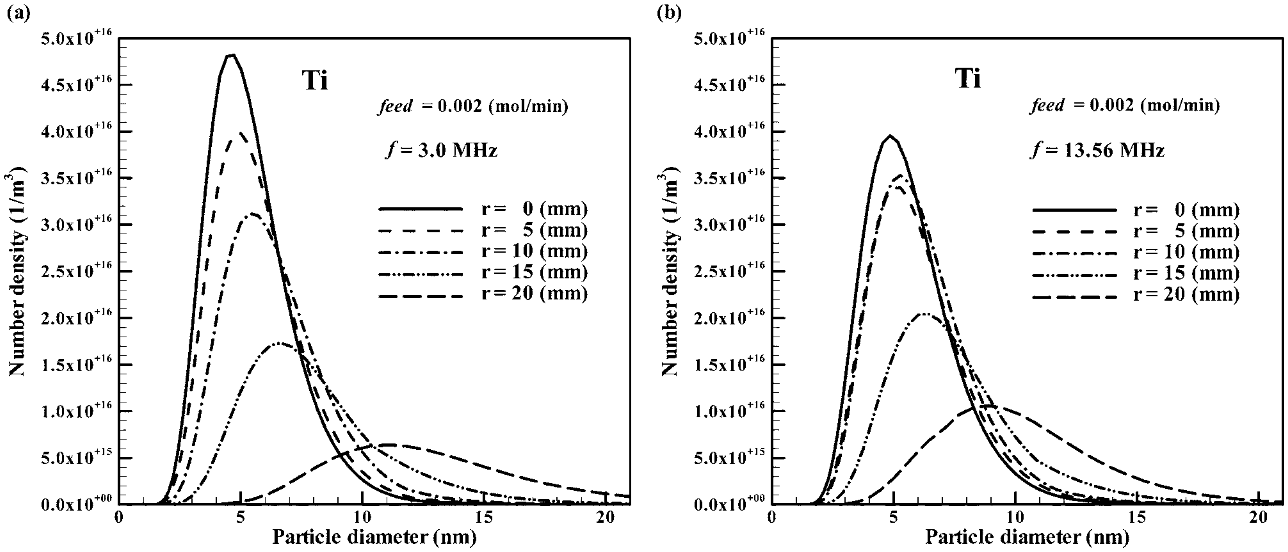

Fig. 7 Particle size distribution: (*a*) $f=3.0$ MHz and (*b*) $f=13.56$ MHz

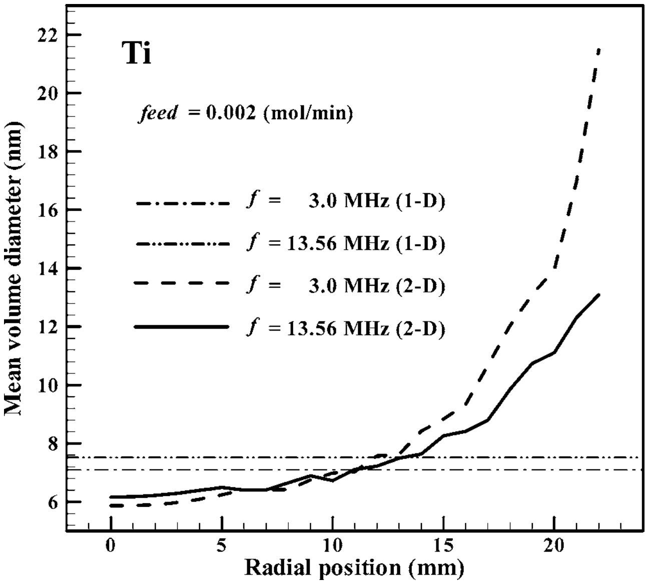

Fig. 8 Radial distribution of mean volume diameters

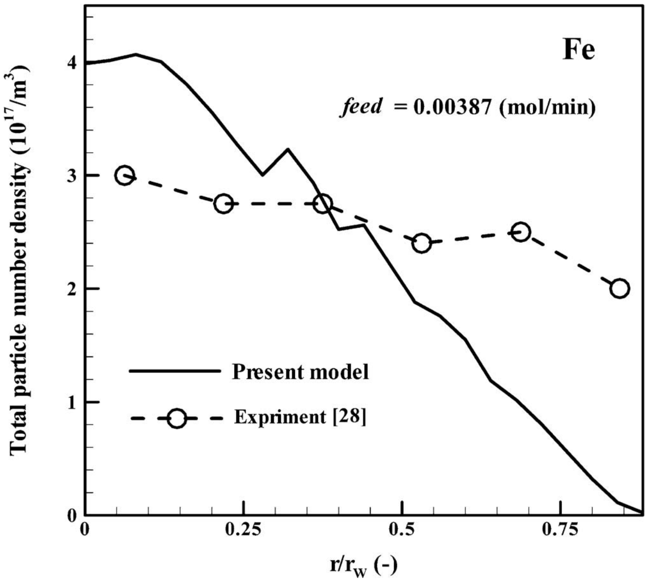

Fig. 10 Comparison of radial distributions of the total particle number densities to experimental data [28]

ever, the experimental one displays a relatively broader distribution in the particle size. In experiments, deviation of raw material and wavering of plasma flame cause a broader distribution of produced nanoparticles. Furthermore, agglomeration of nanoparticles occurs in actual processes. Therefore, it is necessary to consider the effects of nanoparticle agglomeration for realistic modeling as a next step.

Figure 10 shows additional comparison of the radial distributions of the total particle number densities obtained by the present two-dimensional model and the experimental data [28]. The inlet flow rates Q_1, Q_2, and Q_3 were set to be 1.53, 3.0, and 15.0 Sl/min, respectively, in order to match the quantities of the inlet gas flow per unit area. The inlet temperature T_{in}, the input RF power P_{RF}, and the applied coil frequency f were 300 K, 4.5 kW, and 2.9 MHz, respectively. The powder feed rate was 3.87×10^{-3} mol/min.

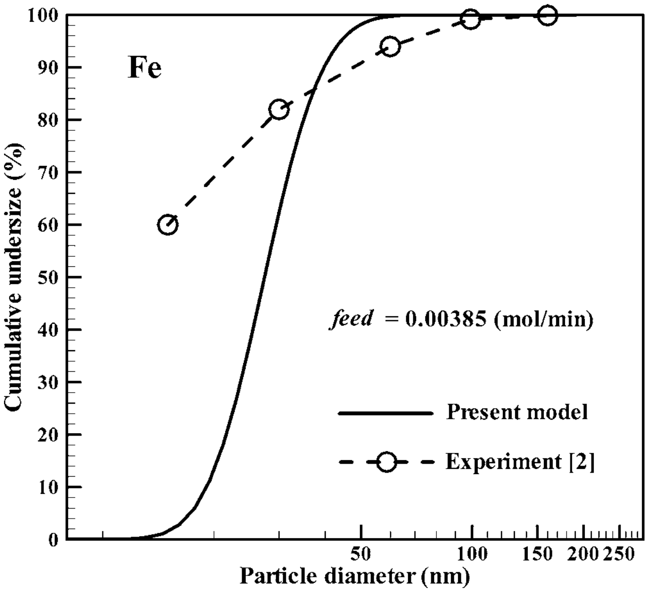

Fig. 9 Comparison of particle size distributions to experimental data [2]

Both results have the same magnitude of 10^{17} /m^3 and the same tendency that the total particle number densities decrease toward the wall. However, the result obtained from the present model shows a steeper profile than those from the experiment. This is because the radial diffusion by the concentration gradient was not taken into account in the present model even though the diffusion is not considerably significant. It may also be necessary to use finer mesh in the radial direction and to consider the effects of Brownian diffusion and thermophoresis for more accuracy. On the other hand, the reason why the experimental results show a relatively flat profile is because of significant mixing induced by the measuring probes inserted into the particle growth tube, according to reference [28]. Furthermore, the effect of turbulence mixing might not be able to be neglected in plasma processes even though the Reynolds number is estimated to be small. It is well known that plasma flame is actually wavering and unstable accompanied with drastic heat/species transfer. It was reported that turbulence effects play an important role in particle processes using RF-ICP flow [29].

Additionally, there is a local spike at $r/r_W = 0.35$ in the present result as shown in Fig. 10. According to Eq. (8), concerning a homogeneous nucleation rate, generation of nuclei is considerably influenced by temperature and supersaturation ratio. High flow velocity leads to high quenching and high supersaturation. Therefore, numbers of produced particles are sensitively determined by the balances among a local quenching rate, degree of supersaturation, and temperature-dependent properties. This indicates that control of the number of nanoparticle generation is challenging and significant.

The present nanoparticle synthesis model shows good agreement in particle size distribution and nanoparticle generation. However, effects of agglomeration, Brownian diffusion, thermophresis, and turbulence mixing of the synthesized nanoparticles should be taken into account for more accuracy in the next study.

5 Conclusions

Numerical investigation was conducted to analyze the mechanism of nanoparticle synthesis in the advanced RF-ICP reactor. The operating conditions, such as the additional DC power and the applied coil frequency for plasma flows, considerably affect production of metallic nanoparticles via controlled thermofluid fields in RF-ICP flows. The remarkable results obtained by our numerical analysis are as follows:

1. In an advanced RF-ICP flow, a high-temperature zone is shifted downstream and a characteristic recirculation zone disappears due to the additional energy and momentum of a DC plasma jet. Larger numbers of nanoparticles with smaller size are produced by using an advanced RF-ICP flow.
2. Thermofluid fields in RF-ICP flows can be controlled by applied coil frequency by means of skin effect. Two-dimensional analysis clarified that larger numbers of nanoparticles with smaller size are produced near the central axis. Dispersion of particle size distributions at the different radial positions can be suppressed by higher applied coil frequency through control of thermofluid fields in RF-ICP flows. Applied coil frequency can be a remarkably effective factor to control nanoparticle size distribution.
3. The results obtained by the present model were compared to the experimental data. They showed good agreement in nanoparticle size distribution and spatial distribution of nanoparticle production. This verifies the present model. However, the model should be improved by the consideration of agglomeration, Brownian diffusion, thermophresis, and turbulence mixing of the synthesized nanoparticles in our future work.

Acknowledgments

This work was supported by a grant-in-aid for Scientific Research (B) from the Japan Society for Promotion Science (2003–2004) and a 21st Century COE Program Grant of the International COE of Flow Dynamics from the Ministry of Education, Culture, Sports, Science, and Technology. This numerical investigation was conducted under the research project (No. E01JUN03) at the Advanced Fluid Information Research Center of the Institute of Fluid Science, Tohoku University, Japan.

Nomenclature

A = vector potential, A H/m
c = mass fraction
D = diffusion coefficient, m^2/s
d = diameter, m
e = electron charge, C
$\boldsymbol{E}$ = electric field vector, V/m
f = coil frequency, Hz
$feed$ = powder feed rate, mol/min
F = net molecular flux, s
G = vapor consumption rate, kg/m^3 s
h = enthalpy, J/kg
$\boldsymbol{H}$ = magnetic field vector, A/m
J = homogeneous nucleation rate, $1/m^3$ s
k = Boltzmann constant, J/K
k_{eq} = equilibrium constant, $1/m^3$
k_{ion} = ionization coefficient, m^3 s
k_{re} = recombination coefficient, m^6/s
Kn = Knudsen number
n = number density, $1/m^3$
p = pressure, Pa
P = input power, W
Q = flow rate, Sl/min
Q_r = radiation loss, W/m^3
r = radial coordinate, m
r_1 = carrier gas nozzle radius, m
r_2 = plasma gas nozzle radius, m
s_1 = surface of a monomer, m^2
S = supersaturation ratio
T = temperature, K
U = velocity
u = axial velocity component, m/s
v = radial velocity component, m/s
v_1 = volume of a monomer, m^3
w = azimuthal velocity component, m/s
z = axial coordinate, m

Greek Symbols

β = collision frequency function, m^3/s
η = viscosity, Pa s
θ = azimuthal coordinate, m
Θ = normalized surface tension
λ = thermal conductivity, W/m K
μ_0 = permeability in vacuum, H/m
ρ = density, kg/m^3
σ = surface tension, N/m
σ_e = electrical conductivity, S/m
ω = angular frequency, rad/s

Subscripts

1 = monomer
Ar = argon atom
Ar^+ = argon ion
Br = Brownian diffusion
con = convection
amb = ambipolar
DC = direct current
RF = radio frequency
e = electron
p = particle
s = saturation
th = thermophoresis
m = molecule
r = radial component
z = axial component
θ = azimuthal component

References

[1] Siegel, R. W., 1993, "Synthesis and Properties of Nanophase Materials," Mater. Sci. Eng., A, **A168**, pp. 189–197.

[2] Yoshida, T., and Akashi, K., 1981, "Preparation of Ultrafine Iron Particles Using an RF Plasma," Trans. Jpn. Inst. Met., **22**(6), pp. 371–378.

[3] Ono, T., Kagawa, M., Syuno, Y., Ikebe, M., and Muto, Y., 1987, "Ultrafine $BaPb_{1-x}Bi_xO_3$ Powders Prepared by the Spray-ICP Technique," Plasma Chem. Plasma Process., **7**(2), pp. 201–209.

[4] Hasegawa, M., Kato, Y., Kagawa, and M., Syuno, Y., 1996, "Effect of Additive Oxides on Ultrafine CeO_2 Particles Synthesized by the Spray-ICP Technique," J. Mater. Sci. Lett., **15**, pp. 1608–1611.

[5] Okuyama, H., Honma, K., and Ohno, S., 1999, "Photocatalytic Activity of Ultrafine TiO_2 Particles Synthesized by an RF Plasma CVD," J. Jpn. Inst. Met., **63**(1), pp. 74–81.

[6] Nishiyama, H., and Shigeta, M., 2002, "Numerical Simulation of an RF Inductively Coupled Plasma for Functional Enhancement by Seeding Vaporized Alkali Metal," Eur. Phys. J.: Appl. Phys., **18**(2), pp. 125–133.

[7] Watanabe, T., Nezu, A., Abe, Y., Ishii, Y., and Adachi, K., 2003, "Formation Mechanism of Electrically Conductive Nanoparticles by Induction Thermal Plasmas," Thin Solid Films, **435**, pp. 27–32.

[8] Girshick, S. L., and Chiu, C.-P., 1990, "Numerical Study of MgO Powder Synthesis by Thermal Plasma," J. Aerosol Sci., **21**(5), pp. 641–650.

[9] Joshi, S. V., Liang, Q., Park, J. Y., and Batdorf, J. A., 1990, "Effect of Quenching Conditions on Particle Formation and Growth in Thermal Plasma Synthesis of Fine Powders," Plasma Chem. Plasma Process., **10**(2), pp. 339–358.

[10] McFeaters, J. S., Stephens, R. L., Schwerdtfeger, P., and Liddell, M., 1994, "Numerical Modeling of Titanium Carbide Synthesis in Thermal Plasma Reactor," Plasma Chem. Plasma Process., **14–3**, pp. 333–360.

[11] Ageorge, H., Megy, S., Chang, K., Baronnet J.-M., Williams, J. K., and Chapman, C., 1993, "Synthesis of Aluminum Nitride in Transferred Arc Plasma Furnaces," Plasma Chem. Plasma Process., **13**(4), pp. 613–632.

[12] Bilodeau, J.-F., and Proulx, P., 1995, "Analysis of the Synthesis of Ultrafine AIN Powders in an Induction Plasma Reactor," *Proc. of 12th Int. Symp. on Plasma Chemistry*, pp. 1201–1206.

[13] Cruz, A. C., and Munz, R. J., 1997, "Vapor Phase Synthesis of Fine Particles," IEEE Trans. Plasma Sci., **25**(5), pp. 1008–1016.

[14] Han, P., and Yoshida, T., 2001, "Numerical Investigations of the Thermophoretic Effects on Clusters Deposition During TPCVD Process," *Proc. of 15th Int. Symp. on Plasma Chemistry*, **2**, pp. 683–689.

[15] Yang, Y., Ong, J. L., and Tian, J., 2002, "In Vivo Evaluation of Modified Titanium Implant Surfaces Produced Using a Hybrid Plasma Spraying Processing," Mater. Sci. Eng., R., **20**, pp. 117–124.

[16] Kawajiri, K., Sato, T., and Nishiyama, H., 2003, "Experimental Analysis of a DC-RF Hybrid Plasma Flow," Surf. Coat. Technol., **171**, pp. 134–139.

[17] Boulos, M. I., Fauchais, P., and Pfender, E., 1994, *Thermal Plasma*, Vol. 1, Plenum Press, New York.
[18] Menart, J., and Lin, H., 1998, "Numerical Study of High-Intensity Free-Burning Arc," J. Thermophys. Heat Transfer, **12**, pp. 500–506.
[19] Hoffert, M. I., and Lien, H., 1967, "Quasi-One-Dimensional, Nonequilibrium Gas Dynamics of Partially Ionized Two-Temperature Argon," Phys. Fluids, **10**, pp. 1769–1776.
[20] Patankar, S. V., 1980, *Numerical Fluid Flow and Heat Transfer*, Hemisphere, New York.
[21] Friedlander, S. K., 1977, *Smoke, Dust and Haze*, Wiley, New York.
[22] Girshick, S. L., Chiu, C.-P., and McMurry, P. H., 1990, "Time-Dependent Aerosol Models and Homogeneous Nucleation Rates," Aerosol Sci. Technol., **13**, pp. 465–477.
[23] Japan Institute of Metals, 1993, *Metal Data Book*, Maruzen, Japan.
[24] Reid, R. C., Prausnitz, J. M., and Sherwood, T. K., 1977, *The Properties of Gases and Liquids*, 3rd edition, McGraw-Hill, New York.
[25] Epstein, P. S., 1956, *Investigations on the Theory of the Brownian Movement*, Dover, New York.
[26] Furth, R., 1924, "On the Resistance Experienced by Spheres in Their Motion Through Gases," Phys. Rev., **23**, pp. 710–733.
[27] Waldmann, L., and Schmitt, K. H., 1966, *Thermophoresis and Diffusiophoresis of Aerosols, Chapter VI in Davies*, Aerosol Science, Academic, New York.
[28] Girshick, S. L., Chiu, C.-P., Muno, R., Wu, C. Y., Yang, L., Singh, S. K., and McMurry, P. H., 1993, "Thermal Plasma Synthesis of Ultrafine Iron Particles," J. Aerosol Sci., **24**(3), pp. 367–382.
[29] Ye, R., Proulx, P., and Boulos, M. I., 2000, "Particle Turbulent Dispersion and Loading Effects in an Inductively Coupled Radio Frequency Plasma," J. Phys. D, **33**, pp. 2154–2162.

Alex J. Heltzel

Senthil Theppakuttai

John R. Howell

Shaochen Chen

Department of Mechanical Engineering,
The University of Texas at Austin,
Austin, TX 78712

Analytical and Experimental Investigation of Laser-Microsphere Interaction for Nanoscale Surface Modification

An analytical and experimental investigation on the features created on silicon by the irradiation of microspheres on the substrate surface with a pulsed laser is presented. Silica microspheres of 1.76 μm *diameter are deposited on the silicon substrate and are irradiated with a pulsed Nd:YAG laser of wavelength* 532 nm*. An analytical model based on Mie theory is developed, which includes all evanescent terms and does not rely on either far-field or size-parameter approximations. The predicted intensity distributions on the substrate indicate a strong near-field enhancement confined to a very small area (nanometer scale). A multidimensional, numerical model was built to simulate the heat transfer through the silicon. An explicit scheme of the enthalpy method was employed to track the solid/liquid phase boundary. The experiment was performed for various laser energies used in the modeling, and the features obtained are characterized using a scanning electron microscope. The experimental results correlate well with the predicted results.* [DOI: 10.1115/1.2039110]

Introduction

The industrial demand for smaller structures required for the manufacture of quantum devices, high-density recording media, etc., have resulted in the need for fabrication technology at the nanometer scale. Thus a variety of structuring techniques such as lithography [1] and focused ion beam patterning [2] have been investigated for nanofabrication. However, most of these techniques are limited either by their inability for large-area fabrication or by the diffraction limit and in most cases the high manufacturing costs.

To overcome the diffraction limit and to spatially control matter on a nanometer scale, several fabrication techniques based on near-field optics have been employed. One such technique for creating structures is utilizing the near-field radiation created around a microsphere by laser radiation. The accidental discovery of particle induced damage during dry laser cleaning of irregularly shaped Al_2O_3 particles on glass [3] has led to this exciting yet simple technique. When spherical colloidal particles such as silica (SiO_2) and polystyrene were used as contaminants on silicon wafers, features with diameters of 200–400 nm and depths of 10–80 nm depending on the irradiation conditions, were found at the former position of the particles. Instead of using colloidal particles, if microspheres are arranged in a periodic monolayer on the substrate, massively parallel nanostructuring could be realized [4].

In this paper, we study the nanofeatures created on silicon by irradiating 1.76 μm silica microspheres with a 532 nm pulsed Nd:YAG laser. The electromagnetic field surrounding the sphere is calculated using the exact solution presented by Mie [5]. The calculation does not rely on simplifying approximations used in limiting cases and previous attempts to describe the near field [6,7]. A phase change heat transfer model based on the enthalpy method was built to employ the enhanced laser intensity distributions. The model predicts the resulting transient, two-dimensional temperature field in the silicon and the location of the moving phase boundary. To corroborate the predicted results, the microspheres are irradiated with different laser energies, and the features obtained experimentally are characterized by a scanning electron microscope (SEM).

Optical Field Modeling

The enhancement of incident intensity can be described from the starting point of Mie's theory of scattering. Born and Wolf [6] presents the rigorous solution to Maxwell's equations describing the scattered electromagnetic field components: $E_r^{(s)}$, $E_\theta^{(s)}$, $E_\phi^{(s)}$, $H_r^{(s)}$, $H_\theta^{(s)}$, $H_\phi^{(s)}$.

The coefficients eB_l and mB_l characterize the wave scattered by the sphere and are often simplified. The exact versions used for calculation in this paper are given by

$$eB_l = i^{l+1}\frac{2l+1}{l(l+1)}\frac{m\psi_l'(q)\psi_l(mq) - \psi_l(q)\psi_l'(mq)}{m\zeta_l^{(1)\prime}(q)\psi_l(mq) - \zeta_l^{(1)}(q)\psi_l'(mq)} \tag{1}$$

$$mB_l = i^{l+1}\frac{2l+1}{l(l+1)}\frac{m\psi_l(q)\psi_l'(mq) - \psi_l'(q)\psi_l(mq)}{m\zeta_l^{(1)}(q)\psi_l'(mq) - \zeta_l^{(1)\prime}(q)\psi_l(mq)} \tag{2}$$

The scattered electromagnetic field components are added to the incident field components (plane wave of the laser) to give the solution to Maxwell's equations both inside and outside the sphere. The parameter m is the complex refractive index of the sphere. The parameter q is equal to κ times the radius of the sphere, where κ is equal to 2π divided by the wavelength of the incident laser.

There is some difficulty associated with the exact calculation of the field components, specifically, the Bessel functions, Legendre functions, and their derivatives. Much of this difficulty can be circumvented by substituting asymptotic approximations for these terms that acceptably describe the field at a large distance from the particle. The critical coefficients eB_l and mB_l can be approximated for relatively large or highly conductive particles. In addition to individual term approximations, the overall intensity of the field is often approximated by squaring the amplitude of the electric vector. Under the conditions of the experiments presented, none of

---

Contributed by the Heat Transfer Division of ASME for publication in the JOURNAL OF HEAT TRANSFER. Manuscript received December 1, 2004; final manuscript received June 20, 2005. Review conducted by: C. P. Grigoropoulos. Paper presented at the 2004 ASME International Mechanical Engineering Congress (IMECE2004), November 13, 2004–November 19, 2004, Anaheim, CA, USA.

these simplifications can be acceptably included. Most important, the far-field approximation cannot be utilized, as it is specifically the near-field enhancement that is assumed responsible for the substrate damage.

Because of the limitations, all terms in Mie's theory were calculated exactly up to the critical value of l_{cutoff}, after which the terms in the infinite sum were equal to zero. This was done through the use of recurrence relations for the Bessel functions and Legendre functions provided by [8,9]. The derivatives of these functions were determined numerically, with 45,000 values calculated in the range of $\theta=0$ to 45°, with the origin taken at the center of the sphere. The summation cutoff value of l was chosen to be

$$l_{cutoff} = \frac{2\pi a n}{\lambda} + 4 \qquad (3)$$

where a is the sphere radius, n is the real component of the refractive index of the sphere, and λ is the incident wavelength of the laser. An investigation was carried out to determine the effectiveness of the l_{cutoff} value. The magnitude of the real and imaginary coefficients, eB_l and mB_l, respectively, fell to zero through four decimal places by the final term included in the summation for all theoretical cases. Therefore, l_{cutoff} was chosen large enough to contain every term of value in the infinite series.

The intensity of the radiation incident on the plane of the substrate is quantified using the Poynting vector of the electromagnetic field. The spherical components of the time-averaged Poynting vector are

$$\begin{aligned} S_r &= I_0\,\mathrm{Re}[E_\theta H_\phi^* - E_\phi H_\theta^*] \\ S_\theta &= I_0\,\mathrm{Re}[E_\phi H_r^* - E_r H_\phi^*] \qquad (4) \\ S_\phi &= I_0\,\mathrm{Re}[E_r H_\theta^* - E_\theta H_r^*] \end{aligned}$$

where I_0 is the intensity of the incident laser, and the asterisk superscript indicates the complex conjugate of the magnetic field components. The z-direction is taken longitudinal to the incident laser and normal to the substrate lying beneath the particle. The z-component of the Poynting vector is therefore a description of the energy incident upon the substrate surface due to the laser and the presence of the microsphere. The coordinate convention used dictates the z-component equal to

$$S_z = \cos\theta\, S_r - \sin\theta\, S_\theta \qquad (5)$$

The effect of secondary reflection of energy between the substrate and sphere boundaries is not accounted for in the S_z value. This is a potential source of error judging by the results of Luk'yanchuck et al. [7], who found an increase in peak enhancement due to substrate effect. However, the Mie calculations in [7] used for comparison neglected the magnetic field components, which were necessarily included in the present work. The Mie results corresponding to identical cases between [7] and this work differ by up to a factor of 4 in peak enhancement values.

The authors are conducting an investigation to determine the necessity of including secondary reflection on the overall heat transfer effect, which will be included in future work if found significant.

S_z has been calculated for certain cases available for experimentation. Figure 1 shows the intensity distribution on the substrate with parameters: $a=0.88$ μm, $\lambda=532$ nm, and $n=1.37$, corresponding to a silica sphere 1.76 μm in diameter. The resulting peak intensity predicted is 14.65 times the incident intensity. A fraction of this energy will be reflected to the environment. At this wavelength, the fluence required to damage the substrate is in the range of 600–650 mJ/cm^2. Theoretically, the enhancement predicted by the model would lower the input energy threshold to roughly 40–45 mJ/cm^2.

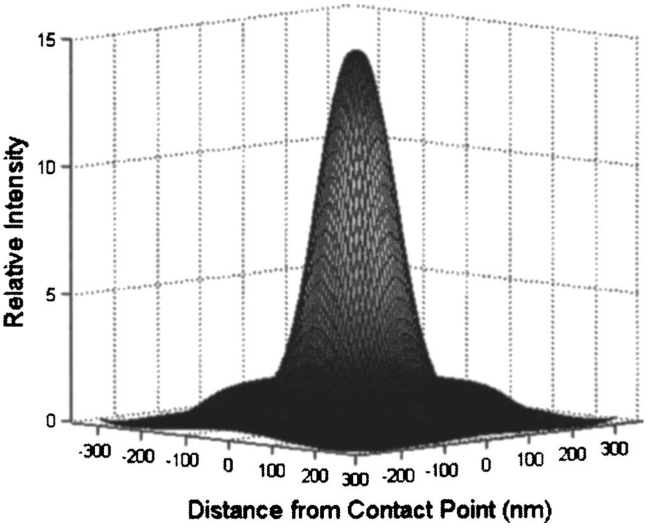

Fig. 1 **Intensity enhancement on silicon surface due to laser-microsphere interaction: $\lambda=532$ nm, silica microsphere 1.76 μm in diameter**

Figure 2 is a cross section of Fig. 1 taken along one of the horizontal axes through the contact point of the sphere and surface. It is evident that for this case, the predicted enhancement is concentrated within a circular area on the substrate surface with radius less than 200 nm.

Figure 3 illustrates the predicted dependence of the enhancement effect on the proximity of the sphere to the surface. S_z was calculated with the sphere moved a single radius away from the surface. The predicted enhancement decreases dramatically and is focused to a lesser degree with the area directly under the sphere.

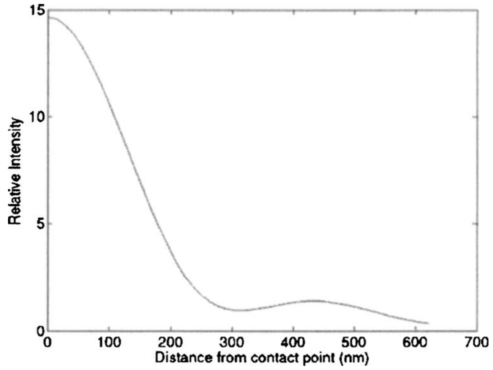

Fig. 2 **Intensity enhancement on silicon from 1.76 μm SiO_2 spheres and 532 nm laser**

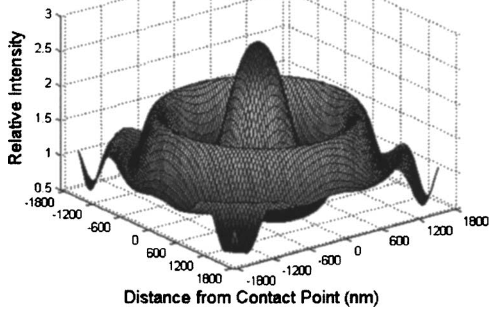

Fig. 3 **Intensity enhancement on silicon substrate from 1.76 μm diameter silica particle elevated 1.76 μm above surface, 532 nm laser**

The secondary and tertiary "waves" of intensity are relatively more significant compared to Fig. 1, and effectively average to unity outside the primary enhancement. The peak enhancement resulting from the Mie calculation is again at the contact point, but this magnitude deviates between cases. At certain distances from the substrate the secondary ring may actually represent the peak near-field enhancement.

Modeling of Heat Transfer in the Substrate

Calculation of the laser intensity enhancement provides a boundary condition to employ in a model of the heat transfer within the substrate. The goal of the simulation is to obtain the temperature and phase (solid/liquid) distribution in the silicon, which indicates the size and shape of the melt zone. This data are then compared with experimental observations characterized using a SEM.

The ~6 ns duration of the laser pulse allows the use of Fourier conduction within the substrate, which is modeled as a semi-infinite slab. The enthalpy method was used explicitly to account for the moving phase boundary within the material (Stefan problem) [10–12]. The heat equation as a function of the enthalpy in the solid silicon is

$$\rho\frac{\partial h}{\partial t}=\frac{\partial}{\partial x}\left(k\frac{\partial T}{\partial x}\right)+\frac{\partial}{\partial y}\left(k\frac{\partial T}{\partial y}\right)+\dot{q} \tag{6}$$

with the generation term $\dot{q}(\mathrm{W/m^3})$ is equal to

$$\dot{q}=(1-R)q_{inc}(x_{int},t)\gamma e^{(-\gamma\cdot z)} \tag{7}$$

where R is the reflectivity of silicon dependent on the wavelength of the incident light and phase of the silicon, and γ is the absorption coefficient, given by

$$R=\frac{(n-1)^2+k_x^2}{(n+1)^2+k_x^2} \tag{8}$$

$$\gamma=\frac{4\pi k_x}{\lambda} \tag{9}$$

q_{inc} is the enhanced value of laser energy taken at x_{int}, the surface intercept node between the node in the solid and the center of the sphere. It follows a Gaussian shape through time given by

$$q_{inc}(x_{int},t)=A\exp[-(B-t)^2/C]I(x_{int}) \tag{10}$$

The constants B and C are fit to the laser wave form, while A ensures the total energy incident corresponds to the proper fluence, and $I(x_{int})$ refers to the intensity distribution in Fig. 1.

New values of h are calculated explicitly every time step, relying only on the surrounding temperatures from the previous iteration. This precludes the need to invert matrices or employ other convergence algorithms, but requires the following expression to be obeyed to prevent divergence of the solution.

$$\frac{\Delta t}{\Delta x^2}\leqslant\frac{\rho c}{2k} \tag{11}$$

This expression limits the numerical time and space steps in terms of the specific heat, density, and thermal conductivity of the material. Using the extreme values of all three variables in the anticipated temperature range, the left-hand side of (11) must be less than approximately 6000. Time steps of 75 fs and space steps of 19.5 nm were used to obtain the following results, and were proven adequate by grid-independence investigations.

At the surface of the substrate in the presence of opaque liquid silicon, an energy conserving boundary condition is used to account for energy loss due to radiation, which was found to be significant.

$$(1-R)q_{inc}-\varepsilon\sigma T^4=k\frac{\Delta T}{\Delta y}+\rho c\Delta y\frac{\Delta T}{\Delta t} \tag{12}$$

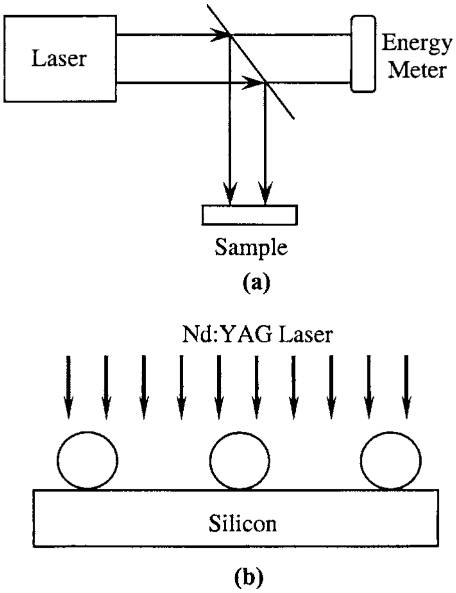

Fig. 4 Laser irradiation of disperse silica spheres on silicon substrate: (*a*) Schematic of the experimental setup; (*b*) schematic of silica microspheres on silicon

The emissivity ε of the liquid silicon is determined from the following relation

$$\varepsilon(\lambda,T)=\frac{4n}{n^2+k_x^2+2n+1} \tag{13}$$

where the refractive indices n and k_x are obtained from [13,14].

The new value of calculated enthalpy determines the temperature at the node based on the following relations

$$\begin{aligned}T_{x,y}^{t+1}&=h_{x,y}^{t+1}/c_l, \quad h^{t+1}<(cT_m)\\ T_{x,y}^{t+1}&=T_m, \quad (cT_m)<h^{t+1}<(cT_m+L)\\ T_{x,y}^{t+1}&=(h_{x,y}^{t+1}-(c-c_l)T_m-L_m)/c_l, \quad h^{t+1}\geqslant(cT_m+L)\end{aligned} \tag{14}$$

The silicon is therefore separated into three regimes: solid, liquid, and a transition zone. The boundaries of these regions are tracked through time using the preceding method.

Experimental Setup

The sample used for patterning is a 500 μm thick n-type (100) polished silicon wafer with a surface roughness of a few nanometers (<2 nm) and a 2–3 nm thick native oxide layer. Before processing the sample, care was taken to ensure that the sample is clean and free of any contaminants. For this reason, it is first cleaned in ethanol solution followed by rinsing in deionized water. After the sample is dried with nitrogen gas, a colloidal suspension of mono-dispersed silica spheres diluted with deionized water is applied on the glass sample and let to dry [15].

The schematic of our experimental setup is shown in Fig. 4(*a*). The output from a pulsed Nd:YAG laser passes through a beam splitter, which splits the incident laser beam into two: one part for patterning and the other for measuring the laser energy. The sample is mounted on a three-dimensional stage and the laser beam is focused onto the sample by using a plano-convex lens.

A single pulse from the laser is incident on the spheres as shown in Fig. 4(*b*). Since the sphere is immediately on top of the substrate, the incident laser beam induces a near-field around the sphere. This enhanced field is responsible for the formation of nanofeatures on the silicon substrate. The features thus obtained were characterized using an SEM and are presented in the results and discussion section of the paper.

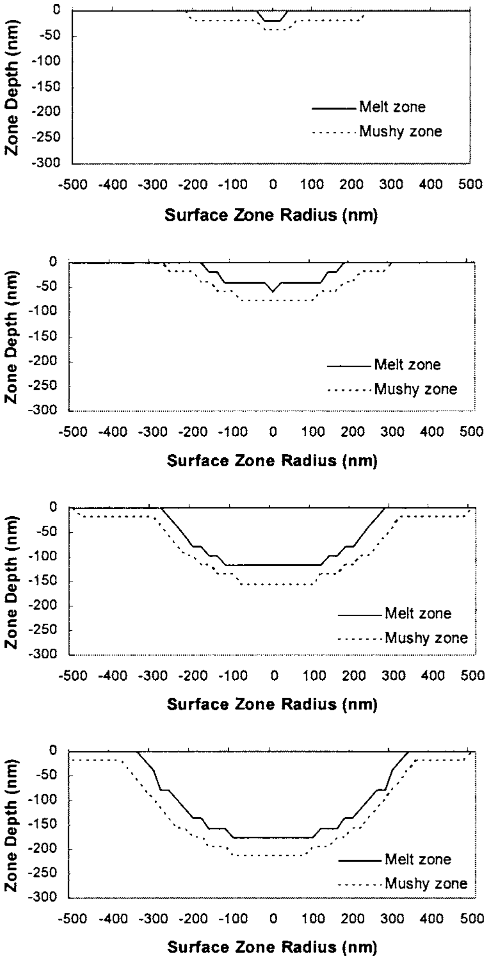

Fig. 5 Predicted geometry of melt and mushy zones in silicon at laser fluence of (*a*) 50 mJ/cm^2, (*b*) 100 mJ/cm^2, (*c*) 200 mJ/cm^2, and (*d*) 300 mJ/cm^2

Results and Discussion

The heat transfer simulations were conducted using 1.76 μm SiO_2 spheres irradiated by a single 532 nm laser pulse at four fluences: 50, 100, 200, and 300 mJ/cm^2. The boundary condition of Figure 2 employed in Eq. (10) was used in all cases. Figure 5 gives the numerical results predicting the width and depth of the melt and mushy zones in the silicon for the four laser energies.

There are essentially two points of comparison available between the SEM micrographs and the simulation results: the size of the surface damage, and the threshold energy below which no damage occurs. At 50 mJ/cm^2, the model predicts that the surface of the substrate barely reaches the melting temperature, with melt zone only a few nm wide and deep, and a mushy or heat-affected zone approximately 430 nm wide. The heat affected zone is very shallow, and in terms of transience the melting temperature is only attained for a few nanoseconds. At 100 mJ/cm^2, the model predicts a melted zone approximately 332 nm in diameter, which a total heat affected region of 548 nm diameter. At 200 mJ/cm^2, a zone of melted silicon 528 nm in diameter is predicted, with a heat affected region 939 nm in diameter. Here the predicted melt depth doubles to 156 nm. At energy of 300 mJ/cm^2, a zone of melted silicon approximately 645 nm with a total heat affected zone of 958 nm in diameter is predicted. A melt depth of 215 nm is also predicted.

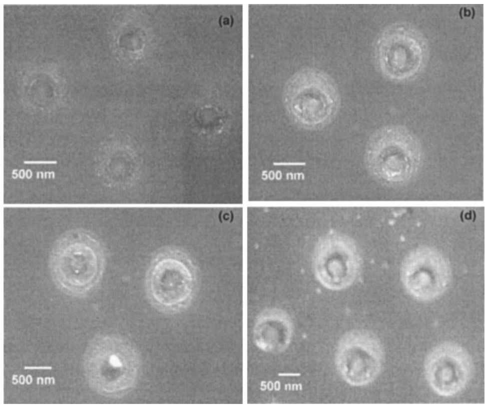

Fig. 6 SEM micrograph of 1.76 μm SiO_2 spheres irradiated by 532 nm laser at a fluence of (*a*) 50 mJ/cm^2, (*b*) 100 mJ/cm^2, (*c*) 200 mJ/cm^2, and (*d*) 300 mJ/cm^2

Figure 6 is a SEM micrograph of the silicon substrate after irradiation of the silica spheres at different laser fluences. At fluences of 200 and 300 mJ/cm^2 the diameter of the features obtained are ~1000 nm, matching the predictions perfectly. However at 50 mJ/cm^2 and 100 mJ/cm^2 the size of the zone shrinks, but not quite to the degree predicted numerically. It can also be observed that some of the features obtained are not perfectly circular as predicted. This is mainly because of the slight variation in the laser incident angle due to the beam delivery optics used in the experiment. A direct comparison of the feature diameters between the predicted and experimental results is presented in Fig. 7.

Both the extent of the surface modification and the damage threshold predicted are very close to what is observed experimentally. The experimental results show very little damage to the substrate when the particles are irradiated at a fluence of 50 mJ/cm^2, and by comparing with the modeling results it is evident that this energy is very close to the threshold below which no damage to silicon occurs. An additional simulation was conducted at a fluence of 40 mJ/cm^2, which returned a peak temperature below the melting point of silicon. This is a strong indication that the level of enhancement obtained from the electromagnetic field calculations is accurate.

Conclusion

Features created on a silicon substrate by the irradiation of microspheres on a silicon substrate surface with a pulsed laser have been presented. The features indicate an enhancement of the incident intensity in the near field due to the presence of the sphere. The near field has been calculated for a single sphere on a substrate using the results of Mie theory without relying on any simplifying approximations. The results of these calculations predict a strong enhancement directly under the sphere, which is assumed to be responsible for the substrate damage. A numerical model was built to simulate the heat transfer through the silicon substrate and track the phase change boundary through time. The dominant

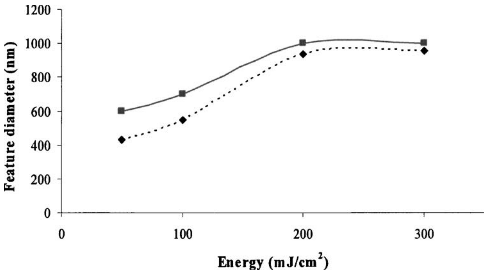

Fig. 7 Comparison of the predicted and experimental feature diameters for 1.76 μm SiO_2 spheres irradiated by 532 nm laser at different laser fluences

modes of heat transfer employed were radiation absorbed in the solid volume, radiation emitted from the surface, and conduction through the volume. The results of the modeling correlate well with the substrate damage characterized with a SEM. The threshold energy required to damage the substrate with the presence of microspheres matches the level of enhancement predicted by the Mie theory calculations.

Acknowledgments

The authors wish to acknowledge support from the National Science Foundation under Grant No. CTS-0243160, and from the University of Texas Advanced Manufacturing Center.

Nomenclature

A = sphere radius
A,B,C = constants describing laser wave form, Eq. (10)
E = electric field vector
H = magnetic field vector
I_o = incident laser intensity
L = enthalpy of fusion
R = surface reflectivity
S = Poynting vector
T = temperature, K
c = specific heat of substrate
eB = wave scattering coefficient, Eq. (1)
h = enthalpy of substrate material
k = thermal conductivity of substrate material
k_x = imaginary refractive index component
mB = wave scattering coefficient, Eq. (2)
n = real refractive index component
q = κa
q_{inc} = laser energy incident on substrate
q = volumetric energy generation rate, $\mathrm{W/m^3}$
r = radial coordinate
t = time
x,y,z = Cartesian coordinates in substrate
γ = absorption coefficient, Eq. (9)
ε = emissivity of liquid substrate surface, Eq. (13)
θ = spherical coordinate
κ = $2\pi/\lambda$
λ = wavelength
ρ = density of substrate material
ϕ = spherical coordinate

Subscripts

$cutoff$ = value at limit of summation, Eq. (8)
inc = incident
l = liquid phase
m = value at the melting point
x = in the x-direction

Superscripts

* = complex conjugate

References

[1] Dial, O., Cheng, C. C., and Scherer, A., 1998, “Fabrication of High-Density Nanostructures by Electron Beam Lithography,” J. Vac. Sci. Technol. B, **16**, pp. 3887–3890.

[2] Terris, B. D., Weller, D., Folks, L., Baglin, J. E. E., and Kellock, A. J., 2000, “Patterning Magnetic Films by Ion Beam Irradiation,” J. Appl. Phys., **87**, pp. 7004–7006.

[3] Halfpenny, D. R., and Kane, D. M., 1999, “A Quantitative Analysis of Single Pulse Ultraviolet Dry Laser Cleaning,” J. Appl. Phys., **86**, pp. 6641–6646.

[4] Lu, Y., Theppakuttai, S., and Chen, S. C., 2003, “Marangoni Effect in Nanosphere-Enhanced Laser Nanopatterning of Silicon,” Appl. Phys. Lett., **82**, pp. 4143–4145.

[5] Mie, G., 1908, “Beitrage zur Optik Truber Medien Speziell Kolloidaler Metallosungen,” Ann. Phys., **25**, pp. 377–445.

[6] Born, M., and Wolf, E., 1999, *Principles of Optics*, 7th ed., Cambridge University, Cambridge, England.

[7] Luk’yanchuck, B. S., Zheng, Y. W., and Lu, Y. F., 2000, “Laser Cleaning of Solid Surface: Optical Resonance and Near-Field Effects,” Proc. SPIE, **4065**, pp. 576–587.

[8] Abramowitz, M., and Stegun, I., 1965, *Handbook of Mathematical Functions*, Dover, New York.

[9] Lowan, A., et al., 1945, *Tables of Associated Legendre Functions*, Columbia University Press, New York.

[10] Xu, X., Grigoropoulos, C. P., and Russo, R. E., 1995, “Heat Transfer in Excimer Laser Melting of Thin Polysilicon Layers,” ASME J. Heat Transfer, **117**, pp. 708–715.

[11] Shamsundar, N., and Sparrow, E. M., 1975, “Analysis of Multidimensional Conduction Phase Change Via the Enthalpy Method,” ASME J. Heat Transfer, **97**, pp. 333–340.

[12] Minkowycz, W. J., and Sparrow, E. M., 1996, *Advances in Numerical Heat Transfer*, Taylor and Francis Group, Washington, DC, Vol. 1.

[13] Jellison, G. E., 1987, “Measurements of the Optical Properties of Liquid Silicon and Germanium using Nanosecond Time-Resolved Ellipsometry,” Appl. Phys. Lett., **51**, pp. 352–354.

[14] Hull, R., 1999, *Properties of Crystalline Silicon*, The Institute of Elec. Eng., London.

[15] Mosbacher, M., Chaoui, N., Siegel, J., Dobler, V., Solis, J., Boneberg, J., Afonso, C. N., and Leiderer, P., 1999, “A Comparison of ns and ps Steam Laser Cleaning of Si Surfaces,” Appl. Phys. A: Mater. Sci. Process., **69**, pp. S331–S334.

A Mixed-Mesh and New Angular Space Discretization Scheme of Discontinuous Finite Element Method for Three-Dimensional Radiative Transfer in Participating Media

X. Cui
Graduate Research Assistant

B. Q. Li[1]
Professor
Fellow ASME
e-mail: li@mme.wsu.edu

School of Mechanical and Materials Engineering,
Washington State University,
Pullman, WA 99164

This paper presents a discontinuous finite element method for the numerical solution of internal thermal radiation problems in three-dimensional (3D) geometries using an unstructured mesh of mixed elements. Mathematical formulation, numerical implementation, and computational details are given. The different domain discretization methods are presented, and a new angular space discretization is also given. Numerical examples are presented for 3D radiative transfer in emitting, absorbing, and scattering media. Computed results compare well with analytical solutions whenever available. The localized formulation intrinsic in discontinuous finite elements is considered particularly useful for computational radiation heat transfer in participating media.
[DOI: 10.1115/1.2039107]

Keywords: radiation, radiative, absorbing, emitting, scattering, medium, unstructured, discontinuous finite element, DFE, Galerkin

1 Introduction

Internal radiation occurs in many high-temperature thermal systems, such as utility boilers, melting furnaces, and gas turbine combustors. Because of its importance to thermal systems, radiative heat transfer has been subject to numerous studying. Many numerical techniques have been developed to obtain computational representations of the radiative intensity distribution in a variety of geometries encountered in engineering applications. Widely used numerical techniques for the solution of radiative transfer equations include the discrete ordinates, finite volume, ray tracing, and Monte Carlo methods. The principles governing the radiative transfer, as well as numerous analytical and numerical methods have been documented [1].

The discontinuous Galerkin finite element method of a boundary value problem, which was first introduced by Reed and Hill [2], follows a very similar procedure to that used for the conventional Galerkin finite element treatment. It starts with the weighted residuals integration, followed by the use of the Galerkin interpolation for the weighted functions. The essential difference between the conventional and the discontinuous finite element formulations lies in the treatment of the interelement boundary conditions. In the former, the interelement variables, such as fluxes and field variables, are strongly enforced. This enforcement requires the use of interpolation functions from the complete finite element space, although nonconfirming elements that passing patch tests are also possible for certain applications. In the latter, however, the field variables and their fluxes are only weakly imposed or a jump in these quantities is assumed to cross the interelement boundaries. It has been demonstrated that the discontinuous finite element formulation is particularly powerful for the convection-dominated problems, where the solutions develop sharp fronts, and also for the hyperbolic type of problems [3].

Since the radiative transport equation is a hyperbolic type equation, the discontinuous finite element method is a viable alternative for the solution of thermal engineering problems [4,5]. The discontinuous finite element (DFE) method combines the salient features of both the finite volume and finite element methods, and it has several important advantages over existing numerical methods for solving thermal radiation problems. First, the method is a local method, which means that a global matrix assembly, required in the conventional finite element solution, is no longer needed. Unlike the continuous method, it takes on multiple values at a nodal point having multiple values, each belonging to an element sharing the node, hence, the discontinuous method. Consequently, the DFE procedure involves element-by-element calculations only. Second, for the numerical solution of the radiative transfer equation (RTE) involving participating media, the conventional finite element method suffers from numerical instability, and artificial numerical diffusion is needed to obtain a stabilized solution [3]. Third, the finite volume method [6,7] uses zero-order interpolation over an element and is not easily extended to the higher-order approximations. The DFE method uses a higher-order interpolation and, thus, overcomes this intrinsic shortcoming. The DFE has become increasingly popular in treating problems with and without internal discontinuities. Its application to virtually all classes of fluid dynamics and heat transfer problems is discussed in [3].

In this paper, a discontinuous finite element computational methodology is presented for the solution of three-dimensional (3D) thermal radiation problems that involve absorbing, emitting, and scattering media. Although the formulations and computational procedures are based on a gray radiative property, they are also applicable for general spectral problems. Mathematical formulations and essential numerical details are given for 3D ele-

---

[1] Corresponding author.

Contributed by the Heat Transfer Division of ASME for publication in the JOURNAL OF HEAT TRANSFER. Manuscript received September 3, 2004; final manuscript received June 8, 2005. Review conducted by: Stefan Thynell. Paper presented at the 2004 ASME International Mechanical Engineering Congress and Exposition.

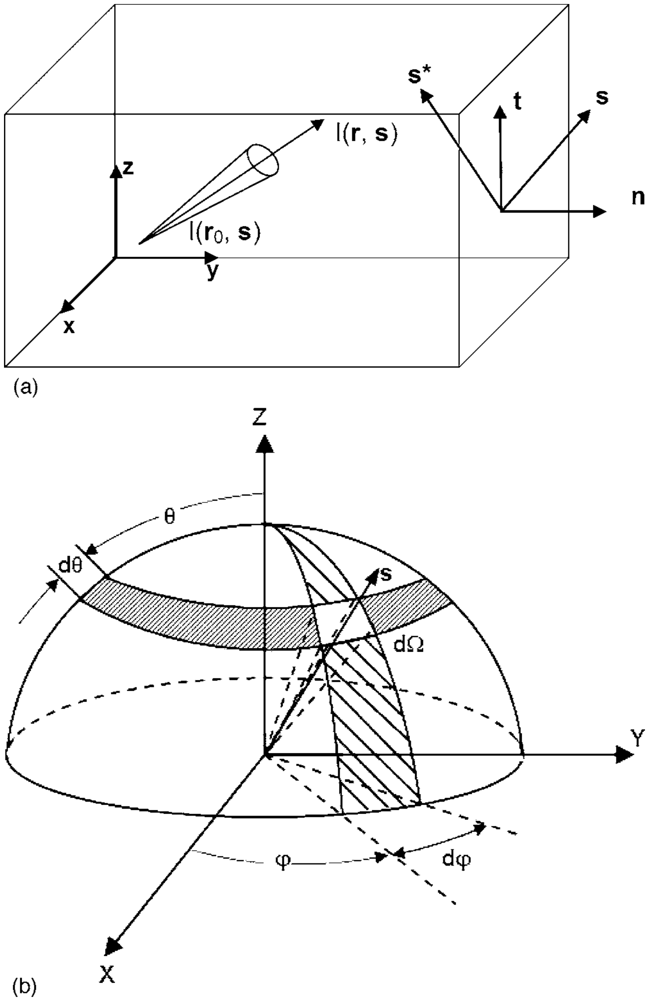

Fig. 1 Schematic representation of radiative transfer in a participating medium (*a*) and definition of the direction of radiation intensity and symmetry boundary condition. (*b*) angular space discretization.

ments of mixed types, including tetrahedra, hexahedra, and pentahedra. In order to compare the efficiency and accuracy of this method with other computational techniques used in radiative heat transfer problems, the use of well-known benchmarks of radiative heat transfer is preferred. Examples of various degrees of difficulty are given and compared to available solutions reported in the literature obtained by other numerical methods. Computations use both unstructured mesh and structured meshes.

2 Radiative Heat Transfer

The radiative transport equation describes the distribution of the radiant intensity $I(\mathbf{r},\mathbf{s})$, which is a function of both coordinates $\mathbf{r}$ and directions $\mathbf{s}$. The governing equation is derived based on the local balance of radiation energy, as shown in Fig. 1(*a*). In steady state, which is often the case for radiative heat transfer applications, the integral-differential equation for the distribution of radiation intensity is [1]

$$\frac{\partial I(\mathbf{r},\mathbf{s})}{\partial s} = -\beta(\mathbf{r})I(\mathbf{r},\mathbf{s}) + \kappa(\mathbf{r})I_b(\mathbf{r}) + \frac{\sigma_s(\mathbf{r})}{4\pi}\int_{4\pi} I(\mathbf{r},\mathbf{s}')\Phi(\mathbf{s},\mathbf{s}')d\Omega' \tag{1}$$

where $\beta(\mathbf{r})=\kappa(\mathbf{r})+\sigma_s(\mathbf{r})$ is the extinction coefficient, $\kappa(\mathbf{r})$ is the absorption coefficient, $\sigma_s(\mathbf{r})$ is the scattering coefficient, and $\Omega(\mathbf{s})$ is the control angle associated direction $\mathbf{s}$ ($\mathbf{s}=\sin\theta\cos\varphi\hat{i}+\sin\theta\sin\varphi\hat{j}+\cos\theta\hat{k}$), with $d\Omega=\sin\theta d\theta d\varphi$ being the differential solid angle, as shown in Fig. 1(*b*). The phase function satisfies the following condition:

$$\frac{1}{4\pi}\int_{4\pi}\Phi(\mathbf{s},\mathbf{s}')d\Omega' = 1 \tag{2}$$

where $\mathbf{s}'$ denotes the incident intensity from other directions. The equation is solved subject to the boundary condition on $I(\mathbf{r},\mathbf{s})$, which for an opaque diffuse surface takes the following form:

$$I(\mathbf{r},\mathbf{s}) = \varepsilon(\mathbf{r})I_b(\mathbf{r}) + \frac{1-\varepsilon(\mathbf{r})}{\pi}\int_{\mathbf{s}'\cdot\mathbf{n}>0} I(\mathbf{r},\mathbf{s}')\mathbf{s}'\cdot\mathbf{n}d\Omega' \tag{3}$$

Symmetry boundary conditions are also used in the computations and are given below [8]

$$\begin{cases} I(\mathbf{r},\mathbf{s}) = I(\mathbf{r},\mathbf{s}^*) \\ \mathbf{n}\cdot\mathbf{s} = -\mathbf{n}\cdot\mathbf{s}^* \\ \mathbf{s}\times\mathbf{s}^*\cdot\mathbf{n} = 0 \end{cases} \tag{4}$$

where the $\mathbf{s}^*$ is the symmetric radiation direction of $\mathbf{s}$ with respect to the tangent of the boundary, with both $\mathbf{s}$ and $\mathbf{s}^*$ lying on the plane of $\mathbf{t}$-$\mathbf{n}$ (see Fig. 1(*a*)).

Once the distribution of radiation intensity is known, various quantities of interest to internal radiation heat transfer can be calculated. Two of the most important quantities are the radiative heat fluxes and their divergence [1], which are determined by

$$q(\mathbf{r})\cdot\mathbf{n} = \int_{4\pi} I(\mathbf{r},\mathbf{s})\mathbf{s}\cdot\mathbf{n}d\Omega \tag{5}$$

$$\nabla\cdot q(\mathbf{r}) = \kappa\left[4\sigma T^4(\mathbf{r}) - \int_{4\pi} I(\mathbf{r},\mathbf{s})d\Omega\right] \tag{6}$$

3 Discontinuous Finite Element Formulation

We consider the discontinuous finite element formulation for radiative heat transfer problems governed by Eq. (1). As with other methods, the domain is first discretized into a collection of finite elements. In this study, an unstructured mixed mesh, consisting of tetrahedral, hexahedral, and pentahedral elements, is used for computational radiative heat transfer in 3D geometries filled with participating media. Here a wedge element in a mixed mesh is used for illustration of discontinuous finite element formulation and its computational procedures. Before integrating Eq. (1), the angular space is discretized into a specified collection of control angles. The method of discretization of angular space will be discussed later in this paper. Specifically, we consider the *i*th element in a 3D mesh, as shown in Fig. 2, and integrate Eq. (1) over the element and a control angle $\Delta\Omega_l$ with respect to a weighting function $v(\mathbf{r},\Omega)$,

$$\int_{\Delta\Omega_l}\int_{V_e} v(\mathbf{r},\Omega)\mathbf{s}\cdot\nabla I dV d\Omega = \int_{\Delta\Omega_l}\int_{V_e} v(\mathbf{r},\Omega)[-\beta(\mathbf{r})I(\mathbf{r},\mathbf{s}) + S(\mathbf{r},\mathbf{s})]dV d\Omega \tag{7}$$

where V_e is the volume of the element under consideration (i.e., the *i*th element), $\mathbf{r}=\mathrm{x}\hat{i}+\mathrm{y}\hat{j}+\mathrm{z}\hat{k}$ and $S(\mathbf{r},\mathbf{s})$ is the source function defined by

$$S(\mathbf{r},\mathbf{s}) = \kappa_b(\mathbf{r})I_b(\mathbf{r}) + \frac{\sigma_s(\mathbf{r})}{4\pi}\int_{4\pi} I(\mathbf{r},\mathbf{s}')\Phi(\mathbf{s},\mathbf{s}')d\Omega' \tag{8}$$

Integration by parts of Eq. (7) with respect to volume once gives

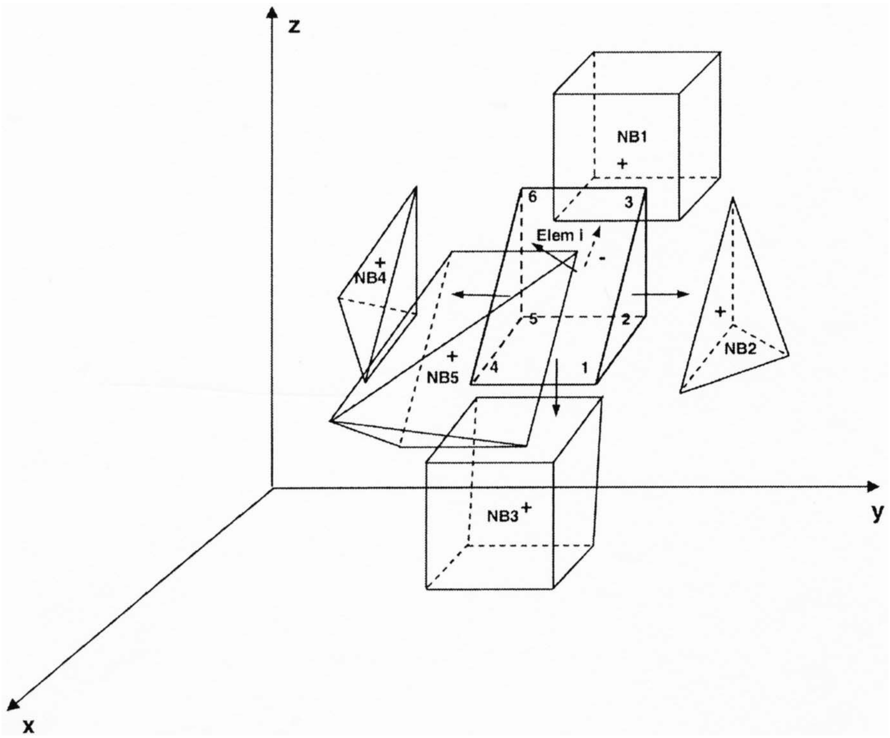

Fig. 2 Schematic illustration of arrangement of mixed elements

$$-\int_{\Delta\Omega_l}\int_{V_e} I\mathbf{s}\cdot\nabla v(\mathbf{r},\Omega)dVd\Omega+\int_{\Delta\Omega_l}\int_{\Gamma} v(\mathbf{r},\Omega)I^{+}\mathbf{n}\cdot\mathbf{s}d\Gamma d\Omega$$
$$=\int_{\Delta\Omega_l}\int_{V_e} v(\mathbf{r},\Omega)[-\beta(\mathbf{r})I(\mathbf{r},\mathbf{s})+S(\mathbf{r},\mathbf{s})]dVd\Omega \tag{9}$$

where I^{+} is used to represent the outside boundary value. Application of integration by parts once again to Eq. (9) yields the following expression:

$$\int_{\Delta\Omega_l}\int_{V_e} v(\mathbf{r},\Omega)\mathbf{s}\cdot\nabla I dVd\Omega+\int_{\Delta\Omega_l}\int_{\Gamma} v(\mathbf{r},\Omega)(I^{+}-I^{-})\mathbf{n}\cdot\mathbf{s}d\Omega d\Gamma$$
$$=\int_{\Delta\Omega_l}\int_{V_e} v(\mathbf{r},\Omega)\mathbf{s}\cdot\nabla I dVd\Omega+\int_{\Delta\Omega_l}\int_{\Gamma} v(\mathbf{r},\Omega)[I]\mathbf{n}\cdot\mathbf{s}d\Omega d\Gamma$$
$$=\int_{\Delta\Omega_l}\int_{V_e} v(\mathbf{r},\Omega)[-\beta(\mathbf{r})I(\mathbf{r},\mathbf{s})+S(\mathbf{r},\mathbf{s})]dVd\Omega \tag{10}$$

where $\mathbf{n}$ is the outward normal of the element boundary and $[I]$ is the jump term across the boundary of the element i. In the above two equations, use has been made of the divergence theorem,

$$\mathbf{s}\cdot\int_A \phi I\mathbf{n}dA-\mathbf{s}\cdot\int_V I\nabla\phi dV=\mathbf{s}\cdot\int_V \phi\nabla I dV \tag{11}$$

to convert the domain integral into the boundary integral. In Eq. (10), Γ is the boundary enclosing the volume V. Note that $\mathbf{s}$ is the unit vector of the direction of radiation intensity $I(\mathbf{r},\mathbf{s})$ and is independent of the volume.

In the conventional finite element formulation, the terms on the boundary disappear when they are combined with neighboring elements or $[I]=0$. In the discontinuous formulation, however, these terms do not cancel when elements are assembled. Instead, the following limiting values are used [9]:

$$I_j^{+}=\lim_{\mathbf{r}_j\to\Gamma^{+}} I(\mathbf{r}_j)\ \text{and}\ I_j^{-}=\lim_{\mathbf{r}_j\to\Gamma^{-}} I(\mathbf{r}_j) \tag{12}$$

where the subscripts "+" refer to being the values outside the element and those by "−" are inside the element, as shown in Fig. 2. This definition is slightly different from the 1D case, but the essential idea is the same [4]. The treatment of the above assumes that the two values I_j^{+} and I_j^{-} across the element boundaries are not the same, and these jumps are often denoted by

$$[I]_j=I_j^{+}-I_j^{-} \tag{13}$$

These jumps may also be modeled by generic numerical fluxes that are single-valued at the boundaries and are a function of field values across the interelement boundaries [9]. For the radiative transfer problems under consideration, the simplest and effective choice is the upwinding, which in the discontinuous finite element literature is some times referred to as the inflow boundary value

$$[I]_j=\begin{cases}[I]_j & \text{if } \mathbf{n}\cdot\mathbf{s}<0\\ 0 & \text{if } \mathbf{n}\cdot\mathbf{s}>0\end{cases} \tag{14}$$

It is important to note that the twice-integration procedure changes the sign of $\mathbf{s}\cdot\nabla I$ twice, which permits the use of the interpolation functions from the finite element broken space, so that the discontinuity across the element boundaries is imposed in the weak sense. This allows an easy incorporation of the upwinding scheme at the element boundaries, and this scheme is essential to ensure stability of the numerical solution to the RTE. This is in contrast to the continuous finite element, which enforces the continuity across the element boundaries, and an artificial diffusion term is often required for achieving a converged numerical solution [3].

We may now use the appropriate interpolation functions, which may be chosen from the finite element broken space that does not demand continuity across the interelement boundaries [3]. A natural choice of shape functions for the internal radiation applications is to take a step function for solid angles and a polynomial function for the spatial variation $v(\Omega,\mathbf{r})=\Psi(\Delta\Omega_l)\phi(\mathbf{r})$. Here $\Psi(\Delta\Omega_l)$

is the step function of the solid angle differential centered at Ω_l, which denotes that the radiation intensity in this control angle is a constant, although it actually varies with direction. In the control angle, the intensity is going to be calculated, $\Psi(\Delta\Omega_l)=1$. Since the step function is used for angular space, which means the discretization of the control angle is not continuous. In addition, the radiative intensity is also discontinuous over the spatial discretization. Therefore, false scattering and ray effects cannot be avoided. $\phi(\mathbf{r})$ is the shape function of spatial coordinates. Substituting this testing function into the integral expression and rearranging, one has the following relation:

$$\int_{\Delta\Omega_l} \mathbf{s}\cdot\int_{V_e}\phi\,\nabla I(\mathbf{r},\mathbf{s})dVd\Omega+\int_{\Delta\Omega_l}\int_{\Gamma}\phi[I](\mathbf{n}\cdot\mathbf{s})d\Gamma d\Omega$$

$$=\int_{\Delta\Omega_l}\int_{V_e}[-\beta(\mathbf{r})\phi I(\mathbf{r},\mathbf{s})+\phi S(\mathbf{r},\mathbf{s})]dVd\Omega \tag{15}$$

This is the final form of integral presentation of the radiative transfer equation. Before numerical implementation is considered, a few points are worth noting. First, if the jump condition $[I]$ is set to zero in Eq. (15), which means that the interelement continuity is enforced, then the conventional finite element formulation is recovered. Second, if a zeroth-order polynomial is chosen as the spatial interpolation function, then we have the common finite volume formulation. Thus, in this sense, the finite volume and finite element methods are two subsets of the discontinuous finite element formulation.

4 Numerical Implementation

Let us return our attention to the ith element and its neighbors, as shown in Fig. 2. For the sake of discussion, the interelement boundaries are plotted separately. There are two different types of nodal values. One is local values, which are defined at the nodal point in the element, and these values belong to the element. The other type is global values, which are the average values of local values of elements associated with the node. In other words, if there are several elements associated with the node, then there will be several nodal values of I, each belonging to an element. This is what is meant by discontinuity. The global values are used to calculate radiative flux and other quantities. In the conventional finite element formulation, the difference is forced to zero; whereas in the DFE formulation, the difference is minimized or continuity is imposed weakly. For a well-behaved function, the difference in the final solution is much smaller than the convergence criterion and the continuity is practically ensured. For the solution that has a discontinuity or a tendency to develop a discontinuity or sharp gradient, the DFE allows various numerical schemes, such as upwinding, to provide a much better approximation. The shape function ϕ can be chosen the same as the traditional finite element method. Since the discontinuity is allowed across the element boundaries, the common geometric node does not have the same field variable value. This is an essential difference between the conventional and discontinuous finite element formulations.

The radiation intensity within a wedge element is interpolated by

$$I(x,y,z;\mathbf{s})=\sum_{m=1}^{NP}\phi_m I_m(\mathbf{s}) \tag{16}$$

where NP is the number of nodes of the element i, and ϕ_m is the value of shape function ϕ_m at node m of the element. By using standard finite element method procedures and substituting the above expression into the general formulation Eq. (15) for every node of elements, we have the following vector form equation:

$$\int_{\Delta\Omega_l}\mathbf{s}d\Omega\cdot\int_{V_e}\begin{bmatrix}\phi_1\\ \phi_2\\ \cdots\\ \phi_{NP}\end{bmatrix}[\nabla\phi_1,\cdots,\nabla\phi_{NP}]\begin{bmatrix}I_1\\ I_2\\ \cdots\\ I_{NP}\end{bmatrix}dV$$

$$+\sum_{j=1}^{Nd}\int_{\Delta\Omega_l}(\mathbf{n}_j\cdot\mathbf{s})d\Omega\int_{\Gamma}\begin{bmatrix}\phi_1\\ \phi_2\\ \cdots\\ \phi_{NP}\end{bmatrix}[\phi_1,\cdots,\phi_{NP}]\begin{bmatrix}[I]_1\\ [I]_2\\ \cdots\\ [I]_{NP}\end{bmatrix}d\Gamma$$

$$=\int_{\Delta\Omega_l}d\Omega\int_{V_e}\left\{-\beta(\mathbf{r})\begin{bmatrix}\phi_1\\ \phi_2\\ \cdots\\ \phi_{NP}\end{bmatrix}[\phi_1,\cdots,\phi_{NP}]\begin{bmatrix}I_1\\ I_2\\ \cdots\\ I_{NP}\end{bmatrix}\right.$$

$$\left.+\begin{bmatrix}\phi_1\\ \phi_2\\ \cdots\\ \phi_{NP}\end{bmatrix}S(\mathbf{r},\mathbf{s})\right\}dV \tag{17}$$

with Nd being the number of boundaries associated with the ith element. The integration over the control angle in Eq. (17) can be carried out analytically,

$$\overline{\mathbf{s}}=\int_{\Delta\Omega_l}\mathbf{s}d\Omega=[0.5(\theta_2-\theta_1)-0.25(\sin 2\theta_2-\sin 2\theta_1)]$$

$$\times[(\sin\varphi_2-\sin\varphi_1)\hat{i}-(\cos\varphi_2-\cos\varphi_1)\hat{j}]$$

$$-0.25(\cos 2\theta_2-\cos 2\theta_1)(\varphi_2-\varphi_1)\hat{k} \tag{18}$$

For convenience, from here on $\int_{\Delta\Omega_l}(\mathbf{n}_j\cdot\mathbf{s})d\Omega$ is denoted by NDS_{ij}, with subscript i referring to the ith element in Eq. (17) and j the jth side of the element. In the DFE treatment, the jump terms have to be selected depending on the sign of $\mathbf{n}_j\cdot\mathbf{s}$. One treatment that works effectively with linear elements is the upwinding scheme. By this scheme, one has

$$\mathrm{NDS}_{ij}\begin{bmatrix}[I]_1\\ [I]_2\\ \cdots\\ [I]_{NP}\end{bmatrix}=-(-\mathrm{NDS}_{ij})\begin{bmatrix}[I]_1\\ [I]_2\\ \cdots\\ [I]_{NP}\end{bmatrix}$$

$$=-\max(0,-\mathrm{NDS}_{ij})\left\{\begin{bmatrix}I_1\\ I_2\\ \cdots\\ I_{NP}\end{bmatrix}_e-\begin{bmatrix}I_1\\ I_2\\ \cdots\\ I_{NP}\end{bmatrix}_{NBj}\right\} \tag{19}$$

where $I_{k,NBj}$ denotes the kth node of neighbor element, which shares the boundary j of the element i. Note that $(I_j^+)_i=(I_j)_{NB}$ by definition (see Fig. 2).

Collecting these terms, Eq. (15) for the element i can be written in terms of the following matrix form as the standard finite element procedures:

$$[K]\{I\}=\{f\} \tag{20}$$

where the expressions for the matrix elements are summarized as follows:

$$k_{ij}=\int_{V_e}\phi_i\,\nabla\,\phi_j dV\cdot\int_{\Delta\Omega_l}\mathbf{s}d\Omega+\beta\int_{\Delta V}\phi_i\phi_j dV\int_{\Delta\Omega_l}d\Omega$$

$$+\sum_{k=1}^{Nd}\max\left(0,-\int_{\Delta\Omega_l}\mathbf{s}\cdot\mathbf{n}_k d\Omega\right)\int_{\Gamma_k}\phi_i\phi_j d\Gamma \tag{21}$$

$$f_i = \int_{V_e} \phi_i S dV \int_{\Delta\Omega_l} d\Omega + \sum_{k=1}^{Nd} \max\left(0, -\int_{\Delta\Omega_l} \mathbf{s}\cdot\mathbf{n}_k d\Omega\right)\int_{\Gamma_k} \phi_i \phi_j I_{NB} d\Gamma \qquad (22)$$

Although derived for a wedge element, Eqs. (21) and (22) are generally applicable to any type of elements. For tetrahedral linear elements, integration can be carried out analytically. For other elements, numerical integration may be required.

The boundary condition is imposed for a gray diffuse boundary

$$I^{+}(\mathbf{r},\mathbf{s}_l) = \varepsilon(\mathbf{r}) I_b(\mathbf{r}) + \frac{1-\varepsilon(\mathbf{r})}{\pi} \sum_{j=0,\mathbf{s}'_j\cdot\mathbf{n}>0}^{N_\Omega} I^{-}(\mathbf{r},\mathbf{s}'_j)|\mathbf{s}'_j\cdot\mathbf{n}|\Delta\Omega'_j \qquad (23)$$

and the following equation is for the symmetry boundary condition:

$$I^{+}(\mathbf{r},\mathbf{s}_l) = I^{-}(\mathbf{r},\mathbf{s}_l^{*}) \qquad (24)$$

Here $\mathbf{s}^*$ is the symmetric direction of $\mathbf{s}$ respected to the boundary and can be calculated by Eq. (4).

The computational procedure using the discontinuous finite element method may be described as follows. With Eq. (20), the calculation for the ith element starts with selecting a direction and then continues element by element until the entire domain and all directions are covered. Because of the boundary conditions, an iterative procedure is required to achieve convergence. The successive substitution method seems to work well for this type of problems. With the definition of incident radiation,

$$G(r) = \int_{4\pi} I(\mathbf{r},\mathbf{s}) d\Omega = \sum_{i=1}^{N_\Omega} I(\mathbf{r},\mathbf{s})\Delta\Omega_i \qquad (25)$$

the following convergence criterion may be used:

$$\max\left(\left| \frac{G^{n+1}(r) - G^{n}(r)}{G^{n}(r)} \right| \right) \leqslant 1.0 \times 10^{-4} \qquad (26)$$

where n is the iteration number. After all elements are calculated, the intensity at a node is averaged within the elements around the node, and then the convergence is checked. The intensity values are updated, and the iterative process continues until convergence is achieved. Then, radiative heat flux and its divergence are obtained by Eqs. (5) and (6).

5 New Angular Space Discretization Scheme

In the literature on radiative heat transport problems, the angular space is discretized uniformly over the two spherical angles defining the solid angle. In this scheme, the azimuthal direction is partitioned into N_ϕ angles, and the polar direction is partitioned into N_θ angles evenly, therefore, the total control angles are $N_\theta \times N_\phi$. Although reasonable, this discretization scheme does not lead to a uniform distribution of the solid angles because the solid angle is a function of cos θ not θ. In the DFE method presented in this paper, a uniform discretization of cos θ is used instead, which gives a uniform distribution of the solid angle. Numerical tests show that the cos θ-based discretization gives much better results with a relatively coarse angular mesh; the difference between the two angular discretization schemes become smaller as the number of angular elements increases.

6 Results and Discussion

In this section, the discontinuous finite element algorithm is applied to solve problems of thermal radiation heat transfer in participating media. Calculations may use either structured or unstructured meshes, though the results computed with the latter are presented below. Gray properties are assumed for all the cases below; unless otherwise indicated, all the data are nondimensionalized.

Case 1: Radiation in a Cube. The first case considers a cube enclosure filled with a purely emitting and absorbing medium. The cube has a length $L=1$. The control angles used in this problem are 4×8; that is, the angular space is divided into four in the azimuthal direction (θ) and eight in the polar direction (φ). The temperature of medium is set at $T_{\text{ref}}=$constant, and all the boundaries of enclosure are black ($\varepsilon=1$) and cold ($T_w=0$). The cube is discretized into three different types of elements, as shown in Fig. 3(a) (the cube is discretized into 3072 tetrahedral elements, 1024 wedge elements, and 512 hexahedral elements or 736 mixed elements, including hexahedral and wedge elements.

The radiative heat flux along the centerline on the top surface ($y/L=0.5$, $z/L=1.0$) can be obtained by using three different types of elements, respectively, as shown in Fig. 3(b). In Fig. 3(b), the radiative heat flux is calculated with $\kappa=0.1$ and $\kappa=1.0$, and the results of three different types of elements agree very well with analytical solutions.

In order to show the accuracy of the DFE method, we compared the results of DFE method and finite volume method, which is one of the most widely used methods. For comparison, the same mesh with 512 hexhadral elements and same angular space discretization (4×8) are used. The radiative heat flux along the centerline ($y=0.5$, $z=1.0$) is plotted in Fig. 3(c) $\kappa=10.0$. Examination of the results shows that the DFE gives a better accuracy than the finite method when the same discretizations are used. This is also observed for other cases with different κ values.

For convenience the radiative heat flux in this paper is nondimensionalized as

$$q^* = \frac{q_r}{\sigma T_{\text{ref}}^4} \qquad (27)$$

Numerical experiments show that more accurate results are obtained with a finer discretization, as expected. For the same number of elements, the DFE method in the present implementation requires roughly the same CPU time and the same number of iterations as the finite volume method. If numerical integration is used in the element calculations, the CPU time is expected to increase. However, our experiences further show that for the same accuracy, the DFE requires fewer elements, which would actually result in a shorter CPU time.

Case 2: Radiation in a 3D Tetrahedron. A 3D tetrahedral enclosure formed by the vertices (0, 0, 0), (1, 0, 0), (0.5, 0.866, 0.0), and (0.5, 0.218, 0.817) is chosen, and the enclosure is filled with a purely emitting and absorbing medium. Again, the enclosure wall is cold and black. The temperature of the medium is constant $T_{\text{ref}}=100$, and the absorption coefficient $\kappa=1.0$. The domain is discretized into 1062 unstructured tetrahedra (see Fig. 4(a)). The fluxes q^* along the line joining the point (0.75, 0.433, 0) and (0.5, 0.218, 0.817), which can represent the characteristic of radiative heat flux on the boundary, is calculated by the DFE method as shown in Fig. 4(b), where q^* denotes the nondimensionalized boundary radiative heat flux in the outward normal direction of the boundary. The result is in good agreement with the ray-tracing method [10].

Case 3: New Angular Space Discretization Scheme. The geometry and conditions of case 1 is used again for comparison purposes. In case 1, we used the traditional angular space discretization scheme, which evenly divides azimuthal and polar angles. Here, a new angular space scheme will be compared to the traditional scheme. As described in a previous section, the angular space can be divided evenly based on the value of cos θ instead of θ. In order to differ from the conventional scheme, the new scheme can be represented by “uniform scheme,” and the conventional scheme can be named as “equivalent scheme.” The solid

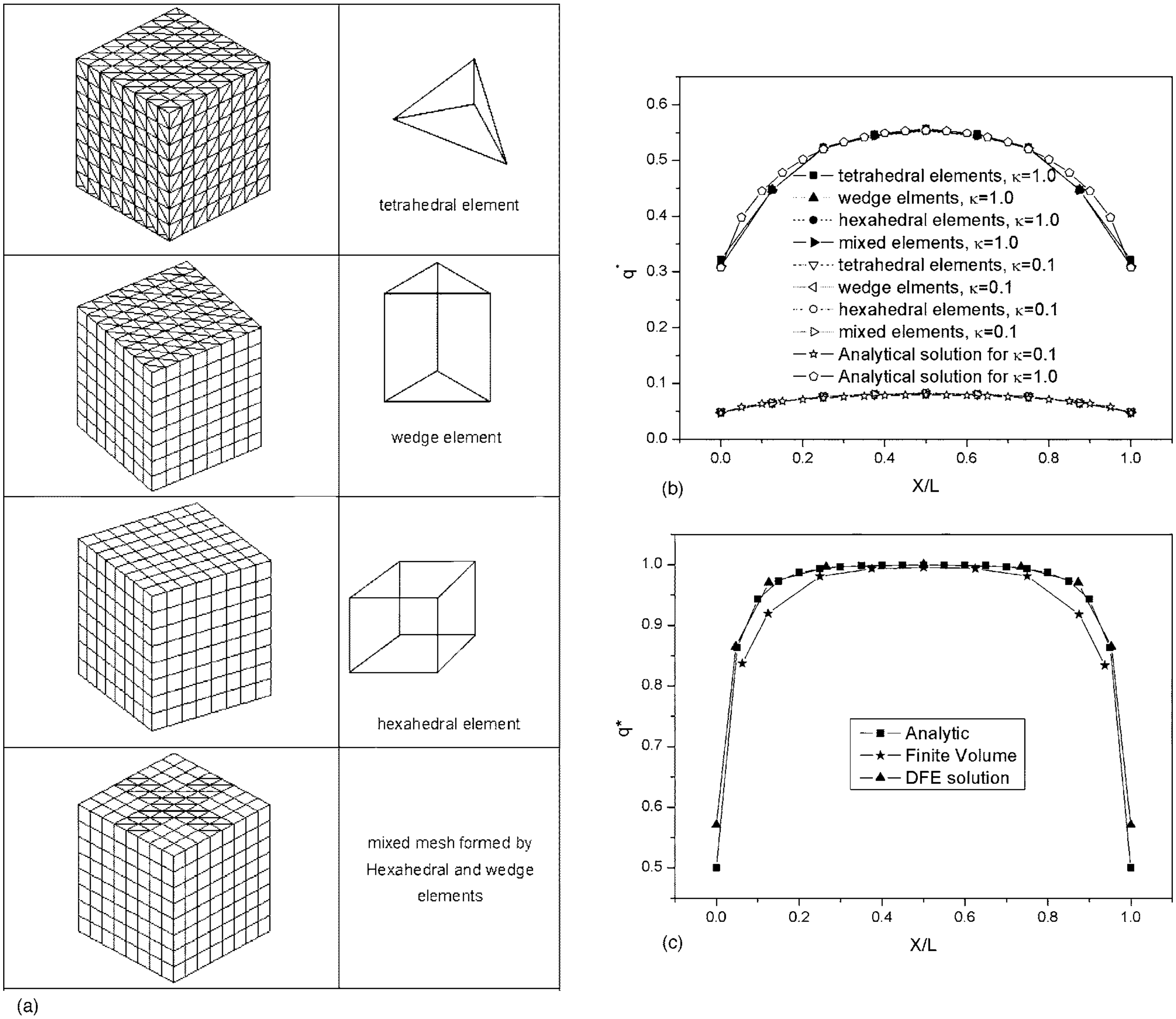

Fig. 3 3D discretization and calculated radiative heat flux q^* along the middle line of top surface $y/L=0.5$, and $z/L=1.0$. (*a*) The cube is discretized with 3072 tetrahedral elements or 1024 wedge elements or 512 hexahedral elements or 736 elements of mixed hexahedra and pentahedra. (*b*) Comparison of radiative heat fluxes calculated using different meshes shown in (*a*). The absorption coefficient varies from $\kappa=0.1$ nd $\kappa=1.0$. (*c*) Comparison of the DFE and the finite volume methods for the solution of RTE for $\kappa=10$.

angles distributions along the θ direction in two different angular space discretizations are shown in Fig. 5(*a*). From the figure, it clearly shows that the solid angle is distributed uniformly in the new scheme and varies in the traditional scheme. Without any doubt, the distribution of solid angles will affect the accuracy of calculation. The reason for this is in the process of derivation of the DFE method; namely, the control equation has to be integrated over control angles. In addition, the radiative intensity in the control angle is considered as constant in the DFE method, which is just an approximation of the actual problem. Based on the two different schemes, the boundary radiative heat flux of the cube is calculated at $\theta\times\varphi=4\times8$ and $\theta\times\varphi=8\times12$, as shown in Fig. 5(*b*). Compared to the analytical solution, the uniform scheme gives better results for these two conditions, although at $\theta\times\varphi=8\times12$, the discrepancy between numerical results and analytical solution in both schemes is very small.

Case 4: Scattering in 3D Geometry. When small particles are suspended within the medium, it scatters the radiation from a given direction into all other directions. Radiation in other directions may also be scattered into the direction under consideration. The scattering effect is included as part of the source term for radiation transfer (i.e, the second term on the right-hand side of Eq. (8)). Scattering effects are usually classified into two categories, isotropic scattering and anisotropic scattering. The former is a theoretical model, which scatters energy into all other directions with the same energy distribution, whereas the latter scatters radiation energy to different directions with varying energy distributions, but is much closer to the real problem.

Anisotropic scattering is more complex and certainly needs more computing time because the scattering function is directionally dependent and all directions need to be calculated. In this paper, there are two different models being used for anisotropic scattering functions [11], forward scattering and backward scattering. These scattering functions may be described by the following generic expression:

$$\Phi(\mathbf{s},\mathbf{s}') = \sum_{j=1}^{Ns} c_j P_j(\cos\psi) \tag{28}$$

where N_s is the number of terms of the series, Ψ is calculated by

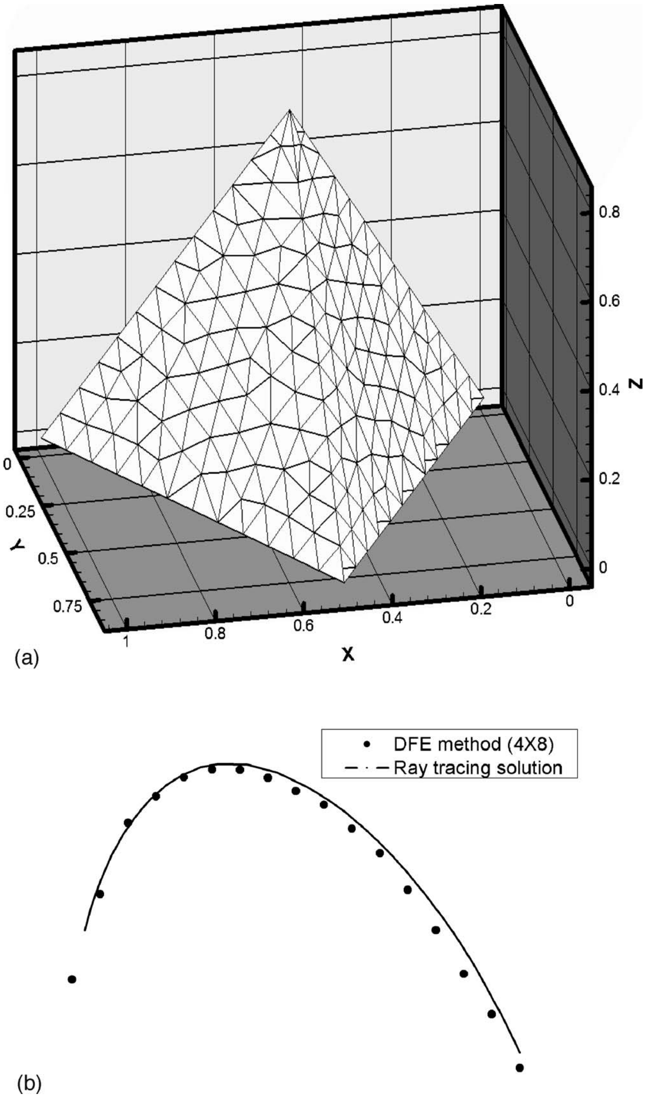

Fig. 4 Unstructured tetrahedral mesh and calculated q^* in a tetrahedral cavity filled with an absorbing and emitting medium. (*a*) Unstructured mesh consisting of 1062 tetrahedral elements. (*b*) Comparison of radiative heat fluxes calculated by the DFE and ray-tracing methods.

$$\psi = \cos\theta\cos\theta' + (1-\cos^2\theta)(1-\cos^2\theta')^{1/2}\cos(\varphi'-\varphi) \tag{29}$$

and P_j is the Legendre function.

For the calculations given here, the values of coefficient c_j in Eq. (29) are taken from the work of Kim and Lee [11], who gave the coefficients of the polynomial for different models by slightly modifying Mie coefficients [12] and the work of Özisik [13] and Siegel and Howell [14]. Based on these coefficients, the four different scattering functions are depicted in Fig. 6(*a*), where F_i ($i=1,2$) denotes the forward scattering functions and B_i ($i=1,2$) the backward scattering functions.

Here we consider again the same problem as in case 1, except the absorption coefficient and extinction coefficient are changed. For different scattering phase functions, Fig. 5(*b*) shows the distribution of q^* along x/L at the line $y/L=0.5$ and $z/L=1.0$ on the top surface of the cube with scattering albedo $\omega=\sigma/\beta=0.5$ and $\beta=1.0$, and Fig. 6(*c*) shows the q^* distributions along the same line as Fig. 6(*b*) except scattering albedo $\omega=\sigma/\beta=0.5$ and $\beta=2.0\ \mathrm{m}^{-1}$. It is clear that for different phase functions the radiative heat flux distributions are different.

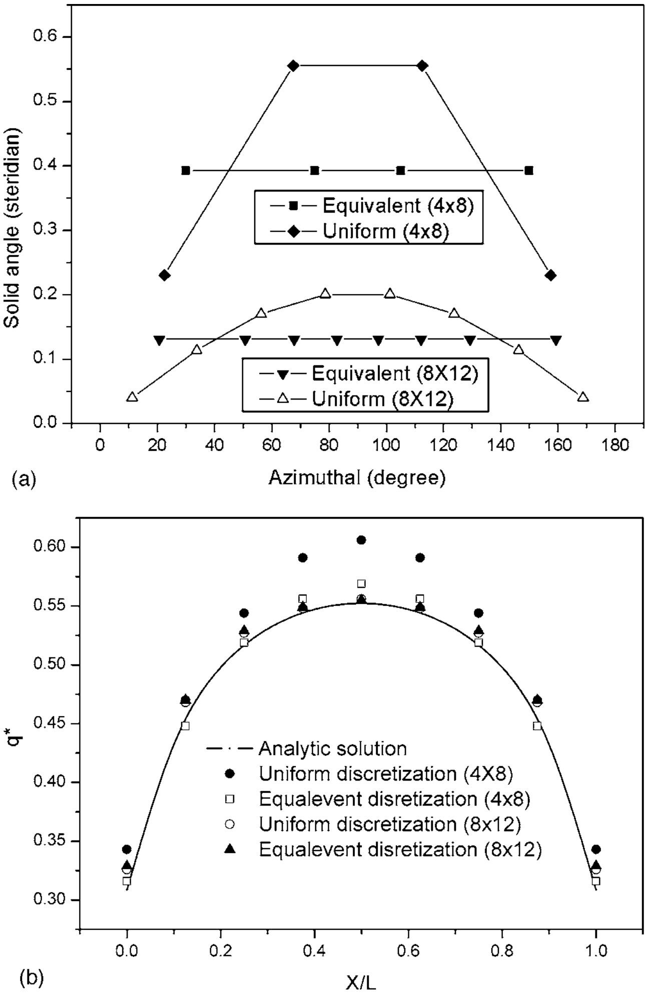

Fig. 5 (*a*) Solid angle distributions of two different angular schemes: the equivalent scheme and the uniform scheme. (*b*) The boundary heat flux along X/L at $Z/L=0.5$, $Y/L=1.0$. The absorption coefficient of this case is $\kappa=1.0$ and without scattering.

One set of results for isotropic scattering is given in Fig. 7. The same unstructured mesh as in case 1 is used for these computations, where the scattering albedo is $\omega=\sigma/\beta=0.5$ and $\beta=1.0$. The present calculations are also compared to those obtained using the Monte Carlo and finite volume methods. The comparison between the DFE results and Monte Carlo results reported [15] is gratifying for all these cases, suggesting that the DFE method is useful for radiative heat transfer calculations. In this case, comparison of CPU time between the DFE and finite volume methods shows that the DFE method does not have advantages if it uses the same number of elements and control angles.

7 Concluding Remarks

This paper has presented a mixed mesh and a new angular space discretization in discontinuous finite element formulation for fully three-dimensional radiative heat transfer problems involving an absorbing, emitting, and scattering medium. Mathematical formulations and essential numerical details using the discontinuous finite element method for internal radiation heat transfer calculations are given for 3D tetrahedral linear elements. Extension of these calculations using higher-order elements can be readily incorporated through numerical integration. Computations using both unstructured and structured meshes consisting of

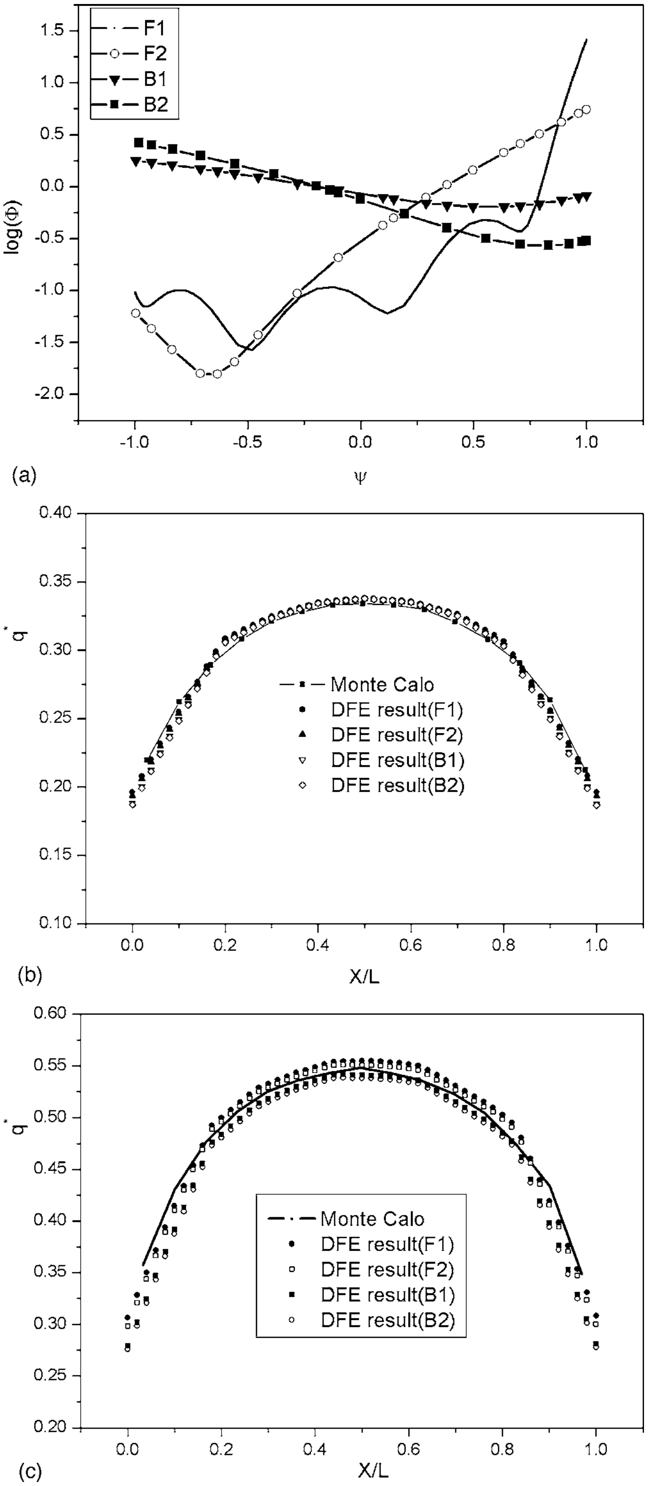

Fig. 6 Radiative transfer in a cubic cavity filled with an absorbing, emitting, and scattering medium. (*a*) Different scattering functions. (*b*, *c*) Radiative heat flux q^* distributions for different anisotropic scattering phase functions calculated by the DFE method; here the Monte Carlo solution for isotropic scattering is plotted as a reference. The q^* distribution is along the middle line ($y/L=0.5$ and $z/L=1.0$) at the top surface of the cube. The extinction coefficients are equal to 1.0 (*b*) and 2.0 (*c*).

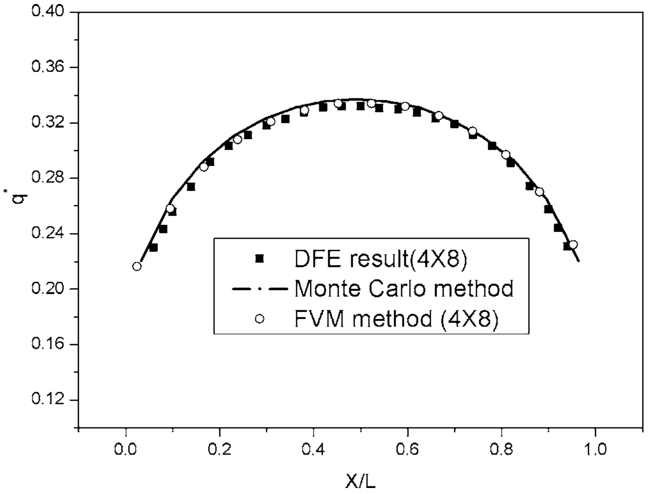

Fig. 7 Comparison of heat flux distributions calculated by the DFE, finite volume, and Monte Carlo methods for an isotropic medium. The radiative heat flux distribution is along the middle line ($y/L=0.5$ and $z/L=1.0$) at the top surface of the cube. The scattering coefficient is 0.5.

a single type and mixed types of elements were given, and the error is <1% at the given conditions. Examples include both nonscattering and scattering cases. The computed results obtained by using the discontinuous finite element method compared well with analytical solutions whenever available or those reported in the references. The results also show that the DFE gives a better accuracy than the finite volume method, as the former allows a higher-order approximation. Although computational studies used only linear elements, higher-order approximations can be readily incorporated.

Acknowledgment

The authors gratefully acknowledge the support of this work by the Air Force Office of Scientific Research, subcontracted through VLOC, Inc. (Grant No. VAN00138704451) and by NASA (Grant No. NAG8-1693). The assistance of Dr. Xin Ai with the unstructured mesh generation is also acknowledged.

Nomenclature

I = intensity
L = characteristic length of geometry
$\mathbf{n}$ = outward normal of boundary or wall
NB = neighboring element
Nd = number of boundaries of element
NP = number of nodes of element
N_Ω = total number of control angles
q = radiative heat flux
$\mathbf{r}$ = position vector
$\mathbf{s},\mathbf{s}'$ = direction vectors
S = source function
$\mathbf{t}$ = vector
V = volume

Greek

β = extinction coefficient
ε = emissivity
ϕ = shape function
Φ = scattering phase function
Γ = boundary
φ = azimuthal angle
κ = absorption coefficient
θ = polar angle
σ = Stefan-Boltzmann constant
σ_s = scattering coefficient
ω = scattering albedo
Ω,Ω' = control angles

$\Delta\Omega$ = solid angle

Subscripts and Superscripts

b = blackbody
e = element
l = the lth direction of radiation
* = symmetric vector

References

[1] Modest, M. F., 1993, *Radiative Heat Transfer*. McGraw-Hill, New York.
[2] Reed, W. H., and Hill, T. R., 1973, "Triangular Mesh Methods for the Neutron Transport Equation," Tech. Report LA-UR-73-479, Los Alamos Scientific Laboratory.
[3] Li, B. Q., 2005, *Discontinuous Finite Elements in Fluid Dynamics and Heat Transfer*, Springer-Verlag, London.
[4] Cui, X., and Li, B. Q., 2004, "A Discontinuous Finite Element Formulation for Internal Radiation Problems," Numer. Heat Transfer, Part B, **46**, pp. 223–242.
[5] Ai, X., and Li, B. Q., 2004, "A Discontinuous Finite Element Method for Hyperbolic Thermal Wave Problems," Eng. Comput., **21**, pp. 577–597.
[6] Chai, J. C., and Patankar, S. V., 2000, "Finite Volume Method For Radiation Heat Transfer," *Advances in Numerical Heat Transfer*, W. J. Minkowycz, and E. M. Sparrow, eds., Taylor & Francis, New York, Vol. 2, Chap. 4.
[7] Raithby, G. D., and Chui, E. H., 1990, "A Finite-Volume Method for Predicting a Radiant Heat Transfer in Enclosure with Participating Media," ASME J. Heat Transfer, **112**, pp. 415–423.
[8] Moder, J. P., Kumar, G. N., and Chai, J. C., 2000, "An Unstructured-Grid Radiative Heat Transfer Module for the National Combustion Code," 38th Aerospace Sciences Meeting & Exhibit, Reno, NV.
[9] Oden, J. T., Babuka, I., and Baumann, C., 1998, "A Discontinuous hp Finite Element Method for Diffusion Problems," J. Comput. Phys., **146**, pp. 491–519.
[10] Murthy, J. Y., and Mathur, S. R., 1998, "Finite Volume Method for Radiative Heat Transfer Using Unstructured Meshes," J. Thermophys. Heat Transfer, **12**, pp. 313–321.
[11] Kim, T. K., and Lee, H., 1998, "Effect of Anisotropic Scattering on Radiative Heat Transfer in Two-Dimensional Rectangular Enclosures," Int. J. Heat Mass Transfer, **31**, pp. 1711–1721.
[12] Wiscombe, W. J., 1980, "Improved Mie Scattering Algorithms," Appl. Opt., **19**, pp. 1505–1509.
[13] Özisik, M. N., 1973, *Radiative Transfer*, Wiley-Interscience, New York.
[14] Siegel, R., and Howell, J. R., 1992, *Thermal Radiation Heat Transfer*, 3rd Edition, Hemisphere, Washington, DC.
[15] Kim, S. H., and Huh, K. Y., 2000, "A New Angular Discretization Scheme of the Finite Volume Method for 3-D Radiative Heat Transfer in Absorbing, Emitting and Anisotropically Scattering Medium," Int. J. Heat Mass Transfer, **43**, pp. 1233–1242.

Multiphase Transport Phenomena in the Diffusion Zone of a PEM Fuel Cell

S. M. Senn

D. Poulikakos[1]
e-mail: dimos.poulikakos@ethz.ch

Department of Mechanical Engineering,
Laboratory of Thermodynamics in Emerging Technologies,
Swiss Federal Institute of Technology
(ETH Zurich),
CH-8092 Zurich, Switzerland

In this paper, a thorough model for the porous diffusion layer of a polymer electrolyte fuel cell (PEFC) is presented that accounts for multicomponent species diffusion, transport and formation of liquid water, heat transfer, and electronic current transfer. The governing equations are written in nondimensional form to generalize the results. The set of partial differential equations is solved based on the finite volume method. The effect of downscaling of channel width, current collector rib width, and diffusion layer thickness on the performance of polymer electrolyte membrane (PEM) fuel cells is systematically investigated, and optimum geometric length ratios (i.e., optimum diffusion layer thicknesses, optimum channel, and rib widths) are identified at decreasing length scales. A performance number is introduced to quantify losses attributed to mass transfer, the presence of liquid water, charge transfer, and heat transfer. Based on this model it is found that microchannels (e.g., as part of a tree network channel system in a double-staircase PEM fuel cell) together with diffusion layers that are thinner than conventional layers can provide substantially improved current densities compared to conventional channels with diameters on the order of 1 mm, since the transport processes occur at reduced length scales. Possible performance improvements of 29, 53, and 96% are reported. [DOI: 10.1115/1.2039108]

Keywords: fuel cell, two-phase, liquid water, microchannel, downscaling, heat transfer

1 Introduction

Thermodynamic optimization of finite-size components and finite-time processes subject to physical constraints is currently emerging as a challenging field in polymer electrolyte membrane (PEM) fuel cell research [1–3]. The method combines modeling and optimization of real devices subject to physical constraints that actually cause the thermodynamic imperfection and irreversible operation of the device [4–6].

Besides diffusion mass transfer, other transport phenomena can be important in the diffusion layer, such as transport of liquid water, electronic current transfer, and heat transfer. Multicomponent diffusion in the diffusion and catalyst layers of PEM fuel cells was investigated by Kulikovsky [7] and Kulikovsky et al. [8,9], considering two different electric potential fields governing the transport of electrons and protons. These two-dimensional models were extended to a quasi-three-dimensional approach [10] taking further into account liquid water in the membrane phase. The presence of liquid water in voids and in the porous diffusion layer was neglected and isothermal conditions were assumed in all their studies [7–10]. Yi and Van Nguyen investigated mass transfer in the porous electrodes of a PEM fuel cell using the interdigitated gas distributor [11]. Natarajan and Van Nguyen [12] and He et al. [13] introduced two-dimensional models, and Natarajan and Van Nguyen [14] also introduced a three-dimensional model for the cathode of a PEM fuel cell, taking into account multicomponent diffusion and transport of liquid water. In these models [11–14], isothermal and electronic current transfer in the diffusion layer is not considered; that is, infinite thermal and electronic conductivities are assumed. Two-phase flow and transport under isothermal conditions along the cathode channel and the cathode diffusion layer were studied in two dimensions [15,16], neglecting gradients in the direction parallel to the membrane underneath the current collector ribs. A three-dimensional, nonisothermal, two-phase flow model was presented by Berning and Djilali [17]. However, one single geometric configuration is considered in their work, and the effect of channel width, rib width, and diffusion layer thickness on the performance of PEM fuel cells is not investigated. A one-dimensional study on nonisothermal two-phase transport in the diffusion layer of a PEM fuel cell was presented by Nam and Kaviany [18]. Another detailed, isothermal, one-dimensional analysis of two-phase transport in the anode and cathode was presented by Weber et al. [19], taking further into account transport within the membrane.

In this paper, a model for the porous diffusion layers of a PEM fuel cell is introduced in which all the governing macroscopic transport phenomena, including multicomponent diffusion, transport of liquid water, electronic current transfer, and heat transfer, are considered at the same time. Although the model can also be used to investigate the transport phenomena in the anode diffusion layer, it is only applied to the cathode diffusion layer in this study. The governing equations are written in nondimensional form to generalize the results. The model is solved in two dimensions, neglecting gradients in the streamwise direction along the channel. The effect of downscaling of channel width, current collector rib width, and diffusion layer thickness on the performance of PEM fuel cells is systematically investigated, and optimum length ratios (i.e., optimum diffusion layer thickness, optimum channel and rib width) are identified. A performance number is introduced to quantify losses in the diffusion layer attributed to mass transfer, the presence of liquid water, charge transfer, and heat transfer.

2 Mathematical Formulation

A nonisothermal, multicomponent, two-phase diffusion layer model is presented in this section. A two-dimensional rectangular computational domain including the porous cathode diffusion layer is considered, as shown in Fig. 1. Isotropic porous media are investigated in this study. The catalyst layer is assumed to be very

---

[1] Corresponding author.

Contributed by the Heat Transfer Division of ASME for publication in the JOURNAL OF HEAT TRANSFER. Manuscript received November 23, 2004; final manuscript received June 20, 2005. Review conducted by: Jacob Chung.

thin and, therefore, is treated as a boundary condition. The *y* coordinate indicates the direction parallel to the membrane where *z* indicates the direction perpendicular to the membrane. In fuel cell channels, the Peclet number (defined based on the channel length) is usually very large, and concentration gradients in the diffusion layer along the flow direction *w* (i.e., in the direction perpendicular to *y* and *z*) are much smaller than the corresponding gradients along *y* and *z*. This implies that in the case of high Peclet numbers the transport phenomena between the anode and cathode channel exhibit a strongly two-dimensional character. Based on this concept, the previously mentioned quasi-three-dimensional models [10] were established.

2.1 Governing Equations. A fluid consisting of two phases, i.e., a gas phase and a liquid phase, is considered. In the gas phase, an ideal three-component gas mixture is assumed, consisting of oxygen, water vapor, and nitrogen. The liquid phase contains only water. Between the phases, mass transfer can occur by means of condensation and evaporation of water. Ordinary diffusion in multicomponent ideal gases at low density can be described by the Stefan-Maxwell equations [20], given by

$$\nabla x_i = \sum_{j=1}^{n} \frac{x_i \boldsymbol{N}_j - x_j \boldsymbol{N}_i}{cD_{i,j}} \tag{1}$$

where x_i is the mole fraction of specie *i*, $\boldsymbol{N}_i$ is the molar flux of species *i* with respect to stationary coordinates, *c* is the total molar concentration, and $D_{i,j}$ is the effective binary diffusion coefficient between species *i* and *j*. For the three-component gas mixture, Eq. (1) yields

$$\nabla x_{O_2} = \frac{x_{O_2}\boldsymbol{N}_{H_2O} - x_{H_2O}\boldsymbol{N}_{O_2}}{cD_{O_2,H_2O}} + \frac{x_{O_2}\boldsymbol{N}_{N_2} - x_{N_2}\boldsymbol{N}_{O_2}}{cD_{O_2,N_2}} \tag{2}$$

and

$$\nabla x_{H_2O} = \frac{x_{H_2O}\boldsymbol{N}_{O_2} - x_{O_2}\boldsymbol{N}_{H_2O}}{cD_{O_2,H_2O}} + \frac{x_{H_2O}\boldsymbol{N}_{N_2} - x_{N_2}\boldsymbol{N}_{H_2O}}{cD_{H_2O,N_2}} \tag{3}$$

where

$$x_{N_2} = 1 - x_{O_2} - x_{H_2O} \tag{4}$$

Note that x_{O_2}, x_{H_2O}, and x_{N_2} are the mole fractions of oxygen, water vapor, and nitrogen, respectively. Conservation of mass requires [20]

$$0 = -\nabla \cdot \boldsymbol{N}_{O_2} \tag{5}$$

$$0 = -\nabla \cdot \boldsymbol{N}_{H_2O} - Q \tag{6}$$

and

$$0 = -\nabla \cdot \boldsymbol{N}_{N_2} \tag{7}$$

where *Q* is a source term that accounts for condensation and evaporation of water. Nitrogen does not participate in the electrochemical reaction, and it does not cross the membrane due to its low diffusivity in the membrane. In the steady state, nitrogen is assumed to be motionless with respect to stationary coordinates and $\boldsymbol{N}_{N_2} \equiv 0$ applies in the diffusion layer [21]. Using Eqs. (2)–(4), the molar fluxes of oxygen and water vapor can then be written as

$$\boldsymbol{N}_{O_2} = \frac{cD_{O_2,N_2}[-D_{H_2O,N_2}(\nabla x_{H_2O} + \nabla x_{O_2})x_{O_2} + D_{O_2,H_2O}\nabla x_{O_2}(-1 + x_{O_2} + x_{H_2O})]}{(-1 + x_{O_2} + x_{H_2O})[-D_{O_2,N_2}x_{H_2O} - D_{H_2O,N_2}x_{O_2} + D_{O_2,H_2O}(-1 + x_{O_2} + x_{H_2O})]} \tag{8}$$

and

$$\boldsymbol{N}_{H_2O} = \frac{cD_{H_2O,N_2}[-D_{O_2,N_2}(\nabla x_{H_2O} + \nabla x_{O_2})x_{H_2O} + D_{O_2,H_2O}\nabla x_{H_2O}(-1 + x_{O_2} + x_{H_2O})]}{(-1 + x_{O_2} + x_{H_2O})[-D_{O_2,N_2}x_{H_2O} - D_{H_2O,N_2}x_{O_2} + D_{O_2,H_2O}(-1 + x_{O_2} + x_{H_2O})]} \tag{9}$$

respectively. In this study, transport of liquid water in hydrophobic porous media is investigated. The capillary pressure equals the difference between the liquid (nonwetting) phase pressure and the gas (wetting) phase pressure, given by

$$p_C = p_L - p_G \tag{10}$$

A uniform gas phase pressure is assumed [18,19] such that the capillary pressure gradient equals the liquid water pressure gradient. The molar flux of liquid water may be written as [18]

$$\boldsymbol{N}_L = -\frac{\rho_L}{M_L}\frac{\kappa\kappa_{rL}}{\mu_L}\nabla p_L, \tag{11}$$

where $\nabla p_L \cong \nabla p_C = (dp_C/dS)\nabla S$. Note that ρ_L is the liquid water density, M_L is the molecular weight, κ is the absolute permeability, κ_{rL} is the relative permeability, μ_L is the dynamic viscosity, p_C is the capillary pressure, and

$$S = \frac{s - s_{\mathrm{im}}}{1 - s_{\mathrm{im}}} \tag{12}$$

is the reduced water saturation, expressed in terms of the liquid water saturation *s* and the immobile saturation s_{im}. Note that *s* is defined as the ratio between the pore volume occupied by liquid water and the entire pore volume. It is assumed that the capillary pressure p_C can be written as a function of the reduced water saturation [18,22],

$$p_C = \frac{\sigma|\cos\theta|}{(\kappa/\varepsilon)^{1/2}}J(S) \tag{13}$$

where σ is the surface tension, θ is the contact angle, and ε is the porosity. The Leverett *J*-function [18,23,24]

$$J(S) = 1.417S - 2.120S^2 + 1.263S^3 \tag{14}$$

is used to describe the relation between the capillary pressure and the reduced water saturation [25]. He suggested that the semi-empirical nondimensional form $J(S) = (p_C/\sigma)(\kappa/\varepsilon)^{1/2}$ can be used to describe capillary versus saturation behavior [18,22,26], where p_C/σ represents a mean interfacial curvature of a meniscus in a pore and $(\kappa/\varepsilon)^{1/2}$ is a pore length scale. Based on Eq. (14), heat transfer considering phase change and capillarity in porous sand packs (spherical grain shape) was investigated by Udell [24]. For the relative permeability,

$$\kappa_{rL}(S) = S^3 \tag{15}$$

is used [18]. The derivative of the capillary pressure with respect to the reduced water saturation is given by

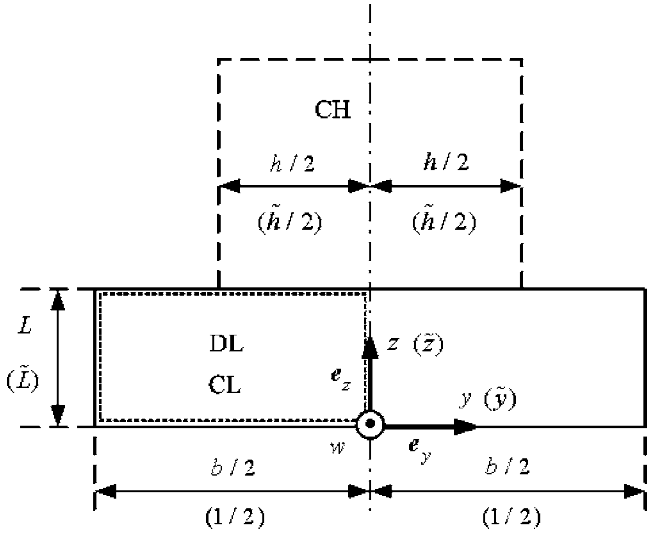

Fig. 1 Schematic drawing of the cathode diffusion layer (DL) and the cathode channel (CH). The catalyst layer (CL) is treated as a boundary condition. The computational domain is indicated by the dotted rectangle, where *b* is the diffusion layer width, *L* is the diffusion layer thickness, and *h* is the channel width.

$$\frac{dp_C}{dS} = \frac{\sigma|\cos\theta|}{(\kappa/\varepsilon)^{1/2}}\frac{dJ}{dS} \tag{16}$$

Conservation of mass for liquid water reads

$$0 = -\nabla \cdot \boldsymbol{N}_L + Q, \tag{17}$$

where Q is a condensation source or an evaporation sink. Heat transfer in the porous electrode is assumed to be dominated by heat conduction, such that conservation of energy can be formulated as

$$0 = \nabla \cdot (k \nabla T) + \chi(\nabla\phi)^2 + Qh_{fg} \tag{18}$$

where k is an effective thermal conductivity, T is the local temperature, χ is an effective electrical conductivity, ϕ is the electric potential, and h_{fg} is the latent heat of condensation. The first term on the right-hand side of Eq. (18) accounts for heat conduction, the second term accounts for joule heating due to electron transfer in the diffusion layer, and the last term accounts for the latent heat of condensation. Electron transport is governed by an electric potential field ϕ, according to

$$0 = \nabla \cdot (\chi \nabla \phi) \tag{19}$$

A volumetric molar condensation rate is defined as

$$Q = \frac{cD_{O_2,\mathrm{Air}}}{\delta}\frac{A}{V}\ln\frac{1-x_{H_2O}^{\mathrm{sat}}}{1-x_{H_2O}} = c\gamma\ln\frac{1-x_{H_2O}^{\mathrm{sat}}}{1-x_{H_2O}} \tag{20}$$

where c is the total molar concentration, δ is a film thickness, A/V is the liquid/gas interfacial area per unit volume, x_{H_2O} is the water vapor mole fraction in the gas phase, and $x_{H_2O}^{\mathrm{sat}}$ is the saturation mole fraction. The logarithmic expression on the right-hand side of Eq. (20) is obtained if the idealized problem is considered in which a condensable vapor is diffusing at steady state through a stagnant film of a noncondensable gas to a cold flat surface where the vapor condenses [20]. A condensation rate constant is defined as $\gamma=(A/V)(D_{O_2,\mathrm{Air}}/\delta)$. In Eq. (20), the driving force for finite-rate phase change is the deviation of the local thermodynamic state from the equilibrium state. For increasing condensation rates, the local thermodynamic state approaches the equilibrium state. The saturation pressure is correlated according to [27]

$$\begin{aligned}\log_{10}(p_{H_2O}^{\mathrm{sat}}10^{-5}) = &-2.1794 + 0.02953(T-273.15)\\ &-9.1837\times10^{-5}(T-273.15)^2\\ &+1.4454\times10^{-7}(T-273.15)^3\end{aligned} \tag{21}$$

and it is related to the saturation mole fraction by

$$p_{H_2O}^{\mathrm{sat}} = x_{H_2O}^{\mathrm{sat}}cRT \tag{22}$$

Effective binary diffusivities

$$D_{i,j} = f(\varepsilon)g(s)D_{i,j,0} \tag{23}$$

are defined in terms of binary diffusivities $D_{i,j,0}$, a porosity function $f(\varepsilon)$, and a liquid-saturation function $g(s)$ [18,21]. The binary diffusivities are obtained from Chapman-Enskog kinetic theory [20]

$$D_{i,j,0} = 5.9543\times10^{-4}\frac{\sqrt{T_h^3(M_i^{-1}+M_j^{-1})}}{cRT_h\varpi_{i,j}^2\Omega_{i,j}} \tag{24}$$

that is written in terms of SI units. The Bruggeman correction is used for the porosity function [18,28],

$$f(\varepsilon) = \varepsilon^{1.5}, \tag{25}$$

and a quadratic behavior is used for the saturation function [18]

$$g(s) = (1-s)^2 \tag{26}$$

2.2 Boundary Conditions.

The catalyst layer is assumed to be sufficiently thin such that it can be treated as a boundary condition. The local transfer current density at the reaction boundary $(z=0)$ can be written as [29]

$$j(y) = ix_{O_2}(y,z=0)\exp\left(\frac{\alpha F}{RT(y,z=0)}\phi(y,z=0)\right) \tag{27}$$

where i is the exchange current density, α is the transfer coefficient, F is the Faraday constant, R is the universal gas constant, and ϕ is the solid phase potential that substitutes the cathode overpotential. Note that the electrolyte phase potential is assumed to be zero (i.e., uniform) at $z=0$ [8]. Three-dimensional models [30] show that this is a reasonable assumption, since in the catalyst layer, the gradient of the electrolyte phase potential along the z direction is much larger than the gradient along the y direction. At the reaction boundary, the local molar fluxes of oxygen and water vapor are coupled to the local transfer current density as

$$\boldsymbol{e}_z \cdot \boldsymbol{N}_{O_2}(y,z=0) = -\frac{j(y)}{a_{O_2}F} \tag{28}$$

and

$$\boldsymbol{e}_z \cdot \boldsymbol{N}_{H_2O}(y,z=0) = \frac{j(y)}{a_{H_2O}F} \tag{29}$$

respectively, where $a_{O_2}=4$ and $a_{H_2O}=2$ are the stoichiometric coefficients of the cathode reaction, and $\boldsymbol{e}_z$ is a unit vector normal to the reaction boundary (see Fig. 1). Electro-osmotic drag in the membrane causes liquid water to be transported from the anode side to the cathode side. Back diffusion of liquid water in the membrane can also be an important transport mechanism. A net liquid water flux is defined at the reaction boundary, given by

$$\frac{\rho_L}{M_L}\frac{\kappa\kappa_{rL}}{\mu_L}\frac{dp_C}{dS}\frac{\partial S(y,z=0)}{\partial z} = -n_d\frac{j(y)}{F} \tag{30}$$

that takes into account both mechanisms. An effective drag coefficient $n_d=1/2$ is used [18], which means that 1/2 molecule H_2O per one proton is transported through the membrane from the anode side to the cathode side. The heat flux at the reaction boundary can be written as

$$k\frac{\partial T(y,z=0)}{\partial z} = -j(y)\phi(y,z=0) - j(y)\frac{T(y,z=0)(-\Delta s)}{a_{O_2}F} \tag{31}$$

where the first and second term on the right-hand side of Eq. (31) account for the irreversible and reversible reaction heat [31], respectively. Note that Δs is the reaction entropy of the cathode half-cell reaction [32], and the solid phase potential ϕ substitutes the cathode overpotential. It is assumed that heat fluxes induced by other heat sources in the fuel cell are not subject to cross the cathode reaction boundary. Such an assumption regarding the thermal management of the entire cell is required, since only the cathode side is modeled. At the reaction boundary ($z=0$), the electric potential field ϕ governing the transport of electrons in the porous diffusion layer is coupled to the transfer current density as

$$\chi\frac{\partial \phi(y,z=0)}{\partial z} = j(y) \tag{32}$$

At the channel boundary ($-h/2 \leqslant y \leqslant 0$, $z=L$), Dirichlet boundary conditions are used for the oxygen mole fraction, the water vapor mole fraction, and the reduced liquid water saturation, given by

$$x_{O_2}(-h/2 \leqslant y \leqslant 0, z=L) = x_{O_2}^h \tag{33}$$

$$x_{H_2O}(-h/2 \leqslant y \leqslant 0, z=L) = x_{H_2O}^h \tag{34}$$

and

$$S(-h/2 \leqslant y \leqslant 0, z=L) = S_h \tag{35}$$

Zero flux boundary conditions are employed for the temperature and the electric potential, given by

$$\boldsymbol{e}_z \cdot \nabla T(-h/2 \leqslant y \leqslant 0, z=L) = 0 \tag{36}$$

and

$$\boldsymbol{e}_z \cdot \nabla \phi(-h/2 \leqslant y \leqslant 0, z=L) = 0 \tag{37}$$

At the current collector boundary ($-b/2 \leqslant y \leqslant -h/2$, $z=L$), Dirichlet boundary conditions are used for the temperature and the electric potential, given by

$$T(-b/2 \leqslant y \leqslant -h/2, z=L) = T_h \tag{38}$$

and

$$\phi(-b/2 \leqslant y \leqslant -h/2, z=L) = \phi_h \tag{39}$$

where zero flux boundary conditions are used for the remaining quantities, given by

$$\boldsymbol{e}_z \cdot \nabla x_{O_2}(-b/2 \leqslant y \leqslant -h/2, z=L) = 0 \tag{40}$$

$$\boldsymbol{e}_z \cdot \nabla x_{H_2O}(-b/2 \leqslant y \leqslant -h/2, z=L) = 0 \tag{41}$$

and

$$\boldsymbol{e}_z \cdot \nabla S(-b/2 \leqslant y \leqslant -h/2, z=L) = 0 \tag{42}$$

In fuel cell stacks with cooling flow patterns between adjacent current collector plates [33], the generated heat is mainly removed by the coolant and not by the fuel cell feed gases in order to provide a uniform cell temperature. Since the thermal conductivity of the current collector material is several orders of magnitude higher than the thermal conductivity of the feed gas, the heat flux between the diffusion medium and the cooling flow pattern is mainly directed through the current collector rib. The convective heat transfer coefficient between the bulk fluid flow in the channel and the channel boundary is given as $\beta_F=(k_F/h)\mathrm{Nu}$, where k_F is the fluid thermal conductivity and Nu is the Nusselt number. In the current collector material, a corresponding heat transfer coefficient may be defined as $\beta_S=k_S/h$, where k_S is the solid thermal conductivity. Using properties of the fluid, the solid material, and typical Nusselt numbers for convective heat transfer in fully developed channel flows, $\beta_S/\beta_F=\mathrm{Nu}^{-1}k_S/k_F \cong 10^3$ is obtained, hence, justifying in this case the adiabatic condition at the channel boundary. At the left and right symmetry boundaries, given by $y=-b/2$ and $y=0$, respectively, zero flux boundary conditions are employed for all quantities.

The average current density j_{avg} is defined as the length average of the local transfer current density $j(y)$, given by

$$j_{\mathrm{avg}} = \frac{1}{b/2}\int_{-b/2}^{0} j(y)dy \tag{43}$$

An additional current density is defined as

$$j_0 = i x_{O_2}^h \exp\left(\frac{\alpha F}{RT_h}\phi_h\right) \tag{44}$$

which represents a maximum current density that could be obtained for infinitely large transport properties (such as mass diffusivities, electrical and thermal conductivities) or for infinitely small length scales. We define a local performance number, given by

$$\Pi = j(y)/j_0 \tag{45}$$

and an average performance number, given by

$$\Pi_{\mathrm{avg}} = j_{\mathrm{avg}}/j_0 \tag{46}$$

that quantify performance losses attributed to the finite size of the diffusion layer.

3 Nondimensional Mathematical Formulation

The governing equations and boundary conditions are nondimensionalized to generalize the results. The diffusion layer width b is used as a length scale, the current collector temperature T_h is used as a temperature scale, and the electric potential ϕ_h of the current collector is used as an electric potential scale, leading to scaled quantities given by

$$\tilde{y}=y/b, \quad \tilde{z}=z/b, \quad \tilde{T}=T/T_h, \quad \tilde{\phi}=\phi/\phi_h \tag{47}$$

where $\tilde{}$ indicates nondimensionalized quantities. Note that $\tilde{h}=h/b$ is the scaled channel width and $\tilde{L}=L/b$ is the scaled diffusion layer thickness. In Appendix A, the governing equations from Sec. 2 are written in nondimensional form. The scaled boundary conditions are listed in Appendix B, and two different sets of scaling parameters are given in Appendix C. It can be seen from Appendix C, that the problem to be solved depends on a set of 19 parameters $\tilde{K}_1,\tilde{K}_2,\tilde{K}_3,\ldots,\tilde{K}_{19}$ or alternatively on a set of 19 parameters $\tilde{\xi}_1,\tilde{\xi}_2,\tilde{\xi}_3,\ldots,\tilde{\xi}_{19}$ in which the current collector width b appears only in $\tilde{\xi}_9$. The problem further depends on the functional forms of $f(\varepsilon)$, $g(s)$, $J(S)$, and $\kappa_{rL}(S)$.

4 Numerical Solution

The governing equations were discretized based on the finite volume method [34] on a structured grid using a second-order scheme with linear interpolation functions between grid points. Grid refinement with four different grids was performed to ensure that the numerical solutions are grid independent. In the standard case, grids consisting of 40×10, 80×20, 160×40, and 320×80 control volumes were used. When comparing contours of x_{O_2}, x_{H_2O}, S, $T-T_h$, and $\tilde{\phi}$, the two finer grids yield practically indistinguishable results. The average current density j_{avg}/j_0 obtained from the 80×20 grid is 0.26% higher than the average current density obtained from the 40×10 grid. The average current density obtained from the 160×40 grid is 0.13% higher than the average current density obtained from the 80×20 grid. The average current density obtained from the 320×80 grid is 0.068% higher than the average current density obtained from the 160×40 grid. In this study, a 160×40 grid is used. The algorithm was implemented in FORTRAN.

Table 1 Standard case parameters

Total width b (mm)	2.0 [d]
Channel width h (mm)	1.0 [d]
Diffusion layer thickness L (mm)	0.25 [d]
Condensation rate constant γ (s^{-1})	900 [a]
Molecular weight of water M_L (kg mol^{-1})	0.018
Viscosity of liquid water μ_L (Pa s)	0.000404 [b]
Absolute permeability κ (m^2)	2.55×10^{-13} [a]
Porosity ε	0.5 [a]
Total molar concentration c (mol m^{-3})	35.1 [c]
Density of liquid water ρ_L (kg m^{-3})	978 [b]
Surface tension σ (N m^{-1})	0.0645 [b]
Contact angle θ (deg)	100.0 [d]
Effective electrical conductivity χ (Ω^{-1} m^{-1})	1000.0 [d]
Effective thermal conductivity k (W m^{-1} K^{-1})	4 [a]
Latent heat of condensation h_{fg} (J mol^{-1})	42,034 [b]
Tafel constant α	0.5 [e]
Exchange current density i (A m^{-2})	0.21 [e]
Stoichiometric coefficient a_{O2}	4
Stoichiometric coefficient a_{H2O}	2
Effective drag coefficient n_d	0.5 [a]
Oxygen mole fraction in the channel x_{O2}^{h}	0.146 [f]
Water vapor mole fraction in the channel x_{H2O}^{h}	0.305 [f]
Channel saturation S_h	0.1 [d]
Immobile saturation s_{im}	0.0 [g]
Current collector temperature T_h (K)	343 [a]
Current collector potential ϕ_h (V)	0.8 [d]

[a] Reference [18].

[b] Reference [36].

[c] Note that $c = p/(RT_h)$, where $p = 1$ bar.

[d] Assumed.

[e] Reference [37].

[f] Corresponding to 100% relative humidity of air at T_h [i.e., $x_{H2O}^{h} = x_{H2O}^{sat}(T_h)$]

[g] In this study, $s_{im} = 0$ is assumed.

5 Results and Discussion

In this section, a standard case is investigated that is based on the parameters listed in Table 1. Several transport and geometry parameters are varied and discussed in more detail. Figures 2–10 are obtained by mirroring the numerical results at the axis of symmetry $y=0$ (see Fig. 1).

Figure 2 shows the distribution of the oxygen mole fraction x_{O_2}, the water vapor mole fraction x_{H_2O}, the liquid water saturation S, the temperature difference $T-T_h$, and the electric potential $\tilde{\phi}_h$ for the standard case. It is seen from Fig. 2(*a*) that the oxygen mole fraction underneath the current collector rib is substantially reduced compared to the oxygen mole fraction underneath the channel. In contrast, the water vapor mole fraction exhibits a much more uniform distribution (see Fig. 2(*b*)). The highest liquid water saturation is found at the reaction boundary underneath the middle of the current collector rib ($\tilde{y}=\pm 1/2$) (see Fig. 2(*c*)). The liquid water saturation levels obtained in this study are in the same range as in the work of Nam and Kaviany [18]. The point with the highest temperature is located at the reaction boundary underneath the middle of the channel ($\tilde{y}=0$) (see Fig. 2(*d*)), whereas the lowest temperature within the domain is found at the current collector boundary. Note that in Fig. 2(*d*) the difference between the local temperature T and the current collector temperature T_h is plotted. The maximum temperature difference within the diffusion layer is ~2.5 K. The electric potential varies only slightly (see Fig. 2(*e*)), and the highest potential difference exists between the current collector and the origin of the frame. It should be noted that the results in this study are based on the functional forms of $f(\varepsilon)$, $g(s)$, $J(S)$, and $\kappa_{rL}(S)$. It is worth noting that, although the methodology presented is general, the accuracy of these functions with respect to specific types of porous diffusion media for PEM fuel cells affects the modeling predictions. Microscopic pore-level modeling and experiments with respect to specific diffusion layer media are currently needed to obtain medium specific and accurate functional forms [35], aiding the macroscopic modeling.

Figure 3(*a*) shows the distribution of the volumetric heat source $\tilde{Q}\tilde{K}_6$ due to phase change. It is seen that in the present case not only condensation (positive sign) can occur in the diffusion layer, but also evaporation (negative sign). Evaporation occurs in a half-circular area adjacent to the channel. Note that the water vapor mole fraction at the channel boundary equals the saturation mole fraction at temperature T_h (see Table 1). The reason for the fact that evaporation can occur is that the temperature at the channel boundary exceeds the current collector temperature T_h (see Fig. 2(*d*)), such that the local saturation pressure is higher than the partial pressure of water vapor. Figure 3(*b*) reveals a strongly nonuniform distribution of the volumetric Joule heat source $\tilde{K}_5(\tilde{\nabla}\tilde{\phi})^2$, with two local maxima at the edges of the current collector ribs. Note that the nondimensional quantities $\tilde{Q}\tilde{K}_6$ and $\tilde{K}_5(\tilde{\nabla}\tilde{\phi})^2$ need to be multiplied by kT_h/b^2 to obtain the respective dimensional quantities Qh_{fg} and $\chi(\nabla\phi)^2$. In the standard case, $kT_h/b^2=343\ \mathrm{W/cm^3}$ applies. Integration of the volumetric condensation heat source $\tilde{Q}\tilde{K}_6$ over the rectangular diffusion layer area ($-1/2\leqslant\tilde{y}\leqslant 1/2$, $0\leqslant\tilde{z}\leqslant 1$) gives a length-specific heat source of 1.2×10^{-3}(1.6 W/m). If the absolute quantity $|\tilde{Q}\tilde{K}_6|$ is integrated accordingly, a value of 4.7×10^{-3}(6.5 W/m) is obtained, implying that the heat source due to condensation is 2.95 $\times 10^{-3}$(4.1 W/m) and the heat sink due to evaporation is 1.75 $\times 10^{-3}$(2.4 W/m). The same integration applied to the volumetric Joule heat source $\tilde{K}_5(\tilde{\nabla}\tilde{\phi})^2$ leads to a length-specific Joule heat source of 1.2×10^{-4}(0.16 W/m). Integration of the irreversible reaction heat flux $\tilde{K}_{13}\tilde{j}\tilde{\phi}$ along the reaction boundary ($-1/2\leqslant\tilde{y}\leqslant 1/2$) gives a length-specific heat flux of 1.3×10^{-2}(18 W/m). Integration of the reversible reaction heat flux $\tilde{K}_{14}\tilde{j}\tilde{T}$ along the reaction boundary gives a length-specific heat flux of 2.5 $\times 10^{-3}$(3.4 W/m). Dividing by the current collector width b provides a membrane-area-specific condensation heat source (0.080 $\mathrm{W/cm^2}$), joule heat source ($8.2\times 10^{-3}\ \mathrm{W/cm^2}$), irreversible reaction heat flux (0.92 $\mathrm{W/cm^2}$), and reversible reaction heat flux (0.17 $\mathrm{W/cm^2}$).

Figure 4 shows the distribution of the absolute values of the oxygen flux $\tilde{N}_{O_2}$, the water vapor flux $\tilde{N}_{H_2O}$, and the liquid water flux $\tilde{N}_L$. Strong non-uniformities of the magnitudes of the different fluxes exist. The highest oxygen fluxes are obtained near the edges of the current collector ribs (see Fig. 4). It can be seen that the oxygen flux near the edges at channel boundary is considerably larger than in the middle of the channel boundary, since oxygen must be provided to the parts of the reaction boundary underneath the current collector ribs. In contrast, the highest water vapor fluxes result in the middle of the channel boundary as well as at the reaction boundary approximately a quarter to the left and right of the symmetry axis. It is interesting to note that the water vapor flux first decreases along the symmetry axis in the positive

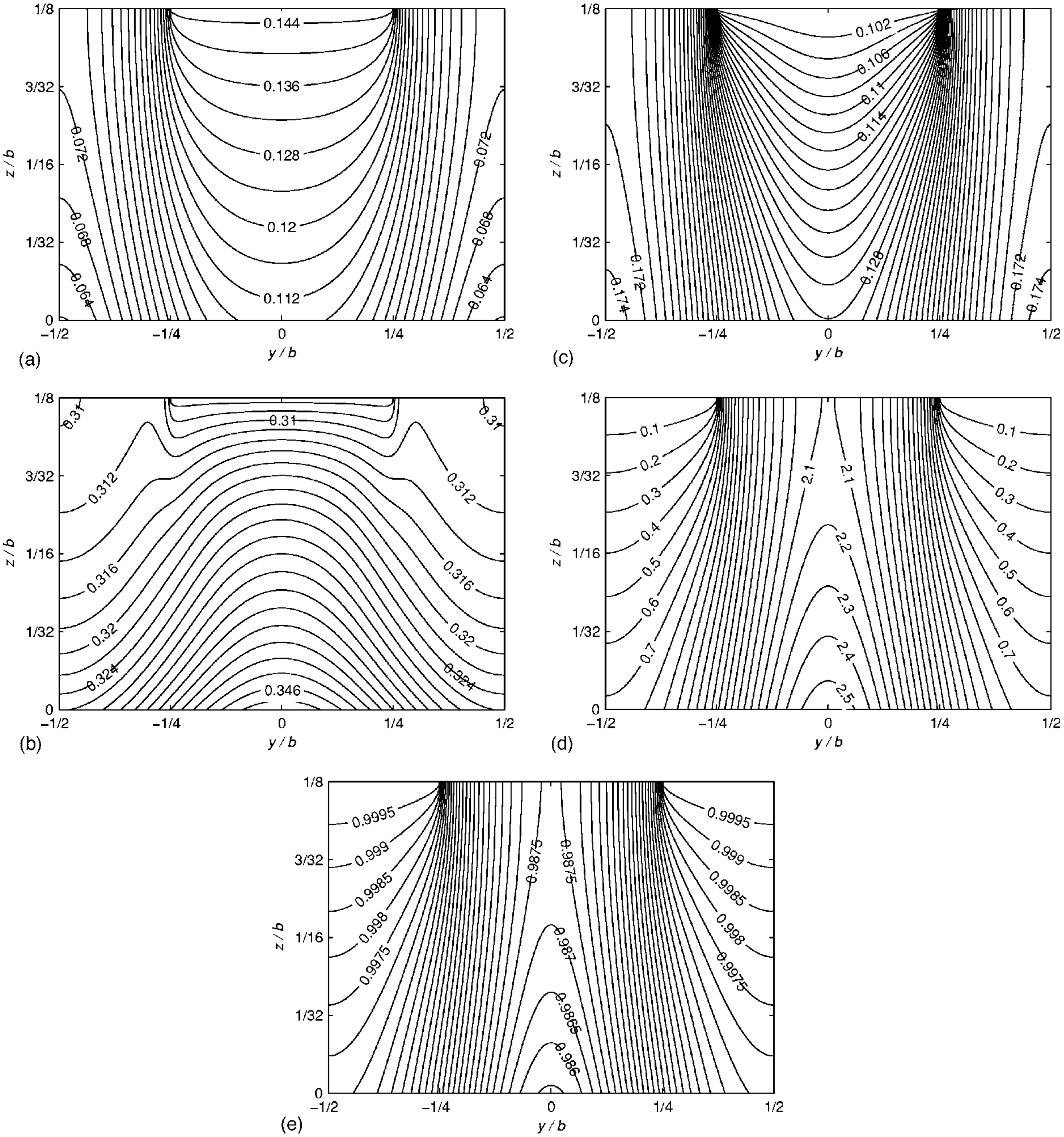

Fig. 2 Standard case: (*a*) Oxygen mole fraction x_{O_2}, (*b*) water vapor mole fraction x_{H_2O}, (*c*) liquid water saturation S, (*d*) temperature difference $\tilde{T}\xi_6-\xi_6(=T-T_h)$ (K), and (*e*) electric potential $\tilde{\phi}$

z direction due to condensation, then reaches a local minimum in the middle of the diffusion layer, and finally increases again near the channel boundary due to evaporation. The highest liquid water fluxes are found near the edges of the current collector ribs. Along the symmetry axis in the positive *z* direction, the liquid water flux first increases due to condensation and then gradually decreases when approaching the channel boundary due to the onset of evaporation, reflecting the opposite behavior of the water vapor flux. These results along with the results of the previous paragraph reveal that it is imperative that heat transfer be included in two-phase models for PEM fuel cells in order to be able to accurately predict liquid water fluxes as well as heat and mass sources due to phase change. Indeed, an isothermal model would not predict evaporation here and, therefore, could also not reflect a decreasing liquid water flux near the channel boundary. In order to mimic isothermal conditions for comparison purposes, the standard case with a very high effective thermal conductivity has been evaluated (not shown here for brevity). The characteristic distribution of the water vapor flux, the liquid water flux, and the heat and mass sources due to phase change are substantially affected, and a 6% higher average current density is obtained in the isothermal case compared to the nonisothermal standard case. The strong two-dimensionality of the transport phenomena in the diffusion layer further suggests that a one-dimensional treatment of the two-phase transport mechanisms along the direction perpendicular to the membrane can be an oversimplified approach.

In Fig. 5(*a*), the distribution of the scaled local current density $j(y)/j_0$ (i.e., the local performance number $\Pi(y)$) at the reaction boundary is plotted for different effective electrical conductivities χ of the diffusion medium. For low conductivities χ, a minimum is found in the middle underneath the channel and two maxima

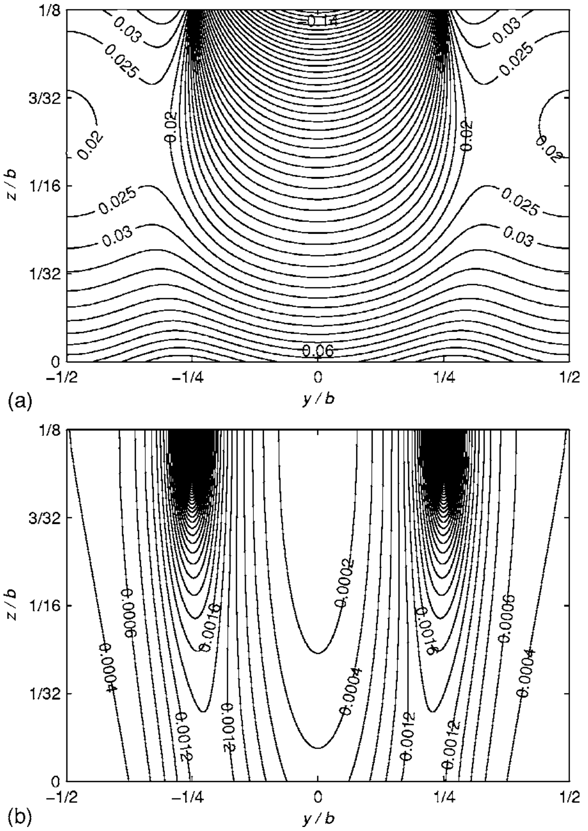

Fig. 3 Standard case: (*a*) volumetric condensation heat source $\tilde{Q}\tilde{K}_6$ and (*b*) volumetric Joule heat source $\tilde{K}_5(\tilde{\nabla}\tilde{\phi})^2$

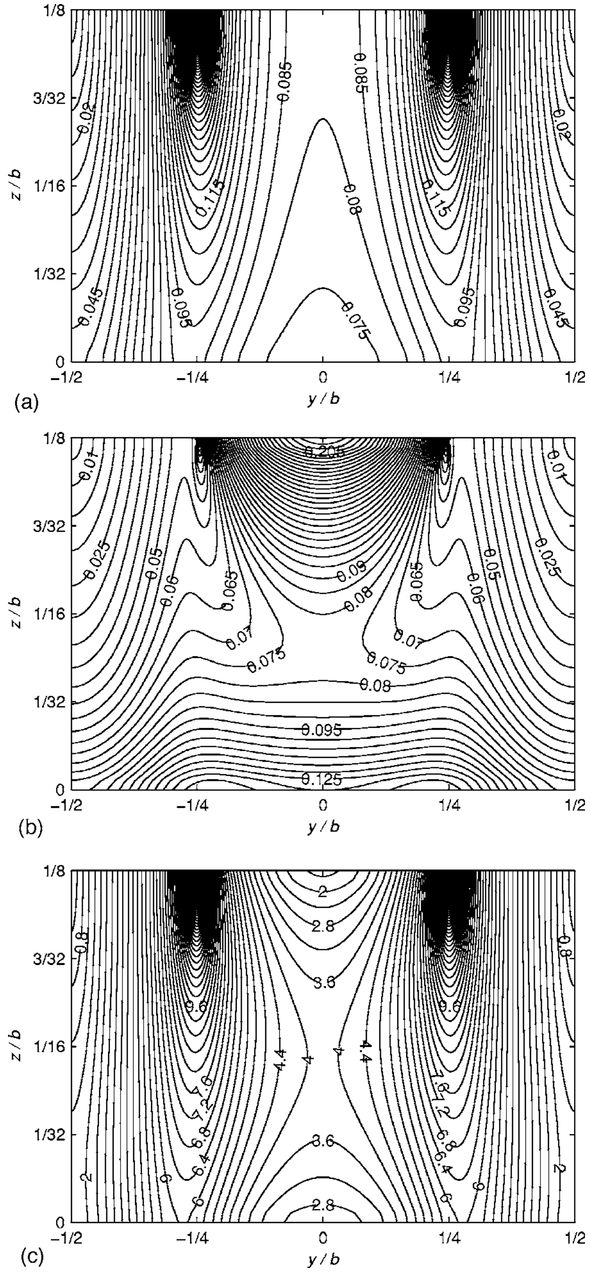

Fig. 4 Standard case: absolute values of molar fluxes, (*a*) $|\tilde{N}_{O_2}|=\sqrt{(e_y\tilde{N}_{O_2})^2+(e_z\tilde{N}_{O_2})^2}$, (*b*) $|\tilde{N}_{H_2O}|=\sqrt{(e_y\tilde{N}_{H_2O})^2+(e_z\tilde{N}_{H_2O})^2}$, and (*c*) $10^4|\tilde{N}_L|=10^4\sqrt{(e_y\tilde{N}_L)^2+(e_z\tilde{N}_L)^2}$

are located underneath the edges of the current collector ribs. For high conductivities χ, a maximum exists in the middle underneath the channel and two minima are located in the middle underneath the current collector rib. In the former case, ohmic and mass transfer resistances are dominant, whereas in the latter case only mass transfer resistances are dominant. If the electrical conductivity χ is increased, then the two maxima of the current density profile are shifted toward the symmetry axis, converging in one single maximum underneath the middle of the channel. Note that in this graph the local performance number $\Pi=j(y)/j_0$ is plotted in which the local current density $j(y)$ is scaled with the maximum current density j_0. It is seen that the local performance number ranges between 21 and 63 %, which means that performance losses attributed to the finite length scales of the device range between 79 and 37 %. In Fig. 5(*b*), the corresponding distributions of the irreversible reaction heat fluxes $-\tilde{K}_{13}\tilde{j}\tilde{\phi}$ (solid lines) and the reversible reaction heat fluxes $-\tilde{K}_{14}\tilde{j}\tilde{T}$ (dashed lines) at the reaction boundary are plotted. Similar characteristic distributions are obtained as for the current density distributions. Figure 5(*c*) shows the distribution of the liquid water saturation S at the reaction boundary. Although the transfer current density at the reaction boundary underneath the channel can be larger than underneath the current collector ribs, the liquid water saturation S at the reaction boundary has always a maximum underneath the middle of the current collector rib (i.e., at $\tilde{y}=\pm 1/2$) and a minimum underneath the middle of the channel (i.e., at $\tilde{y}=0$). The higher the effective electrical conductivity χ of the diffusion medium, the higher the local transfer current densities and water production rates from electrochemical reactions are, resulting in enhanced liquid water saturations (see Fig. 5(*c*)).

In Fig. 6, the effect of the contact angle θ (indicative of the wetting of the diffusion layer material by water) on the distribution of the local current density $j(y)/j_0$ and liquid water saturation S at the reaction boundary is investigated. Figs. 6(*a*) and 6(*b*) show that the higher the contact angle θ (less wetting), the lower the local liquid water saturation S at the reaction boundary is and the higher the local current density $j(y)/j_0$ is. It is seen that the contact angle θ has a major influence on the liquid water saturation level. It should be noted that the nondimensional formulation of the governing equations further allows for a more general interpretation of the results in Fig. 6. The set of curves essentially corresponds to a variation of the scaling parameter $\tilde{\xi}_4$ (see Appendix C), such that the results of Figs. 6(*a*) and 6(*b*) can also be understood as a variation of the absolute permeability κ. Higher contact angles θ and higher absolute permeabilities κ provide reduced liquid water saturations. In Fig. 7, the effective drag coef-

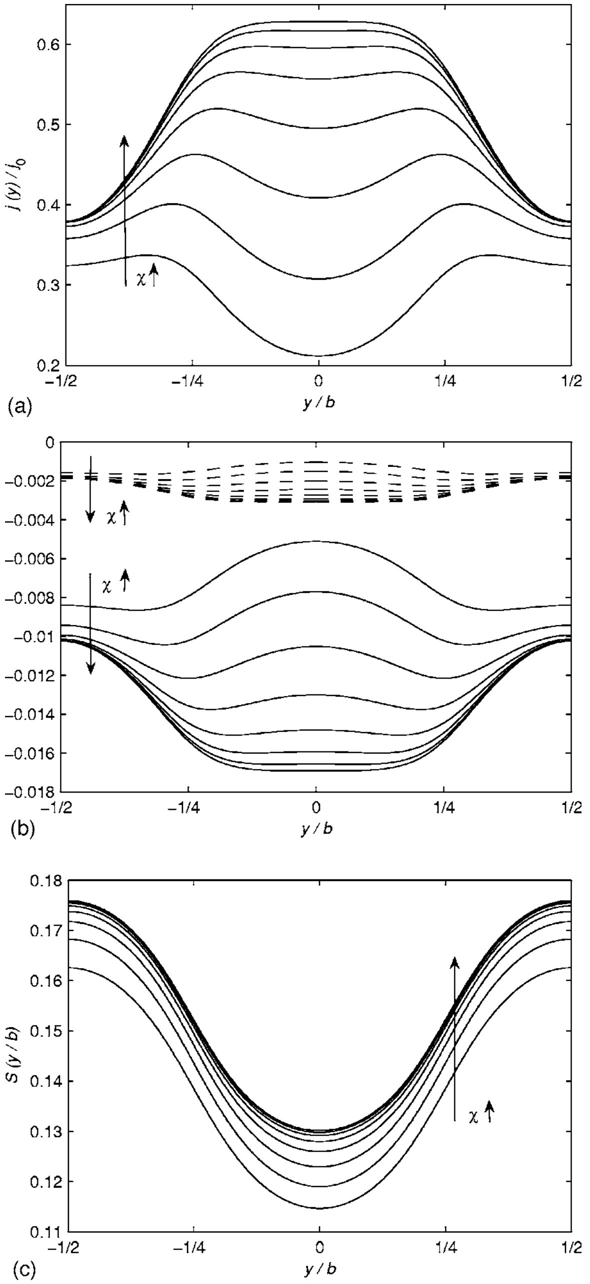

Fig. 5 Standard case with different effective electrical conductivities (i.e., $\chi=62.5,125,250,500,1000,2000,4000,8000\ \Omega^{-1}\ \mathrm{m}^{-1}$). Distributions at the reaction boundary $\tilde{z}=0$: (*a*) current density $j(y)/j_0$, (*b*) irreversible reaction heat fluxes $-\tilde{K}_{13}\tilde{j}\tilde{\phi}$ (solid lines) and reversible reaction heat fluxes $-\tilde{K}_{14}\tilde{j}\tilde{T}$ (dashed lines), and (*c*) liquid water saturation $S(y/b)$.

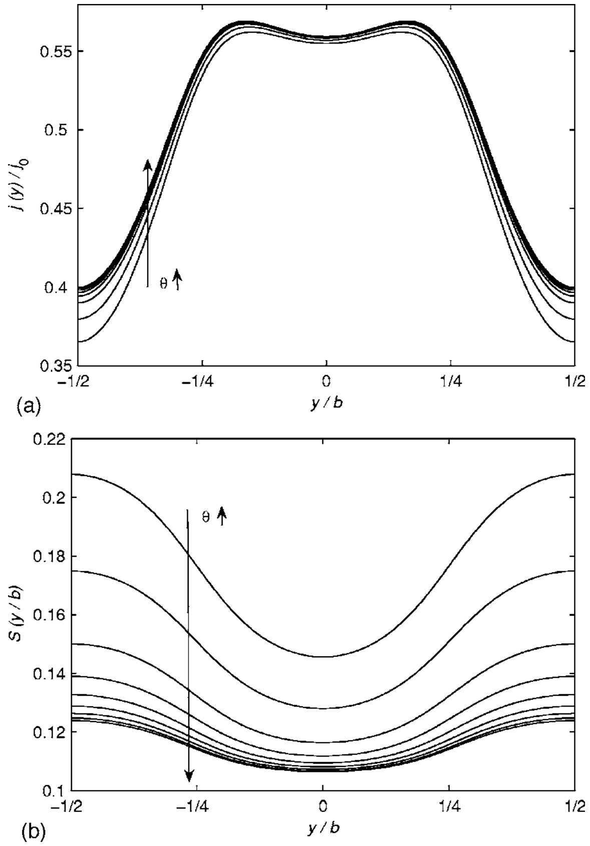

Fig. 6 Standard case with different contact angles [i.e., $\theta=95,100,110,120,130,140,150,160,170$ deg]. Note that the curves also represent the standard case with different absolute permeabilities (i.e., $\kappa=0.077,0.31,1.2,2.6,4.2,6.0,7.6,9.0,9.9\times10^{-13}\ \mathrm{m}^2$, respectively). Distributions at the reaction boundary $\tilde{z}=0$: (*a*) current density $j(y)/j_0$ and (*b*) liquid water saturation $S(y/b)$.

ficient n_d for water transport across the membrane is varied. A rather large variation of the effective drag coefficient is required to obtain a significant change in the liquid water saturation distribution and the current density distribution at the reaction boundary.

In Fig. 8, the distributions of the water vapor mole fraction x_{H_2O}, the liquid water saturation S, and the condensation heat source $\tilde{Q}\tilde{K}_6$ are presented for two different condensation rate constants (i.e., $\gamma=90{,}9000\ \mathrm{s}^{-1}$). Note that $\gamma=(A/V)(D_{O_2,\mathrm{Air}}/\delta)$ applies, such that the condensation rate constant is the product of a liquid-gas interfacial area per unit volume and a mass transfer coefficient. Figures 2(*b*), 2(*c*), and 3(*a*) are the corresponding graphs that represent the standard case with $\gamma=900\ \mathrm{s}^{-1}$. The distribution of the water vapor mole fraction x_{H_2O} is shown in Figs. 8(*a*), 2(*b*), and 8(*d*) for γ values of 90, 900, and 9000 s^{-1}, respectively. The difference between the maximum and minimum water vapor mole fraction within the diffusion layer decreases as the condensation rate constant increases. If the condensation rate constant is increased, then a relative humidity of unity is approached within the diffusion medium. The characteristic distribution of the water vapor mole fraction changes drastically if the condensation rate constant is increased, which means that the shape of the contour lines transforms from featuring a minimum to featuring a maximum at the centerline. The distribution of the liquid water saturation S is shown in Figs. 8(*b*), 2(*c*), and 8(*e*) for γ values of 90, 900, and 9000 s^{-1}, respectively. It is seen that the characteristic distribution of the liquid water saturation remains similar for the different values. The maximum liquid water saturation slightly increases if the condensation rate constant is increased. The distribution of the condensation heat source $\tilde{Q}\tilde{K}_6$ is shown in Figs. 8(*c*), 3(*a*), and 8(*f*) for γ values of 90, 900, and 9000 s^{-1}, respectively. The condensation heat source is positive in regions of the diffusion medium where condensation occurs, that is, next to the reaction boundary, and it is negative where evaporation occurs, that is, next to the channel boundary. The characteristic distribution of the condensation heat source is dramatically changed if the condensation rate constant increases. At high condensation rate constants, water vapor mainly condenses close to the reaction boundary and also mainly evaporates close to the channel boundary, whereas low condensation rates result in a spatially more gradual transition between condensation and evaporation.

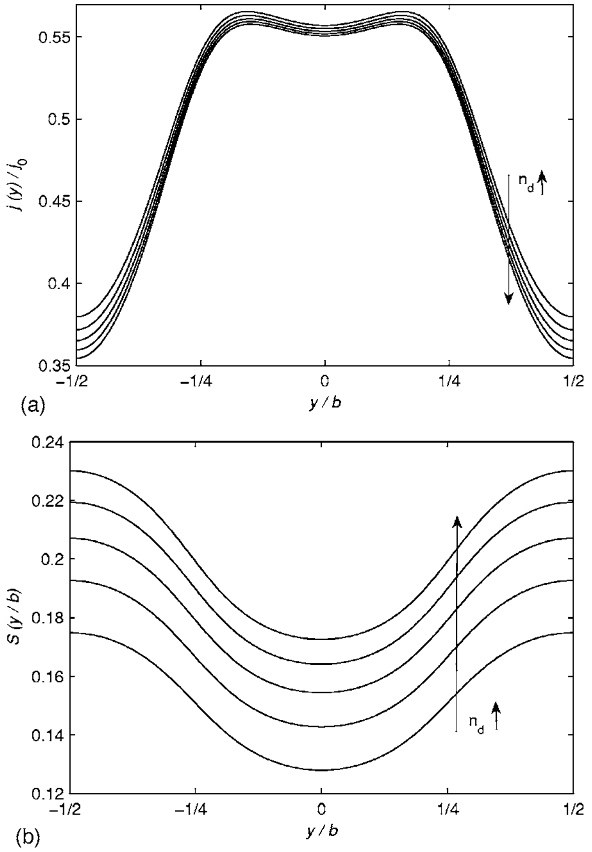

Fig. 7 Standard case with different drag coefficients (i.e., $n_d = 0.5, 1.0, 1.5, 2.0, 2.5$). Distributions at the reaction boundary $\tilde{z} = 0$: (*a*) current density $j(y)/j_0$ and (*b*) liquid water saturation $S(y/b)$.

Figure 9(*a*) shows the distribution of the local current density $j(y)/j_0$ at the reaction boundary for different current collector potentials ϕ_h. At low potentials ϕ_h, the current density distribution is quite uniform. The higher the current collector potential ϕ_h, the more nonuniform the current density distribution $j(y)$ at the reaction boundary is and the lower the local performance numbers $\Pi = j(y)/j_0$ are. In Fig. 9(*b*), the liquid water saturation distributions S at the reaction boundary are plotted. The local liquid water saturation level increases as the current collector potential increases because of enhanced transfer current densities. Maximum liquid water saturations exist underneath the middle of the current collector ribs (i.e., at $\tilde{y} = \pm 1/2$), whereas minimum saturations exist underneath the middle of the channel (i.e., at $\tilde{y} = 0$). It is seen that the saturation distribution at the reaction boundary exhibits a U-shape. If $\phi_h < 0.6$ V, the distribution is almost uniform. For values near $\phi_h = 0.8$ V, the strongest nonuniformity is found. At higher potentials ϕ_h, the distribution becomes more uniform again, due to oxygen depletion underneath the current collector rib.

In Fig. 10, the effect of downscaling of the channel width h, the current collector width b, and the diffusion layer thickness L on the distribution of the transfer current density $j(y)/j_0$ and the liquid water saturation S at the reaction boundary is investigated. In Figs. 10(*a*) and 10(*b*), the effect of the variation of the diffusion layer thickness on the current density and liquid water saturation distribution is investigated. The channel and rib widths are kept constant and their values correspond to the ones of the standard case. Figure 10(*a*) shows that for small diffusion layer thicknesses, the transfer current density distribution at the reaction boundary has two maxima underneath the edges of the current collector ribs (i.e., near $\tilde{y} = \pm 1/4$). If the diffusion layer thickness is increased, the two maxima combine into one single maximum located underneath the middle of the channel. The larger the diffusion layer thickness, the more uniform the current density distribution is; that is, the smaller the difference is between the maximum and the minimum local transfer current density. From Fig. 10(*b*) it can be seen that the maximum liquid water saturation is always found underneath the middle of the current collector rib (i.e., at $\tilde{y} = \pm 1/2$) and that the minimum liquid water saturation always exists underneath the middle of the channel (i.e., at $\tilde{y} = 0$). The smaller the diffusion layer thickness is, the larger the maximum liquid water saturation, and the larger the difference between the maximum and the minimum liquid water saturation. In Figs. 10(*c*) and 10(*d*), the channel width and the current collector rib widths are scaled down by a factor of two. Since the same nondimensional set of diffusion layer thicknesses is investigated as before, this implies that the dimensional diffusion layer thicknesses are divided by two. As an example, a diffusion layer thickness of 1/32 in Figs. 10(*a*) and 10(*b*) is identical to a diffusion layer thickness of 2/32 in Figs. 10(*c*) and 10(*d*). It is seen that a variation of the diffusion layer thickness leads to similar characteristic current density and liquid water saturation distributions at the reaction boundary as before. However, the current density distributions are shifted upward, whereas the liquid water saturation profiles are shifted downward in the graph. Hence, higher local current densities and lower local liquid water saturations can be obtained at decreasing length scales. It should be noted that the graphs reveal substantial local current density improvements. In Figs. 10(*e*) and 10(*f*), the channel width and the current collector rib width are scaled down again by a factor of two, leading to identical conclusions as before. Substantial local current density improvements can still be achieved.

In Fig. 11(*a*), the corresponding average densities j_{avg}/j_0 (i.e., the performance numbers Π) are plotted. It can be seen that for all three channel widths, there exists an optimum diffusion layer thickness that provides a maximum average current density. He et al. [13] and Natarajan and Van Nguyen [12] already predicted the existence of an optimum diffusion layer thickness. However, they did not account for electron transport and heat transfer in their studies [12,13]. This paper shows that both electron transport and multicomponent nonisothermal two-phase transport in the diffusion layer need to be considered in optimizing the diffusion layer thickness. The optimum diffusion layer thickness decreases as the channel width decreases. For channel widths h of 1.0, 0.5, and 0.25 mm and $h = b/2$, maximum performance numbers of 0.51, 0.66, and 0.78 are obtained at optimum diffusion layer thicknesses $\tilde{L}(L)$ of 0.084 (168 μm), 0.088 (88 μm), and 0.093 (46 μm), respectively. This study, therefore, makes a rather strong claim: based on the standard case, downscaling of the channel and rib width by a factor of 2 allows for a 29% (0.66/0.51) performance improvement, downscaling by a factor of 4 allows for a 53% (0.78/0.51) performance improvement, and infinite downscaling allows for a theoretical maximum performance improvement of 96% (1.0/0.51). It is important to note that downscaling of the channel width also requires downscaling of the diffusion layer thickness to achieve maximum average current densities. If the channel width is scaled down while maintaining a constant diffusion layer thickness, the average current density improvement can be much smaller. These results reveal that substantial current den-

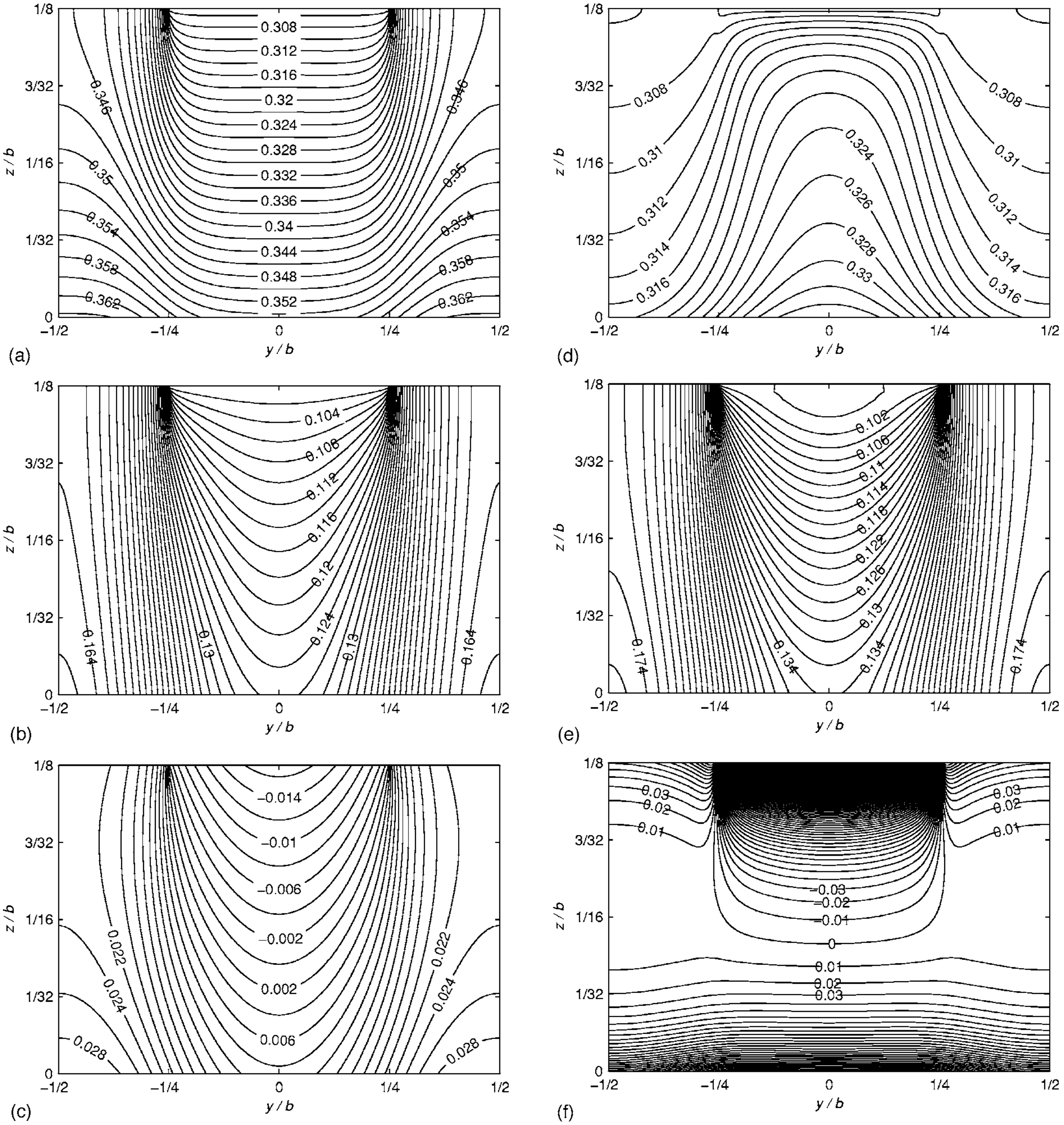

Fig. 8 Standard case with different condensation rate constants (i.e., $\gamma=90,9000\ \mathrm{s}^{-1}$): (*a*) water vapor mole fraction x_{H_2O} ($\gamma=90\ \mathrm{s}^{-1}$), (*b*) liquid water saturation *S* ($\gamma=90\ \mathrm{s}^{-1}$), (*c*) condensation heat source $\tilde{Q}\tilde{K}_6$ ($\gamma=90\ \mathrm{s}^{-1}$), (*d*) water vapor mole fraction x_{H_2O} ($\gamma=9000\ \mathrm{s}^{-1}$), (*e*) liquid water saturation $S(y/b)$ ($\gamma=9000\ \mathrm{s}^{-1}$), and (*f*) condensation heat source $\tilde{Q}\tilde{K}_6$ ($\gamma=9000\ \mathrm{s}^{-1}$).

sity improvements can be obtained at decreasing length scales, e.g., within double-staircase PEM fuel cells.

In Fig. 11(*b*), the effect of the variation of the channel width $\tilde{h}$ on the average density j_{avg}/j_0 (i.e., the performance number Π) is investigated. An optimum channel width exists that provides a maximum average current density. In the standard case, an optimum channel width $\tilde{h}$ of 0.70 is found. If the effective electrical conductivity χ of the diffusion medium is reduced by 50%, a smaller optimum channel width $\tilde{h}$ of 0.63 results. The optimum channel width $\tilde{h}$ decreases as the effective electrical conductivity χ decreases. If χ is increased toward infinity, then the optimum channel width asymptotically approaches 1.0. As a result, it should be noted that optimum channel widths can only be predicted if an electric potential field governing the transport of electrons is included in the model. Combining the results of Figs. 11(*a*) and 11(*b*), it follows that for a given width *b*, there exists an optimum pair (L,h) of diffusion layer thickness and channel width that provides a maximum average current density.

It should be noted that differences between the in-plane and through-plane effective electrical conductivity in the diffusion layer may exist. The distribution of the effective electrical conductivity may also depend on the magnitude of compression between the bipolar plates. Underneath the current collector ribs where the diffusion layer is compressed, one would expect higher effective electrical conductivities than underneath the flow channels. The investigation of the resulting complex two-dimensional distribution of the effective electrical conductivity and its impact

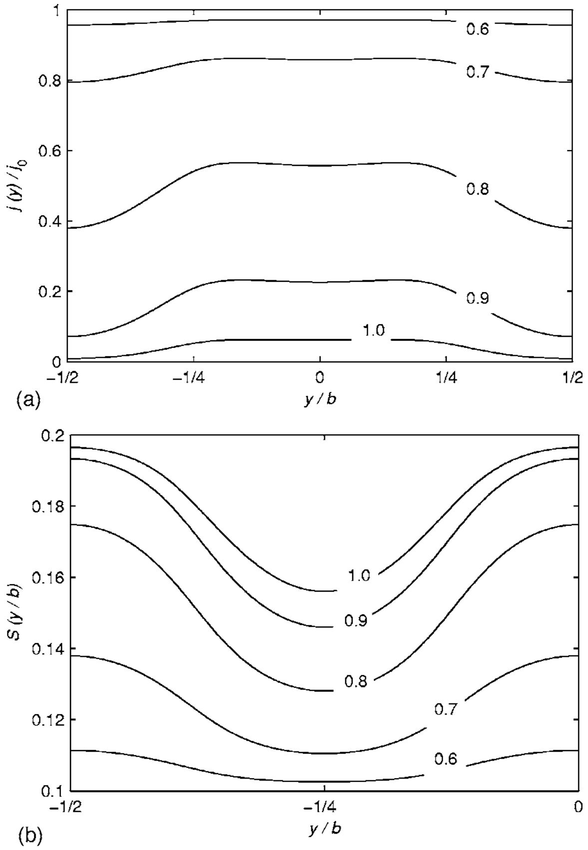

Fig. 9 Standard case with different electric potentials (i.e., $\phi_h=0.6, 0.7, 0.8, 0.9, 1.0$ V). Distributions at the reaction boundary $\tilde{z}=0$: (*a*) current density $j(y)/j_0$ and (*b*) liquid water saturation $S(y/b)$.

on the results of this study is the subject of future research. Contact resistances may also play a role in this study but are neglected because it would be difficult to quantify them.

6 Conclusions

In this study, a thorough model for the porous diffusion layers of a PEM fuel cell was presented in which all the governing macroscopic transport phenomena, including multicomponent diffusion, transport of liquid water, electronic current transfer, and heat transfer, are considered. A nondimensional mathematical formulation of the model was introduced to generalize the results. The model was applied to the cathode diffusion layer. A performance number was introduced to quantify losses in the diffusion layer attributed to mass transfer, the presence of liquid water, charge transfer, and heat transfer. The results show a strong two-dimensionality and coupling of the two-phase transport phenomena in the diffusion layer and, therefore, also imply that a one-dimensional treatment of the transport mechanisms along the direction perpendicular to the membrane can be an oversimplified approach.

Based on this two-phase model, the effect of downscaling of channel width, current collector rib width, and diffusion layer thickness on the performance of PEM fuel cells was systematically investigated and optimum length ratios (i.e., optimum diffusion layer thicknesses, optimum channel and rib width) were identified at decreasing length scales. It was also shown that the optimum diffusion layer thickness scales down as the channel width is scaled down. In other words, for smaller channel and current collector widths, the optimum diffusion layer thickness is also smaller. The results of this study reveal the great potential of downscaled PEM fuel cells in achieving enhanced power densities.

Acknowledgment

This work was supported by the Swiss Federal Office of Energy (BFE) under Contract No. 87100 (program manager Dr. A. Hintermann).

Nomenclature

a = stoichiometric coefficient
b = current collector width (m)
c = molar concentration (mol m^{-3})
$D_{i,j}$ = effective binary diffusion coefficient, m^2 s^{-1}
$D_{i,j,0}$ = binary diffusion coefficient, m^2 s^{-1}
$\boldsymbol{e}_y$ = unit vector in y direction
$\boldsymbol{e}_z$ = unit vector in z direction
F = Faraday constant, 96,485, C mol^{-1}
$f(\varepsilon)$ = porosity function
$g(s)$ = saturation function
h = channel width, m
h_{fg} = latent heat of condensation, J mol^{-1}
i = exchange current density, A m^{-2}
$J(S)$ = Leverett J-function
j = transfer current density, A m^{-2}
K = parameter
k = effective thermal conductivity, Wm^{-1} K^{-1}
L = diffusion layer thickness, m
M = molecular weight, kg mol^{-1}
$\boldsymbol{N}$ = mass flux, mol m^{-2} s^{-1}
Nu = Nusselt number
n_d = effective drag coefficient
p = pressure, Pa
p_{C} = capillary pressure, Pa
Q = condensation rate, mol m^{-3} s^{-1}
R = universal gas constant, 8.314 J K^{-1} mol^{-1}
S = reduced liquid water saturation
Δs = entropy change, J K^{-1} mol^{-1}
s = liquid water saturation
s_{im} = immobile saturation
T = temperature, K
w = coordinate, m
x = mole fraction
y = coordinate, m
z = coordinate, m

Greek Letters

α = Tafel constant
β = heat transfer coefficient, Wm^{-2} K^{-1}
χ = effective electrical conductivity, Ω^{-1} m^{-1}
δ = film thickness, m
ε = porosity
ϕ = electric potential, V
γ = condensation rate constant, s^{-1}
κ = absolute permeability, m^2
κ_{rL} = relative permeability
μ_L = viscosity of liquid water, Pa s
Π = performance number
Ω = collision integral
ϖ = collision diameter, Å
θ = contact angle, rad
ρ_L = density of liquid water, kg m^{-3}
σ = surface tension, N m^{-1}
ξ = parameter

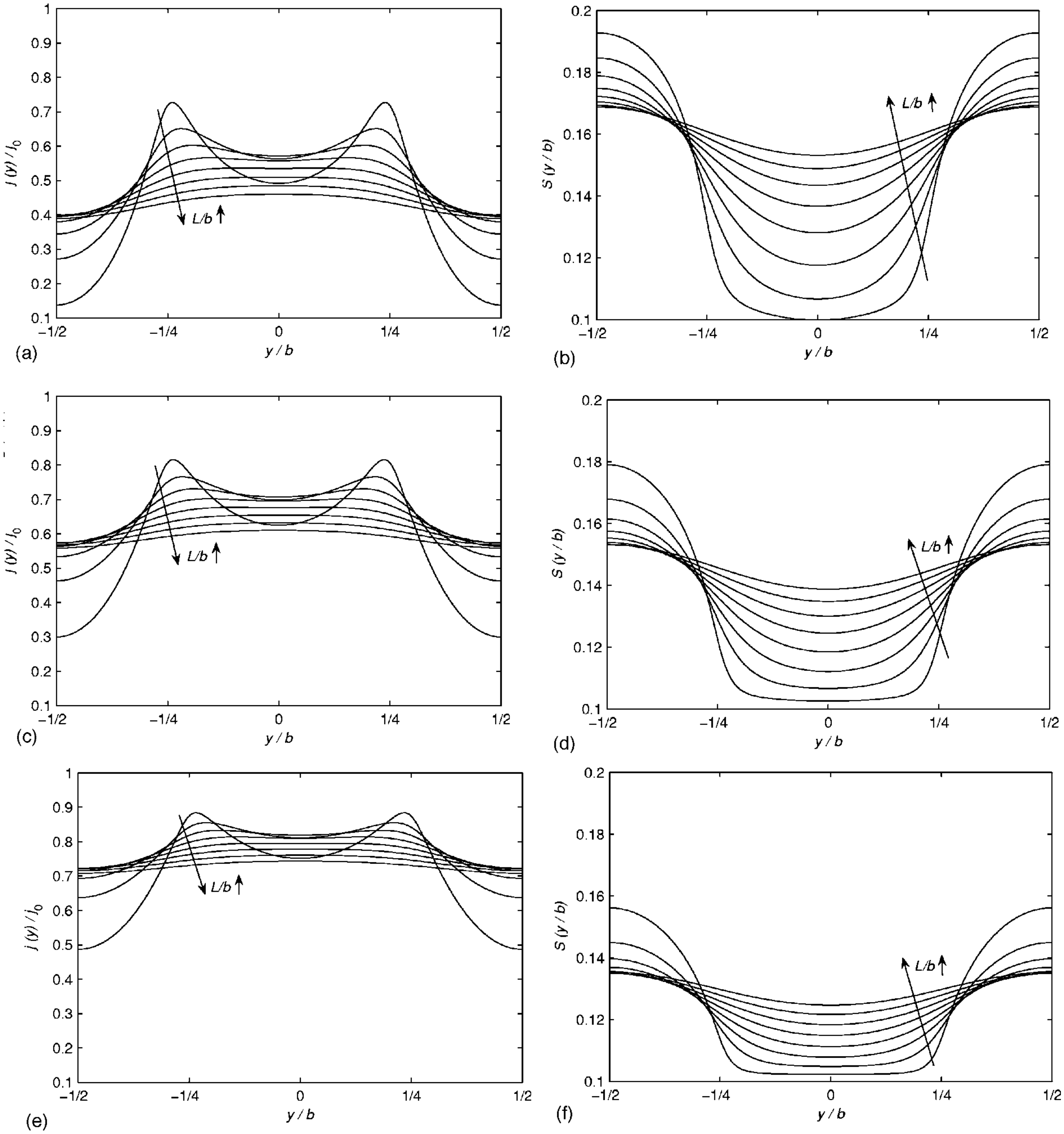

Fig. 10 Standard case with different electrode widths *b* (i.e., *b*=2.0,1.0,0.5 mm) and electrode thicknesses $\tilde{L}$ (i.e., $\tilde{L}=\frac{1}{32},\frac{2}{32},\frac{3}{32},\frac{4}{32},\frac{5}{32},\frac{6}{32},\frac{7}{32},\frac{8}{32}$). Distributions at the reaction boundary $\tilde{z}=0$: (*a*) current density $j(y)/j_0$ (*b*=2.0 mm), (*b*) liquid water saturation $S(y/b)$ (*b*=2.0 mm), (*c*) current density $j(y)/j_0$ (*b*=1.0 mm), (*d*) liquid water saturation $S(y/b)$ (*b*=1.0 mm), (*e*) current density $j(y)/j_0$ (*b*=0.5 mm), and (*f*) liquid water saturation $S(y/b)$ (*b*=0.5 mm).

Subscripts

avg = average
F = fluid
G = gas phase
H_2O = water vapor
h = top boundary
L = liquid water
O_2 = oxygen
S = solid
0 = maximum

Superscripts

~ = dimensionless
h = top boundary
sat = saturation

Appendix A. Nondimensional Governing Equations

$$0 = -\tilde{\nabla}\cdot\tilde{N}_{O_2} \tag{A1}$$

$$0 = -\tilde{\nabla}\cdot\tilde{N}_{H_2O} - \tilde{Q}\tilde{K}_3 \tag{A2}$$

$$0 = -\tilde{\nabla}\cdot\tilde{N}_L + \tilde{Q}\tilde{K}_4 \tag{A3}$$

$$0 = \tilde{\nabla}\cdot(\tilde{\nabla}\tilde{T}) + \tilde{K}_5(\tilde{\nabla}\tilde{\phi})^2 + \tilde{Q}\tilde{K}_6 \tag{A4}$$

$$0 = \tilde{\nabla}\cdot(\tilde{\nabla}\tilde{\phi}) \tag{A5}$$

$$\tilde{\boldsymbol{N}}_{O_2} = \frac{-(\tilde{\nabla}x_{H_2O} + \tilde{\nabla}x_{O_2})x_{O_2} + \tilde{K}_1\tilde{\nabla}x_{O_2}(-1 + x_{O_2} + x_{H_2O})}{(-1 + x_{O_2} + x_{H_2O})[-\tilde{K}_2x_{H_2O} - x_{O_2} + \tilde{K}_1(-1 + x_{O_2} + x_{H_2O})]}f(\varepsilon)g(s) \tag{A6}$$

$$\tilde{\boldsymbol{N}}_{H_2O} = \frac{-(\tilde{\nabla}x_{H_2O} + \tilde{\nabla}x_{O_2})x_{H_2O} + \dfrac{\tilde{K}_1}{\tilde{K}_2}\tilde{\nabla}x_{H_2O}(-1 + x_{O_2} + x_{H_2O})}{(-1 + x_{O_2} + x_{H_2O})\left[-x_{H_2O} - \dfrac{1}{\tilde{K}_2}x_{O_2} + \dfrac{\tilde{K}_1}{\tilde{K}_2}(-1 + x_{O_2} + x_{H_2O})\right]}f(\varepsilon)g(s) \tag{A7}$$

$$\tilde{\boldsymbol{N}}_L = -\kappa_{rL}\frac{dJ}{dS}\tilde{\nabla}S \tag{A8}$$

$$\tilde{Q} = \ln\frac{1 - x_{H_2O}^{\text{sat}}}{1 - x_{H_2O}} \tag{A9}$$

$$x_{H_2O}^{\text{sat}} = \frac{p_{H_2O}^{\text{sat}}(K_7\tilde{T})}{K_8\tilde{T}} \tag{A10}$$

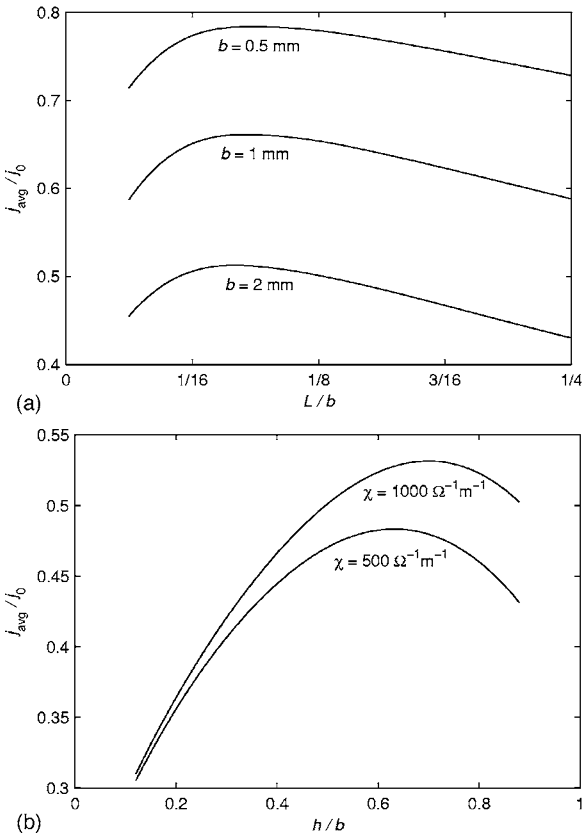

Fig. 11 (***a***) **Standard case with different electrode thicknesses** $\tilde{L}$ **(i.e.,** $\frac{1}{32} \leqslant \tilde{L} \leqslant \frac{8}{32}$**) and electrode widths** b **(i.e.,** $b = 2.0, 1.0, 0.5$ **mm), subject to** $h = b/2$**. Average current densities** j_{avg}/j_0 **for** $b = 2$ **mm (bottom curve),** $b = 1$ **mm (middle curve), and** $b = 0.5$ **mm (upper curve). (*b*) Standard case with different channel widths** $\tilde{h}$ **(i.e.,** $0.12 \leqslant \tilde{h} \leqslant 0.88$**) and effective electrical conductivities (i.e.,** $\chi = 500, 1000\ \Omega^{-1}\ \text{m}^{-1}$**). Average current densities** j_{avg}/j_0 **for** $\chi = 500\ \Omega^{-1}\ \text{m}^{-1}$ **(bottom curve) and** $\chi = 1000\ \Omega^{-1}\ \text{m}^{-1}$ **(upper curve).**

$$\tilde{\boldsymbol{N}}_{O_2} = \frac{b}{cD_{O_2,N_2,0}}\boldsymbol{N}_{O_2} \tag{A11}$$

$$\tilde{\boldsymbol{N}}_{H_2O} = \frac{b}{cD_{H_2O,N_2,0}}\boldsymbol{N}_{H_2O} \tag{A12}$$

$$\tilde{\boldsymbol{N}}_L = \frac{bM_L\mu_L(\kappa/\varepsilon)^{1/2}}{\rho_L\kappa\sigma|\cos\theta|}\boldsymbol{N}_L \tag{A13}$$

$$\tilde{Q} = Q/(c\gamma) \tag{A14}$$

Appendix B. Nondimensional Boundary Conditions

B.1 Reaction Boundary $\tilde{z} = 0$.

$$\tilde{j} = j/i = x_{O_2}\exp\left(\frac{\tilde{K}_9\tilde{\phi}}{\tilde{T}}\right) \tag{B1}$$

$$\tilde{j}_0 = x_{O_2}^h\exp(\tilde{K}_9), \quad \tilde{j}_0 = j_0/i \tag{B2}$$

$$\tilde{j}_{\text{avg}} = \int_{-1/2}^{+1/2}\tilde{j}(\tilde{y})d\tilde{y}, \quad \tilde{j}_{\text{avg}} = j_{\text{avg}}/i \tag{B3}$$

$$\boldsymbol{e}_z \cdot \tilde{\boldsymbol{N}}_{O_2} = -\tilde{K}_{10}\tilde{j} \tag{B4}$$

$$\boldsymbol{e}_z \cdot \tilde{\boldsymbol{N}}_{H_2O} = \tilde{K}_{11}\tilde{j} \tag{B5}$$

$$\kappa_{rL}\frac{dJ}{dS}\frac{\partial S}{\partial\tilde{z}} = -\tilde{K}_{12}\tilde{j} \tag{B6}$$

$$\frac{\partial\tilde{T}}{\partial\tilde{z}} = -\tilde{K}_{13}\tilde{j}\tilde{\phi} - \tilde{K}_{14}\tilde{j}\tilde{T} \tag{B7}$$

$$\frac{\partial\tilde{\phi}}{\partial\tilde{z}} = \tilde{j}\tilde{K}_{13}/\tilde{K}_5 \tag{B8}$$

B.2 Other Boundaries.

$$x_{O_2}(-\tilde{h}/2 \leqslant \tilde{y} \leqslant 0, \tilde{z} = \tilde{L}) = \tilde{K}_{15} \tag{B9}$$

$$x_{H_2O}(-\tilde{h}/2 \leqslant \tilde{y} \leqslant 0, \tilde{z} = \tilde{L}) = \tilde{K}_{16} \tag{B10}$$

$$S(-\tilde{h}/2 \leqslant \tilde{y} \leqslant 0, \tilde{z} = \tilde{L}) = \tilde{K}_{17} \tag{B11}$$

$$\tilde{T}\left(-\tfrac{1}{2} \leqslant \tilde{y} \leqslant -\tilde{h}/2, \tilde{z} = \tilde{L}\right) = 1 \tag{B12}$$

$$\tilde{\phi}\left(-\tfrac{1}{2} \leqslant \tilde{y} \leqslant -\tilde{h}/2, \tilde{z} = \tilde{L}\right) = 1 \tag{B13}$$

Appendix C. Scaling Parameters

$$\tilde{K}_1 = D_{\mathrm{O_2,H_2O},0}/D_{\mathrm{H_2O,N_2},0} = \tilde{\xi}_1 \tag{C1}$$

$$\tilde{K}_2 = D_{\mathrm{O_2,N_2},0}/D_{\mathrm{H_2O,N_2},0} = \tilde{\xi}_2 \tag{C2}$$

$$\tilde{K}_3 = b^2\gamma/D_{\mathrm{H_2O,N_2},0} = \tilde{\xi}_2\tilde{\xi}_3\tilde{\xi}_9^2 \tag{C3}$$

$$\tilde{K}_4 = \frac{M_L\mu_L b^2(\kappa/\varepsilon)^{1/2}c\gamma}{\rho_L\kappa\sigma|\cos\theta|} = \tilde{\xi}_2\tilde{\xi}_3\tilde{\xi}_4\tilde{\xi}_9^2 \tag{C4}$$

$$\tilde{K}_5 = \chi\phi_h^2/(kT_h) = \tilde{\xi}_5^{-1}\tilde{\xi}_8^2\tilde{\xi}_{14} \tag{C5}$$

$$\tilde{K}_6 = h_{fg}b^2c\gamma/(kT_h) = \tilde{\xi}_2\tilde{\xi}_3\tilde{\xi}_5^{-1}\tilde{\xi}_9^2 \tag{C6}$$

$$K_7 = T_h = \xi_6 \tag{C7}$$

$$K_8 = cRT_h = \xi_7 \tag{C8}$$

$$\tilde{K}_9 = \alpha F\phi_h/(RT_h) = \tilde{\xi}_8 \tag{C9}$$

$$\tilde{K}_{10} = bi/(a_{\mathrm{O_2}}FcD_{\mathrm{O_2,N_2},0}) = \tilde{\xi}_9 \tag{C10}$$

$$\tilde{K}_{11} = bi/(a_{\mathrm{H_2O}}FcD_{\mathrm{H_2O,N_2},0}) = \tilde{\xi}_2\tilde{\xi}_9\tilde{\xi}_{10} \tag{C11}$$

$$\tilde{K}_{12} = \frac{n_dM_L\mu_L i}{F\rho_L\kappa}\frac{(\kappa/\varepsilon)^{1/2}b}{\sigma|\cos\theta|} = \tilde{\xi}_2\tilde{\xi}_4\tilde{\xi}_9\tilde{\xi}_{11} \tag{C12}$$

$$\tilde{K}_{13} = i\phi_h b/(kT_h) = \tilde{\xi}_2\tilde{\xi}_5^{-1}\tilde{\xi}_8\tilde{\xi}_9\tilde{\xi}_{12} \tag{C13}$$

$$\tilde{K}_{14} = i(-\Delta s)b/(ka_{\mathrm{O_2}}F) = \tilde{\xi}_2\tilde{\xi}_5^{-1}\tilde{\xi}_9\tilde{\xi}_{13} \tag{C14}$$

$$\tilde{K}_{15} = x_{\mathrm{O_2}}^h = \tilde{\xi}_{15} \tag{C15}$$

$$\tilde{K}_{16} = x_{\mathrm{H_2O}}^h = \tilde{\xi}_{16} \tag{C16}$$

$$\tilde{K}_{17} = S_h = \tilde{\xi}_{17} \tag{C17}$$

$$\tilde{K}_{18} = \tilde{h} = \tilde{\xi}_{18} \tag{C18}$$

$$\tilde{K}_{19} = \tilde{L} = \tilde{\xi}_{19} \tag{C19}$$

$$\tilde{\xi}_3 = (a_{\mathrm{O_2}}^2F^2/i^2)c^2D_{\mathrm{O_2,N_2},0}\gamma \tag{C20}$$

$$\tilde{\xi}_4 = \frac{M_L\mu_L(\kappa/\varepsilon)^{1/2}cD_{\mathrm{H_2O,N_2},0}}{\rho_L\kappa\sigma|\cos\theta|} \tag{C21}$$

$$\tilde{\xi}_5 = kT_h/(cD_{\mathrm{H_2O,N_2},0}h_{fg}) \tag{C22}$$

$$\tilde{\xi}_{10} = a_{\mathrm{O_2}}/a_{\mathrm{H_2O}} \tag{C23}$$

$$\tilde{\xi}_{11} = n_da_{\mathrm{O_2}} \tag{C24}$$

$$\tilde{\xi}_{12} = a_{\mathrm{O_2}}RT_h/(\alpha h_{fg}) \tag{C25}$$

$$\tilde{\xi}_{13} = (-\Delta s)T_h/h_{fg} \tag{C26}$$

$$\tilde{\xi}_{14} = \frac{\chi R^2T_h^2}{\alpha^2F^2h_{fg}cD_{\mathrm{H_2O,N_2},0}} \tag{C27}$$

References

[1] Senn, S. M., and Poulikakos, D., 2004, "Tree Network Channels as Fluid Distributors Constructing Double-Staircase Polymer Electrolyte Fuel Cells," J. Appl. Phys., **96**(1), pp. 842–852.

[2] Vargas, J. V. C., Ordonez, J. C., and Bejan, A., 2004, "Constructal Flow Structure for a PEM Fuel Cell," Int. J. Heat Mass Transfer, **47**(19–20), pp. 4177–4193.

[3] Senn, S. M., and Poulikakos, D., 2005, "Multistage Polymer Electrolyte Fuel Cells Based on Nonuniform Cell Potential Distribution Functions," Electrochem. Commun., **7**(7), pp. 773–780.

[4] Bejan, A., 2000, *Shape and Structure, From Engineering to Nature*, Cambridge University Press, Cambridge.

[5] Bejan, A., 1996, "Entropy Generation Minimization: The New Thermodynamics of Finite-Size Devices and Finite-Time Processes," J. Appl. Phys., **79**(3), pp. 1191–1218.

[6] Senn, S. M., and Poulikakos, D., "Pyramidal Direct Methanol Fuel Cells," International Journal of Heat and Mass Transfer, [under review].

[7] Kulikovsky, A. A., 2000, "Two-Dimensional Numerical Modeling of a Direct Methanol Fuel Cell," J. Appl. Electrochem., **30**(9), pp. 1005–1014.

[8] Kulikovsky, A. A., Divisek, J., and Kornyshev, A. A., 1999, "Modeling the Cathode Compartment of Polymer Electrolyte Fuel Cells: Dead and Active Reaction Zones," J. Electrochem. Soc., **146**(11), pp. 3981–3991.

[9] Kulikovsky, A. A., Divisek, J., and Kornyshev, A. A., 2000, "Two-Dimensional Simulation of Direct Methanol Fuel Cell—A New (Embedded) Type of Current Collector," J. Electrochem. Soc., **147**(3), pp. 953–959.

[10] Kulikovsky, A. A., 2003, "Quasi-3D Modeling of Water Transport in Polymer Electrolyte Fuel Cells," J. Electrochem. Soc., **150**(11), pp. A1432–A1439.

[11] Yi, J. S., and Van Nguyen, T., 1999, "Multicomponent Transport in Porous Electrodes of Proton Exchange Membrane Fuel Cells Using the Interdigitated Gas Distributors," J. Electrochem. Soc., **146**(1), pp. 38–45.

[12] Natarajan, D., and Van Nguyen, T., 2001, "A Two-Dimensional, Two-Phase, Multicomponent, Transient Model for the Cathode of a Proton Exchange Membrane Fuel Cell Using Conventional Gas Distributors," J. Electrochem. Soc., **148**(12), pp. A1324–A1335.

[13] He, W. S., Yi, J. S., and Van Nguyen, T., 2000, "Two-Phase Flow Model of the Cathode of PEM Fuel Cells Using Interdigitated Flow Fields," AIChE J., **46**(10), pp. 2053–2064.

[14] Natarajan, D., and Van Nguyen, T., 2003, "Three-Dimensional Effects of Liquid Water Flooding in the Cathode of a PEM Fuel Cell," J. Power Sources, **115**(1), pp. 66–80.

[15] Wang, Z. H., Wang, C. Y., and Chen, K. S., 2001, "Two-Phase Flow and Transport in the Air Cathode of Proton Exchange Membrane Fuel Cells," J. Power Sources, **94**(1), pp. 40–50.

[16] You, L. X., and Liu, H. T., 2002, "A Two-Phase Flow and Transport Model for the Cathode of PEM Fuel Cells," Int. J. Heat Mass Transfer, **45**(11), pp. 2277–2287.

[17] Berning, T., and Djilali, N., 2003, "A 3D, Multiphase, Multicomponent Model of the Cathode and Anode of a PEM Fuel Cell," J. Electrochem. Soc., **150**(12), pp. A1589–A1598.

[18] Nam, J. H., and Kaviany, M., 2003, "Effective Diffusivity and Water-Saturation Distribution in Single- and Two-Layer PEMFC Diffusion Medium," Int. J. Heat Mass Transfer, **46**(24), pp. 4595–4611.

[19] Weber, A. Z., Darling, R. M., and Newman, J., 2004, "Modeling Two-Phase Behavior in PEFCs," J. Electrochem. Soc., **151**(10), pp. A1715–A1727.

[20] Bird, R. B., Stewart, W. E., and Lightfoot, E. N., 1960, *Transport Phenomena*, Wiley, New York.

[21] Meyers, J. P., and Newman, J., 2002, "Simulation of the Direct Methanol Fuel Cell—II. Modeling and Data Analysis of Transport and Kinetic Phenomena," J. Electrochem. Soc., **149**(6), pp. A718–A728.

[22] Kaviany, M., 1991, *Principles of Heat Transfer in Porous Media*, Springer, New York.

[23] Pasaogullari, U., and Wang, C. Y., 2004, "Two-Phase Transport and the Role of Micro-Porous Layer in Polymer Electrolyte Fuel Cells," Electrochim. Acta, **49**(25), pp. 4359–4369.

[24] Udell, K. S., 1985, "Heat Transfer in Porous Media Considering Phase-Change and Capillarity—The Heat Pipe Effect," Int. J. Heat Mass Transfer, **28**(2), pp. 485–495.

[25] Leverett, M. C., 1941, "Capillary Behavior in Porous Solids," Trans. AIME, **142**, pp. 152–169.

[26] Scheidegger, A. E., 1960, *The Physics of Flow Through Porous Media*, University of Toronto Press, Toronto.

[27] Springer, T. E., Zawodzinski, T. A., and Gottesfeld, S., 1991, "Polymer Electrolyte Fuel-Cell Model," J. Electroanal. Chem. Interfacial Electrochem., **138**(8), pp. 2334–2342.

[28] Dagan, G., 1989, *Flow and Transport in Porous Formations*, Springer, Berlin.

[29] Kulikovsky, A. A., 2002, "The Voltage-Current Curve of a Polymer Electrolyte Fuel Cell: "Exact" and Fitting Equations," Electrochem. Commun., **4**(11), pp. 845–852.

[30] Senn, S. M., and Poulikakos, D., 2004, "Polymer Electrolyte Fuel Cells With Porous Materials as Fluid Distributors and Comparisons With Traditional Channeled Systems," ASME J. Heat Transfer, **126**(3), pp. 410–418.

[31] Bevers, D., Wohr, M., Yasuda, K., and Oguro, K., 1997, "Simulation of a Polymer Electrolyte Fuel Cell Electrode," J. Appl. Electrochem., **27**(11), pp. 1254–1264.

[32] Lampinen, M. J., and Fomino, M., 1993, "Analysis of Free-Energy and En-

tropy Changes for Half-Cell Reactions," J. Electrochem. Soc., **140**(12), pp. 3537–3546.

[33] Senn, S. M., and Poulikakos, D., 2004, "Laminar Mixing, Heat Transfer and Pressure Drop in Tree-Like Microchannel Nets and Their Application for Thermal Management in Polymer Electrolyte Fuel Cells," J. Power Sources, **130**(1–2), pp. 178–191.

[34] Patankar, S. V., 1980, *Numerical Heat Transfer and Fluid Flow*, Hemisphere, New York.

[35] Mantzaras, J., Freunberger, S. A., Büchi, F. N., Roos, M., Brandstätter, W., Prestat, M., Gauckler, L. J., Andreaus, B., Hajbolouri, F., Senn, S. M., Poulikakos, D., Chaniotis, A. K., Larrain, D., Autissier, N., and Maréchal, F., 2004, "Fuel Cell Modeling and Simulations," Chimia, **58**(12), pp. 857–868.

Dynamics of Bubble Motion and Bubble Top Jet Flows From Moving Vapor Bubbles on Microwires

David M. Christopher
e-mail: dmc@tsinghua.edu.cn

Hao Wang

Xiaofeng Peng

Thermal Engineering Department,
Tsinghua University,
Beijing, China 100084

Rapid bubble sweeping along heated wires was observed during subcooled nucleate boiling experiments on very fine wires with jet flows emanating from the tops of the vapor bubbles for a variety of conditions. This paper presents experimental results with a numerical analysis of the physical mechanisms causing the experimentally observed bubble motion and jet flows. The results show that the moving bubble creates a nonuniform temperature distribution in the wire by cooling the wire as it moves along the wire with significant heat transfer in the wake behind the bubble. The results verify that the bubble motion is driven by the temperature difference from the front to the back of the bubble, which causes Marangoni flow. The Marangoni flow then thrusts the bubble forward along the wire with the calculated bubble velocities agreeing well with experimental measurements. In addition, the temperature difference from the bottom to the top of the bubble creates a vertical component to the Marangoni flow that results in the jet flows from the bubble tops. Comparisons with experimental observations suggest that the condensation heat transfer at the bubble interface is restricted by noncondensable gases that increase the surface temperature gradient and the resulting Marangoni flow. The numerical results also show that the heat transfer from the wire due to the Marangoni flow is significantly larger than the heat transfer due to the evaporation under the bubble.
[DOI: 10.1115/1.2039109]

1 Introduction

Nucleate boiling is encountered in many fields, such as energy utilization, manufacturing, and chemical processing. In the last part of the 20th century, boiling was increasingly applied to many new areas, such as spacecraft thermal control, electronic cooling, and bioengineering. However, no general theoretical models are available to accurately predict boiling heat and mass transfer for a variety of conditions and even the basic mechanisms are not entirely understood [1,2]. Dhir [1] presented an extensive review of the available research, but noted that "Boiling is an extremely complex and illusive process, which continues to baffle and challenge inquisitive minds."

The phenomenon of bubble motion along a heated wall has been investigated many times, especially in forced flow boiling, tube boiling and boiling on downward facing or inclined walls. During forced convection boiling on vertical walls with upflow [3], the bubbles slide along the heater wall and typically do not lift off, while with downflow, the bubbles either lift off directly from the nucleation site or slide a short distance and then lift off. The process of vapor bubble sliding appears to enhance the energy transfer from the heating surface as evidenced by larger heat transfer coefficients for upflow than for downflow for otherwise identical operating conditions. Similarly, the heat transfer for boiling around tubes is more due to bubbles sliding around the tubes than the nucleation on the surface [4–6]. Cornwell et al. [5] and Cornwell and Grant [6] showed that the heat transfer during bubble motion around tubes was largely through a thin layer of liquid under the bubble as the bubble slid.

On a microscale level, the flows in and around a vapor bubble attached to a wall during nucleate boiling drive the boiling heat transfer mechanisms. The development of digital measurement and visualization techniques has provided a new tool for studying the microscale heat transfer effects during boiling. Peng et al. [7] observed nucleation jets from inverted stationary vapor bubbles. Wang et al. [8,9] observed jet flows emanating from the microwire or from bubbles on the microwire including stationary bubbles and bubbles sweeping along microwires with jet plumes trailing behind the bubbles. Single and multiple jet flows were observed around both stationary and moving bubbles [10,11] with numerical investigations showing that for stationary bubbles, multiple jets would develop if the bubble diameter was larger than the wire diameter.

The analysis by Wang et al. [10] of the flow mechanisms for stationary bubbles on microwires showed that Marangoni flow is the most significant force driving the single phase jet flows that seem to flow out of the tops of vapor bubbles. Their experimental and numerical results both verified that natural convection had little effect on the flow field, most likely due to the very small size of the wires (0.1 mm in diameter). However, the flow field around a bubble on a flat surface, either above or below the heated surface, would be very different due to the much larger area.

The present paper presents experimental and analytical results describing the flow mechanisms driving jet flows observed emanating from nucleation bubbles moving along heated platinum microwires. The analysis is based on the experimental conditions for ethanol, but similar moving bubbles were also observed in water. The analysis considers the effects of natural convection and Marangoni flow as well as the heat transfer due to the convection and evaporation within the bubble.

2 Experimental System

Experimental observations of bubble sweeping along microwires were made using visual observations and particle image velocimetry (PIV) measurements of the fluid velocities. The visual observations provided qualitative descriptions of the bubble mo-

---

Contributed by the Heat Transfer Division of ASME for publication in the JOURNAL OF HEAT TRANSFER. Manuscript received December 1, 2004; final manuscript received June 15, 2005. Review conducted by: Jacob Chung.

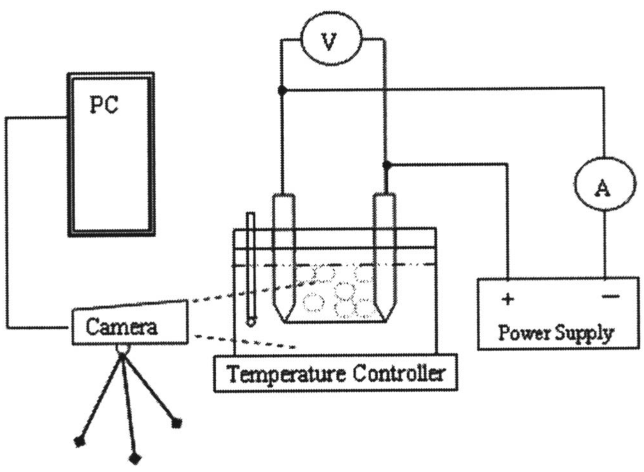

Fig. 1 Experimental system

tion, bubble interactions and bubble top jet flow characteristics as well as quantitative measurements of the bubble velocities. The PIV measurements supplemented these results with fluid velocity measurements in the bubble vicinity for both stationary and moving bubbles.

The test setup used a heated 0.1 mm or 0.025 mm diameter 49 mm long platinum wire immersed horizontally in a liquid pool as shown in Fig. 1. In other tests, the wire was placed vertically or at various other angles in the pool. The wire was heated with direct current from an Agilent 6031A power supply. The current was limited to less than 6 A so as to not melt the wire. The liquid pool was exposed to atmospheric pressure. Tests were conducted with both deaerated ethanol and deionized, deaerated water. The liquid pool was contained in a glass container 13 cm wide by 13 cm deep. The wire was 6–8 cm under the liquid surface. The liquid height varied during the experiment due to evaporation, but the evaporation rate was quite small even for the ethanol because the heat input was very low; therefore, the changes in liquid height were assumed to have no effect on the results. The entire physical setup was described in detail by Wang [12].

A small number of bubbles were generated by carefully controlling the heat input into the wire. Relatively high heat fluxes produced large numbers of bubbles as described by Wang [12]. At relatively low heat fluxes (5×10^5 to 1×10^6 W/m^2 for water and $(3-5)\times10^5$ W/m^2 for ethanol), individual bubbles would form on the wire and remain there for varying lengths of time. The bubbles had various sizes and appeared on all sides of the wire, often with hot jet flows emanating from the top of the bubble seemingly independent of gravity. The hot jets were observable since their densities differed from the surrounding liquid density, but the differences were only obvious at relatively large liquid subcoolings of 20 to 50°C. Wang et al. [10] showed that the jets on stationary bubbles are due to Marangoni flow around the bubble. At various times, the bubbles would suddenly start sweeping across the wire until they encountered some obstruction that would affect their motion, most often another bubble. The bubbles would then either just stop, reverse direction, move in tandem with the other bubble, or combine with the other bubble [11]. The distances that the bubbles moved along the wires varied considerably depending upon the positions of other bubbles (stationary or moving) on the wire. The number of sweeps back and forth along the wire also varied considerably as a function of the types of interactions that the bubbles had with the other bubbles [13].

Visual observations of the bubble motion and the jet structures were recorded with a Kodak SR_Ultra digital video camera at up to 2000 fps. Individual frames of the movies were analyzed with image analysis software which could be used to measure the bubble positions and diameters with accuracies of less than 7%. The bubble velocities were also measured with the software by comparing the bubble positions in every three to ten frames with uncertainties in the measured bubble velocities of about 7% since the frame speed was accurately controlled to the specified rate by the camera controller. The experimental photographs given in the results section also unfortunately show numerous other small circles in addition to the bubble and the wire. These circles, which do not move, are small spots on the glass walls of the container. The bulk liquid temperatures were measured with a thermocouple. The platinum wire temperature was determined from the wire resistance which was linearly related to the temperature. The wire resistance was calculated from the measured current and voltage into the wire. The uncertainty in the average wire temperature was approximately ±3 K, but significant local variations in the wire temperature are known to occur due to the significant heat transfer caused by the bubbles on the wire.

The PIV measurement system supplied by TSI used a CCD camera with zoom lenses and 1 μm aluminum seed particles to enhance the signal. The CCD camera was a PIVCAM 10–30, which has a minimum frame straddling of 200 ns and a sustained frame rate of 30 fps. The particles were illuminated by a sheet of laser light from a YAG laser. The particle locations in the pictures were then automatically evaluated and correlated using the Insight version 3.5 software supplied by TSI. The overall uncertainties in the velocities measured by the PIV system were estimated to be less than 6% [12].

3 Theoretical Analysis

3.1 Driving Mechanisms for Bubble Sweeping. The bubble motion is postulated to be a result of the horizontal Marangoni flow driven from the front to the rear of the bubble by the surface tension gradient due to the front bubble surface being warmer than the rear surface. As shown in Fig. 2(*a*), the large amount of heat transfer to the bubble depresses the wire and fluid temperatures in the vicinity of the bubble relative to the effect of natural convection. As the bubble begins to move (to the right) due to some perturbation, the leading edge of the bubble moves into warmer fluid while the trailing edge is exposed to cooler fluid. Thus, the front surface is warmer than the back surface creating Marangoni flow from the front to the back, as shown in Fig. 2(*b*), which provides thrust to further move the bubble forward. The bubble quickly accelerates until the increasing drag balances the thrust and the bubble appears to move at a uniform velocity. The bubble continues to move with a uniform velocity until it encounters some obstacle, typically another bubble. The bubble then either stops, rebounds so as to begin moving in the opposite direction,

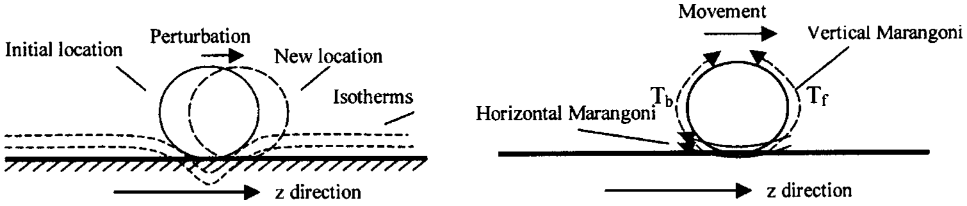

Fig. 2 Asymmetrical temperature distribution model [9]

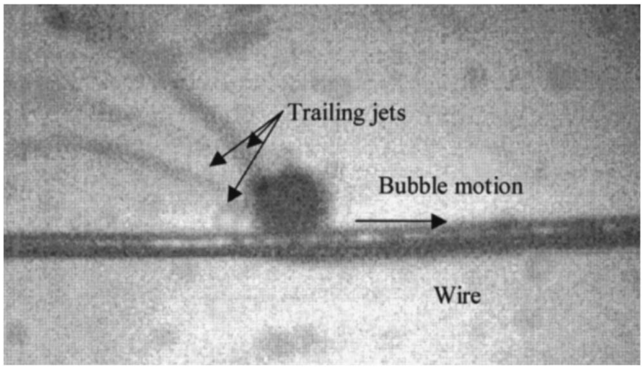

Fig. 3 Typical moving bubble with trailing jets

moves in tandem with the other bubble, or coalesces with the other bubble, which usually results in sufficient lift to overcome the downward Marangoni thrust. The bubble motion was analyzed numerically to verify if the Marangoni thrust was sufficient to drive the bubbles at the observed velocities.

As illustrated by the diagram in Fig. 2(*b*), vertical Marangoni flow also develops from the bottom to the top of the bubble due to the vertical temperature gradient along the bubble interface. Since the vertical temperature gradient is larger than the horizontal temperature gradient, the vertical velocities are larger with obvious jet plumes observed in the experiments. The jet plumes were especially evident in the jet plumes above stationary bubbles [14], but were also observed from moving bubbles, as shown in Fig. 3. As will be shown in Sec. 4 this vertical flow tended to push the bubbles towards the wire, as seen experimentally when a larger bubble jumped away from the wire as it overtook a smaller bubble, but was then immediately thrust back to the wire by the vertical Marangoni flow. The experimental observations also showed that the bubbles moved in various directions relative to gravity with little or no observable effect of the gravitational force, so this description of the mechanisms refers to a bubble on a horizontal wire only to simplify the description.

3.2 Numerical Solution of the Navier-Stokes Equations. A typical moving bubble is shown in Fig. 3. The measured bubble movement velocities were typically in the range of 20 to 60 mm/s with the bubbles very quickly accelerating to a steady-state speed and then suddenly stopping or reversing direction when encountering another bubble. The analysis only considers the steady-state bubble motion since the bubble velocities were constant most of the time. The three-dimensional flow geometry modeled in the analysis included the heated wire, the bubble with evaporation and condensation at its surface, and a large liquid region around the bubble. The bubble-wire geometry and coordinate system are illustrated in Fig. 4. The bottom surface of the bubble was assumed to be separated from the wire surface by a 2 μm thick microlayer based on visual observations made during the experiments that the bubble did not seem to be actually touching the wire and on previous [15] observations that the microlayer is 0.5–2.5 μm thick. The flow and heat transfer were analyzed by numerically solving the steady-state, laminar, three-dimensional Navier-Stokes equations with the energy equation in standard Cartesian coordinates with the origin of the coordinate system placed at the center of the bubble and the bubble motion along the *z* axis. The problem statement was transformed so that the bubble was stationary while everything else, the bulk fluid, the wire, and the outer surface, moved in the *z* direction at the desired bubble velocity. The Boussinesq approximation was used to model the natural convection.

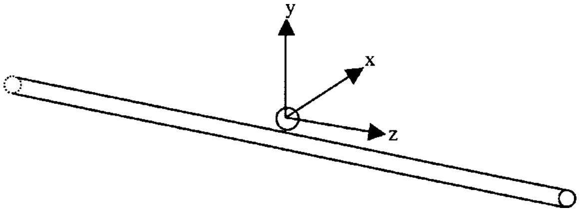

Fig. 4 Bubble-wire geometry and coordinate system

The energy equation boundary conditions included a heat source in the wire (Q) and a specified bulk subcooling temperature at the outer boundary which was 30 bubble diameters away from the wire. The outer boundary was specified as a moving, solid wall to facilitate convergence. Tests with larger boundaries and open (constant pressure) boundaries indicated that the outer boundary was sufficiently far removed to have no effect on the flow field near the bubble. The boundary condition at the bubble interface used to model the evaporation and condensation at the interface was based on a convective heat transfer coefficient model of the condensation and evaporation [2] given by

$$h = \frac{2\hat{\sigma}}{2-\hat{\sigma}} \frac{h_{fg}^2 \rho_v}{T_v} \left(\frac{\overline{M}}{2\pi \overline{R} T_v} \right)^{1/2} \left[1 - \frac{p_v}{2 h_{fg} \rho_v} \right] \tag{1}$$

and a vapor temperature equal to the saturation temperature for the pressure inside a bubble of the given size based on the Clausius-Clapeyron equation

$$T_v = T_s + \frac{2\sigma T_s}{h_{fg} \rho_v R_b} \tag{2}$$

For ethanol at atmospheric pressure with the bubble radius of 0.1 mm used in most of the calculations, the correction to the vapor pressure in Eq. (2) is only about 0.1°C. The accommodation coefficient in Eq. (1) is generally assumed to be 0.03 as suggested for water and ethanol [2].

The computational domain included the solid wire so that there were no boundary conditions in the *x* and *y* directions for the wire. The two ends of the wire in the ±*z* direction were assumed to have a zero temperature gradient. The wire was heated by a specified heat source term that was specified as described in Sec. 4.

The momentum equation boundary conditions at the wire were the no slip condition with the wire moving at the bubble velocity. The boundary condition for the momentum equation at the bubble interface was modeled using the Marangoni boundary condition

$$-\mu \left(\frac{\partial u_s}{\partial n} \right)_{R_b} = \frac{\partial \sigma}{\partial T} \left(\frac{\partial T}{\partial s} \right)_{R_b} \tag{3}$$

where *n* indicates the normal direction and *s* indicates the tangential direction to the interface. The inlet conditions were a specified uniform axial flow velocity equal to the bubble velocity with *u*, *v*, and *T* distributions calculated assuming only natural convection from the wire as would occur for an undisturbed wire in the liquid pool.

The equations were solved using the finite volume method with second-order central differencing of the advection terms. First-order upwind differencing was first used to approach a converged solution with the differencing method then changed to second-order central differencing to finish the calculation. A large jump in the wire temperatures was typically observed when the differencing method was changed.

The grid included about 320,000 tetrahedral elements with a double layer of hexahedrons on the bubble interface since the Marangoni boundary condition calculation is only accurate with hexahedrons. Calculations with about 450,000 elements yielded similar results, in terms of the bubble velocity, fluid velocities, and heat fluxes, to those described here. The results with about 120,000 elements were somewhat different with lower equilibrium bubble velocities and an unrealistic temperature distribution along the wire due to the restricted heat transfer between the bubble and the wire caused by the small number of nodes there. Consideration of the various grid distributions used to estimate the effect of the grid dependence suggests that the calculated equilibrium bubble velocities and the energy source values in the wire are accurate to within 15%.

3.3 Equilibrium Force Balance on the Bubble. The equilibrium bubble velocity (actually the velocities of the inlet, the wire, and the outer surface) was determined by balancing the pressure drag on the bubble and the thrust caused by the Marangoni flow. The pressure drag on the bubble was calculated by integrating the pressure component in the z direction over the bubble surface, as

$$F_P = \int p(\vec{n}\cdot k)dA_b \tag{4}$$

The thrust due to the Marangoni flow along the bubble interface was calculated by integrating the z component of the tangential shear stress $(\tau_{r,\phi})$ over the bubble surface, where the (r,θ,ϕ) spherical coordinate system is used for convenience with the coordinate ϕ as the polar angle originating from the z axis. The other component of the tangential shear stress $(\tau_{r,\theta})$ exerts no force in the z direction since it is always normal to the bubble motion in the z direction in the (r,θ,ϕ) spherical coordinate system. In spherical coordinates [16],

$$\tau_{r,\phi} = -\mu\left(\frac{1}{R_b\sin(\theta)}\frac{\partial u_r}{\partial \phi} + \frac{\partial u_\phi}{\partial r} - \frac{u_\phi}{R_b}\right) \tag{5}$$

The first term is zero since the radial component of the velocity at the interface is negligible as discussed in Sec. 4. Since the calculation is based on the three Cartesian velocities, the tangential velocity and its derivative in the normal direction in Eq. (5) are defined in terms of the Cartesian velocities and their derivatives in the Cartesian coordinate system. u_ϕ is given in Cartesian velocities as

$$u_\phi = \cos(\theta)\cos(\phi)u_x + \sin(\theta)\cos(\phi)u_y - \sin(\phi)u_z \tag{6}$$

The partial derivative in the radial direction in Cartesian coordinates is [17]

$$\frac{\partial}{\partial r} = \cos(\theta)\sin(\phi)\frac{\partial}{\partial x} + \sin(\theta)\sin(\phi)\frac{\partial}{\partial y} + \cos(\phi)\frac{\partial}{\partial z} \tag{7}$$

Since the geometry was always arranged so that the bubble was at the center, the trigonometric functions can be written in terms of the coordinates of the points on the bubble surface, as

$$\cos(\theta) = \frac{x}{\sqrt{x^2+y^2}}, \quad \sin(\theta) = \frac{y}{\sqrt{x^2+y^2}}, \quad \cos(\phi) = \frac{z}{R_b},$$

$$\sin(\phi) = \frac{\sqrt{x^2+y^2}}{R_b} \tag{8}$$

The total thrust exerted on the bubble would then be the horizontal component of $\tau_{r,\phi}$:

$$F_{thrust} = \int [-\tau_{r,\phi}\sin(\phi)]dA_b \tag{9}$$

After substitution of the Cartesian velocity components in Eq. (6) and the Cartesian derivatives in Eq. (7), the result can be written in terms of Cartesian coordinates using Einstein summation (repeated indices indicate summation) as

$$F_{thrust} = \int \frac{\mu}{R_b^3}\left[xz\left(x_i\frac{\partial u_x}{\partial x_i} + u_x\right) + yz\left(x_i\frac{\partial u_y}{\partial x_i} + u_y\right) - R_b^2\left(x_i\frac{\partial u_z}{\partial x_i} + u_z\right)\right]dA_b \tag{10}$$

A negative value indicates thrust while a positive value indicates drag. The steady-state bubble velocity occurs when the pressure force on the bubble given by Eq. (4) balances the thrust on the bubble given by Eq. (10).

4 Results

Vapor bubble movement along heated wires was observed experimentally and then analyzed by solving the Navier-Stokes and energy equations to model the flow around the bubble moving along a heated wire. For the analytical results, the solution domain also included the heated wire since the temperature gradients in the wire are the primary cause of the movement. The two bubble sizes analyzed in the calculations, with diameters of 0.2 mm and 0.4 mm, were typical of the experimentally observed bubbles. The heated wire was a 0.1 mm diameter platinum wire. The results reported here are based on the properties of ethanol at the boiling point, 77°C. Similar results were observed in water. The bulk liquid subcooling in the analyses was varied from 20°C to 50°C as in the experiments. For these conditions, the convective heat transfer coefficient at the bubble interface given by Eq. (1) is 153,000 $\mathrm{W/m^2\,K}$. The Marangoni number (Ma), based on a bubble diameter of 0.2 mm and a liquid subcooling of 30°C was about 1.6×10^4 for ethanol. For water, Ma would be about 2.3×10^4 for the same conditions, indicating that the Marangoni flow with water might be slightly stronger than with ethanol, but the differences would not be large.

Since these bubbles were relatively large, the saturation temperature at the vapor pressure inside the bubble would also be essentially 77°C. The wire temperatures in the experiments were 5°C–15°C above saturation with heat generation rates in the wire of about $1\times10^{10}\ \mathrm{W/m^3}$. However, since energy was also lost from the wire to the supports and there were numerous bubbles on the wire affecting the heat transfer and the wire temperature distribution, the measured heat generation rates in the wire were not accurate enough to be input directly into the calculations. Instead, the heat generation rate in the wire was adjusted until the evaporation and condensation rates in the bubble were in equilibrium, which gave reasonable values of the wire superheat and gave heat generation rates that were only somewhat below the experimentally measured values.

4.1 Experimental Results. Bubble sweeping on microwires was observed for a variety of conditions. Figure 5(*a*) shows a typical bubble moving to the right along the wire with a jet plume flowing from the top of the bubble. The bubble diameter was about 0.3 mm and its speed was about 40 mm/s. The 0.1 mm horizontal wire was in water with a bulk temperature of 40°C. The wire had an average heat generation rate of $2.9\times10^{10}\ \mathrm{W/m^3}$ and an average temperature of 106°C. The frame speed was 500 frames/s. A tenth of a second later, the bubble encountered another bubble which caused it to reverse direction and return with the same speed as shown in Fig. 5(*b*). The bubble moved back and forth several times across the wire for about half a second until other bubbles formed that changed the motion pattern. The jet flow from the top of the bubble trails behind the bubble as it moves down the wire. Vertical bubble top jets were observed emanating from the tops of stationary bubbles in other tests [14]. These jet trails were due to hot liquid rather than microbubbles which were clearly observed at higher heat fluxes.

Various kinds of interactions occurred when a moving bubble encountered another bubble. The interactions included reversal of the movement direction as shown in Fig. 5 without physical contact, both bubbles continuing in the same direction again without physical contact but as separate bubbles, both bubbles just standing still, and coalescence into one bubble. Figure 6(*a*) shows the same larger bubble as in Fig. 5 just 0.670 s after Fig. 5(*a*) still traveling at about 40 mm/s overtaking a smaller bubble with a diameter of 0.15 mm traveling at about 25 mm/s. In Fig. 6(*b*), the larger bubble has bounced up as it contacted and absorbed the smaller bubble. The bubble reached a maximum height of about 1

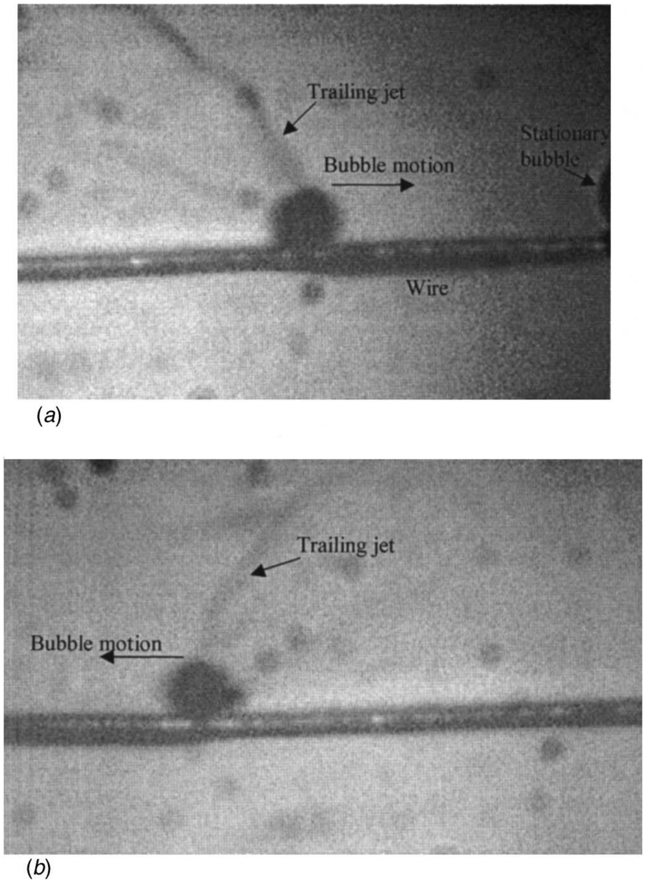

Fig. 5 (***a***) **Larger bubble moving to the right at about 40 mm/s in water for a heat flux of 7.29×10^5 W/m^2, a bulk liquid temperature of 40°C, and an average wire temperature of 106°C. (*b*) Same bubble moving to the left at the same speed 0.1 s later.**

wire diameter (0.1 mm) above the wire and was then pushed back against the wire in the next frame in Fig. 6(*c*) by the jet flow from the bubble top. The jet plume from the bubble seen in Fig. 6(*c*) was disturbed by the larger bubble's vertical jump and subsequent return to the wire as it contacted the smaller bubble.

Figure 7 shows another smaller bubble having a diameter of about 0.15 mm traveling back and forth at about 25 mm/s with a bubble top jet that was more evident in the movies than in this single still picture. Other bubbles were observed sweeping on horizontal, vertical, and inclined wires with the observed sweeping velocities seemingly independent of the orientation [12]. For stationary vapor bubbles, Wang et al. [14] observed that the measured velocities in the bubble top jets were also essentially independent of orientation relative to gravity with the effect of gravity only felt at least several bubble diameters away from the bubble as the warm jet expanded into the cooler liquid.

A typical set of PIV velocity measurements for a sweeping bubble are given in Fig. 8 for a somewhat slower bubble. The velocity vectors are only slightly inclined towards the back of the bubble because the bubble was moving relatively slowly. The larger measured liquid velocities immediately above the bubble ranged from 15–35 mm/s.

These and numerous other experimental observations abundantly illustrated the bubble sweeping phenomenon and the bubble top jets emanating from the bubbles. The measured sweeping velocities varied from 20 to 50 mm/s with the measured liquid velocities from 15–100 mm/s. These measured velocities

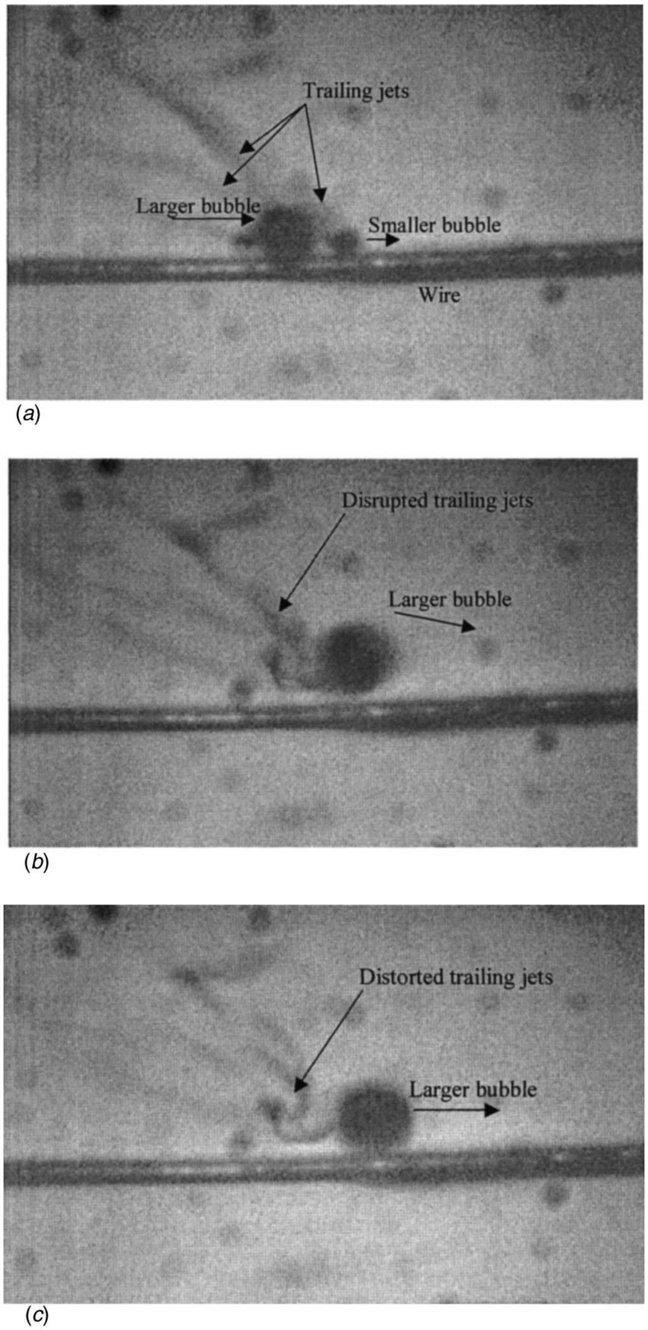

Fig. 6 (***a***) **Large bubble overtaking a smaller bubble at *t* =0.670 s in water with the same conditions as for Fig. 5. (*b*) Larger bubble has bounced over and absorbed the smaller bubble at *t*=0.674 s. (*c*) Larger bubble has been thrust back onto the wire and continues traveling to the right at *t*=0.676 s.**

were not strongly dependent on the type of liquid with similar velocities measured in water and ethanol, but were strongly dependent on the liquid subcooling.

4.2 Analytical Results. The flow and heat transfer around a typical bubble were analyzed for various bubble sizes and liquid subcoolings by numerically solving the three-dimensional laminar Navier-Stokes and energy equations with the Boussinesq buoyancy term and the Marangoni boundary condition at the bubble interface. The analysis only considered a single, isolated, constant volume bubble moving on the wire so the results are only applicable to relatively low heat flux, subcooled nucleate boiling con-

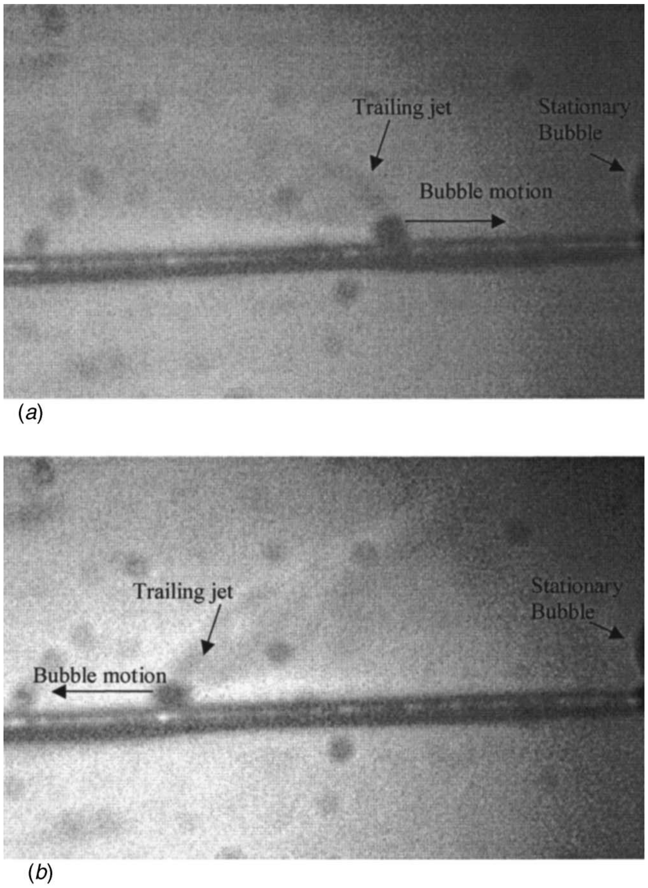

Fig. 7 (*a*) Small bubble about 0.15 mm in diameter moving at about 25 mm/s to the right. (*b*) Smaller bubble returning to the left at the same speed.

ditions. Larger heat fluxes would result in a much larger bubble density on the wire which would alter the temperature distribution in the wire and the flow field around the bubbles. Larger heat fluxes would also result in larger bubbles, especially as bubbles combine as they move along the wire, which would then tend to depart from the wire due to buoyancy.

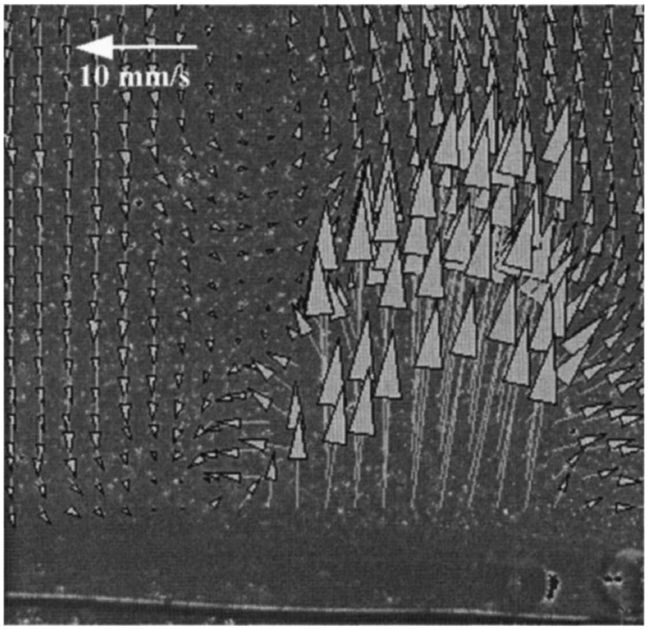

Fig. 8 PIV velocity measurements for 0.35 mm bubble moving in water with a bulk temperature of 40°C. The wire temperature was 108°C, the heat flux was 840 kW/m^2 and the bubble velocity was about 11 mm/s. The arrow represents the size scale of the velocity vectors.

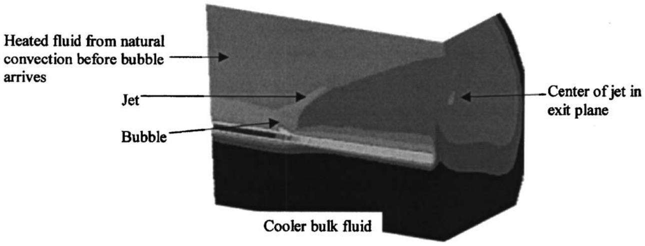

Fig. 9 Temperature contours in centerplane and exit plane of flow region showing asymmetric jet for bubble diameter of 0.4 mm and velocity of 47.1 mm/s

Since the analysis was based on a constant volume bubble and a steady bubble velocity, the heat generation rate in the wire and the bubble velocity were varied until the evaporation and condensation heat transfer rates in the bubble were in equilibrium and until the forces on the bubble were in equilibrium. The evaporation rate in the bubble is strongly related to the heat generation rate in the wire while the condensation rate is not so strongly related, so that increases in the wire heat generation rate increase the evaporation heat transfer relative to the condensation rate. The final average wire temperatures for the various cases were all within the experimental uncertainties of the measured temperatures. The calculated heat generation rates were somewhat lower than the measured rates due to heat losses in the experiments to the support posts and to larger bubble densities on the wire in the experiments than modeled in the numerical analyses. At the same time, the bubble velocity was varied until the pressure drag and the thrust were in equilibrium, which would indicate a steady-state velocity. The analysis showed that for these conditions, the bubble heat transfer rate could only be balanced if the condensation heat transfer coefficient within the bubble was much less than the evaporation rate. Marek and Straub [18] showed that the condensation heat transfer coefficient could be reduced by more than 90% by a very small amount of noncondensable gases in the bubble. The evaporation coefficient is probably not affected much by the noncondensable gases, or the effect is quite small, because such gases tend to accumulate at the condensing surface. A reduced condensation rate increases the Marangoni flow driving force because it increases the temperature gradient along the bubble interface. The calculations showed that for these conditions, the thrust balanced the pressure drag for condensation heat transfer coefficients that were at least 20 times smaller than the evaporation coefficient. For larger condensation heat transfer coefficients, the resulting smaller temperature gradient on the bubble interface resulted in less Marangoni flow, so that the thrust did not balance the pressure drag. In addition, smaller condensation heat transfer coefficients actually increased the heat transfer from the wire to the bubble by causing more Marangoni flow which enhanced the convection effects around the bubble.

Typical temperature contours along the centerplane passing though the center of the bubble and the center of the wire and along the exit plane of the computational region are shown in Fig. 9. These results are for a bubble moving to the left with a velocity of 47.1 mm/s, a diameter of 0.4 mm, a subcooling of 50°C, a heat generation rate of 9.8×10^9 W/m^3, an average wire temperature of 92.2°C (superheat of 15.2°C) and an evaporation/condensation heat transfer coefficient ratio of 100. The calculation was based on the properties of ethanol at its boiling point. Figure 9 shows that in this case the jet does not flow in the centerplane but is displaced to one side by a small amount. Since the computational region assumed symmetry and included only half of the

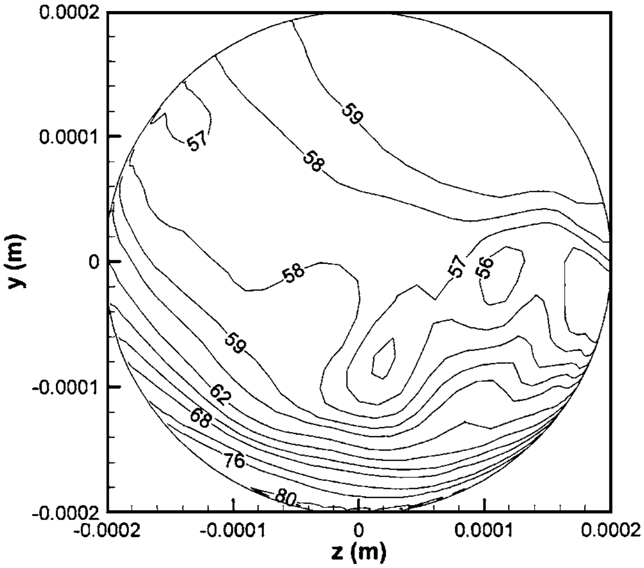

Fig. 10 Temperature contours on the bubble surface for a bubble moving to the left for the conditions in Fig. 9.

flow region, there are actually two symmetric jets on either side of the centerplane. The multiple jets were only observed with larger bubbles and were more evident at larger subcoolings. The smaller bubble (0.2 mm diameter) only produced single jets flowing along the centerplane. Multiple jets were also observed experimentally in the moving bubble experiments as well as in numerous stationary bubble experiments. The analyses for stationary bubbles showed that the multiple jets occurred when the bubble diameter was at least twice the wire diameter for the stationary bubbles [10]. Such a distinctive jet can only occur as a result of Marangoni flow along the interface. The calculated velocities near the bubble ranged from 50–100 mm/s which agrees with the range of the measured velocities for these conditions. In addition, the fluid velocities directly above the bubble were basically vertical which agrees with the experimental PIV measurements in Fig. 8 and indicates that the Marangoni induced velocities in the horizontal direction are much smaller than the velocities in the vertical direction. The temperature contours on the bubble interface are shown in Fig. 10 for the same conditions. The top and back sides of the bubble are the coolest while the bottom next to the heated wire is the hottest. The Marangoni effect would cause the liquid on the surface to flow towards these two minimum temperature locations with jets leaving the surface at these points. However, these jets quickly coalesce into one jet which in this case flows off to the side of the centerplane. The surface velocities are largest at the bottom where the temperature gradient is the largest and decrease upward along the interface. The surface velocities are the lowest between the two dark spots with a small recirculating zone above the bubble between these two points which reduces the heat transfer in that area and increases the surface temperature.

Figure 9 also shows that the moving bubble absorbs the energy in the boundary layer around the wire as it moves across the wire. The liquid temperature distribution in front of the bubble shows a normal heated boundary layer around the wire. However, the temperature distribution behind the wire shows that the liquid is substantially cooler due to the heat transfer to the bubble. The temperature difference between the liquid regions just in front of and just behind the bubble then contributes to the bubble surface temperature differences. The reduced heat transfer due to the higher fluid temperatures in the front would be somewhat increased by the higher heat transfer coefficients caused by the flow impinging the front of the bubble; however, since the front surface of the bubble is hotter than the back surface, the effect of the different fluid temperatures on the heat transfer is more important than the effect of the different heat transfer coefficients.

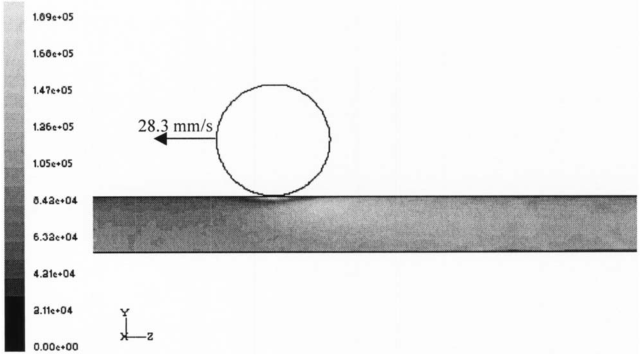

Fig. 11 Heat flux variation along the wire near the bubble. The light region behind the bubble experiences the greatest heat flux.

Other numerical results clearly showed that natural convection alone without Marangoni flow could not create such a distinctive plume but instead resulted in maximum velocities that were far less than measured experimentally. Therefore, the numerical results verify that Marangoni flow is the most likely mechanism causing the bubble to move. The thrust pushing the bubble forward is a result of the horizontal component of the velocities along the bubble interface given in Eq. (9), which is the result of the horizontal temperature gradient along the bubble interface. The surface temperatures in Fig. 10 decrease from the front towards the back (left to right in Fig. 10) with an average temperature difference from the front to the back in the vicinity of $y=0$ of about 3°C in this case. Although most of the flow is directed upwards, the flow has a small horizontal component that is sufficient to push the bubble forward. The temperature gradient from the front to the back occurs as the large amount of heat transfer associated with the bubble cools the liquid and the wire near the bubble, causing the back side of the bubble to be cooler than the front side.

The surface normal velocities due to the evaporation and condensation at the surface can also be estimated from the numerical results. The maximum evaporation rate, which occurred only in a very small region under the bubble near the wire, was approximately $8\times10^5\ \mathrm{W/m^2}$, which would result in a liquid velocity normal to the bubble interface of about 1 mm/s, which is far less than the velocities in that region. The condensation rates were far less since they were spread over a much larger area, so the velocities due to condensation would also be negligible. Although the surface normal velocities due to evaporation and condensation can be neglected, the heat transfer due to evaporation and condensation cannot be neglected since both have a significant effect on the temperature distribution around the bubble. In addition, if the evaporation and condensation heat transfer are neglected, the top of the bubble is much cooler than the bottom resulting in extremely large, unrealistic velocities due to the Marangoni flow. Therefore, the heat transfer effects were included in the numerical model while the normal velocities were not.

The heat flux variations along the wire near the bubble are shown in Fig. 11 for a typical case (ethanol with a subcooling of 30°C, a bubble diameter of 0.2 mm, a bubble velocity of 28.3 mm/s, a heat generation rate of $3.6\times10^9\ \mathrm{W/m^3}$ and an evaporation/condensation heat transfer coefficient ratio of 100). Although the maximum heat flux is directly under the bubble, the affected area under the bubble is quite small and not readily apparent in Fig. 11. Figure 11 shows another larger area of increased heat flux just behind the bubble and on the upper quadrant of the wire surface (the light colored region to the right of the bubble) which is due to the increased convection around the wire caused by the Marangoni flow around the bubble and by the flow disturbances in the wake behind the bubble. The heat transfer in this

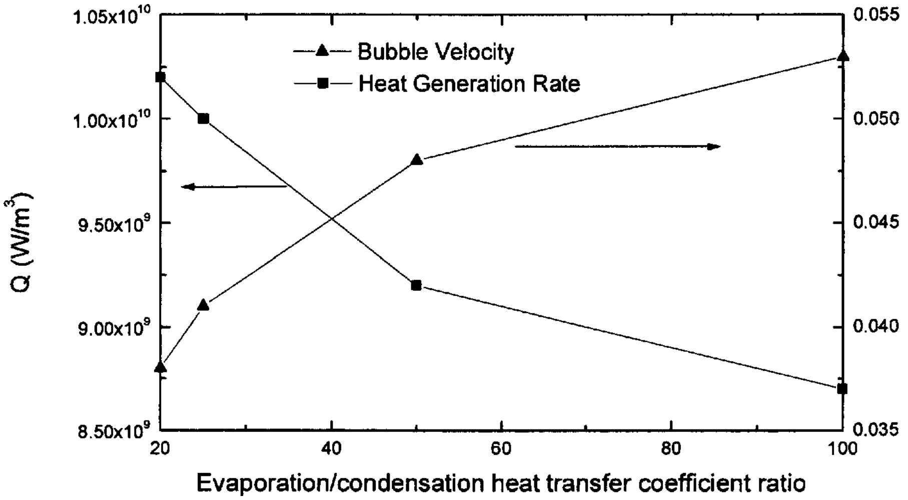

Fig. 12 Effect of evaporation/condensation heat transfer coefficient ratio on the bubble velocity for a 0.2 mm diameter bubble in ethanol and a subcooling of 50°C

region is enhanced as relatively cool fluid is drawn up from below the wire by the Marangoni effect so that it substantially increases the cooling of the wire in that area. The calculated heat transfer due to evaporation into the bubble for this case was 0.00044 *W*. The excess heat transfer in the light colored region shown in Fig. 11 (including the heat transfer due to the evaporation underneath the bubble), which was in excess of the average heat transfer over the entire wire, was 0.0027 W, significantly more than the heat transfer just due to evaporation. Therefore, the heat transfer due to the Marangoni driven flow is much greater than that due to evaporation for these conditions. In general, the heat transfer rates due to the Marangoni induced convection would be expected to be higher than the evaporation heat transfer rates for the highly subcooled nucleate boiling analyzed here which creates the large Marangoni flow rates. Smaller subcoolings or saturated boiling would create much smaller Marangoni driven flow rates, which would reduce the relative importance of the heat transfer due to the Marangoni flow.

The effect of the evaporation/condensation heat transfer coefficient ratio is shown in Fig. 12. In the calculations, the coefficient ratio was increased by keeping the evaporation coefficient constant at 153,000 $\mathrm{W/m^2\,K}$ while reducing the condensation coefficient. Figure 12 shows that as the ratio was increased from 20 to 100 (which corresponds to a reduced condensation coefficient), the amount of heat generation within the wire to maintain equilibrium between the evaporation and condensation rates decreased by about 20% since the reduced condensation coefficient reduces the evaporation/condensation heat transfer across the bubble. The evaporation heat transfer under the bubble decreased by more than half as the ratio was increased from 20 to 100, while the excess heat transfer from the wire surface behind the bubble decreased by about 20%. Figure 12 also shows that the bubble velocities increased with increasing ratios because the reduced condensation increases the temperature differences around the bubble, which in turn increases the Marangoni flow in both the vertical direction, which pushes the bubble against the wire, and in the horizontal direction, which increases the bubble velocity. Ratios of 10 or less still generated a jet flow, but did not have enough of a temperature difference from front to back to move the bubble.

The effects of the liquid subcooling on the bubble velocity and the heat generation rate in the wire are shown in Fig. 13 for 0.2 mm and 0.4 mm diameter bubbles. As expected, the required heat generation rate in the wire increases dramatically as the subcooling is increased due to the increased heat transfer from the bubble to the cooler liquid and the increased natural convection from the wire. The bubble velocity also increases as the increased subcooling increases the temperature gradients along the bubble surface, which increase the vertical Marangoni flow along the interface that in turn accentuates the horizontal temperature difference and the resulting horizontal Marangoni flow. The velocities of the larger bubble are somewhat less than those of the smaller bubble as the increased drag of the larger bubble does not overcome the larger temperature differences (but smaller temperature gradients) on the bubble interface. The heat transfer rates due to the larger bubble are greater than those due to the smaller bubble since the larger surface area of the larger bubble transfers more heat despite the lower velocities.

Experimental observations showed that the bubble top jet flows are essentially independent of orientation relative to gravity with bubble top jet flows going sideways and down as well as up. Bubble motion was also observed experimentally on vertical wires with bubbles moving both up and down the wire at essentially the same velocities; however, bubbles were not observed moving underneath heated horizontal wires, even though stationary bubbles were observed underneath wires. The numerical results confirmed that bubble motion under the wire is less likely with a much lower bubble velocity of 8 mm/s predicted for the 0.2 mm diameter bubble with a subcooling of 30°C (rather than 28.3 mm/s for a bubble on top of the wire). The bubble moves much slower because the heated boundary layer under the wire is much smaller than on top of the wire so that as the bubble moves along the wire, the temperatures around the bubble are more uniform which reduces the Marangoni flow driving the bubble. Even though the bubble velocity was reduced, the heat transfer due to a bubble

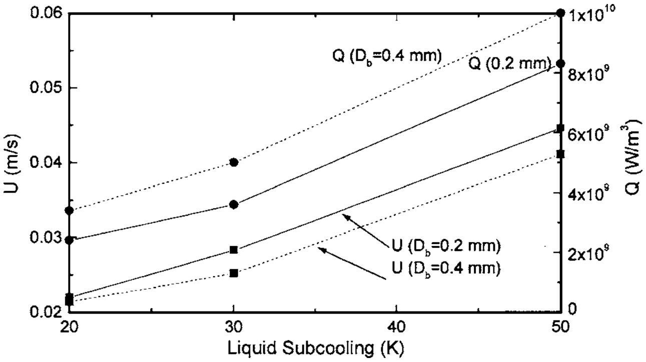

Fig. 13 Effect of subcooling on the heat generation rate and bubble velocity for 0.2 mm and 0.4 mm diameter bubbles in ethanol with an evaporation/condensation heat transfer coefficient ratio of 100

underneath the wire was increased by about 30% relative to the case with a bubble on top of the wire. Of course, buoyancy would also tend to push a moving bubble from underneath the wire to on top of the wire, which would reduce the probability of seeing moving bubbles underneath wires.

5 Conclusions

The heat transfer and fluid motion around a nucleation bubble moving on a heated wire in a subcooled liquid were investigated experimentally and analyzed numerically by solving the Navier-Stokes equations with the energy equation. The bubble velocities were calculated by balancing the drag around the bubble with the horizontal thrust due to the Marangoni flow that propels the bubble forward. Both the experimental and numerical results focused on individual bubbles moving at steady velocities along the wire, so that the results are relevant to relatively low heat flux, subcooled nucleate boiling. Smaller subcoolings or saturated nucleate boiling conditions are not expected to produce the observed bubble motion. The experiments showed bubbles moving on both vertical and horizontal wires with jets of hot liquid emanating from the bubble tops flowing far into the bulk liquid indicating that buoyancy does not have a major effect on the observed bubble motions and jet flows. The numerical results showed that the bubble motion must be driven by Marangoni flow due to the temperature difference between the front and back surfaces of the bubble with significant jet flows into the bulk liquid and that buoyancy had little effect on the bubble motion and liquid velocities. The evaporation and condensation velocities normal to the interface were too small to significantly influence the velocity field; although the heat transfer due to the evaporation and condensation is very significant. The results also showed that the temperature gradients on the bubble surface and the resulting Marangoni flow will not be sufficiently strong unless noncondensable gases are present to reduce the condensation heat transfer at the interface. The calculated fluid velocities and bubble velocities all agreed well with the measured velocities.

The numerical results show that the convective heat transfer from the wire due to the Marangoni induced flow is substantially larger than the heat transfer due to evaporation under the bubble. Thus, the bubble motion and the Marangoni flow both contribute to enhancing the heat transfer from the surface for the relatively large liquid subcoolings investigated here. The numerical results also show that the bubble velocity increases at larger liquid subcoolings with slightly slower velocities for larger bubbles.

Acknowledgments

This project was supported by the National Natural Science Foundation of China (Contract No. 50476014).

Nomenclature

A_b = bubble surface area
F_p = pressure force on bubble
F_{thrust} = thrust acting on bubble
$\bar{M}$ = vapor molecular weight
Ma = Marangoni number$=\gamma\Delta T_{sub}\, d/\mu\alpha$
Q = distributed energy source term in wire
R_b = bubble radius
$\bar{R}$ = universal gas constant
T = liquid or wire temperature
T_s = saturation temperature
U = bubble movement velocity
d = bubble diameter
h = equivalent interface heat transfer coefficient
h_{fg} = heat of vaporization
k = z-direction vector
n = normal direction
p = pressure
p_v = vapor pressure
r = radial coordinate
s = tangential direction
t = time
u_s = bubble surface velocity
x, y, z = Cartesian coordinates
α = thermal diffusivity
ϕ = polar angle from the z axis
μ = dynamic viscosity
ρ_v = vapor density
θ = azimuthal angle in the x-y plane from the x axis
σ = surface tension
$\hat{\sigma}$ = accommodation coefficient
$\tau_{r,\theta}$ = tangential shear stress
$\tau_{r,\phi}$ = tangential shear stress

Subscripts

b = back side of bubble, bubble
f = front side of bubble
i = summation index
r, θ, ϕ = spherical coordinate directions
p = pressure force
s = saturation, bubble surface
sub = subcooling
x, y, z = Cartesian coordinate directions
v = vapor

References

[1] Dhir, V. K., 1990, "Nucleate and Transition Boiling Heat Transfer Under Pool Boiling and External Flow Conditions," *Heat Transfer 1990* (*9th International Heat Transfer Conference*, Jerusalem), Hemisphere, New York, 1, pp. 129–155.
[2] Carey, V. P., 1992, *Liquid Vapor Phase-transition Phenomena*, Hemisphere, New York, pp. 112–120.
[3] Thorncroft, G. E., Klausner, J. F., and Mei, R., 1998, "An Experimental Investigation of Bubble Growth and Detachment in Vertical Upflow and Downflow Boiling," Int. J. Heat Mass Transfer, **41**(23), pp. 3857–3871.
[4] Cornwell, K., 1990, "The Role of Sliding Bubble in Boiling on Tube Bundles," *Heat Transfer 1990* (*9th International Heat Transfer Conference*, Jerusalem), Hemisphere, New York, pp. 455–460.
[5] Cornwell, K., Houston, S. D., and Addlesee, A. J., 1992, "Sliding Bubble Heat Transfer on a Tube Under Heating and Cooling Conditions," *Pool and External Flow Boiling, Engineering Foundation Conference*, ASME, New York, pp. 49–53.
[6] Cornwell, K., and Grant, I. A., 1998, "Heat Transfer to Bubbles Under Horizontal Tubes," Int. J. Heat Mass Transfer, **41**(10), pp. 1189–1197.
[7] Peng, X. F., Huang, Y. J., and Lee, D. J., 2001, "Transport Phenomenon of a Vapor Bubble Attached to a Downward Surface," Int. J. Therm. Sci., **40**(9), pp. 797–803.
[8] Wang, H., Peng, X. F., Wang, B. X., and Lee, D. J., 2002, "Jet Flow Phenomena During Nucleate Boiling," Int. J. Heat Mass Transfer, **45**(6), pp. 1359–1363.
[9] Wang, H., Peng, X. F., Wang, B. X., and Lee, D. J., 2003, "Bubble Sweeping Mechanisms," Sci. China, Ser. E: Technol. Sci., **46**(3), pp. 225–223.
[10] Wang, H., Peng, X. F., Christopher, D. M., and Lin, W. K., 2005, "Investigation of Bubble-Top Jet Flow During Subcooled Boiling on Wires," Int. J. Heat Fluid Flow, **26**(3), pp. 485–494.
[11] Wang, H., Peng, X. F., Wang, B. X., Lin, W. K., and Pan, C., 2005, "Experimental Observations of Bubble Dynamics on Ultrathin Wires," Exp. Heat Transfer, **18**(1), pp. 1–11.
[12] Wang, H., 2004, "Multiplicity of Nucleation and Near-wall Bubble Dynamics of Subcooled Boiling on Micro Wires," Ph.D thesis, Tsinghua University, Beijing.
[13] Lu, J. F., and Peng, X. F., "Bubble Separation and Collision on Thin Wires During Subcooled Boiling," unpublished.
[14] Wang, H., Peng, X. F., Lin, W. K., Pan, C., and Wang, B. X., 2004, "Bubble-top Jet Flow on Microwires," Int. J. Heat Mass Transfer, **47**, pp. 2891–2900.
[15] Sharp, R. R., 1964, "The Nature of Liquid Film Evaporation during Nucleate Boiling," NASA TND-1997.
[16] Bird, R. B., Stewart, W. E., and Lightfoot, E. N., 2002, *Transport Phenomena*, Wiley, New York.
[17] Weisstein, E. W., 1999, "Spherical Coordinates," From Math World—A Wolfram Web Resource, http://mathworld.wolfram.com/SphericalCoordinates.html.
[18] Marek, R. and Straub, J., 2001, "The Origin of Thermocapillary Convection in Subcooled Nucleate Pool Boiling," Int. J. Heat Mass Transfer, **44**, pp. 619–632.

Yoav Heichal

Sanjeev Chandra[1]
e-mail: chandra@mie.utoronto.ca

Departmental of Mechanical & Industrial
Engineering,
University of Toronto,
5 King's College Road,
Toronto, Ontario, Canada M5S 3G8

Predicting Thermal Contact Resistance Between Molten Metal Droplets and a Solid Surface

Thermal contact resistance between molten metal droplets (aluminum alloy 380 and bismuth) and solid plates (steel and brass) was measured experimentally. The diameter of the droplets was 4 mm, *and droplet impact velocity ranged between* 1 *and* 3 m/s. *Substrate temperature was varied from* 25 to 300°C *and roughness from* 0.06 to 5.0 μm. *Substrate temperature variation under impacting droplets was measured using fast temperature sensors that had a response time of* 40 ns *and recorded substrate temperatures at five different radial locations under each droplet. Thermal contact resistance during the first few milliseconds of impact was obtained by matching measured surface temperature variation with an analytical solution of the one-dimensional transient heat conduction equation. An analytical model of the deformation of a free liquid surface in contact with a rough solid was used to calculate the true area of contact between them and, thereby, the thermal contact resistance. Test results agreed well with predictions from the analytical model. Thermal contact resistance values ranged from* 10^{-7} to 3×10^{-6} m^2 K/W, *increasing with surface roughness and decreasing with rising impact velocity.* [DOI: 10.1115/1.2039114]

1 Introduction

Molten metal hits a cold, solid surface and freezes rapidly in many manufacturing processes, such as die casting, spray coating, and melt spinning. Knowing the rate of heat transfer at the solid-liquid interface is crucial in designing such processes because it determines the rate of metal solidification and also metallurgical properties, such as grain size and structure. If metal injected into a die through narrow passages freezes too rapidly, it may fail to fill the cavity completely. During spray deposition, the shape of splats formed by impact and solidification of molten droplets depends on their solidification rate, which influences physical properties of the deposit, such as porosity and roughness [1].

When molten metal comes suddenly in contact with a rough, solid surface, air is trapped in crevices at the liquid-solid interface, creating a temperature difference between the molten metal and the substrate, whose value depends on surface finish, contact pressure, and material properties. To quantify the magnitude of this effect, the thermal contact resistance (R_c) is defined as the temperature difference between the droplet (T_d) and substrate (T_s) divided by the heat flux (q'') between the two

$$R_c = \frac{T_d - T_s}{q''} \tag{1}$$

Two approaches have been used in the past to evaluate thermal contact resistance. One way is to measure, experimentally, the cooling rate of the metal and then to calculate the contact resistance, assuming there is no temperature gradient in the splat and the substrate is at constant temperature [2]. More sophisticated techniques use a numerical model of heat transfer within the substrate and splat and account for temperature gradients within them [3]. The second method is indirect, in which microstructural properties, such as the dendrite arm spacing or eutectic interlamellar spacing, are measured and then the cooling rate is evaluated from a known relationship between the cooling rate and the relevant parameter [4].

Wang and Matthys [5] reviewed much of the available literature on measurements of thermal contact resistance (or its reciprocal, the thermal contact conductance, which some authors prefer to use) and compiled an exhaustive list of data available in the literature. Values of contact resistance show a large range of values, from 10^{-3} to 10^{-6} m^{2}K/W, and depend on several parameters, such as the physical properties of liquid metal and substrate, surface roughness, and liquid impact velocity. They also depend on the response time of the temperature measurement method. Solidification starts very rapidly when molten metal contacts a colder substrate, typically within milliseconds; unless the temperature-measuring instrument is much faster, the thermal contact resistance measured is that of a solid-solid interface, not solid-liquid.

A widely used method of measuring contact resistance has been to release a drop of molten metal onto a solid surface, measure transient substrate or droplet temperature, and fit the data to a numerical or analytical heat transfer model to calculate contact resistance [3,6–9]. Liu et al. [3] and Wang and Matthys [6] used an optical pyrometer with a 1.5 ms response time to measure the cooling rate of nickel and copper droplets falling on copper plates. Contact resistance was initially low ($\sim 10^{-6}$ m^{2}K/W) and then increased rapidly ($R_c > 10^{-4}$ m^{2}K/W) with the onset of solidification. Loulou et al. [7] used thermocouples with a response time of 0.1 ms to measure substrate and droplet temperature for impacting tin, lead, and zinc drops and calculated $R_c \sim 10^{-4}$ m^{2}K/W at times much after the droplet had solidified. Aziz and Chandra [8] used a thermocouple with a 10 μs response time to record substrate temperature variation under tin droplets and used an analytical heat transfer model to calculate $R_c \sim 10^{-6}$ m^{2}K/W. Wang and Qiu [9] measured heat transfer to a copper block on whose surface was sputtered a thin Constantan film that acted as a thermocouple with a 5 μs response time. When the block was dropped onto the surface of a pool of molten solder from heights of a few centimeters, contact resistances of 10^{-5} m^{2}K/W were recorded, decreasing with greater impact velocity.

---

[1] Corresponding author.

Contributed by the Heat Transfer Division of ASME for publication in the JOURNAL OF HEAT TRANSFER. Manuscript received February 8, 2005; final manuscript received June 9, 2005. Review conducted by: Ranga Pitchumani.

Table 1 Molten metal properties

	Tin	Bismuth	Aluminum 380
Melting point [°C]	232	271	*solidus:* 538 *liquidus:* 593
Thermal conductivity [W/mK]	32	7.9	109
Specific Heat [J/kgK]	253	120	963
Density [kg/m^3]	6970	9750	2760
Surface Tension [N/m]	0.53	0.37	0.89

The large volume of contact resistance data available [5] produces a rather confusing picture. Values of contact resistance span several orders of magnitude, and it is not clear how much of it is based on true measurement of solid-liquid contact. There is also no general theory that would allow generalization of experimental measurements or to predict contact resistance for other material properties, surface roughness, or liquid impact velocity.

This study had three principal objectives. First, to develop a sensor to measure substrate temperature under impacting molten metal droplets with a response time of <1 μs, much less than the spreading time of a droplet (typically $>2-3$ ms), ensuring that we recorded temperatures prior to the onset of solidification. The second objective was to measure contact resistance for a range of substrate and droplet properties, substrate temperature, substrate roughness, and droplet impact velocity. Finally, we wanted to develop an analytical model that could predict thermal contact resistance at the interface between a liquid-metal and solid surface and validate the model using our experimental results.

We formed droplets ($\sim$4 mm dia) of molten aluminum 380 alloy and bismuth and dropped them onto a flat horizontal plate made of either steel (H-13 tool steel or 303 stainless steel) or brass. These metals were chosen to give a wide range of material properties, such as density, surface tension, and thermal conductivity; Tables 1 and 2 list thermophysical properties of both droplet and substrate materials. Initial substrate temperature was varied from 25 to 300°C, impact velocity from 1 to 3 m/s, and average surface roughness from 0.06 to 5.0 μm. We recorded substrate temperature evolution under impacting droplets and used a one-dimensional heat conduction model in the substrate to calculate thermal contact resistance. A model of the deformation of the free liquid surface in contact with a rough solid was used to calculate the true area of contact between them and, therefore, the thermal contact resistance.

2 Experimental Methods

Molten aluminum alloy 380 (Al 85.5%, Si 8.5%, Cu 4%, Fe 2%) and bismuth (99.9% pure) droplets were formed with a pneumatic droplet generator. The drop generator consisted of a heated graphite chamber containing molten metal. Droplets were forced out through a 2.0 mm dia synthetic sapphire nozzle set in the bottom of the chamber by applying a rapid pulse of compressed nitrogen. Cheng et al. [10] have given a detailed description of the droplet generator and its operation. Droplet size was kept constant at 4.0 mm in all experiments. Measurements of droplet weight showed drop-to-drop variation was less than ±2%. The droplet generator was supported on a frame so that its height above the substrate could be adjusted, giving impact velocities of $1-3$ m/s.

Test surfaces (50.8 mm × 50.8 mm × 6.35 mm in size) were made of either H-13 tool steel, 303 stainless steel, or brass and bolted to a copper heating block containing two 125 *W* cartridge heaters. Substrate temperature could be set to within ±1°C using a temperature controller. The test surface and heater block assembly were mounted on two high-precision stages, which permitted accurate positioning of the temperature sensors under impacting droplets.

Table 2 Substrate properties

	H13 Tool Steel	SS303	Brass 330
Thermal conductivity [W/mK]	24	15	115
Specific Heat [J/kgK]	460	500	500
Density [kg/m^3]	7800	8027	8500

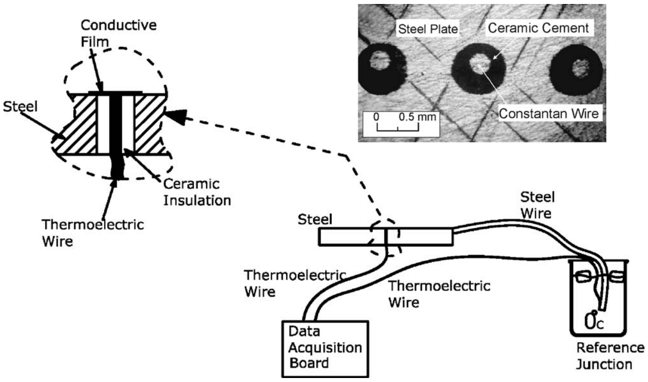

Fig. 1 Schematic diagram of a thin-film thermocouple. The inset shows a photograph of three thermocouples spaced 1.15 mm apart.

Test surfaces were finished by placing them on an electric belt sander, producing surface grooves in the direction of belt motion. Belts with grit sizes between 50 and 90 produced average surface roughness (R_a) between 5.0 and 0.5 μm. More polished surfaces ($R_a = 0.06$ μm) were created with 200–300 grit sand paper. Average surface roughness was measured with a surface profilometer (PDI Surfometer 400, Precision Devices Inc., Milan, MI), with the stylus moving at right angles to the direction of surface grooves. Averages of five measurements were recorded for each surface; individual roughness measurements were reproducible within ±2% of the mean for each surface.

Photographs of droplet impact [11] showed that they spread and flattened out in $\sim$2 ms from a nominal diameter of 4 mm to a maximum diameter of 12.0 mm. To record surface temperature variation in this time required a temperature sensor with a response time of, at most, a few microseconds. Thin film resistance temperature sensors proved too delicate to survive contact with molten metal droplets. Aziz and Chandra [8] used a commercially available thermocouple with a 10 μs response time. However, attempts to change surface roughness by sanding or grit blasting destroyed the thermocouple junction. For this study we required a temperature sensor with response time of <1 μs that was rugged enough to withstand contact with molten aluminium. The sensor had to be built on both rough and smooth metal surfaces.

Figure 1 shows a schematic diagram of the thin film thermocouple used. The conductive substrate (either H-13 tool steel, 303 stainless steel, or brass 330) acted as one of the thermocouple materials. A 0.254 mm dia Constantan wire (SPCI-010, Omega Engineering Inc., Stamford, CT) was inserted through a 0.57 mm dia hole drilled in the substrate and held in place by ceramic cement that also acted as an electrical insulator between the wire and substrate. The inset to Fig. 1 shows a photograph of three sensors spaced 1.15 mm apart, viewed from above. A graphite rod, sharpened to a fine point, was drawn across the surface under a microscope, leaving a thin conductive film that made an electrical connection between the wire and surrounding steel. This could be done in a repeatable manner by measuring the electrical resistance between the wire and surface and applying enough graphite to give a resistance of $30-70$ Ω. Changes to surface roughness, if any, were confined to a very small area as the graphite film was only about 200 μm long. Heichal [11] has given further details of sensor fabrication.

The voltage difference between the two junctions formed where the conductive film contacted the steel substrate and the wire, and a third junction kept in an ice bath at 0°C was a function of the temperature of the thin film. The steel wire (see Fig. 1) was machined from the same block of H-13 tool steel as the substrate, inserted into a hole in the plate, and hammered with a center punch into place to give a good electrical connection. To calibrate thermocouple junctions they were placed in a small, variable temperature furnace. Substrate temperature was measured with an accuracy of ±1°C using two K-type thermocouples attached to the substrate. A multimeter (HP3468A, Hewlett-Packard, Palo Alto, CA) measured the thermoelectric voltage generated between the thin-film thermocouple and its reference junction with a resolution of 1 μV.

Calibration of the thermocouples was done by increasing substrate temperature from room temperature to 650°C in increments of 50°C. The graphite film was destroyed by oxidation when the temperature was kept above 600°C for an extended period of time; at lower temperatures, the oxidation rate was low enough to not affect the film during experiments. At each setting, the surface temperature was allowed to reach steady state and the voltage generated by the thermocouple recorded. The surface was then allowed to cool with temperature decrements of 50°C, and the voltage noted again. This process was repeated twice for each thin-film thermocouple. The results were reproducible within ±9 μV, corresponding to an error of ±0.2°C. A fourth-order polynomial was fitted to each set of data. The voltage outputs of steel-Constantan and brass-Constantan junctions were very similar to those of standard iron-Constantan (J-type) and copper-Constantan (T-type) thermocouples, respectively.

Film thickness was estimated by measuring the surface area of the film under a microscope and its electrical resistance, which was typically 30–70 Ω. Knowing the specific resistivity of the material and assuming the film was uniform, its thickness could be estimated. Thicknesses varied from 0.1 to 2 μm in our test, and this variation had no effect on the sensor output voltage. If radiant heat impinges on a thin film of thickness L, the time t_r for the thermal disturbance to propagate through the thickness of the film may be estimated, assuming one-dimensional transient heat conduction, by $t_r \sim L^2/\alpha$, where α is the thermal diffusivity of the graphite film, with a value of $\sim 1.5 \times 10^{-5}$ m^2/s. Assuming $L = 0.5$ μm, t_r is ~17 ns, which is extremely fast for a temperature sensor. The response time of the thermocouple was tested by exposing it to a 15 ns long, 0.3 μJ pulse from a diode-pumped Nd:YAG laser, while recording its output using a digital oscilloscope. The response time of the sensor was confirmed to be <40 ns [11].

Substrate temperature variation under an impacting droplet was measured by an array of thin-film thermocouples spaced 1.15 mm apart. In the 2 ms duration of measurement, heat penetrated into the surface only to the depth of a few microns. Therefore heat losses because of conduction along the thermocouple wire produced negligible error in temperature measurements. The voltage generated by the thin-film thermocouples was recorded by a data acquisition system (NI PCI-MIO-16XE-10, National Instruments Inc., Austin, TX) connected to a personal computer. The data were stored in real time on the DAQ system buffers and downloaded onto the personal computer hard drive. The voltage measurements recorded by the DAQ system had a resolution of 1 μV, and the sampling rate varied from 10 to 50 KHz, depending on the number of sensors that were sampled.

3 Results and Discussion

3.1 Experimental Results Figure 2 shows the surface temperature variation of the H-13 tool steel substrate during the impact of an aluminium 380 alloy droplet with an initial temperature of 630°C (the liquidus temperature of the alloy, where it starts melting, is 593°C; the solidus temperature is 538°C). Temperature gradients within droplets were negligible, since the droplet Biot number was always much less than 1. The thermocouple at one end of the array was located exactly at the point of impact ($r=0$), and other temperature measurements were done at five different radial locations spaced 1.15 mm apart. The substrate was mounted on two micrometer stages, which were used to align it precisely under the droplet generator nozzle. The surface temperature, initially at 25°C, increased after the impact, reaching a maximum of ~500°C after 3.0–5.0 ms. The temperature variations at different radial locations under the droplet were approximately the same during the droplet impact process ($t < 5$ ms), with the maximum temperature at the center of the splat. Surface temperature at $r=4.6$ mm, close to the rim of the splat, decreased substantially at $t=25$ ms due to curl up of the splat rim as it cooled and contracted.

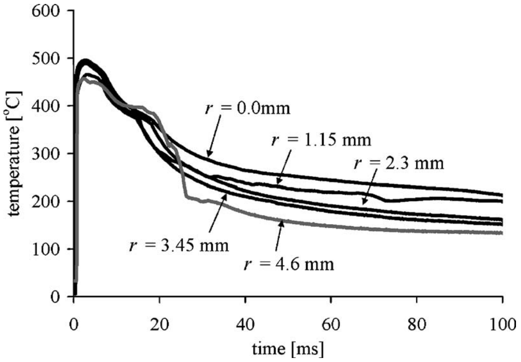

Fig. 2 Surface temperature variation of a H-13 tool steel substrate during the impact of an aluminium 380 alloy droplet with an initial temperature of 630°C. Initial substrate temperature 25°C, droplet impact velocity 3 m/s, and surface roughness 0.5 μm.

During the initial impact and spreading of the droplet, heat transfer to the surface was, for all practical purposes, one-dimensional. Considering the 6.35 mm thick steel plate to be a semi-infinite body for the ~2 ms droplet spread time, an analytical solution to the transient, one-dimensional heat conduction equation in the substrate can be obtained [12] assuming the droplet remains isothermal during impact and thermal contact resistance (R_c) at the solid-liquid interface is constant. Surface temperature T_s variation is given by

$$T_s = T_{s,0} + (T_{d,0} - T_{s,0})\left[1 - \exp\left(\frac{\alpha_s t}{(R_c K_s)^2}\right)\mathrm{erfc}\left(\frac{\sqrt{\alpha_s t}}{R_c K_s}\right)\right] \quad (2)$$

where $T_{s,0}$ and $T_{d,0}$ are the initial surface and droplet temperatures, K_s and α_s are the thermal conductivity and thermal diffusivity, respectively, of the substrate, and t is time.

The above assumptions are valid for the short, initial period of time in which droplet temperature can be assumed to be uniform. Contact resistance was estimated by matching the predicted surface temperature from Eq. (2) with experimental surface temperature measurements $[T_s(t)]$ for the first 2 ms after impact, when the droplet was still spreading. A least-squares fit was used to determine the value of contact resistance that gave the best match between theoretical and experimental temperature variations. Figure 3 shows a typical surface temperature measurement for a droplet landing on a surface initially at 300°C and calculated variations for different values of R_c. Best fit was achieved with $R_c = 2.4 \times 10^{-6}$ m^2 K/W. Similar values have been reported earlier for tin droplets landing on stainless-steel substrates [8]. The predicted temperature variation was quite sensitive to the value chosen of R_c.

Figure 4 summarizes our measurements of thermal contact resistance of molten aluminum 380 droplets on an H-13 tool steel substrate, for different initial substrate temperatures and average surface roughness. Each data point represents the average of five measurements. The uncertainty in measured contact resistance, shown by error bars in Fig. 4, was estimated by assuming a maxi-

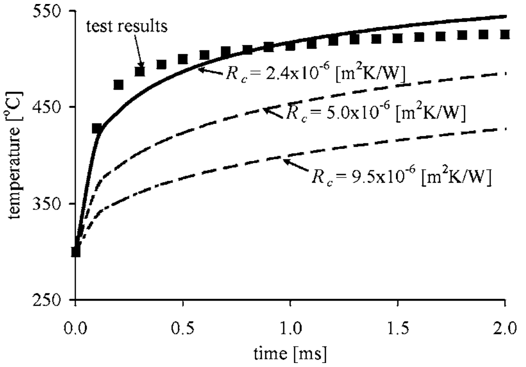

Fig. 3 Estimation of contact resistance by curve fitting to experimentally measured surface temperature variation

mum possible variation of ±2 °C in surface temperature measurement and ±4 °C in initial droplet temperature. The properties of H-13 tool change only slightly between 25 and 300 °C. Though it is possible to insert temperature variable properties in the analysis, it would greatly complicate the equations while giving only small improvements in accuracy. We therefore assumed ±5% uncertainty in physical property values. The overall error in contact resistance measurements, combining all these uncertainties, was approximately ±10%. Contact resistance increases with average surface roughness. Contact resistance variation with surface temperature is more complex, first decreasing and then increasing. Reasons for this variation are not quite clear. Initial heating of the surface to 100 °C may lead to evaporation of adsorbed water vapor and other volatile compounds, cleaning the surface and reducing contact resistance. Further heating produced surface oxidation (visible as a darkening of surface color), increasing contact resistance.

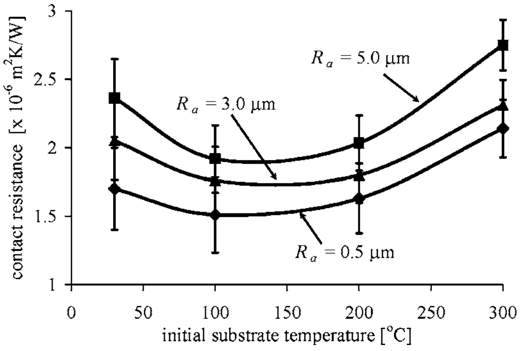

Fig. 4 Thermal contact resistance values between molten aluminium 380 and H-13 tool steel substrate

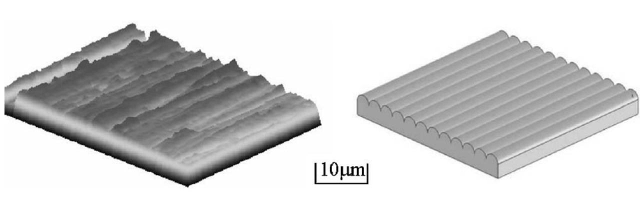

Fig. 5 A scan of the H-13 tool steel substrate with R_a =2.7 μm taken by an optical surface profilometer (on left) and an idealized model of it (on right)

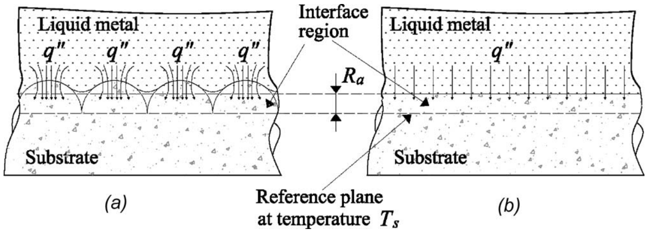

Fig. 6 Heat transfer from the molten metal at temperature T_d to (*a*) an idealized rough surface and (*b*) a perfectly smooth surface. The temperature of the reference plane is T_s. Heat conduction takes place through a solid layer of thickness R_a.

3.2 Contact Resistance Model. Modeling contact resistance requires, first of all, a description of the rough surface. Figure 5 shows a scan of an H-13 tool steel surface taken with an optical surface profilometer (NT-300 Dynamic Surface Profilometer, Wyco, Racine, IL). Surface roughness is unidirectional, corresponding to the motion of the belt sander used for finishing the surface following the procedure used for die-casting molds. Average roughness from the optical scan was R_a=2.7 μm and agreed within 3% with measurements by the stylus surface profilometer. For the surfaces that we used, R_a appears to describe the surface well. It is possible that with other surface-preparation methods we could produce more complicated surface topologies that cannot be described by R_a alone, but that is beyond the scope of the present study. We can model such a surface as consisting of a series of half cylinders placed next to each other, all having the same radius β. Surface roughness R_a is defined as the arithmetic average of the height of surface peaks above a hypothetical perfectly smooth plane. For the periodically varying surface shown in Fig. 5, the average roughness is

$$R_a = \frac{\int_0^{2\beta} y(x)dx}{2\beta} = \frac{\int_0^{\pi} \beta^2 \sin^2(\psi)d\psi}{2\beta} = \frac{\pi\beta}{4} \qquad (3)$$

Figure 6 shows an idealized representation of liquid metal in contact with a rough solid substrate. Surface tension prevents the metal from penetrating the valleys between surface peaks. Thermal contact resistance is defined with respect to a plane passing through the base of surface asperities (see Fig. 6(*a*)), whose temperature is T_s. To be consistent the position of this reference plane is fixed in space, so that for a perfectly smooth surface (Fig. 6(*b*)) the temperature T_s is assumed to be a distance R_a below the liquid-solid interface. Heat conduction (q) from the liquid at temperature T_d to this plane through a solid interface region of thermal conductivity K_s is

$$q = \frac{K_s(T_d - T_s)}{R_a}A \qquad (4)$$

where A is the area of the reference plane. For a rough surface (Fig. 6(*a*)) heat conduction from the liquid to the solid is

$$q = \frac{K_s(T_d - T_s)}{R_a}Af \qquad (5)$$

where Af is the true contact area between liquid metal and the rough substrate. Radiation and convection are assumed to be negligible: heat transfer because of conduction produces an effective heat transfer coefficient $h=1/R_c$, which is $\sim 10^6$ W/m^2 °C. Estimates of radiation and convective heat transfer coefficients show that they are both several orders of magnitude smaller than this value. The heat transfer model is a fairly simple one; however, it appears adequate to predict, within an order of magnitude, the contact resistance. Using a more complex description of heat transfer will not help unless we have a much more detailed description of the surface geometry available. Combining Eq. (5) with the definition of thermal contact resistance (Eq. (1)) gives

$$R_c = \frac{R_a}{K_s f} \qquad (6)$$

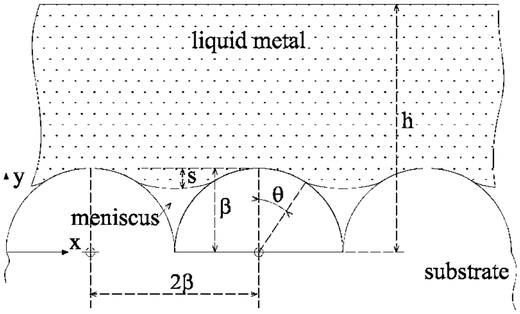

Fig. 7 Molten metal layer of thickness *h* in contact with an idealized rough surface

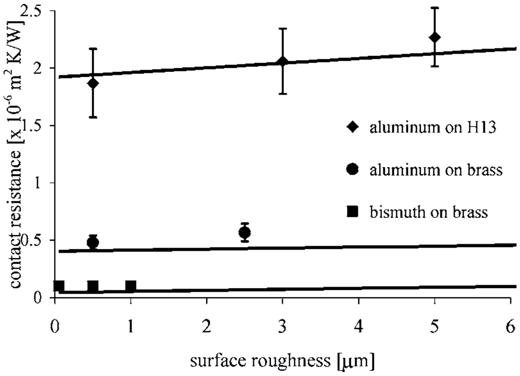

Fig. 8 Thermal contact resistance values for molten metal droplets impacting with V_0=3 m/s on steel and brass plates. Lines represent predicted values from Eq. (12).

For a perfectly smooth substrate $f=1$ and $R_c=R_a/K_s$. For a rough substrate we need to evaluate the true area of contact when a liquid-metal column is pressed against it. Figure 7 shows the geometry of the interface, where a liquid layer of height h is supported on a solid surface consisting of an array of semi-circular protrusions of radius β. The liquid metal is assumed to have high surface tension so that it does not wet the solid, and the liquid meniscus enters the valleys between surface asperities only partially, to depth s below the tip of the asperities. The liquid-solid contact area subtends an angle θ, defined in Fig. 7. The ratio between the true (projected) area of contact and the nominal projected area of the solid surface is

$$f = \frac{2\beta \sin\theta}{2\beta} = \sin\theta \tag{7}$$

Timsit [13] derived a model to calculate the profile of the liquid meniscus by using variational methods to determine the shape that minimized the total potential and surface energy of the system. To obtain an analytical solution it was assumed that surface asperities were much smaller than the liquid film thickness ($\beta \ll h$), that the liquid surface underwent only small deformation (i.e., $s \ll \beta$), and the liquid-solid contact angle was 180 deg. The amplitude of the meniscus was shown to be [13]

$$s = \frac{\beta^2 h}{\gamma^2 + \beta h} \tag{8}$$

where γ is the capillarity length defined as $\gamma=(\sigma/\rho g)^{1/2}$. To confirm the accuracy of Eq. (8), we measured the average surface roughness of the bottom of solidified splats formed by impact of molten aluminum 380 alloy droplets landing on H-13 tool steel plates. A splat landing on a surface with $R_a=0.5$ μm had an average roughness of 0.008 μm, compared to calculated $s=0.004$ μm. For a splat landing on a surface with $R_a=5.0$ μm, Eq. (8) predicts $s=0.38$ μm and we measured a roughness of 0.21 μm. This confirmed that we did, in fact, have $s \ll \beta$ and that the analytical expression predicts the order of magnitude of liquid surface deformation with reasonable accuracy. Timsit [13] also calculated that

$$f = \frac{\beta h}{\gamma^2 + \beta h} \tag{9}$$

The height of the liquid column h represents the hydrostatic head that presses the liquid down. In the case of a droplet impacting with velocity V_0, the hydrostatic head can be replaced by a dynamic pressure so that

$$h = \frac{V_0^2}{2g} \tag{10}$$

Substituting Eqs. (3) and (10) into Eq. (9) gives an expression for f

$$f = \frac{2\rho_d V_0^2 R_a}{2\rho_d V_0^2 R_a + \pi\sigma} \tag{11}$$

Substituting Eq. (11) into Eq. (6) allows us to calculate thermal contact resistance as a function of the impact velocity, material properties, and average surface roughness

$$R_c = \frac{2\rho_d V_0^2 R_a + \pi\sigma}{2\rho_d V_0^2 K_s} \tag{12}$$

The thermal contact resistance can be nondimensionalized by defining a Biot number ($\mathrm{Bi}=D/R_c K_s$). If we also define a Weber number ($\mathrm{We}=\rho V_0^2 D/\sigma$) and a normalized surface roughness ($R_a^* = R_a/D$), Eq. (12) can be written in dimensionless form

$$\mathrm{Bi}R_a^* = \frac{\mathrm{We}R_a^*}{\mathrm{We}R_a^* + \pi/2} \tag{13}$$

Droplet diameter D is used as a length scale in defining Bi and We to be consistent with previously published data on droplet impact. However, contact resistance does not depend on droplet size; note that the products $\mathrm{Bi}R_a^*$ and $\mathrm{We}R_a^*$ are independent of droplet diameter and the only remaining length scale is surface roughness R_a. Equation (13) can therefore be applied to any mass of liquid metal striking a solid wall, irrespective of size, and accounts for variations in physical properties, impact velocity, and average surface roughness.

In the limiting case that We becomes very large, $\mathrm{Bi}R_a^*=1$ and the contact resistance $R_c=R_a/K_s$. In this case, for a perfectly smooth surface ($R_a=0$) contact resistance goes to zero. If, however, both We and R_a are large, perfect contact may still be obtained if impact velocity is high or liquid surface tension is low so that liquid metal fills all the crevices in the solid surface. However, for a rough surface there is no planar interface between the liquid and solid. The thermal contact resistance we measure is that of the "interface region" shown in Fig. 6(*b*), that lies between the bulk liquid and solid. In the limit that We=0, Eq. (13) predicts that Bi=0, or that contact resistance is infinite. This is because we have assumed in Eq. (10) that the hydrostatic head is negligible compared to the dynamic pressure during droplet impact. In the case of zero velocity, there will be no contact between solid and liquid.

3.3 Model Validation. Figure 8 shows measured values of thermal contact resistance for aluminum 380 and bismuth droplets falling with $V_0=3$ m/s on H-13 tool steel and brass surfaces initially at room temperature, compared to predictions from Eq. (12). There was only a modest increase in R_c with surface roughness. Contact resistance on brass surfaces was much lower than on steel surfaces, as a consequence of its higher thermal conductivity (see

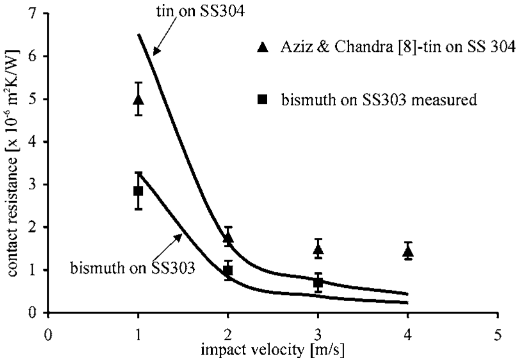

Fig. 9 A comparison between the analytical model predictions and tests results for different impact velocities. Solid lines represent predictions from Eq. (12).

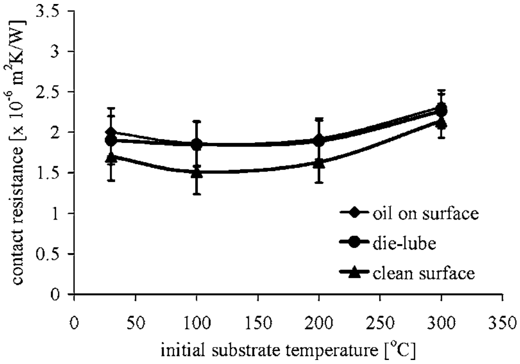

Fig. 11 Average thermal contact resistance for aluminium 380 droplets impacting with a velocity of 3 m/s on H-13 tool steel substrates covered with a thin film of oil or die-lube. Droplet impact velocity=3 m/s and surface roughness 0.5 μm.

Table 2). Bismuth has much higher density and lower surface tension than aluminum alloy (see Table 1) and, therefore, penetrates deeper into surface asperities, producing lower contact resistance.

Figure 9 shows the variation of contact resistance with impact velocity, including both our results for bismuth on stainless steel 303 at room temperature and those of Aziz and Chandra [8] for molten tin droplets on stainless steel 304. In both cases $R_a = 0.5\ \mu$m. The variation of contact resistance predicted by Eq. (12) is also shown for both sets of experimental results. Increasing velocity from 1 to 2 m/s produced a large decrease in R_c; further velocity increases had much less effect on contact resistance. The analytical model predicted the general variation in contact resistance; at higher velocities, though, it tended to underpredict values of R_c. The model does not account for the presence of surface contaminants such as oxides, which will make a greater contribution to the total resistance as surface roughness diminishes. Figure 10 shows the effect of surface oxidation on contact resistance. Freshly polished H-13 tool steel plates were oxidized by heating them to 300°C and leaving them exposed to the atmosphere for a half hour. Darkening of the surface due to oxidation was clearly visible. The substrate was then allowed to cool and reheated to the requisite temperature before contact-resistance experiments were done. Oxidation increased contact resistance, though the effect was much more noticeable on the smooth surface (R_a=0.5 μm) than the rough surface (R_a=5.0 μm).

Other contaminants on the surface may also increase contact resistance. Figure 11 shows the effect of wiping the H-13 tool steel surface with a cloth soaked in either machine oil or a commercially available die lube (Chem Trend RDL 3299), a silica-based lubricant suspended in water that is sprayed on cavity walls during the aluminum die-casting process to allow easy removal of solidified parts. Both substances produced a small increase in contact resistance.

Equation (13), which is in nondimensional form, correlates contact resistance for all combinations of materials, roughness, and impact velocity. Figure 12 shows the variation of BiR_a with WeR_a for all the measurements made in this study, compared with the prediction of Eq. (13). Most of the data points lie close to the calculated value; the poorest agreement is for the case of bismuth droplets landing on brass substrates. Bismuth has low surface tension and high density, and penetrates deepest into surface cavities. The assumption made in the model that liquid surface deformations are small may not be justified in this case. Also, the model neglects the effect of air trapped in surface asperities; when this air is significantly compressed, its pressure rises, resisting the intrusion of molten metal. For large liquid surface deformation, this effect becomes significant and has to be accounted for when calculating the area of liquid-solid contact. Doing so, however, requires a numerical solution.

4 Conclusions

Experimentally measured thermal contact resistance between molten metal droplets (aluminum alloy 380 and bismuth) and solid plates (steel and brass) ranged from 10^{-7} to 3×10^{-6} m^2 K/W. Contact resistance is determined by the area of contact between the molten metal and rough solid substrate. Factors that increase thermal contact resistance include greater surface roughness, low impact velocity, and contaminants on the surface, such as oxides or oil. Substrates with high thermal

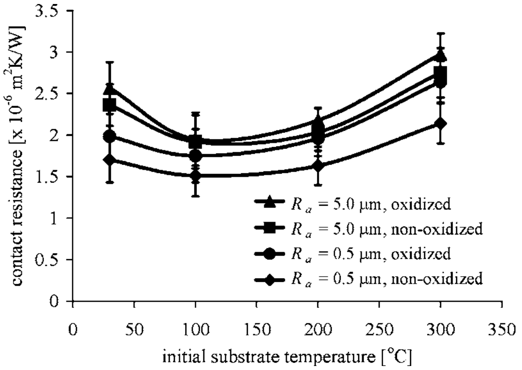

Fig. 10 Average thermal contact resistance variation with surface temperature for aluminium 380 droplets impacting with a velocity of 3 m/s on oxidized and nonoxidized H-13 tool steel substrates with two different surface roughness values.

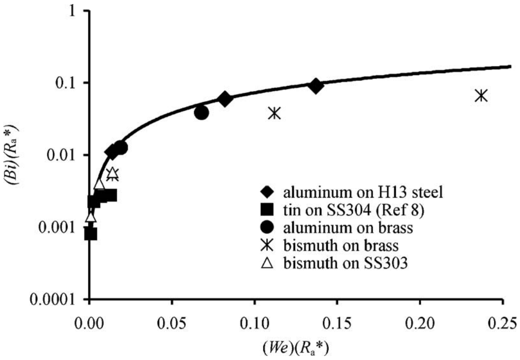

Fig. 12 Comparison of measured contact resistance values (represented by data points) with predictions (solid line) from Eq. (13)

conductivity (such as brass) or liquid metals with high density and low surface tension (such as bismuth) provide thermal low contact resistance. An analytical model of the deformation of a free liquid surface in contact with a rough solid was used to calculate the true area of contact between them and, thereby, the thermal contact resistance. The analytical model predicted variation of contact resistance with surface roughness, substrate, and droplet thermophysical properties and droplet impact velocity.

Acknowledgments

The authors gratefully acknowledge financial support for this project provided by Exco Ltd. and Materials and Manufacturing Ontario.

Nomenclature

A = surface area
C = specific heat
D = droplet diameter
g = gravity acceleration
f = ratio between true projected contact area and nominal contact area
h = liquid column height
K = thermal conductivity
L = film thickness
q'' = heat flux
R_a = average surface roughness
R_a^* = normalized average surface roughness ($R_a^* = R_a/D$)
R_c = thermal contact resistance
s = distance of bottom of meniscus from tip of surface asperities
t = time
t_r = sensor response time
T = temperature
T_{do} = initial droplet temperature
T_m = droplet melting temperature
T_{so} = initial substrate surface temperature.
V_o = droplet impact velocity
W = energy of a system
x = linear coordinate
y = linear coordinate

Greek Symbols

α = thermal diffusivity ($\alpha = k/\rho C$)
β = asperity radius
γ = capillarity length ($\gamma = (\sigma/\rho g)^{1/2}$)
ρ = density
σ = surface tension
θ = angle subtending contact area between liquid and solid

Subscripts

d = droplet
s = substrate

Dimensionless Numbers

Bi = Biot number ($D/R_c K_s$)
We = Weber number ($\rho V_o^2 \cdot D/\sigma$)

References

[1] Pasandideh-Fard, M., Pershin, V., Chandra, S., and Mostaghimi, J., 2002, "Splat Shapes in a Thermal Spray Coating Process: Simulations and Experiments," J. Therm. Spray Technol., **11**, pp. 206–217.
[2] Predecki, P., Mullendorf, A. W., and Grant, N. J., 1965, "A Study of the Splat Cooling Technique," Trans. Soc. Min. Eng. AIME, **233**, pp. 1581–1586.
[3] Liu, W., Wang, G. X., and Matthys, E. F., 1995, "Thermal Analysis and Measurements for a Molten Metal Drop Impacting on a Substrate: Cooling, Solidification and Heat Transfer Coefficient," Int. J. Heat Mass Transfer, **38**, pp. 1387–1395.
[4] Burden, M. H., and Jones, H., 1970, "Determination of Cooling Rate in Splat-Cooling From Scale of Microstructure," J. Inst. Met., **98**, pp. 249–252.
[5] Wang, G. X., and Matthys, E. F., 1996, "On the Heat Transfer at the Interface Between a Solidifying Metal and a Solid Substrate," *Metal Spinning, Strip Casting and Slab Casting*, E. F. Matthys and W. G. Truckner, eds., Minerals, Metals and Materials Society, Warrendale, PA, pp. 205–226.
[6] Wang, G. X., and Matthys, E. F., 2002, "Experimental Determination of the Interfacial Heat Transfer During Cooling and Solidification of Molten Metal Droplets Impacting on a Metallic Substrate: Effect of Roughness and Superheat," Int. J. Heat Mass Transfer, **45**, pp. 4967–4981.
[7] Loulou, T., Artyukhin, E. A., and Bardon, J. P., 1999, "Estimation of Thermal Contact Resistance During the First Stages of Metal Solidification Process: II-Experimental Set-up and Results," Int. J. Heat Mass Transfer, **42**, pp. 2119–2127.
[8] Aziz, S. D., and Chandra, S., 2000, "Impact Recoil and Splashing of Molten Metal Droplets," Int. J. Heat Mass Transfer, **43**, pp. 2841–2857.
[9] Wang, W., and Qiu, H. H., 2002, "Interfacial Thermal Conductance in Rapid Contact Solidification Process," Int. J. Heat Mass Transfer, **45**, pp. 2043–2053.
[10] Cheng, S., Li, T., and Chandra, S., 2005, "Producing Molten Metal Droplets With a Pneumatic Droplet-on-Demand Generator," J. Mater. Process. Technol., **159**, pp. 295–302.
[11] Heichal, Y., 2005, "Measuring Thermal Contact Resistance Under an Impacting Droplet of Molten Metal," MASc thesis, University of Toronto, Toronto, Ontario, Canada.
[12] Carslaw, H. S., and Jaeger, J. C., 1959, Conduction of Heat in Solids, Oxford University Press, London, p. 72.
[13] Timsit, R. S., 1982, "The True Area of Contact Between a Liquid and a Rough Solid: Elementary Considerations," Wear, **83**, pp. 129–141.

Journal of Heat Transfer

Technical Briefs

Diffusion-Based Thermal Tomography

Vadim F. Bakirov
Research Fellow

Ronald A. Kline
Professor

San Diego Center for Materials Research,
San Diego State University, San Diego, CA

Thermal imaging is one of the fastest growing areas of nondestructive testing. The basic idea is to apply heat to a material and study the way the temperature changes within the material to learn about its composition. The technique is rapid, relatively inexpensive, and, most importantly, has a wide coverage area with a single experimental measurement. One of the main research goals in thermal imaging has been to improve flaw definition through advanced image processing. Tomographic imaging is a very attractive way to achieve this goal. Although there have been some attempts to implement tomographic principles for thermal imaging, they have been only marginally successful. One possible reason for this is that conventional tomography algorithms rely on wave propagation (either electromagnetic or acoustic) and are inherently unsuitable for thermal diffusion without suitable modifications. In this research program, a modified approach to thermal imaging is proposed that fully accounts for diffusion phenomena in a tomographic imaging algorithm. Here, instead of the large area source used in conventional thermal imaging applications, a raster scanned point source is employed in order to provide the well-defined source-receiver positions required for tomographic imaging. An algorithm for the forward propagation problem, based on the Galerkin finite element method in connection with the corresponding weak formulation for the thermal diffusion is considered. A thermal diffusion modified version of the algebraic reconstruction technique (ART) is used for image reconstruction. Examples of tomographic images are presented from synthetically generated data to illustrate the utility of the approach. [DOI: 10.1115/1.2039115]

1 Introduction

Thermal imaging has become an important nondestructive evaluation method in the last decade. The development of highly sensitive infrared imaging systems has resulted in widely utilized thermal inspection systems with improved detection capability and spatial resolution. Thermal inspection is normally performed with flash lamp heating and infrared imaging cameras to provide rapid, full-field, low-cost inspection capability for large structures. The major shortcoming of thermal imaging to date is that it is principally a qualitative technique. To this point in its development, thermal imaging provides less quantitative information about the size, shape, precise location (especially depth information) of potential flaws than competing techniques. Nor does conventional thermal imaging provide any significant insight about the nature or composition of a material as does ultrasound (via stiffness).

It is important to note that, just as for sound and electromagnetism, conductive heat propagation in a solid is governed by well-understood mathematical relationships involving fundamental material parameters (thermal conductivity, heat capacity, and density). Hence thermal studies can, in principle, provide similarly quantitative materials characterization information as other methods. Furthermore, using thermal techniques, this type of information can be generated relatively simply and inexpensively. Tomographic imaging is one way in which this information can be extracted from thermal measurements.

Thermal tomography has been studied by several investigators recently [1–6]. Two main approaches have been utilized to date: (i) temporal-based imaging and (ii) thermal wave analogy. Temporal imaging is used to reconstruct planar slices of thermal image information based principally on surface arrival times at the heated surface. The theoretical bases for these techniques are primarily one-dimensional models for heat diffusion. Surface temperature measurements can be used, in principle, to obtain depth-dependent information about the internal structure of a material. In practice, simple time-gating procedures have been inefficient in resolving depth information with sufficient accuracy for imaging purposes and alternative signal processing methods have been utilized. Several investigators have empirically observed that depth estimates can be improved by using derivatives of the contrast temperature versus time curves on a pixel-by-pixel basis, where the contrast temperature is defined as the temperature difference between unflawed region of the material and the temperature of the point of interest. Several researchers report that the peak slope of the temperature contrast curve is a more reliable indicator of depth than the peak in contrast time measurement [1–3]. Winfree and Plotnikov use this parameter as a characteristic time for obtaining depth estimates, which are then used to reconstruct image slices through the thickness of a sample [4]. However, this approach provides no quantitative information about the composition of a material nor is it truly tomographic.

A second approach to the problem is based on the use of a pseudowave propagation analogy. If one introduces a harmonically varying thermal source, the governing diffusional differential equation for heat conduction becomes the Helmholtz pseudowave equation. This equation admits a wave-type solution that is extremely dispersive and highly attenuative so there is a major question as to its physical significance. Nonetheless, this approach does provide the computational framework for alternative methods of extracting depth information from thermal data. Mandelis et al. have used this formalism for two different types of image

---

Contributed by the Heat Transfer Division of ASME for publication in the JOURNAL OF HEAT TRANSFER. Manuscript received May 17, 2004; final manuscript received January 26, 2005. Review conducted by: Kenneth Kihm.

reconstruction [5–9]. In their work, a point source (focused laser) periodically heats one side of a specimen and a thin pyroelectric film mounted on the opposite side is used for detection. The localized nature of the source is needed to better establish the source-sensor geometry needed for reconstruction. One approach in their work is a ray optics solution with an acoustic tomography reconstruction algorithm used in the reconstruction. This is a truly tomographic approach to thermal imaging using a well-established approach. A second technique is a wave diffraction-based reconstruction algorithm to achieve improved results. Although these approaches are interesting and do point the way toward a solution, they suffer from some major drawbacks, most notably image quality.

The wave analogy basis for the analysis is imperfect at best, and there is no well-defined wave front or established ray trajectories to deal with, as in acoustics. This is a diffusion phenomena and must be analyzed as such in order to obtain an accurate solution. This is the objective of this research effort. The method is designed to take advantage of the rapid, full-field capabilities of thermal imaging. In this paper, an approach to thermal imaging is proposed that fully accounts for diffusion phenomena in a tomographic imaging algorithm. A thermal diffusion modified version of algebraic reconstruction technique (ART) is used for image reconstruction.

2 Reconstruction Techniqe for Diffusion-Based Tomography

The main goal of this section is to show how a tomographic reconstruction technique, originally developed for acoustic wave propagation can be adapted to tomographic reconstruction from thermal data. To illustrate this tomographic reconstruction technique, take as an example two-dimensional (2D) heat transfer problem in a solid.

The governing balance equation that describes the thermal diffusion process in situations involving two independent variables is given by [9]

$$\nabla \cdot [k \nabla T(x,y,t)] + q(x,y,t) - \gamma \frac{\partial T(x,y,t)}{\partial t} = 0 \quad \text{in } D \qquad (1)$$

where D is the interior of the domain, x and y are coordinates, t is the time, T is the temperature, $q=q(x,y,t)$ is the energy generation rate per unit volume, $k=k(x,y)$ is thermal conductivity, and $\gamma=\gamma(x,y)=\rho(x,y)c(x,y)$ is heat capacity with density of material $\rho=\rho(x,y)$ and specific heat of material $c=c(x,y)$.

The most realistic boundary condition encountered is that of a conductive media surrounded by air. If the temperature of air is denoted by T_∞ and surface coefficient of heat transfer by h, then Newton's law of cooling gives the boundary condition for Eq. (1)

$$k\mathbf{n} \nabla T + h(T - T_\infty) = 0 \text{ on } \Gamma \qquad (2)$$

where Γ is the boundary of the domain D, $\mathbf{n}$ is the outward pointing unit normal vector.

The typical initial condition for Eq. (1) is

$$T(x,y,0) = T_\infty \qquad (3)$$

For our tomographic applications, it is convenient to use a weak form of the differential equation governing heat transfer. The weak form of a differential equation is a weighted-integral statement that is equivalent to both the governing differential equation as well as the associated boundary condition

$$\int\int_D \nabla \psi k \nabla T dA + \int\int_D \psi\gamma \frac{\partial T}{\partial t} dA + \int_\Gamma \psi h(T - T_\infty) ds$$
$$= \int\int_D \psi q dA \qquad (4)$$

where $\psi(x,y)$, arbitrary weighting function, is the weak formulation for the two-dimensional thermal diffusion problem [10,11] as stated in Eqs. (1) and (2). The first step for tomographic imaging is the discretization of the domain D. Consider, for example, square domain D. Then we discretize the domain into n by n square pixels, as shown in Fig. 1. By the analogy with wave based tomography, it is assumed that, in any pixel, material properties are uniform and isotropic. Therefore, we assume that thermal conductivity k and heat capacity γ are constants (or are equal to effective average values on each pixel). We denote these values by $k_{(i,j)}$ and $\gamma_{(i,j)}$ for the (i,j) pixel as illustrated in Fig. 1.

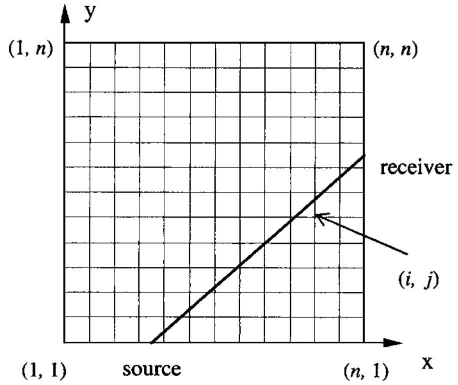

Fig. 1 Source and receiver locations for transit time computation on a $n \times n$ pixel grid

For this simulation of a prototype thermal tomography experiment, an instantaneous heat flux (thermal heat source) is inserted at one of the edge nodes of the model. We represent the thermal heat source as

$$q(x,y,t) = q_S \delta(x - x_S) \delta(y - y_S) \delta(t) \qquad (5)$$

where δ is a δ function, x_S and y_S are coordinates of the heat source as shown in Fig. 1, and q_S is the value of the energy of the heat source.

Here, we model the forward propagation problem, using a Galerkin finite element method in connection with the weak formulation of the problem (4) for thermal diffusion. We choose the Galerkin method for numerical solution of the forward propagation problem, where the geometrical shape of the finite element corresponds to the geometrical shape of the pixel in a tomographic imaging algorithm. Temperature is calculated as a function time for every node in the domain, in particular, on the boundary Γ. If x_R and y_R are coordinates of the receiver as shown in Fig. 1, we can find from function $T=T(x_R,y_R,t)$ important parameters: maximum temperature and time for reaches this maximum (transit time).

Finally, we apply the standard ART algorithm [12] for our inverse problem. Information about maximum temperature and transit time for many source-receiver combinations allows reconstruction of both thermal conductivity $k_{(i,j)}$ and heat capacity $\gamma_{(i,j)}$, and also, therefore, thermal diffusivity $\alpha_{(i,j)}=k_{(i,j)}/\gamma_{(i,j)}$. In this paper we assume a known distribution of $\gamma_{(i,j)}$ and consider only one-parameter reconstruction for unknown distribution of thermal conductivity $k_{(i,j)}$ by using transit time τ for many source-receiver combinations. For an $n \times n$ pixel grid in Fig. 1, there are $4n$-4 possible source positions, and for each source position there are $4n$-5 possible receiver positions. This meant that a total $(4n\text{-}4) \times (4n\text{-}5)$ source-receiver pairs is used for tomographic reconstruction. In its many forms, ART is a straightforward iterative approach to the inverse problem. One begins with a set of initial guesses and then adjusts the parameters of interest in an iterative fashion to obtain an image of the material. We begin with initial guesses for thermal conductivity $k^{(0)}_{(i,j)}$ for each (i,j) pixel. Then

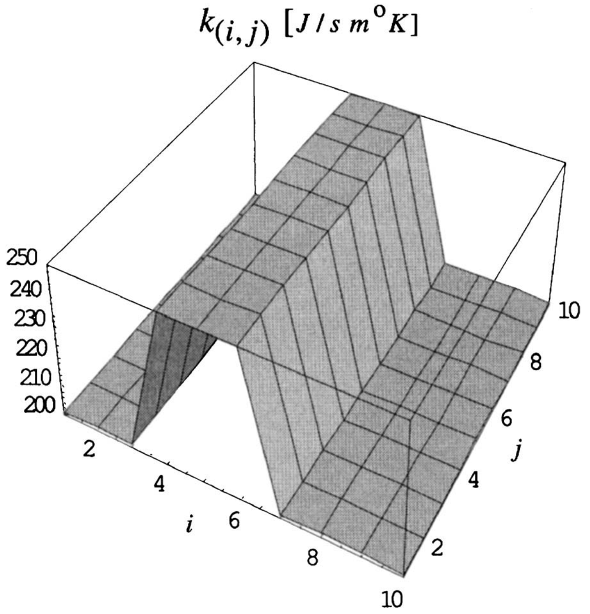

Fig. 2 Actual thermal conductivity distribution

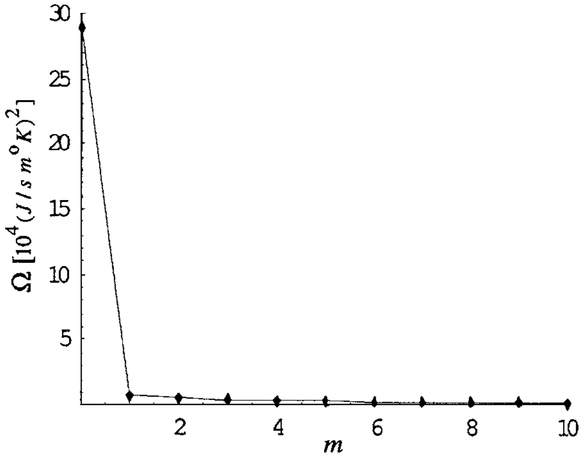

Fig. 4 Error of reconstruction Ω in dependence on number of complete iteration cycles *m*

these guesses are adjusted to bring the calculation of transit time into agreement with the measured results. As for conventional ART, only one source-receiver combination is considered at a time. An estimated transit time for the *p*th iteration is formally written as

$$\tau^{(p)} = f(k^{(p)}_{(1,1)}, k^{(p)}_{(1,2)}, \ldots, k^{(p)}_{(n,n)}) \tag{6}$$

Since the estimated transit time usually does not match the measured transit time τ, suitable correction factors must be added to the current values of $k^{(p)}_{(1,1)}, k^{(p)}_{(1,2)}, \ldots, k^{(p)}_{(n,n)}$

$$\Delta k^{(p)}_{(i,j)} = \frac{\dfrac{\partial f}{\partial k^{(p)}_{(i,j)}} \Delta \tau^{(p)}}{\displaystyle\sum_{i,j=1}^{n} \left[\frac{\partial f}{\partial k^{(p)}_{(i,j)}} \right]^2} \quad (i,j = 1,2, \ldots, n) \tag{7}$$

so

$$k^{(p+1)}_{(i,j)} = k^{(p)}_{(i,j)} + \Delta k^{(p)}_{(i,j)} \tag{8}$$

The process is then repeated for each source-receiver combination to complete one iteration cycle. This represents the completion of a typical cycle *m* in the ART algorithm process. This process is repeated for each iteration cycle until convergence, as measured by the sum of the squares of the parameter changes: $\Omega = \sum^{n}_{i,j=1} [\Delta k^{(p)}_{(i,j)}]^2$ is obtained.

3 Numerical Examples

In this research, a computational framework for a diffusion-based thermal tomography reconstruction of unknown distribution of thermal conductivities from thermal measurements was developed based on algorithms of Sec. 2. For this study, a 10×10 domain *D* was utilized. The size of the domain *D* is equal to *L*

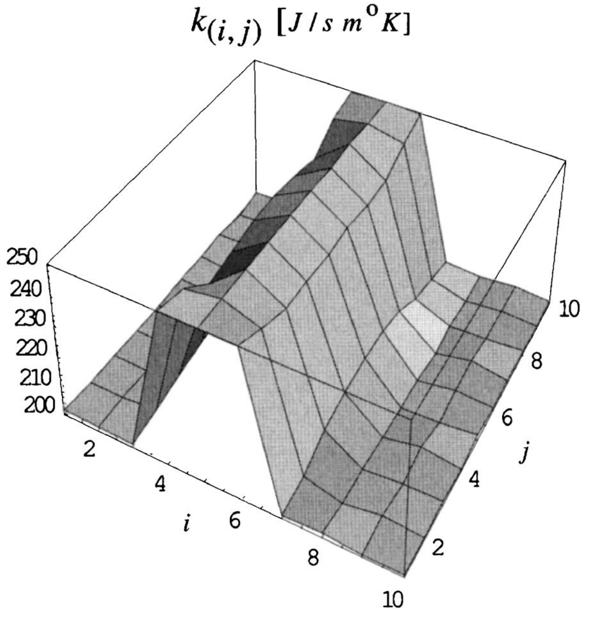

Fig. 3 Reconstruction of the thermal conductivity distribution

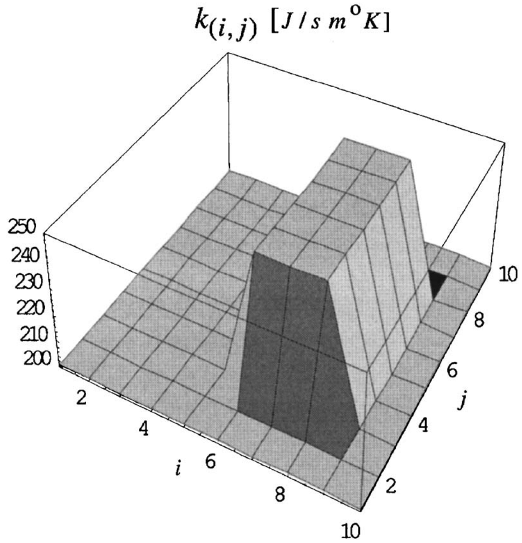

Fig. 5 Actual thermal conductivity distribution

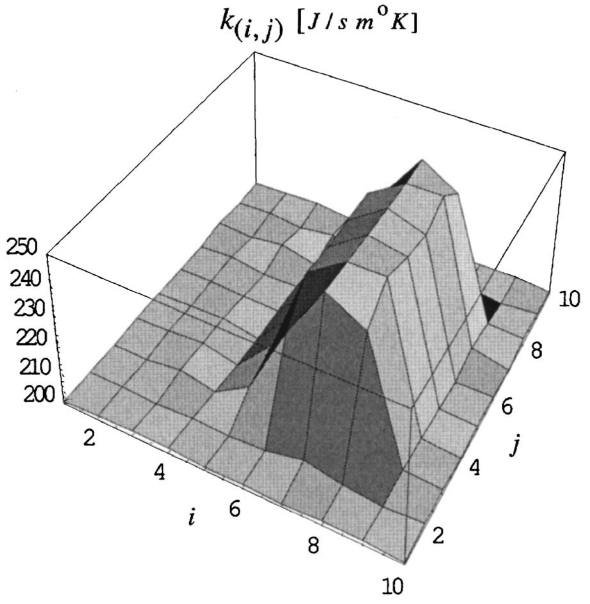

Fig. 6 Reconstruction of the thermal conductivity distribution

$=0.05$ m. In the first example, the actual thermal conductivity distribution is shown in Fig. 2. The following other material parameters were used: $\gamma_{(i,j)}=2.33\times10^6$ J/m^3 K $(1\leqslant i,j\leqslant n)$ and $h=50$ J/s m^2 K, which are typical for aluminum. The value of the energy of the heat source was $q_S=4.19\times10^4$ J/m. Tomographic reconstruction from these numerically simulated data was performed. The result for the reconstruction of the thermal conductivity distribution after ten complete iteration cycles (with a set initial guess $k_{(i,j)}^{(0)}=167$ J/s m K for each (i,j) pixel) is presented in Fig. 3. Function Ω (error of reconstruction) versus the number of complete iteration cycles m in the ART algorithm process is presented in Fig. 4. In the second example, the actual thermal conductivity distribution is shown in Fig. 5. The result for the reconstruction of the thermal conductivity distribution is presented in Fig. 6. Good agreement between the actual thermal conductivity values and the reconstruction results was observed.

4 Conclusion

In this work, a diffusion-based thermal tomographic algorithm was developed for thermal property analysis of structures. The time of the maximum temperature in the temperature versus time curve is used as the parameter for characterization of the transit time. A one-parameter version of the algebraic reconstruction technique (ART) is used for the reconstruction of the thermal conductivity distribution. To illustrate the potential utility of the approach, synthetic data were generated and used as inputs into the tomographic algorithm. Target values and reconstruction results for thermal conductivity were found to be in good agreement with one another.

References

[1] Ringermacher, H. I., Mayton, D. J., Howard, D. R., and Cassenti, B. N., 1998, "Towards a Flat-Bottom Hole Standard for Thermal Imaging," Rev. Prog. Quant. Nondestr. Eval., **17**, pp. 425–429.
[2] Vavilov, V. P., Grinzato, E., Bison, P. G., Marinetti, S., and Bressan, C., 1996, "Thermal Characterization and Tomography of Carbon Fiber Reinforced Plastics Using Individual Identification Technique," Mater. Eval., **54**, pp. 604–610.
[3] Favro, L. D., Kuo, P. K., Thomas, R. L., Ahmed, T., Xiaoyan, Han, and Wang, X., 1994, "Progress in the Development of the Pulse-Echo Thermal Wave Imaging for NDE," Rev. Prog. Quant. Nondestr. Eval., **13**, pp. 395–399.
[4] Winfree, W. P., and Plotnikov, Y. A., 1999, "Defect Characterization in Composites Using a Thermal Tomography Algorithm," Rev. Prog. Quant. Nondestr. Eval., **18**, pp. 1343–1350.
[5] Munidasa, M., and Mandelis, A., 1991, "Photopyroelectric Thermal-Wave Tomography of Aluminum With Ray-Optic Reconstruction," J. Opt. Soc. Am. A, **8**, pp. 1851–1858.
[6] Munidasa, M., Mandelis, A., and Ferguson, C., 1992, "Resolution of Photothermal Tomographic Imaging of Sub-Surface Defects in Metals With Ray-Optic Reconstruction," Appl. Phys. A: Solids Surf., **54**, pp. 244–250.
[7] Mandelis, A., 1991, "Theory of Photothermal Wave Diffraction Tomography via Spatial Laplace Spectral Decomposition," J. Phys. A, **24**, pp. 2485–2505.
[8] Pade, O., and Mandelis, A., 1994, "Thermal-Wave Slice Tomography Using Wave-Field Reconstruction," Inverse Probl. Eng., **10**, pp. 185–197.
[9] Sucec, J., 1985, *Heat Transfer*, Wm. C. Brown Publishers, Iowa.
[10] Reddy, J. N., and Gartling, D. K., 1994, *The Finite Element Method in Heat Transfer and Fluid Dynamics*, CRC Press, Boca Raton.
[11] Shih, T. M., 1984, *Numerical Heat Transfer*, Hemisphere, Washington.
[12] Herman, G. T., 1980, *Image Reconstruction From Projections: The Fundamentals of Computerized Tomography*, Academic Press, New York.

An Investigation Into the Effect of Subcooled Liquid Inertia on Flow-Change-Induced Transient Flow Surges in Horizontal Condensing Flow Systems

C. J. Kobus
Department of Mechanical Engineering,
Oakland University, Rochester, MI 48309
e-mail: cjkobus@oakland.edu

The objective of this research is to investigate large-scale transient flow surges of the condensate leaving in-tube condensing flow systems because of perturbations in the inlet vapor flow rate, and the influence of the subcooled liquid inertia of the condensate on these transient responses. Small changes in the inlet vapor flow rate momentarily cause large transient flow surges in the outlet liquid flow rate. Condensate inertia is seen to destabilize the system into an underdamped behavior where the flow rate can overshoot the final steady-state position several times. A one-dimensional, two-fluid, distributed parameter system mean void fraction (SMVF) model of the time-dependent distribution of liquid and vapor within the two-phase region is developed for predicting these transient characteristics, which it is seen to do quite well, especially when consideration is given to the complex nature of the problem. [DOI: 10.1115/1.2039116]

Keywords: two-phase, condensing, transient, heat transfer

Introduction

A fundamental understanding of the transient characteristics and stability behavior of in-tube condensing flow systems is important in a broad spectrum of energy transport and conversion processes, ranging from reheat, reboiler, and submerged evaporator systems associated with nuclear and conventional power plants [1,2] to applications in the process and chemical industries, as well as systems associated with refrigeration, air conditioning, and space power generation. Large flow excursions of the condensate in single and multitube condensing flow systems could substantially affect the performance and control of the processes taking place within these systems and, in turn, cause damage to associated mechanical equipment and components and endanger the safety of such systems. For example, large flow oscillations in the subcooled liquid at the end of the condensation process, including possible flow reversals, are likely to cause process control problems and/or large impulse loads that may result in substantial damage to various system components.

Although there are many two-phase flow models in existence, their source can be tracked back to four distinctively different types of modeling techniques. Collier and Thome [3] and Wallis [4] have listed these techniques as the homogeneous-flow, separated-flow, drift-flux, and flow pattern models. All four of these models have been applied to mostly steady-state evaporating flow systems. All these modeling techniques are formulated from the fundamental principles governing single- and multiphase flow phenomena, in general—that is, the conservation of mass, conservation of energy, and the momentum principle, along with various constitutive relationships. Some have been applied to transient condensing flows. A good summary of all these modeling techniques has been compiled by Kobus [5,6].

The separated flow model [2–4] has been the most utilized for *transient* condensing flows. It considers the two phases to be artificially separated into two streams: a liquid stream and a vapor stream. The model is sometimes referred to as the "two-fluid" or "unequal velocity" model and increases in complexity as more differences in the streams are considered. The basic assumptions behind the separated flow model are that liquid and vapor velocities, although they may be different, are assumed to be uniform across any cross section; also, thermodynamic equilibrium is assumed to exist between phases (although this assumption does not have to be made, in general) and viscous dissipation and kinetic and gravitational potential energies are considered negligible. The system mean void fraction (SMVF) model is a type of separated flow model. Unlike the partial differential equation formulations of other modeling techniques, such as the drift-flux model, the SMVF model does not contain any empirically determined coefficients and results in ordinary differential equations derived from integral formulations of the fundamental principles. The major simplifying attribute of the SMVF model is the time invariance of the system mean void fraction. This time-invariance assumption has the effect of uncoupling the conservation of mass and energy equations governing the extent of the two-phase region from the *transient* form of the momentum equation, an analytical simplification of considerable magnitude. From a mathematical perspective, time invariance of the system mean void fraction is guaranteed by the existence of a similarity relationship, which from a physical perspective requires that a specific redistribution of liquid and vapor within the two-phase region take place at a rate faster than that of the particular flow transient under consideration. This implies that within the two-phase region, only the *steady-state* form of the momentum principle is necessary.

With any two-phase flow phenomena, in general, inherent stochastic fluctuations in system quantities, such as flow rate and pressure, are always present. Most transient and, in fact, steady-state measurements reported in the literature, therefore, represent time-averaged quantities; that is, quantities where the averaging time is large enough to eliminate the stochastic fluctuations, but short enough so as not to interfere with the deterministic transient, which is the focus of interest in transient two-phase flow phenomena.

System Mean Void Fraction Model

The primary purpose of the research described in this paper is to extend the predictive capability of the system mean void fraction (SMVF) model to include the capability of predicting transient-response characteristics in cases where the effects of condensate inertia are significant, which has not been done in prior research. The detail of the analysis was presented by Kobus et al. [7] for single- or multitube condensing flow systems. In this prior research, inertia was considered in developing the governing differential equations, but was later neglected for obtaining the solution.

A schematic of a single-tube condensing flow system is depicted in [8]. Viscous dissipation, longitudinal heat conduction, and changes in kinetic energy are negligible. The spatially averaged heat flux for the condenser tube is assumed to be time invariant. Since thermodynamic equilibrium is assumed to exist in the two-phase region, all thermodynamic properties are assumed to be saturated properties, independent of axial position, and evaluated at the mean condensing system pressure, which is, however, allowed to vary with time. The local flow quality and local area void fraction are allowed to vary within the two-phase region with both axial position and time. The region upstream of the two-phase region is assumed to be adiabatic and saturated.

Contributed by the Heat Transfer Division of ASME for publication in the Journal of Heat Transfer. Manuscript received January 24, 2004; final manuscript received March 15, 2005. Review conducted by: Ramendra P. Roy.

The system mean void fraction model is a one-dimensional, two-fluid, distributed parameter integral model representing a way of modeling the transient characteristics of the effective point of complete condensation $\eta(t)$. The SMVF model incorporates the concept of a time-invariant system mean void fraction $\overline{\alpha}$. Although the system mean void fraction is assumed to be time invariant, changes in the local area void fraction $\alpha(z,t)$ are allowed by the model in both axial position in the tube and time. The validity of this simplifying assumption can only be demonstrated by the success of the SMVF model in predicting a wide range of transient evaporating and condensing flow phenomena, consisting of single- and multitube systems, for dynamic response characteristics and unstable flow phenomena. Although there must inevitably be limiting bounds for this very fundamental assumption, it has yet to be found experimentally. The differential equation governing the effective point of complete condensation, obtained from the combined conservation of mass and energy equations [7], is expressed as follows:

$$\tau_c \frac{d\eta(t)}{dt} + \eta(t) = x_i \frac{(h' - h)}{\overline{f_q} P} m_{t,i}(t) \tag{1}$$

$$\text{where } \tau_c = \frac{\rho'(h' - h)\overline{\alpha} A_t}{\overline{f_q} P} \tag{2}$$

In Eqs. (1) and (2), $\overline{f_q}$ represents the spatially averaged heat flux, which can be found prior to running the experiment by theoretical means [9]. The system mean void fraction $\overline{\alpha}$ is defined in terms of the local area void fraction $\alpha(z,t)$ and represents the integral form of the mean value theorem; thus,

$$\begin{aligned}\overline{\alpha} \equiv \frac{1}{\eta(t)} \int_{z=0}^{\eta(t)} \alpha(z,t) dz = \frac{1}{(1-a)} \\ + \frac{a}{x_i(1-a)^2} \text{Ln} \left| \frac{a}{a + (1-a)x_i} \right|; \quad a = (\rho'/\rho)^{2/3}\end{aligned} \tag{3}$$

The particular void fraction model used in Eq. (3) is that of Zivi [10], chosen for its simplicity, yet sufficiently accurate for these types of condensing flow problems. However, any void fraction-flow quality relationship that is valid over the *full range* of flow qualities would yield similar results. It was established in previous early research that the system mean void fraction is essentially time invariant. The differential equation governing the outlet liquid flow rate, $m_{t,o}(t)$, is expressed as

$$\begin{aligned}\tau_i \tau_f \frac{d^2 m_{t,o}(t)}{dt^2} + \tau_f \frac{dm_{t,o}(t)}{dt} + m_{t,o}(t) = \{[(\rho/\rho') - 1]x_i + 1\} m_{t,i}(t) \\ - [(\rho/\rho') - 1] \frac{\overline{f_q} P \eta(t)}{(h' - h)}\end{aligned} \tag{4}$$

where

$$\tau_i = \frac{1}{k_o^*} \left(\frac{L_o^*}{A_t} \right); \quad L_o^* = (L - \eta_i) \tag{5}$$

$$\tau_f = \left(\frac{\rho}{\rho'} \right) \left\{ \left(\frac{\rho'}{\rho} \right) \{[(\rho/\rho') - 1]x_i + 1\} V_u + V_{2\phi} + V_{p,\text{eff}} \} \gamma^* k_o^* \right\} \tag{6}$$

and where

$$V_{2\phi} = A_t \overline{\alpha} \eta_i \tag{7}$$

$$V_{p,\text{eff}} = A_t \beta_o \eta_i \tag{8}$$

$$\beta_o = \frac{\rho(1 - \overline{\alpha})}{(h' - h)} \left(\frac{\beta^*}{\gamma^*} \right) \tag{9}$$

$$k_o^* = \frac{2k_o}{\rho A_t^2} m_{t,i} \tag{10}$$

$$\eta_i = x_i \frac{(h' - h)}{\overline{f_q} P} m_{t,i} \tag{11}$$

In Eq. (5), τ_i is the system inertia time constant, comprised of the length of the condensing flow system L (condenser subcooled liquid plus liquid length downstream of the condenser) the cross-sectional area, and the flow resistance at the outlet k_o^*. Equation (6) represents the compressible flow system time constant and depends largely on the system vapor volume, including the upstream vapor volume V_u, the vapor volume in the two-phase region, Eq. (7), as well as an effective vapor volume due to changes in the fluid properties with pressure changes, Eq. (8). It also depends on the flow resistance coefficient, Eq. (10), which depends mostly on an outlet flow resistance coefficient obtained from pressure drop calculations [7].

To solve the above set of one-way coupled governing differential equations, represented by Eqs. (1) and (4), Eq. (1) may first be solved for $\eta(t)$. For the case of an exponential inlet vapor flow-rate variation,

$$m_{t,i}(t) = m_{t,f} - (m_{t,f} - m_{t,i}) e^{-t/\tau_m} \tag{12}$$

Substituting Eq. (12) into (1), a closed-form solution for $\eta(t)$ may be obtained; thus,

$$\frac{\overline{f_q} P \eta(t)}{(h' - h)} = x_i m_{t,f} - \frac{x_i (m_{t,f} - m_{t,i})}{[1 + (\tau_c/\tau_m)]} \{ e^{-t/\tau_m} + (\tau_c/\tau_m) e^{-t/\tau_c} \} \tag{13}$$

This solution, in turn, may be substituted into Eq. (4), which may then be solved for the transient outlet liquid flow rate leaving the condensing flow system, $m_{t,o}(t)$. The differential equation is

$$\begin{aligned}\tau_i \tau_f \frac{d^2 m_{t,o}(t)}{dt^2} + \tau_f \frac{dm_{t,o}(t)}{dt} + m_{t,o}(t) = m_{t,f} - (m_{t,f} - m_{t,i}) e^{-t/\tau_m} \\ + x_i (m_{t,f} - m_{t,i}) [(\rho/\rho') - 1] \frac{(\tau_c/\tau_m)(e^{-t/\tau_m} - e^{-t/\tau_c})}{[(\tau_c/\tau_m) - 1]}\end{aligned} \tag{14}$$

The solution of Eq. (14) involves obtaining both a complimentary and a particular solution. Since the differential equation is second order, the complimentary solution will involve a natural frequency, $\omega_{n,i}$, and a damping coefficient ζ_i. The complimentary solution, $m_{t,o}^c(t)$, can thus be obtained from the following differential equation:

$$\frac{d^2 m_{t,o}^c(t)}{dt^2} + 2\zeta_i \omega_{n,i} \frac{dm_{t,o}^c(t)}{dt} + \omega_{n,i}^2 m_{t,o}^c(t) = 0 \tag{15}$$

where

$$\zeta_i = \frac{1}{2} \left(\frac{\tau_f}{\tau_i} \right)^{1/2} \tag{16}$$

$$\omega_{n,i} = \frac{1}{(\tau_i \tau_f)^{1/2}} \tag{17}$$

Referring to Eq. (15), the outlet liquid flow rate may overshoot and oscillate about its final steady-state position because of the presence of inertia. The oscillations would eventually decay and converge to the final flow rate $m_{t,f}$, for the *underdamped* case, $\zeta_i < 1$. If the effects of inertia are negligible, then the outlet liquid flow rate would not overshoot the final value of the flow rate after the initial flow surge. The solution of Eq. (14) thus depends on the magnitude of the damping coefficient ζ_i. For the case of underdamping, which is of interest here, the solution of Eq. (14) involves the homogeneous solution of Eq. (15), with the differential operator D, where, for the case where the damping coefficient is less than unity,

$$D_{1,2} = \omega_{n,i}(\zeta_i \pm j\sqrt{1-\zeta_i^2}) \tag{18}$$

Since Eq. (18) contains two imaginary and unequal expressions, the complimentary solution will be the sum of two trigonometric functions with unknown coefficients. The particular solution may be obtained by the method of undetermined coefficients. Once the initial conditions are specified for the total solution, the transient dimensionless outlet liquid flow rate, $[m_{t,o}(t)-m_{t,i}]/[m_{t,f}-m_{t,i}]$, where $m_{t,f}$ and $m_{t,i}$ are the final and initial flow rates, respectively, may be expressed as

$$\begin{aligned}\frac{m_{t,o}(t)-m_{t,i}}{m_{t,f}-m_{t,i}} &= 1 + \lambda_3 e^{-t/\tau_c} - \lambda_4 e^{-t/\tau_m} + (\lambda_4 - \lambda_3 \\ &\quad - 1)e^{-\zeta_i \omega_{n,i} t}\cos\lfloor \omega_{n,i} t\sqrt{1-\zeta_i^2}\rfloor \\ &\quad + \frac{1}{\sqrt{1-\zeta_i^2}}\left\{\zeta_i(\lambda_4-\lambda_3-1) + \frac{\lambda_3}{(\omega_{n,i}\tau_c)} - \frac{\lambda_4}{(\omega_{n,i}\tau_m)}\right\} \\ &\quad \times e^{-\zeta_i\omega_{n,i}}\sin\lfloor \omega_{n,i} t\sqrt{1-\zeta_i^2}\rfloor\end{aligned} \tag{19}$$

where

$$\lambda_3 = \frac{\left(\dfrac{\tau_c}{\tau_m}\right)\left[\left(\dfrac{\rho}{\rho'}\right)-1\right]}{\left[\left(\dfrac{\tau_c}{\tau_m}\right)-1\right]\left\{\dfrac{1}{(\omega_{n,i}\tau_c)^2} - \dfrac{2\zeta_i}{(\omega_{n,i}\tau_c)} + 1\right\}} \tag{20}$$

$$\lambda_4 = \frac{\left[\left(\dfrac{\rho}{\rho'}\right)\left(\dfrac{\tau_c}{\tau_m}\right)-1\right]}{\left[\left(\dfrac{\tau_c}{\tau_m}\right)-1\right]\left\{\dfrac{1}{(\omega_{n,i}\tau_c)^2} - \dfrac{2\zeta_i}{(\omega_{n,i}\tau_c)} + 1\right\}} \tag{21}$$

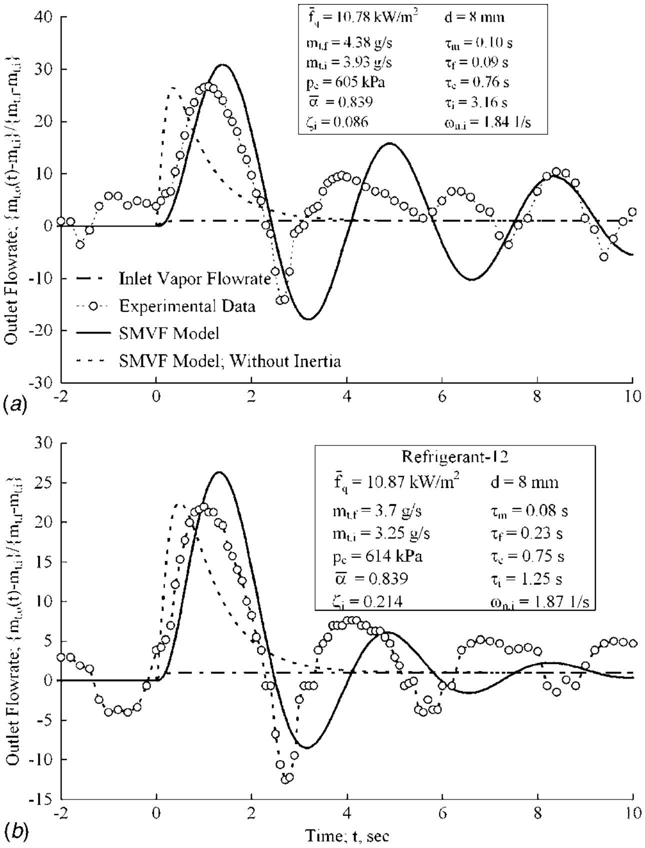

Fig. 1 Comparison between SMVF model and experimental data; vapor flow-rate increase (*a*) and (*b*) with moderate inertia length

Experimental Verification

The experimental apparatus used in the present research is the same as described by Kobus et al. [7]. Therefore, the details of the experimental apparatus will not be repeated here. Briefly, however, uncertainties in differential pressure measurements were less than ±0.138 kPa (±0.02 psi) because, prior to every test, all pressure transducers were calibrated against a digital pressure transducer (Mensor model 14000 digital pressure gage), whose accuracy was better than ±0.069 kPa (±0.01 psi). Uncertainties in absolute pressure measurements were ±1.38 Pa (±0.2 psi). Temperature measurement uncertainties were ±0.42°C (±0.75°F). The standards that were used for flow-measurement calibration were liquid and vapor turbine-type flowmeters, which had an accuracy of ±2% of flow. The calibration curve for the inlet orifice vapor flowmeter was accurate to within ±5% of the flow rate, whereas the outlet variable-orifice liquid flowmeter had a slightly higher uncertainty of ±7–8%. However, steady-state tests showed that the inlet orifice vapor flowmeter measured the flow rate to within 3% of that measured by the vapor turbine flowmeter in the feeder tube for a wide range of flow rates.

Once the system was settled to a steady state, a flow change was initiated with the manual flow control valve and the response recorded. Different conditions could be obtained by changing the temperature of the hot water in the vapor generator, the chilled water circulating around the condenser tube, and the cold water in the low-pressure reservoir. Different flow rates were obtained simply by adjusting the manual flow control valve on the apparatus. Also, the length of the section downstream of the condenser tube was changed to increase the effect of inertia. In this case a length of up to 10 m was added to achieve sufficient mass. Tests were repeated by returning flow and temperature conditions to what they were prior to the transient. Although many sets of data were run (~30 sets for just the transient flow surge phenomenon), the following illustrations are representative of the bulk of the data where the influence of inertia was most prominent. Based on prior research [8], it was seen that the flow surges were of greatest magnitude when the condensing flow system time constant τ_c was small, which is the case when the heat flux is high. Therefore, all of the tests in the current research were run under the highest heat flux obtainable by the experimental apparatus, ~10.8 kW/m^2. Also based on this prior research, the flow surge phenomenon was maximized by faster perturbations. Therefore, the inlet flow change was minimized with τ_m ~0.1 s for all tests. In addition, the effect of compressibility had to be minimized enough to maximize the influence of inertia. The most varied experimental parameter in the current research is the inertia system time constant τ_i, Eq. (5). By keeping the outlet flow resistance small k_o^* and the area of the tube A_t constant, the length downstream of the condenser was the easiest parameter to change.

Figure 1(*a*) illustrates the effect that a small increase (10 and 12% for Figs. 1(*a*) and 1(*b*), respectively, as indicated by the difference in the initial and final flowrates, $m_{t,i}$ and $m_{t,f}$, in the Fig. 1 parameters) in the inlet vapor flow rate has on the outlet liquid flow rate. It is clear that a flow surge of large magnitude, in this case ~300% of the mean flow rate, occurs. Superimposed on Fig. 1 is the prediction of the system mean void fraction model from prior research [8], which did not account for the effect of subcooled liquid inertia. Also superimposed is the prediction of the current SMVF model that includes the effect of inertia. In this case, it is clear that the system is substantially underdamped, as indicated by the overshoot characteristics observed both in the experimental data as well as the prediction of the current model. Note that the damping coefficient is very low, $\zeta_i = 0.086$, primarily resulting from a large inertia system time constant τ_i, which, in turn, is large because of a long test section. Also, comparing the current SMVF model to its predecessor [8], it is clear that the prediction of the current model is far superior, accurately predicting the initial lag in the flow surge due to the condensate inertia and the overshoot characteristics, which are entirely missing from the prediction of the prior SMVF model where inertia was not considered. As seen in the above figure, the initial overshoot following the flow surge is of a large enough magnitude that the flow rate actually becomes negative, signifying a flow reversal (condensate leaving the condenser momentarily stops and heads back into the condenser), which is shown both in the experimental data and the prediction of the current SMVF model.

Figure 1(*b*) illustrates another case of an underdamped transient response following a vapor flow-rate increase. In this case, the system is less underdamped than that in Fig. 1(*a*), with a damping coefficient of 0.214, larger than that of Fig. 1(*a*) because of a smaller inertia system time constant due to shorter condensing system total length. Similar to what was seen in Fig. 1(*a*), the current SMVF model again predicts the initial flow surge, including initial delay, as well as the overshoot characteristics before a new steady state is reached.

Physically, flow surges in in-tube horizontal condensing flow systems occur because, as the vapor flow rate is increased, lower density vapor tends to displace the higher density liquid in the two-phase region. This displacement, in turn, simultaneously causes a temporary excess of vapor in the two-phase region, and the higher density liquid to leave the condenser, resulting in a flow surge. Once this excess vapor is condensed, the system reaches a new steady-state condition. The liquid inertia will temporarily delay this type of flow surge, but, once it occurs, the inertia will then try to keep the flow surge from decaying back to the new steady-state position, potentially resulting in a surge of larger magnitude than would otherwise occur when inertia effects are small.

Conclusions

The current research presents the experimentally verified predictive capability of a system mean void fraction (SMVF) model that predicts large transient flow surges due to perturbations in the inlet vapor flow rate entering the condenser, including the effects of subcooled liquid inertia of the condensate leaving the condensing flow system. The SMVF model was seen to be in good agreement with the experimental data. One of the salient features of the SMVF model is its simplicity, especially in light of the various complexities in modeling two-phase flow phenomena. Yet, in spite of such simplicity, the SMVF model appears to retain the dominant physical mechanisms necessary for accurately predicting transient flow surges and frequency-response characteristics in condensing flow systems, including the effects of inertia coupled with compressibility in the upstream and two-phase vapor regions, property variations with pressure changes, and local and spatial variations of the local area void fraction.

Acknowledgment

The authors would like to acknowledge the contributions of the Oakland University Research Committee and the Michigan Space Grant Consortium for their parts in funding of this research. Acknowledgement is also given to Ryan Ahler, Reena Datta, and Tracy Zapczynski, students who assisted the author in running the experimental apparatus.

Nomenclature

A_t = total cross-sectional area, m^2
d = inside channel diameter, m
D = differential operator
$\overline{f_q}$ = spatially average heat flux, $\mathrm{W/m}^2$
h = enthalpy of saturated liquid, J/kg
k_o = lumped effective outlet orifice coefficient, $\Delta p/\rho v^2$
k_o^* = linearized flow resistance at outlet, $\mathrm{kN\,s/m^2\,g}$
L = length, m
L_o^* = linearized downstream liquid length, m
$m_{t,i}$ = initial steady-state total mass flowrate, kg/s
$m_{t,i}(t)$ = total time-dependent mass flowrate at system inlet, kg/s
$m_{t,f}$ = final steady-state total mass flowrate, kg/s
$m_{t,o}(t)$ = total time-dependent mass flowrate at system outlet, kg/s
P = inside circumference of flow channel, m
t = time, s
$V_{p,\mathrm{eff}}$ = effective vapor volume due to property-pressure variations, m^3
V_u = upstream vapor volume, m^3
$V_{2\phi}$ = total two-phase vapor volume, m^3
x_i = quality of flow entering at the system inlet
z = axial position coordinate from beginning of condensation process, m

Greek symbols

$\alpha(z,t)$ = local area void fraction
$\overline{\alpha}$ = system mean void fraction
β^* = rate of change of saturated liquid enthalpy with pressure, dh/dp, $\mathrm{J\cdot m^2/kg\cdot kN}$
β_o = dimensionless thermodynamic parameter
γ^* = vapor compressibility coefficient; $d\rho'/dp$, kg/m·kN
λ_j = solution coefficients defined in Eq. (19)
η_i = initial position of effective point of complete condensation, m
$\eta(t)$ = position of effective point of complete condensation, m
ρ = density of saturated liquid, $\mathrm{kg/m}^3$
τ_c = condensing flow system time constant, s
τ_f = compressible flow system time constant, s
τ_i = system inertia time constant, s
τ_m = inlet vapor flowrate variation time constant, s
$\omega_{n,i}$ = natural frequency, 1/s
ζ_i = damping coefficient

Subscripts and Superscripts

Primed ($'$) symbols of quantities refer to saturated vapor. Symbols of quantities generally refer to time-averaged quantities where the averaging time is small enough so as to just eliminate the inherent fluctuations but not interfere with the deterministic transient.

References

[1] El-Wakil, M. M., 1984, *Powerplant Technology*, McGraw-Hill, New York.
[2] Hewitt, G. F., Shires, G. L., and Bott, T. R., 1993, *Process Heat Transfer*, Begell House, New York, and CRC Press, Boca Raton.
[3] Collier, J. G., and Thome, J. R., 1994, *Convective Boiling and Condensation*, Oxford University Press, New York.
[4] Wallis, G. B., 1969, *One-Dimensional Two-Phase Flow*, McGraw-Hill, New York.
[5] Kobus, C. J., 2003 "An Investigation Into the Effect of Subcooled Liquid Inertia on Flowrate Induced Frequency-Response Characteristics of Horizontal Condensing Flow Systems," *Proc. of 6th ASME/JSME Thermal Engineering Joint Conference (AJTEC)*, March 16–23, Hawaii.
[6] Kobus, C. J., 2003, "An Investigation into the Effect of Subcooled Liquid Inertia on Flowrate Induced Transient Flow Surges in Horizontal Condensing Flow Systems," *Proc. of ASME Summer Heat Transfer Conference, Las Vegas, July 21–23*.

[7] Kobus, C. J., Wedekind, G. L., and Bhatt, B. L., 2001, "Predicting the Onset of a Low-Frequency Self-Sustained Oscillatory Flow Instability in Multitube Two-Phase Condensing Flow Systems," ASME J. Heat Transfer, **123**(2), pp. 319–330.

[8] Bhatt, B. L., and Wedekind, G. L., 1980, "Transient and Frequency Response Characteristics of Two-Phase Condensing Flows: With and Without Compressibility," ASME J. Heat Transfer, **102**(3), pp. 495–500.

[9] Bhatt, B. L., and Wedekind, G. L., 1984, "An Experimental and Theoretical Study Into the Determination of Condensing Length," *Basic Aspects of Two-Phase Flow and Heat Transfer, 22nd National Heat Transfer Conference*, V. K. Dhir and V. E. Schrock, eds., Niagara Falls, pp. 179–183.

[10] Zivi, S. M., 1964, "Estimation of Steady-State Steam Void Fraction by Means of the Principle of Minimum Entropy Production," ASME J. Heat Transfer, **86**, p. 247.